ELECTRODIFUSION OF MANGANESE ATOMS IN SILICON

Xalmurat M. Iliyev, Zafar B. Khudoynazarov, Bobir O. Isakov*, Mirahmat X. Madjitov, Abduvokhid A. Ganiyev

Tashkent State Technical University, University St., 2, 100095, Tashkent, Uzbekistan
*Corresponding Author e-mail: bobir6422isakov@gmail.com
Received April 2, 2024; revised May 3, 2024; accepted May 11, 2024

The paper describes the research and study of the process of electrically induced diffusion of Mn atoms in silicon directly from a *Si* surface layer that was preliminarily enriched with *Mn*. To ensure the so-called electrically induced diffusion process, a constant electric field was applied to the investigated samples. It has been revealed that as a result of the diffusion of *Mn* impurity atoms into samples placed at the negative pole of the electrical diffusion unit, the proportion of *Mn* atoms was 75.4% (relative to silicon atoms), while in samples placed at the positive pole this indicator tended to be 2.7% (relative to silicon atoms). Besides that, for the first time, an experimental increase in the electro-active concentration of *Mn* impurity atoms in silicon (at $T = 900°C$) was detected under the influence of an external constant-value electric field. In this case, the maximum solubility of impurity atoms of *Mn* at a temperature of $T = 900°C$ was $N_{Mn} \sim 2.27 \cdot 10^{14}$ cm^{-3}, while the average concentration of electro-active *Mn* atoms diffused into silicon under the influence of an external constant electric field reached $N_{Mn}^* \sim 2.62 \cdot 10^{14}$ cm^{-3}.

Keywords: *Resistivity; Silicon; Impurity atoms; Diffusion; Mobility of charge carriers; Concentration of charge carriers; Electrically induced diffusion*
PACS: 61.72.uf, 68.43.Jk

1. INTRODUCTION

Over recently, of great interest to many researchers in the field of semiconductor physics was the issue of engineering fundamentally novel materials by modifying the functional parameters of semiconductors, especially *Si* [1,2]. One of the most promising ways appears to be the technique of engineering of binary compounds of type *III-V* and *II-VI* in the bulk matrix of *Si* material [3,4,5,6,7] and on its surface alike [8,9,10,11]. However, in times of creating compounds of type *II-VI* in the silicon crystal lattice, due to the insufficient solubility ratio of elements of groups *II* and *VI* in the *Si* material $(\sim 10^{15} \div 10^{18})$, it is almost impossible to prove the phenomenon of a significant change in the functional parameters of *Si* by using the existing instrumentation. In this regard, a significant increase in the solubility of impurity atoms in a *Si* crystal has both scientific and practical significance.

The authors of the study expect that using the proposed technique of electrically induced diffusion, it would be possible not only to increase the solubility of impurity atoms in silicon, but also to theoretically increase the diffusion coefficients of impurity atoms in silicon under the influence of an external electric field. This could help not only to increase the solubility of elements of groups *II* and *VI* in silicon, but also to boost diffusion coefficients of elements of groups *III* and *V* in silicon, which are traditionally characterized by comparatively low diffusion coefficients, but quite a high $(\sim 10^{18} \div 10^{21})$ solubility [12-15].

This paper presents the results of elemental analysis and studies of the electrical parameters of silicon samples doped with *Mn* impurity atoms under the influence of an external electric field.

2. MATERIALS AND METHODS

Silicon wafers of *p*-type conductivity ($\rho \sim 5$ $\Omega \cdot$cm; $N_B \sim 5 \times 10^{15}$ cm^{-3}) were the starting material. Samples sized $1 \times 5 \times 10$ mm^3 were cut from the wafers using an *STX-402*-type diamond cutter. Surfaces of the silicon samples were chemically cleaned with *HF* acid. Manganese atoms (purity 99.999%) were deposited onto the surface of the samples using a *VUP-4* vacuum deposition unit, after which thin layers of manganese were formed on the surfaces of the samples. 2 silicon samples with thin layers of *Mn* were placed into the electrical diffusion unit with thin layer surfaces facing each other. In this case, one of the samples was placed at the positive pole side of the electrical diffusion unit, and the other - at the negative one.

The investigated samples were divided into 3 groups:

Group I consisted of silicon samples with thin layers of manganese on the surface, which were placed at the positive pole of the electrical diffusion unit;

Group II consisted of silicon samples with thin layers of manganese on the surface, which were placed at the negative pole of the electrical diffusion unit;

Group III consisted of samples with thin layers of manganese on the surface, which were placed in an evacuated quartz ampoule for diffusion in a furnace.

In samples of groups I and II, the process of electrically induced diffusion was carried out by ensuring the flow of a direct current with density of $50 \div 100$ A/cm^2. Due to the presence of electrical resistance at the points of contact of the samples, the samples normally heat up. The heating temperature can be controlled by adjusting the electric current value. The temperature resulting from the flow of electric current in the samples during the experiment was $T = 900°C$.

In samples of group III, diffusion was carried out in a diffusion furnace at a temperature of 900°C.

After electrically induced diffusion, elemental analysis of samples of groups I and II was carried out using a *JSM-IT 200* scanning electron microscopes [16] (Fig. 1).

Group I

Group II

a)

b)
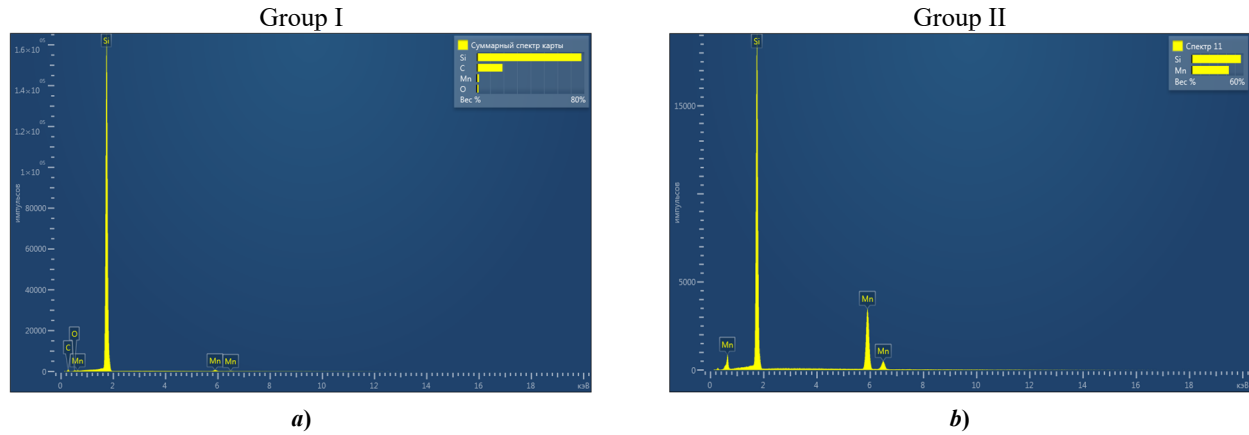
Element	Type of curve	Weight %	Sigma weight %
Si	K series	77.89	0.20
C	K series	18.95	0.20
Mn	K series	2.1	0.50
O	K series	1.06	0.50
Total:		100.00	

Element	Type of curve	Weight %	Sigma weight %
Si	K series	57.01	0.20
Mn	K series	42.99	0.20
Total:		100.00	

Figure 1. Elemental analysis of a silicon sample with Mn impurity atoms using the electrically induced diffusion method: *a*) sample belonging to the group I (sample placed at the positive pole of the electrical diffusion unit); *b*) the group II sample (sample placed at the negative pole of the electrical diffusion unit)

The profiles of distribution of impurity atoms across the depth received in the course of a layer-by-layer chemical etching of samples of groups I, II and III, were studied using the Hall effect measurement unit *HMS-3000* from ECOPIA [17] (Fig. 2).
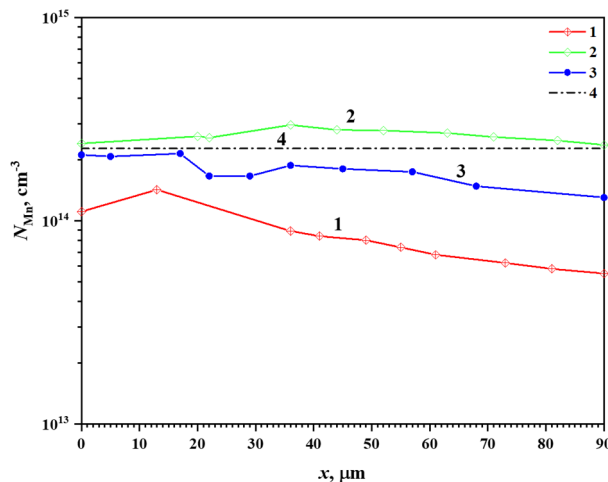
Figure 2. Distribution profile across the depth of impurity atoms of manganese in samples belonging to groups I, II and III: curve 1 - group I; curve 2 - sample of group II; curve 3 - sample of group III; curve 4 reflects the maximum solubility of manganese impurity atoms in silicon at a temperature of 900°C.

3. RESULTS AND DISCUSSION
3.1. Analysis of the SEM-investigation results

Figures 1-*a*) and 1-*b*) show elemental analyzes of samples placed at the positive and, accordingly, negative poles at a constant electric field. Tables *a*) and *b*) provide numerical elemental analysis data for the samples shown in Figures 1*a*) and 1*b*), respectively. From Figure 1 and the table it is clear that manganese atoms appear to have penetrated more towards

the sample placed at the negative pole at a constant electric field. Moreover, in tables *a*) and *b*), when calculating using the formula for the weight of manganese atoms relative to silicon atoms, it was established that in silicon samples placed at the negative pole of the electrical diffusion unit, the fraction of manganese atoms appears to be 75.4%, while in silicon samples placed at the positive pole, this figure was 2.7%.

3.2. Analysis of electrophysical parameters

The Figure 2 proves that the concentration of impurity atoms of manganese in the group II sample placed at the negative pole of the electrical diffusion unit, noticeably exceeds the concentration of impurity atoms of manganese in samples belonging to groups III and I. In this case, the average concentration of electro-active manganese atoms in samples of group I was $N_{Mn}^I \sim 8.23 \cdot 10^{13}$ cm^{-3}, the average concentration of electro-active manganese atoms in samples of group II was $N_{Mn}^{II} \sim 2.62 \cdot 10^{14}$ cm^{-3}, the average concentration of electro -active manganese atoms in samples of group III was $N_{Mn}^{III} \sim 1.78 \cdot 10^{14}$ cm^{-3}, and the maximum solubility of impurity Mn atoms at a temperature of $T = 900$°C was $N_{Mn} \sim 2.27 \cdot 10^{14}$ cm^{-3}.

The diffusion coefficient of impurity atoms of manganese in silicon at a certain temperature is determined using the equation (1), the solubility is determined using the equation (2).

$$D_{Mn}(T) = 2.6 \cdot 10^{-1} \cdot \exp\left(-\frac{1.3}{k \cdot T}\right) \tag{1}$$

$$N_{Mn}(T) = 2.5 \cdot 10^{23} \cdot \exp\left(-\frac{2.1}{k \cdot T}\right) \tag{2}$$

The Table 1 proves that the maximum solubility of manganese atoms at a temperature of $T = 900$°C is $2.27 \cdot 10^{14}$ cm^{-3}. However, the concept of solubility is applicable to the grand total concentration of both electro-active and non-electro-active manganese atoms.

Table 1. Diffusion coefficients and solubility of impurity atoms manganese in silicon at a given temperature

T, °C	700	750	800	850	900	950	1000
$D_{Mn}(T)$	$4.65 \cdot 10^{-8}$	$9.94 \cdot 10^{-8}$	$1.98 \cdot 10^{-7}$	$3.7 \cdot 10^{-7}$	$6.58 \cdot 10^{-7}$	$1.11 \cdot 10^{-6}$	$1.81 \cdot 10^{-6}$
$N_{Mn}(T)$	$3.15 \cdot 10^{12}$	$1.07 \cdot 10^{13}$	$3.27 \cdot 10^{13}$	$9.01 \cdot 10^{13}$	$2.27 \cdot 10^{14}$	$5.33 \cdot 10^{14}$	$1.17 \cdot 10^{15}$

An analysis of the reference data showed that impurity atoms of manganese in silicon normally create 3 energy levels in silicon (2 donor levels with the values $E_c = -0.12$ and $E_c = -0.41$ eV and 1 acceptor level with the value $E_v = +0.32$ eV) [18,19,20]. Impurity atoms of manganese could be present in a silicon matrix in the form of a Mn^- ion (adding one electron), a neutral Mn^0 atom without having to add or donate one electron, a singly positively charged Mn^+ ion with the transfer of one electron, and a doubly positively charged ion Mn^{++}. The total concentration of impurity atoms of manganese in silicon is determined by formula (3):

$$N_{Mn}^{total} = N_{Mn^-} + N_{Mn^0} + N_{Mn^+} + N_{Mn^{++}} \tag{3}$$

However, using the Hall measurement method, only the concentration of electro-active atoms of Mn can be determined. Therefore, in this study, provided that impurity atoms of Mn presumably have compensated impurity atoms of boron in silicon, so the authors have determined only the sum of the concentrations of Mn^+ and Mn^{++} ions (the concentration determined from Fig. 2 is equal to the sum of concentrations).

CONCLUSION

Thus, it can be assumed that the Mn^+ and M^{++} ions most probably migrate towards the negative pole of the electrical diffusion unit both under the influence of temperature and under the influence of an external constant electric field, while the Mn^- ions both under the influence of temperature and under the influence of external constant electric field seem to migrate towards the positive pole of the electrical diffusion unit. Behavior of neutral Mn^0 atoms is not affected by the external electric field, however neutral atoms appear to diffuse into the sample under the influence of temperature.

The experimental results showed that in the sample placed at the negative pole of the electrical diffusion unit, the concentration of electroactive impurity atoms of Mn tended to increase under the influence of an external constant electric field. These results were also confirmed by SEM analysis.

ORCID
Xalmurat M. Iliyev, https://orcid.org/0000-0002-2742-0190; **Bobir O. Isakov**, https://orcid.org/0000-0002-6072-3695

REFERENCES
[1] M.K. Bakhadyrkhanov, A.Sh. Mavlyanov, U.Kh. Sodikov, and M.K. Khakkulov, "Silicon with Binary Elementary Cells as a Novel Class of Materials for Future Photoenergetics", Applied Solar Energy, **51**(4), 258–261 (2015). https://doi.org/10.3103/S0003701X1504009X
[2] M.K. Bakhadyrkhanov, S.B. Isamov, N.F. Zikrillaev, and M.O. Tursunov, "Anomalous Photoelectric Phenomena in Silicon with Nanoclusters of Manganese Atoms," Semiconductors, **55**(6), 542–545 (2021). https://doi.org/10.1134/S1063782621060038

[3] X.M. Iliyev, V.B. Odzhaev, S.B. Isamov, B.O. Isakov, B.K. Ismaylov, K.S. Ayupov, Sh.I. Hamrokulov, and S.O. Khasanbaeva, "X-ray diffraction and Raman spectroscopy analyses of GaSb-enriched Si surface formed by applying diffusion doping technique," East Eur. J. Phys. (3), 363 (2023). https://doi.org/10.26565/2312-4334-2023-3-38

[4] X.M. Iliyev, S.B. Isamov, B.O. Isakov, U.X. Qurbonova, and S.A. Abduraxmonov, "A surface study of Si doped simultaneously with Ga and Sb", East Eur. J. Phys. (3), 303 (2023). https://doi.org/10.26565/2312-4334-2023-3-29

[5] J. Liu, and S. Yue, "Fabrication of ZnS layer on silicon nanopillars surface for photoresistor application," Chemical Physics Letters, **801**, 139716 (2022). https://doi.org/10.1016/j.cplett.2022.139716

[6] J. Kang, J.-S. Park, P. Stradins, and S.-H. Wei, "Nonisovalent Si-III-V and Si-II-VI alloys: Covalent, ionic, and mixed phases," Physical Review B, **96**, 045203 (2017). https://doi.org/10.1103/PhysRevB.96.045203

[7] N.F. Zikrillaev, M.K. Khakkulov, and B.O. Isakov, "The mechanism of the formation of binary compounds between Zn and S impurity atoms in Si crystal lattice," East Eur. J. Phys. (4), 177 (2023). https://doi.org/10.26565/2312-4334-2023-4-20

[8] M. Niehle, J.-B. Rodriguez, L. Cerutti, E. Tournie, and A. Trampert, "On the origin of threading dislocations during epitaxial growth of III-Sb on Si(001): A comprehensive transmission electron tomography and microscopy study," Acta Materialia, **143**, 121-129 (2018). https://doi.org/10.1016/j.actamat.2017.09.055

[9] J. Liu, M. Tang, H. Deng, S. Shutts, L. Wang, P.M. Smowton, C. Jin, et al., "Theoretical analysis and modelling of degradation for III–V lasers on Si," Journal of Physics D: Applied Physics, **55**, 404006 (2022). https://doi.org/10.1088/1361-6463/ac83d3

[10] Y. Goswami, P. Asthana, and B. Ghosh, "Nanoscale III–V on Si-based junctionless tunnel transistor for EHF band applications," Journal of Semiconductors, **38**(5) 054002 (2017). https://doi.org/10.1088/1674-4926/38/5/054002

[11] N.F. Zikrillayev, S.B. Isamov, B.O. Isakov, T. Wumaier, Li wen Liang, J.X. Zhan, and T. Xiayimulati, "New Technological Solution for the Tailoring of Multilayer Silicon-based Systems with Binary Nanoclusters Involving Elements of Groups III and V," Journal of nano- and electronic physics, **15**(6), 06024 (2023). https://doi.org/10.21272/jnep.15(6).06024

[12] D. Senk, and G. Borchardt, "Solubility and Diffusivity of Manganese in Silicon at High Temperatures," Mikrochimica Acta, **80**, 477–490, (1983). https://doi.org/10.1007/BF01202026

[13] N.A. Arutyunyan, A.I. Zaitsev, N.G. Shaposhnikov, and S.F. Dunaev, "The Thermodynamic Properties of Solid Solutions of Manganese and Iron in Silicon", Russian Journal of Physical Chemistry A, **84**(9), 1498–1501 (2010). https://doi.org/10.1134/S0036024410090084

[14] A. Mostafa, and M. Medraj, "Binary Phase Diagrams and Thermodynamic Properties of Silicon and Essential Doping Elements (Al, As, B, Bi, Ga, In, N, P, Sb and Tl)", Materials, **10**(6), 676 (2017). https://doi.org/10.3390/ma10060676

[15] F.A. Trumbore, "Solid Solubilities of Impurity Elements in Germanium and Silicon", The Bell system technical journal, **39**, 205-233, (1960). https://doi.org/10.1002/j.1538-7305.1960.tb03928.x

[16] N.F. Zikrillaev, G.A. Kushiev, Sh.I. Hamrokulov, and Y.A. Abduganiev, "Optical Properties of Ge_xSi_{1-x} binary compounds in silicon," Journal of nano- and electronic physics, **15**(3), 03024-1 - 03024-4, (2023). https://doi.org/10.21272/jnep.15(3).03024

[17] N.F. Zikrillaev, G.A. Kushiev, S.V. Koveshnikov, B.A. Abdurakhmanov, U.Kh. Kurbanova, and A.A. Sattorov, "Current status of silicon studies with Ge_xSi_{1-x} binary compounds and possibilities of their applications in electronics," East European journal of physics, (3), 334-339 (2023). https://doi.org/10.26565/2312-4334-2023-3-34

[18] H. Nakashima, and K. Hashimoto, "Deep impurity levels and diffusion coefficient of manganese in silicon," Journal of Applied Physics, **69**, 1440 (1991). https://doi.org/10.1063/1.347285

[19] N.F. Zikrillaev, O. B. Tursunov, and G. A. Kushiev, "Development and Creation of a New Class of Graded-Gap Structures Based on Silicon with the Participation of Zn and Se Atoms," Surf. Engin. Appl. Electrochem. **59**(5), 670–673 (2023). https://doi.org/10.3103/S1068375523050198

[20] N.F. Zikrillaev, S.V. Koveshnikov, S.B. Isamov, B.A. Abdurahmonov, and G.A. Kushiev, "Spectral dependence of the photoconductivity of Ge_xSi_{1-x} type graded-gap structures obtained by diffusion technology," Semiconductors, 56(1), 29-31 (2022). https://doi.org/10.1134/S1063782622020191

ЕЛЕКТРОДИФУЗІЯ АТОМІВ МАРГАНЦЮ В КРЕМНІЇ

Халмурат М. Ілієв, Зафар Б. Худойназаров, Бобір О. Ісаков, Мірахмат Х. Маджитов, Абдувохід А. Ганієв
Ташкентський державний технічний університет, вул. Університетська, 2, 100095, Ташкент, Узбекистан

У статті описано дослідження та дослідження процесу електроіндукованої дифузії атомів *Mn* у кремнії безпосередньо з поверхневого шару *Si*, попередньо збагаченого *Mn*. Для забезпечення так званого процесу електроіндукованої дифузії до досліджуваних зразків прикладали постійне електричне поле. Виявлено, що в результаті дифузії атомів домішки Mn в зразки, розміщені на негативному полюсі електродифузійної установки, частка атомів *Mn* становила 75,4% (відносно атомів кремнію), а в зразках, розташованих на позитивному полюсі полюсі цей показник мав тенденцію до 2,7% (відносно атомів кремнію). Крім того, вперше експериментально виявлено збільшення електроактивної концентрації атомів домішки *Mn* у кремнії (при *T = 900°C*) під впливом зовнішнього постійного електричного поля. При цьому максимальна розчинність домішкових атомів *Mn* при температурі *T = 900°C* становила $N_{Mn} \sim 2{,}27 \cdot 10^{14}$ *см⁻³*, а середня концентрація електроактивних атомів *Mn* дифундувала в кремній під впливом зовнішнього постійне електричне поле досягло $N_{Mn*} \sim 2{,}62 \cdot 10^{14}$ *см⁻³*.

Ключові слова: *питомий опір; кремній; домішкові атоми; дифузія; рухливість носіїв заряду; концентрація носіїв заряду; електрично індукована дифузія*

ELECTRIC FIELD ENHANCEMENT BY GOLD NANO-SPHERE AND ITS CLUSTERS

P.K. Kushwaha[a,b]*, **K.Y. Singh**[a,b], **Himmat Singh Mahor**[a,b], **Pramod Kumar Singh**[c],
Ravish Sharma[a,b], **Kash Dev Sharma**[a,b]

[a]Department of Physics, B.S.A. (P.G.) College, Mathura (U.P.) India 281004
[b]Dr. Bhimrao Ambedkar University, Agra (U.P.) India 282004
[c]Department of Physics, Hindustan College of Science & Technology, Farah, Mathura (U.P.) India 281122
*Corresponding Author e-mail: pankaj08au@gmail.com
Received March 10, 2024; revised April 1, 2024; accepted April 23, 2024

The confinement of electrons in gold nanoparticles results in Surface Plasmon Resonance (SPR), which is characterized by electric field enhancement in the vicinity of these nanoparticles. This property has been extensively studied and applied in various fields. In our research, we conduct a detailed investigation of plasmonic coupling in spherical gold nanoparticles. Specifically, we use the Discrete Dipole Approximation (DDA) method implemented in DDSCAT to simulate the coupling of electric fields in a doublet of nanoparticles as a function of the distance between them. Our simulations show that the coupling of SPR between two nanoparticles occurs up to a separation of 12 nm. Moreover, we extend our simulations to study the coupling of nanoparticles in linear chains consisting of up to five nanoparticles and in clustered forms. Our results indicate that the SPR coupling in a linear chain occurs, and as the number of nanoparticles increases, the field enhancement also increases. However, we observe that this effect saturates after four nanoparticles in a line. Our study provides insights into the plasmonic coupling in gold nanoparticles, which can aid in the design and optimization of plasmonic devices for various applications.
Keywords: *Surface Plasmon resonance (SPR); Gold Nano particles; Discrete Dipole Approximation (DDA); DDSCAT; Field Enhancement*
PACS:71.45.Gm, 81.07.−b, etc.

INTRODUCTION

Noble metal particles exhibit exceptional optical properties owing to plasmonic resonances at metal-dielectric interfaces [1]. These resonances are a collective oscillation of free electrons on the surface of the nanoparticle triggered by incident electromagnetic waves. As a result, there is a strong confinement of the electromagnetic field along the surface normal of the nanoparticle, leading to a significant enhancement of the electromagnetic field. This enhancement causes strong absorption and scattering near the plasmon resonance frequency. Raman Spectroscopy has gained considerable attention due to its ability to provide molecular information with high sensitivity by analyzing molecules absorbed on metallic surfaces or metal nanostructures [2].

To fully utilize the potential of these enhanced electric fields, it is necessary to understand the various phenomena resulting from the highly intense and confined field. These fields generate strong electric field gradients, which alter selection rules, and mode intensities and have profound effects on Raman Spectra [3-9]. Knowledge of field distribution and polarization is critical to arrive at approximate enhancement factors. In light of this, we conducted a study of the electric field distribution around gold nanoparticle clusters. Several methods have been presented in the literature for simulating the electric field distribution around a particle. The most commonly used among these are Mie-Scattering, T-matrix method, Finite Element Method (FEM), Finite Difference Time Domain (FDTD), and Discrete Dipole Approximation (DDA) based methods. Each of these methods has its advantages and disadvantages. Mie Scattering and T-matrix methods are fast but are limited to structures with certain symmetry in the geometry. FEM and FDTD methods can determine the scattered electric field distribution of arbitrarily shaped particles, but the computation time for these methods is very large [10]. We opted to use the DDA method because it is fast and can compute field distribution for arbitrarily shaped particles [11-14].

DISCRETE DIPOLE APPROXIMATION (DDA) METHOD

The Discrete Dipole Approximation (DDA) is an effective method to model particles as a group of finite cubic elements [11]. By considering only dipole interactions with the incident electric field and induced-fields from neighboring elements, the solution of the Maxwell equations can be simplified into an algebraic problem of many coupled dipoles. Each dipole in the assembly responds to both the external electric field and the electric fields from its neighboring dipoles by acquiring a dipole moment. To solve the electromagnetic scattering problem of a continuous assembly, the induced dipole moment of each dipole is given by $\mathbf{P}_i = \alpha_i \mathbf{E}_{local}$, where α_i denotes the polarizability of the material associated with the dipole element. The polarizability, which can be expressed as Clausius-Mossotti polarizability, plays a crucial role in determining the behavior of the electromagnetic scattering problem and can be used to predict the electromagnetic responses of the assembly.

$$\alpha_i^{CM} = \frac{3d^3}{4\pi} \frac{\varepsilon_i - 1}{\varepsilon_i + 2}.$$ (1)

The Clausius-Mossotti polarizability is a concept used to describe the interactions between electric fields and matter. However, it is only accurate in the limit of a DC (direct current) field, which means when the wave vector is very small. This model does not take into account the size-dependent effects that are observed in nanoparticles. To address this discrepancy, Draine and Goodman [11] conducted a study on wave propagation on an infinite lattice with discrete spacing between lattice points. They were able to derive a dispersion relation in the long wavelength limit, which led to a more accurate description of polarizability in nanoparticles.

$$\alpha^{LDR} = \frac{\alpha^{CM}}{1 + \left(\alpha^{CM} / d^3\right)\left[\left(b_1 + m^2 b_2 + m^2 b_3 S\right)(kd)^2 - (2/3) i (kd)^3\right]},$$ (2)

b1= -1.891531; b2=0.1648469; b3 = -1.7700004; $S = \sum_{i=1}^{3} \left(\hat{a}_i \hat{e}_i\right)^2$.

Where a and e are unit vectors defining the incident direction and polarization state, "m" are complex refractive index of the material in the medium and "d" is lattice spacing and ε is the complex dielectric constant of the material in medium. Equation (2) holds good in the long wavelength limits and is also accurate to O $(kd)^3$.

The electric field at any point in the space due to the incident plane wave is given by the

$$\vec{E}_{local} = \vec{E}_{inc,i} + \sum_{j=1, i \neq j} \vec{E}_j ,$$ (3)

$$\vec{E}_{local} = \vec{E}_{inc,i} - \sum_{j=1, i \neq j} A_{ij} \vec{P}_j .$$ (4)

Where $\mathbf{E}_{local}$ is the electric field at r_i due to the incident wave ($\mathbf{E}_{inc,i}$), plus a contribution $\mathbf{E}_j = - \mathbf{A}_{ij}\mathbf{P}_j$, the radiated electric field of an individual dipole at r_j. The interaction matrix ($\mathbf{A}_{ij}$) is given by

$$A_{ij} = \frac{\exp(ikr_{ij})}{r_{ij}} \left[k^2 \left(\hat{r}_{ij}\hat{r}_{ij} - 1_3\right) + \frac{ikr_{ij} - 1}{r_{ij}^2} \left(3\hat{r}_{ij}\hat{r}_{ij} - 1_3\right) \right]. \ i \neq j ,$$ (5)

Where k=ω/c, $r_{ij} = |\mathbf{r}_i - \mathbf{r}_j|$, 1_3 is a 3x3 unit matrix.

Defining $\mathbf{A}_{ii} = \alpha_i^{-1}$ reduces the scattering problem to finding the polarizations $\mathbf{P}_i$ that satisfy a system of 3N complex linear equations

$$\sum_{j=1}^{N} A_{ij} \vec{P}_i = \vec{E}_{inc,i} .$$ (6)

Once the equation (6) is solved for unknown polarization $\mathbf{P_i}$, the extinction and absorption cross-section C_{ext} and C_{abs} may be evaluated as

$$C_{ext} = \frac{4\pi k}{|E_0|^2} \sum_{i=1}^{N} \text{Im}\left(E_{inc,i}^* \cdot P_i\right),$$ (7)

$$C_{abs} = \frac{4\pi k}{|E_0|^2} \sum_{i=1}^{N} \left\{ \text{Im}\left(P_i.(\alpha_i^{-1})^* \cdot P_i^*\right) - \frac{2}{3} k^3 |P_i|^2 \right\} .$$ (8)

The scattering cross-section $C_{sca} = C_{ext} - C_{abs}$. In the far field, the scattered electric field is given by

$$E_{sca} = \frac{k^2 \exp(ikr)}{r} \left[\sum_{i=1}^{N} \exp\left(-ik\hat{r} \cdot \vec{r}_j\right)\left(\hat{r}\hat{r} - 1_3\right) \vec{P}_j \right].$$ (9)

The DDA computations have specific criteria that must be met to be applicable [12]. These criteria are as follows:
1) The distance between the dipoles, also known as the inter-dipole separation 'd', must be smaller than the wavelength in the medium, such that |m|kd ≤ 1.
2) The inter-dipole separation 'd' should be small enough or the number of dipoles 'N' should be large enough to accurately represent the target shape.

SIMULATION RESULTS
Simulation of Surface Plasmon Resonance (SPR) of Spherical Nanospheres
The present study concerns the wavelength dependence of the extinction cross-section of an isolated spherical gold nanoparticle with a diameter of 40 nm. The calculations were performed within the wavelength range of 450-700 nm,

which corresponds to the surface plasmon resonance (SPR) band. To investigate the influence of the number of dipoles on the results, the calculations were repeated several times with varying numbers of dipoles, ranging from approximately 500 to 22500, as shown in Table 1.

In this study, we compared the results obtained through experimental analysis with the analytical calculations for a sphere, using the well-known Bohren and Huffman code based on the Mie scattering theory [14]. Our research focuses on the extinction spectra of a 20 nm radius Au sphere in an aqueous medium (water n = 1.33), with the refractive index of the gold nanoparticles taken from Johnson and Christy [15]. Figure 1 displays the obtained extinction spectra, which demonstrate that the accuracy of the computed extinction coefficients improves with an increasing number of dipoles used in the computation. This observation is consistent with the existing literature, which highlights that the inter dipole spacing of 1-2 nm range is required to obtain the optical properties of the metallic nanoparticles with great accuracy.
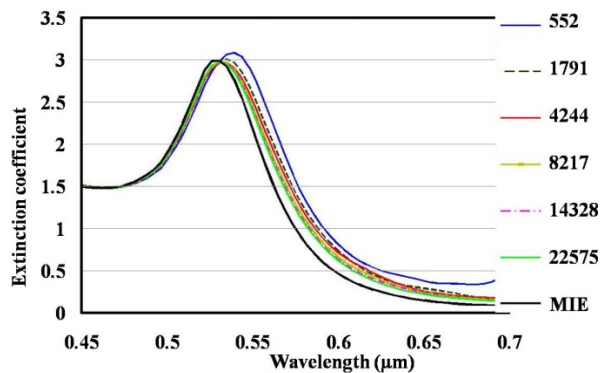
Table 1. The lattice spacing corresponding to the number of dipoles

Number of Dipoles	Lattice Spacing (nm)
552	3.930
1791	2.665
4224	1.994
8217	1.598
14328	1.327
22575	1.141

Figure 1. Convergence of extinction spectra obtained by DDA to Mie - Scattering with the increase in the number of the dipoles

We conducted a study to examine the impact of the size of a sphere on the spectral position of resonance. To do this, we analyzed three spheres with varying radii of 10, 20, and 30 nm, while keeping the lattice spacing at approximately 1.5 nm. We then calculated their surface plasmon resonance (SPR), and the results are presented in Figure 2. We also included a table (Table 2) that lists the SPR for each nanoparticle.
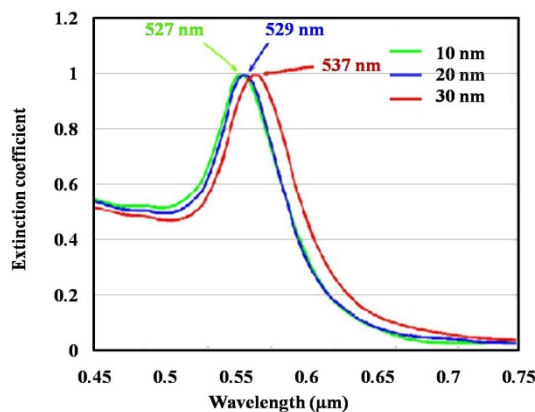
Table 2. Surface Plasmon Resonance vs. Radius

Radius (nm)	Resonance Peak (nm)
10	527
20	529
30	537

Figure 2. Extinction spectra of 10, 20, and 30 nm radius sphere in water
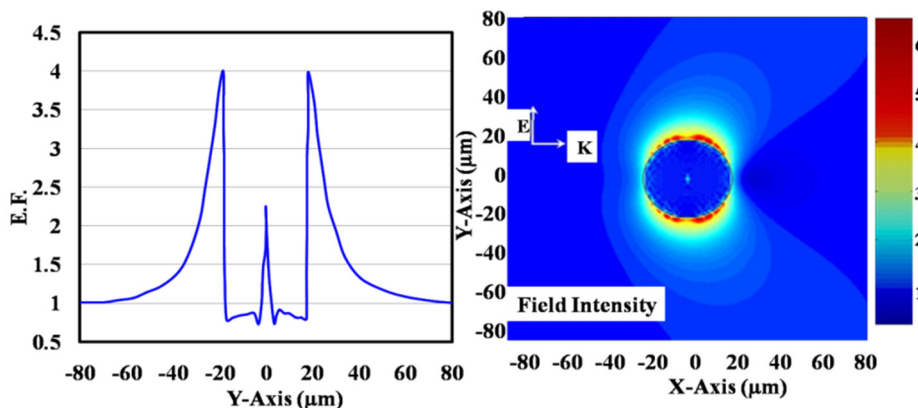
Figure 3. Electric field pattern of a 20 nm radius sphere (K‖X, E‖Y) on the right, and on the left field enhancement around a nano-sphere along the Y-axis

As expected, we observed a red shift in the SPR peak with an increase in the sphere's diameter (size). Moreover, we studied the scattered electric field distribution around 20 nm radius gold (Au) sphere in water (Figure 3).

We analyzed the variation of the electric field enhancement (FE) across the nanoparticle and found that within the range of a few tens of nanometers, the field value drops to the magnitude of the incident electric field. This information can be used to compute the electric field gradient near the nanoparticles.

AGGREATES OF NANO SPHERES

Self-assembled clusters of nanospheres have garnered significant interest due to their low-cost approach for a wide range of plasmonic applications. Compared to other nanofabrication techniques, such as electron beam lithography and focused ion beam, these clusters offer an affordable alternative. By varying the composition, number, and position of the nanoparticles in these clusters, the plasmonic properties can be controlled and exhibit sharp resonances and steep enhancements, also known as hot spots. We have conducted simulations of the electric field of simple clusters consisting of up to five spherical particles of nano size.

DOUBLETS OF NANOSPHERES

The plasmonic properties and electric field distribution around doublets of nano-sphere were simulated for various separations between spheres. It was observed that there are two SPR peaks in the case of doublets; one identical to that obtained in an isolated sphere (transverse mode) and a red-shifted mode attributed to the longitudinal SPR mode. The longitudinal mode is due to plasmon oscillation along the line joining the two spheres. The longitudinal mode is very sensitive to the separation between the two spheres and shifts towards the transverse mode as the spacing is increased. It merges with the transverse mode when the separation becomes too large for any significant interaction between the plasmonic oscillations in the two spheres. Figure 4 shows the extinction spectra of the doublet structure for various separations, and the spectral position of the longitudinal mode is listed in Table 3. The field enhancement increases as the separation between two spheres decreases.
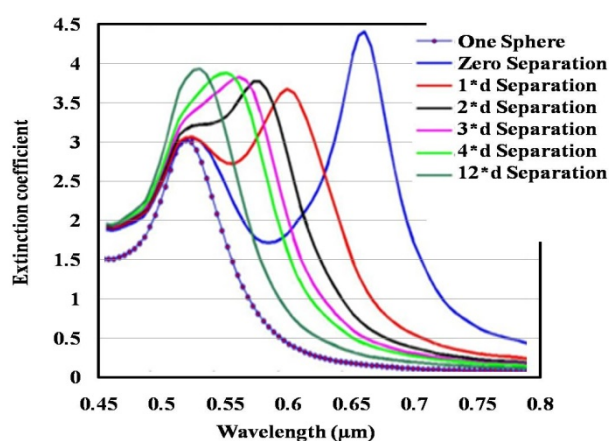
Table 3. Longitudinal modes with separation

Separation Between two spheres in terms of d (d = 1.1nm)	Longitudinal mode (nm)
Zero	665
1*d	605
2*d	584
3*d	570
4*d	560
12*d	540

Figure 4. Extinction spectra of doublet structure with the separation.

a)   b)   c)
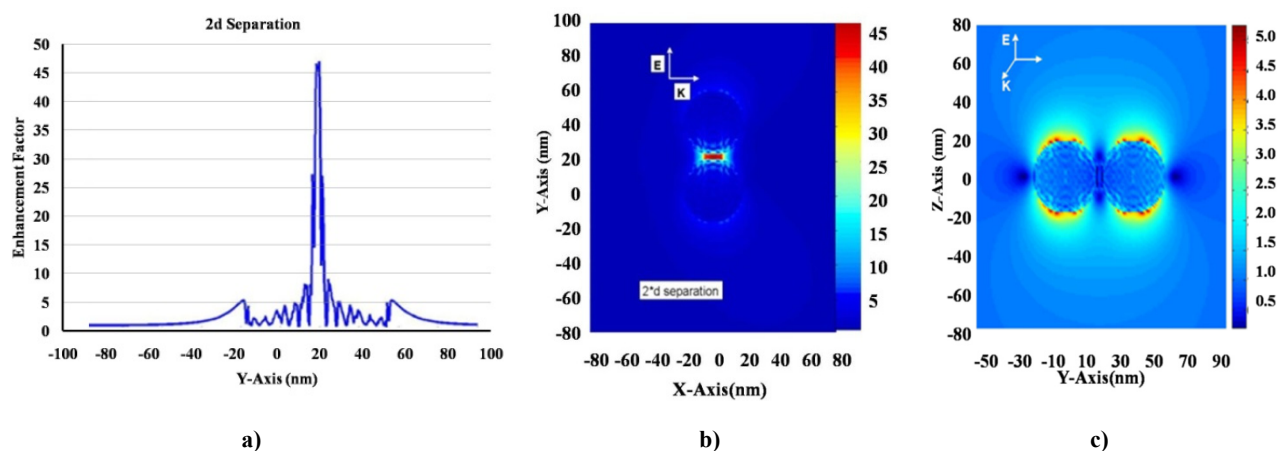
Figure 5. Electric field patterns (5b & 5c) and its magnitude (5a) along Y-axis of a doublet of 20 nm radius sphere separated about 2 nm (2*d, d = 1.1 nm)

Figure 5 depicts the electric field distribution around a doublet structure consisting of two nano-spheres with a 2 nm separation. In figure 5a, the field enhancement factor along the Y-axis for the orientation of the particle shown in

Figure 5b is demonstrated. It indicates that the gradient field is significantly high in the region between the two spheres. The coupling between the two spheres is only feasible for a specific polarization of the incident light, i.e., coupling occurs only when the polarization is along the longer axis of the doublet, as shown in Figure 5c.

CLUSTERS FORMED BY THREE OR MORE NUMBER OF NANO SPHERES

A comprehensive electric field simulation was conducted to analyze the clusters formed by up to five nanospheres. To create these nanoscale structures, three nanospheres were arranged either in a linear chain or at the vertices of an equilateral triangle, as illustrated in Figure 6.
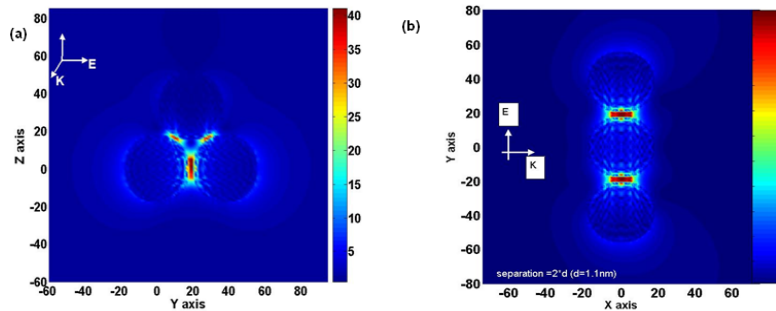
Figure 6. Electric field patterns when 3-spheres are in triangular (a) and linear (b) configurations
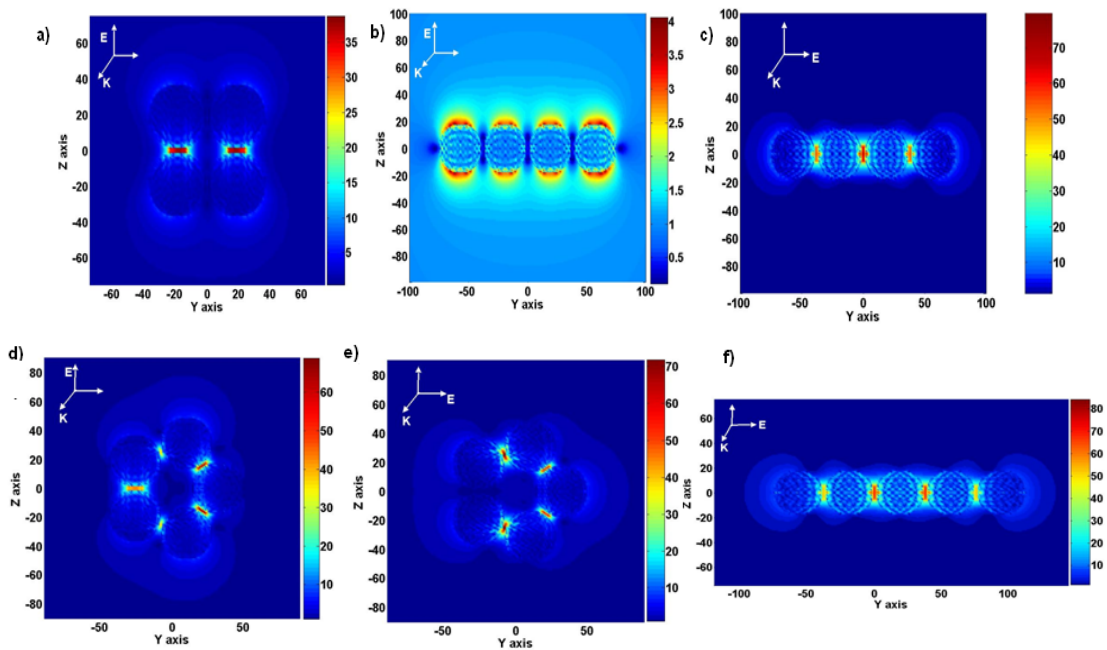
Figure 7. Electric field patterns for 4 & 5 spheres in different configurations

To ensure symmetry, a pair of nanospheres spaced 2 nm apart was chosen as it demonstrated the maximum field enhancement. A third nanosphere was then added to create a symmetrical object either in a linear chain or a triangle. A detailed analysis of the electric field distributions within the resulting object was carried out and is also depicted in Figure 6. The results demonstrate that the field enhancement is more prominent in linear chains of nanospheres as compared to that of triangles. This study provides valuable insight into the behavior of nanoscale structures under an electric field and can aid in the development of novel nanoscale devices with enhanced performance.

Figure 7 shows the electric field pattern of clusters containing four and five spheres. The enhancement is higher in a linear pattern for all cases. However, it is important to note that the enhancement factor does not increase linearly with the number of spheres. It tends to saturate. The enhancement factor of the incident field is polarization-dependent, as mentioned above. The saturation in the field enhancement occurs due to the resistive losses taking place during the oscillations of electrons.

CONCLUSIONS

This study conducted extensive simulations to investigate the characteristics of field enhancement in gold nanospheres. Through our analysis, we found that the number of spheres present has a direct influence on the degree of field enhancement, with greater numbers leading to more significant enhancements. Moreover, we found that the linear arrangement of these spheres produces a higher degree of enhancement compared to other arrangements. Our research

also revealed that the enhancement factor exhibits a saturation effect beyond a certain threshold of spheres, implying that the maximum level of enhancement can be reached. Overall, our investigations provide valuable insights into the field enhancement properties of gold nanospheres, which can be useful in a variety of scientific and technological fields.

ORCID

P.K. Kushwaha, https://orcid.org/0009-0004-1003-3452; **K.Y. Singh,** https://orcid.org/0009-0004-4109-4899
Pramod Kumar Singh, https://orcid.org/0000-0001-6633-8379; **Ravish Sharma,** https://orcid.org/0009-0003-7431-7123
Kash Dev Sharma, https://orcid.org/0009-0004-4686-3845

REFERENCES
[1] C.N. Banwell and E.M. Mc-Cash, *Fundamentals of molecular spectroscopy*, 4th Edition, (Tata Mc Graw Hill, India, 1995).
[2] F. Lu, W. Zhang, L. Sun, T. Mei, and X. Yuan, Optics Express**, 30**, 12 21377 (2022). https://doi.org/10.1364/OE.460394
[3] L. Meng, Y. Wang, M. Gao, and M. Sun, J. Phys. Chem. C, **125**, 10 5684 (2021). https://doi.org/10.1021/acs.jpcc.0c10922.
[4] A. Szaniawska, and A. Kudelski, Frontiers in Chemistry, **9**, 664134 (2021). https://doi.org/10.3389/fchem.2021.664134.
[5] H. Zhou, X. Li, L. Wang, Y. Liang, A. Jialading, Z. Wang, and J. Zhang, Reviews in Analytical Chemistry, **40** (1), 173 (2021). https://doi.org/10.1515/revac-2021-0132
[6] M.M. Joseph, N. Narayanan, J.B. Nair, V. Karunakaran, A.N. Ramya, P.T. Sujai, et al., Biomaterials, **181**,140 (2018). https://doi.org/10.1016/j.biomaterials.2018.07.045
[7] S. Khan, R. Ullah, A. Khan, R. Ashraf, H. Ali, M. Bilal, and M. Saleem, Photo diagnosis and Photodynamic Therapy, **23**,89 (2018). https://doi.org/10.1016/j.pdpdt.2018.05.010
[8] D.W. Shipp, F. Sinjab, and I. Notingher, Advances in Optics and Photonics, **9**(2), 315 (2017). https://doi.org/10.1364/AOP.9.000315
[9] J. Parsons, C.P. Burrows, J.R. Sambles and W.L. Barnes, Journal of Modern Optics, **57**, 1362 (2010). https://doi.org/10.1080/09500341003628702
[10] B.T. Draine, and P.J. Flatau, J. Opt. Soc. Am. A,**11**,1491 (1994). https://doi.org/10.1364 /JOSAA.11. 001491
[11] B.T. Draine, and J. Goodman, The Astrophysics journal, **405**, 685 (1993). https://doi.org/10.1086/172396
[12] B.T. Draine, and P. J. Flatau, J. Opt. Soc. Am. A,**25** (11)**,**2693 (2008). https://doi.org/10.1364/JOSAA.25.002693
[13] M.A. Yurkin, and M. Huntemann, J. Phys. Chem. C, **119**, 52, 29088 (2015). https://doi.org/10.1021/acs.jpcc.5b09271
[14] C. Mätzler, *MATLAB Functions for Mie Scattering and Absorption*, (Institute of Applied Physics, University of Bern, 2002). https://omlc.org/software/mie/maetzlermie/Maetzler2002.pdf
[15] P.B. Johnson, and R.W. Christy, Phys. Rev. B, **6**, 4370 (1972). https://doi.org/10.1103/PhysRevB.6.4370

ПІДСИЛЕННЯ ЕЛЕКТРИЧНОГО ПОЛЯ НАНОСФЕРОЮ ЗОЛОТА ТА ЇЇ КЛАСТЕРАМИ
П.К. Кушваха[a,b], К.Й. Сінгх[a,b], Хіммат Сінгх Махор[a,b], Прамод Кумар Сінгх[c], Равіш Шарма[a,b], Каш Дев Шарма[a,b]
[a]Департамент фізики, B.S.A. (P.G.) коледж, Матхура (U.P.) Індія 281004
[b]Університет доктора Бхімрао Амбедкара, Агра (U.P.), Індія 282004
[c]Департамент фізики, Індустанський коледж науки та технологій, Фарах, Матхура (Великобританія), Індія 281122
Утримання електронів у наночастинках золота призводить до поверхневого плазмонного резонансу (SPR), який характеризується посиленням електричного поля поблизу цих наночастинок. Ця властивість була широко вивчена і застосована в різних областях. У нашому дослідженні ми проводимо детальне дослідження плазмонного зв'язку в сферичних наночастинках золота. Зокрема, ми використовуємо метод дискретної дипольної апроксимації (DDA), реалізований у DDSCAT, щоб симулювати зв'язок електричних полів у дублеті наночастинок як функцію відстані між ними. Наше моделювання показує, що зв'язок SPR між двома наночастинками відбувається на відстані до 12 нм. Крім того, ми розширюємо наше моделювання, щоб вивчити зв'язок наночастинок у лінійних ланцюгах, що складаються з п'яти наночастинок, і в кластерних формах. Наші результати показують, що відбувається зв'язок SPR у лінійному ланцюзі, і зі збільшенням кількості наночастинок посилення поля також збільшується. Однак ми спостерігаємо, що цей ефект насичується після чотирьох наночастинок у ряду. Наше дослідження дає уявлення про плазмонний зв'язок у наночастинках золота, що може допомогти в розробці та оптимізації плазмонних пристроїв для різних застосувань.
Ключові слова: *поверхневий плазмонний резонанс (ППР); наночастинки золота; дискретне дипольне наближення (DDA); DDSCAT; покращення поля*

SPECIFIC FEATURES OF CARBON NANOPARTICLE FORMATION UNDER THE INFLUENCE OF A LASER OPERATING IN A DOUBLE-PULSE GENERATION MODE

Maria I. Markevich[a], Amangeldi B. Kamalov[b], Dauran J. Asanov[b]*
Daryabay M. Esbergenov[c], Manzura A. Kazakbaeva[b]
[a]Physico-Technical Institute of the National Academy of Sciences of Belarus, Minsk
[b]Nukus State Pedagogical Institute Named After Ajiniyaz, Nukus, Republic of Karakalpakstan
[c]Nukus Branch of Tashkent University of Information Technologies Named After al-Khwarizmi, Republic of Karakalpakstan
*Corresponding Author e-mail: dauranbek83@list.ru
Received April 1, 2024; revised April 21, 2024; accepted May 6, 2024

This study investigates the morphology of carbon nanoparticles generated through the ablation of an MPG-6 carbon target in an aqueous environment. The ablation process utilized an LS-2134D aluminum yttrium garnet laser (wavelength: 1064 nm) operating in a double-pulse mode (pulse separation: 3 μs, pulse duration: 10 ns, pulse repetition rate: 10 Hz, single pulse energy: ~0.05 J). The results demonstrate the formation of a diverse range of carbon nanoparticles with varying sizes and shapes during laser ablation. Additionally, the study showcases the ability to control the ablation process and subsequent synthesis of carbon nanoparticles, achieving efficient generation of nanoparticles suitable for various applications.
Keywords: *Nanoparticles; Laser irradiation; Nanosecond pulse duration; Double-pulse regime; Carbon*
PACS: 42.55.Ye, 61.82.Rx, 78.67.Bf

INTRODUCTION

Currently, numerous scientists both abroad and within our country are increasingly employing various forms of carbon for the high-temperature synthesis of SHS materials. It has been established that obtaining graphite particles of different sizes can be utilized to control the SHS reaction [3].

Furthermore, carbon particles are extensively used as pigment fillers and additives to enhance the strength and electrical conductivity of materials. The production of various cable and wire products typically involves the use of carbon particles. The diversity of colors in polymer materials is achieved by varying the size and concentration of carbon particles [1-4].

Among the various methods for modifying the surface of graphite, laser treatment, particularly in a two-pulse mode, remains significantly understudied [5-6].

In our work, we will explore the production of carbon particles of different sizes using laser ablation. Laser ablation offers vast potential for obtaining nanoparticles in solutions, as the particles produced by this method are characterized by high purity. This is based on the unique properties of laser radiation: coherence, monochromaticity, short duration of exposure, high energy densities in the pulse, absence of direct contact between the material and the energy source, sterility of the process, and the rapid nature of the method. Laser ablation of various substances in liquids has been investigated in studies [9-10].

MATERIAL AND METHOD

Sample analysis was conducted using a Hitachi S-4800 scanning electron microscope (SEM). For material processing, an yttrium aluminum garnet (YAG) laser (LS-2134D) with a wavelength of 1064 nm was employed. The laser operated in a two-pulse mode with the following parameters: Pulse separation: 3 μs, pulse duration: 10 ns, pulse repetition rate: 10 Hz single pulse energy: ~0.05 J, exposure time: 60 minutes, power density range: $1.3\text{-}2\times10^7$ W/cm² [7-8]. The object of investigation was an MPG-6 carbon target submerged in distilled water. The liquid was not forcibly stirred. The sample dimensions were: Length: 20 mm, width: 10 mm, thickness: 3 mm

DESCRIPTION AND ANALYSIS OF RESULTS

Table 1 presents the key characteristics of MPG-6 Graphite Composite, outlining its physical and electrical properties. The data reveals that MPG-6 exhibits a combination of desirable features, including:

Good electrical conductivity: With a specific electrical resistivity of 11-16 μΩ·m, MPG-6 demonstrates its ability to conduct electricity efficiently, making it suitable for applications where electrical conductivity is crucial.

Lightweight nature: Its bulk density of 1.76-1.88 g/cm³ signifies that MPG-6 is relatively lightweight compared to many metals, offering potential advantages in weight-sensitive applications.

High purity: The low ash content of 0.25-0.1% indicates a high degree of purity in the composite, which can be important for specific applications.

Stiffness and strength: While not as stiff as some metals, the Young's modulus of 10-12 GPa demonstrates that MPG-6 maintains respectable stiffness and strength.

Porous structure: The 9% porosity indicates the presence of some void space within the material. This characteristic may influence its behavior in certain applications, and further investigation into its implications could be beneficial. By presenting these properties, Table 1 provides valuable insights into the nature of MPG-6 Graphite Composite, aiding in the understanding of its potential applications and limitations.

Table 1. Characteristics of MPG-6 Graphite Composite

	Units of Measurement	MPG -6
Specific electrical resistivity	μΩ·m	11-16
Bulk density	g/cm³	1,76-1,88
Porosity	%	9
Ash content	%	0,25-0,1
Grain size	μm	30-150
Young's modulus	GPa	10-12

Data on the phase composition of the irradiated graphite surface were obtained from the analysis of Raman scattering (RS) spectra at a wavelength of 532 nm. The RS spectra were measured using a spectral-analytical complex based on a Nanofinder High End scanning confocal microscope from LOTIS-TII (Belarus-Japan). The RS spectra were excited by a line of a solid-state Nd laser with a wavelength of 532 nm and recorded at room temperature. A cooled CCD camera served as the detector. The probing spot had a diameter of 1 μm [9-20].

When a series of nanosecond laser pulses is applied to the surface of a carbon sample located in water, a region consisting of water vapor, products of an erosive laser torch, is formed near the surface. The ablation plasma formed as a result of the evaporation of a substance under the influence of the first pulse creates an area in the near-surface layer with an increased temperature and a reduced density of particles, which leads to a more complete use of the energy of the second pulse for laser ablation [12-15].

Figure 1 shows micrographs of carbon nanoparticles obtained using SEM at various magnifications. Formed as a result of laser exposure. Power density 1.67×10^7 W/cm², exposure time 60 min.

a   *b*
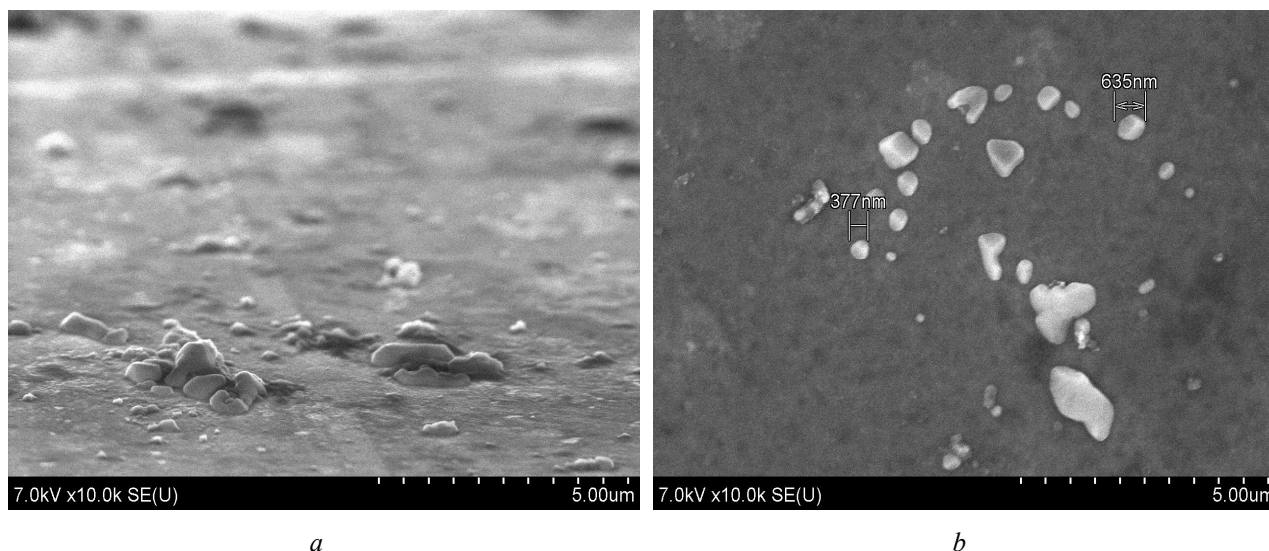
Figure 1. Surface morphology of carbon nanoparticles

Analysis of the SEM images reveals that the synthesized nanoparticles exhibit both spherical and anisotropic (non-spherical) shapes. The particle size varies from 30 nm to 1 μm. Some particles have a width of approximately 700 nm and a length of ~1 μm. Additionally, smaller nanoparticles with sizes ranging from 20 to 100 nm are also observed.

Figure 2 displays surface images of irradiated and non-irradiated areas of MPG-6 carbon, obtained using scanning microscopy before and after laser exposure.

Comparison of the images shows that the surface nanolayer is significantly modified. The porous structure of the surface in the crater zone is clearly visible. This fine-crystalline material is a spatial network of crystallites, possibly with an amorphous intercrystallite boundary. It is likely that the surface destruction occurs more intensively from the intercrystallite phase. The observed changes in the relief of the surface layer of the sample subjected to laser action may be associated with a change in the phase composition. The results of studies of the modified surface by Raman scattering showed a change in the phase composition.

a - before irradiation   *b* - after irradiation
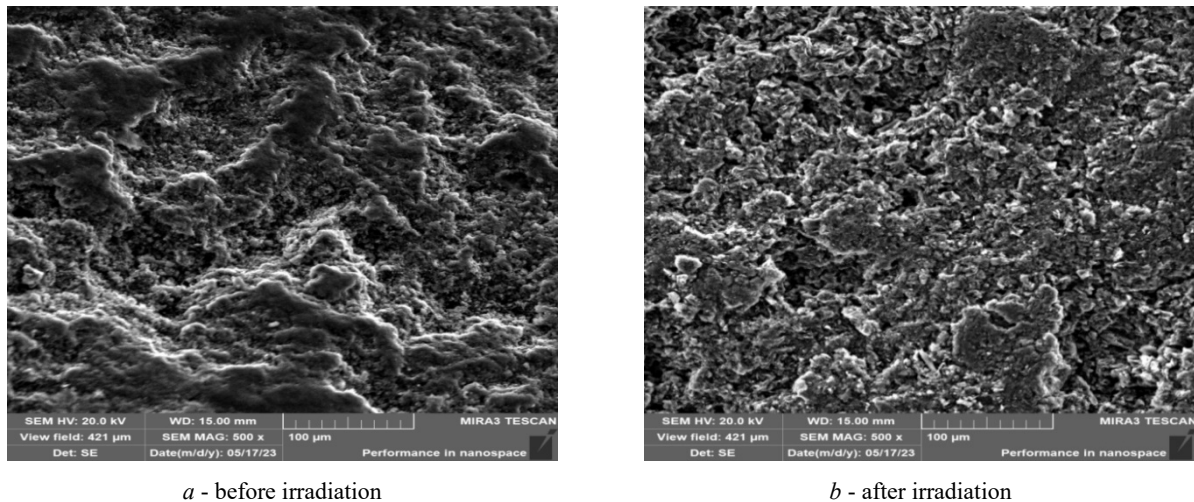
Figure 2. Morphology of the surface of MPG-6 graphite before and after laser modification

We have carried out studies by the method of Raman scattering, the Raman spectra of graphite and the results of the decomposition of their spectral contour are presented (the Lorentz contour was used).

a) before laser treatment   *b)* after laser treatment
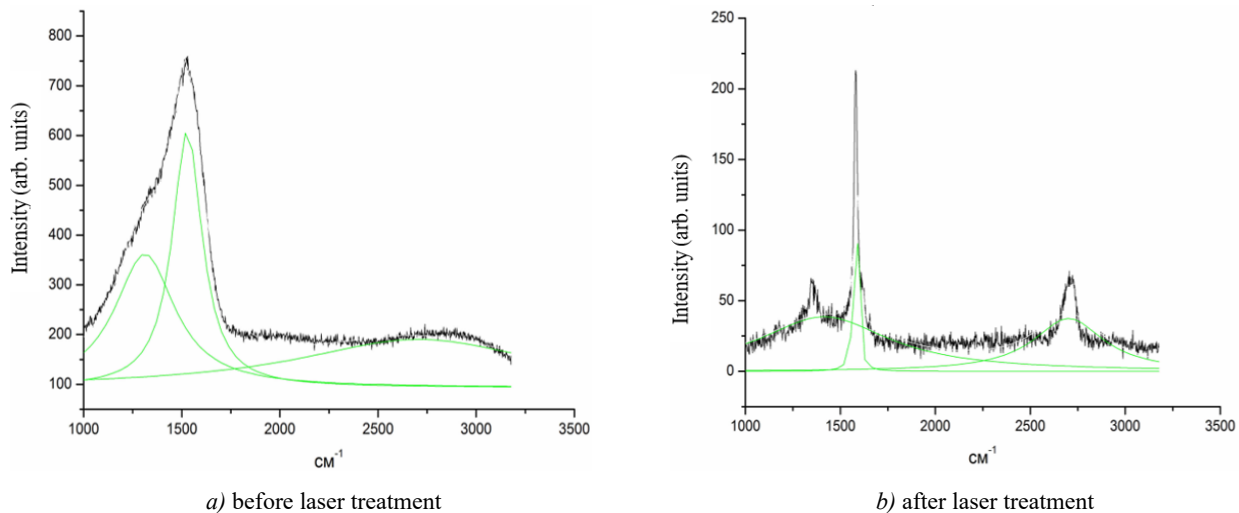
Figure 3. Raman scattering spectra of MPG-6 graphite

The spectra before and after laser exposure differ significantly from each other. After exposure, three intense scattering bands are clearly visible in the spectrum. The appearance of a well-defined D line ($\sim$1354 cm^{-1}) is associated with inelastic scattering of excited electrons on phonons and elastic scattering of electrons on defects. The appearance of the D line indicates the presence of structural disorder in the ideal hexagonal structure (grain boundaries, defects, etc.). The 2D line ($\sim$2700 cm^{-1}) is not associated with the presence of structural defects and is present in most carbon materials with a graphite-like structure.

CONCLUSION

This study demonstrates the possibility of controlling the ablation process and the yield of carbon nanoparticles from an MPG-6 target in an aqueous medium. Effective generation of nanoparticles for use in various applications has been achieved. The morphology of nanoparticle conglomerates ranging in size from 30 nm to 1 μm has been studied. The shape of the particles is diverse. The surface of the MPG-6 crater is smooth, and the surface relief is significantly altered. The results of studies of the modified surface by Raman scattering showed a change in the phase composition.

ORCID
Amangeldi B. Kamalov, https://orcid.org/0000-0003-1460-0747; Dauran J. Asanov, https://orcid.org/0000-0003-0091-8105
Daryabay M. Esbergenov, https://orcid.org/0000-0002-7544-4031

REFERENCES
[1] C. Thamaraiselvan, J. Wang, D.K. James, P. Narkhede, S.P. Singh, D. Jassby, J.M. Tour, and C.J. Arnusch, "Laser-induced graphene and carbon nanotubes as conductive carbon-based materials in environmental technology," Materials Today, **34**, 115-131 (2020). https://doi.org/10.1016/j.mattod.2019.08.014

[2]   R. Ye, X. Han, D.V. Kosynkin, Y. Li, C. Zhang, B. Jiang, A.A. Martí, and J.M. Tour, "Laser-induced conversion of teflon into fluorinated nanodiamonds or fluorinated graphene," ACS nano, **12**(2), 1083-1088 (2018). https://doi.org/10.1021/acsnano.7b05877

[3]   S. Juodkazis, H. Misawa, T. Hashimoto, E.G. Gamaly, and B. Luther-Davies, "Laser-induced microexplosion confined in a bulk of silica: formation of nanocavities," Applied Physics Letters, **88**(20), 201909 (2006). http://dx.doi.org/10.1063/1.2204847

[4]   F. Migliorini, S. Belmuso, D. Ciniglia, R. Dondè, and S. De Iuliis, "A double pulse LII experiment on carbon nanoparticles: insight into optical properties," Physical Chemistry Chemical Physics, **24**(33), 19837-19843 (2022). https://doi.org/10.1039/D2CP02639B

[5]   K. Habiba, V.I. Makarov, B.R. Weiner, and G. Morell, "Fabrication of Nanomaterials by Pulsed Laser Synthesis," Manufacturing Nanostructures, **10**, 263-92 (2014). http://dx.doi.org/10.13140/RG.2.2.16446.28483

[6]   E. Rodriguez, and L. Fernandez, "Role of laser parameters in the formation of carbon nanoparticles under dual-pulse irradiation," Optics Express, **30**(18), 25400-25410 (2022). https://doi.org/10.1364/OE.30.025400

[7]   A. Rybaltovsky, E. Epifanov, D. Khmelenin, A. Shubny, Y. Zavorotny, V. Yusupov, and N. Minaev, "Two Approaches to the Laser-Induced Formation of Au/Ag Bimetallic Nanoparticles in Supercritical Carbon Dioxide," Nanomaterials, **11**(6), 1553 (2021). https://doi.org/10.3390/nano11061553

[8]   Y. Shao, A. Pan, H. Yang, W. Zhang, X. Zhang, and G. Wang, "Formation mechanism of graphene quantum dots assisted by nitrogen and its application in detection of Hg^{2+}," Journal of Colloid and Interface Science, **512**, 777-785 (2018). https://doi.org/10.1016/j.jcis.2017.10.044

[9]   F. Liu, and H.M Cheng, "Hydrothermal synthesis of graphene-based materials: Progress and challenges," Chemical Communications, **49**(50), 5203-5212 (2013). https://doi.org/10.1039/C3CC00165J

[10] O.O. Kurakevych, V.L. Solozhenko, and Y.L. Godec, "Single-crystal structures of carbon nitrides obtained by decomposition of melamine under high pressure," The Journal of Physical Chemistry C, **115**(45), 22392-22398 (2011). https://doi.org/10.1021/jp2073456

[11] J. Wang, X. Zhang, Y. Chen, and M. Sommerfeld, "Ultrafast formation of graphene on dielectric surfaces," Applied Physics Letters, **108**(11), 111602 (2016). https://doi.org/10.1063/1.4943961

[12] Z Wang, X. Lu, and C. Wang, "Laser-induced graphene: preparation, functionalization, and applications," Chemical Society Reviews, **44**(9), 2629-2642 (2015). https://doi.org/10.1039/C4CS00320G

[13] A. Kaczmarek, P. Denis, M. Krajewski, T. Mościcki, A. Małolepszy, and J. Hoffman, "Improved Laser Ablation Method for the Production of Luminescent Carbon Particles in Liquids," Materials, **14**(9), 2365 (2021). https://doi.org/10.3390%2Fma14092365

[14] O.A. Lazăr, A.S. Nikolov, C.C. Moise, and M. Enachescu, "Pulsed Laser Ablation in Liquids for Fabrication of Noble Metal Nanostructures," in: *Laser Ablation – Applications and Modeling*, edited by Dr. M. Harooni, (IntechOpen, 2023). http://dx.doi.org/10.5772/intechopen.111550

[15] D. Qi, X. Li, P. Wang, S. Chen, W. Huang, C. Li, K. Huang, et al., "Evolution of Laser-Induced Specific Nanostructures on SiGe Compounds via Laser Irradiation Intensity Tuning," **6**(1), 1-5 (2014). http://dx.doi.org/10.1109/JPHOT.2013.2294631

[16] A.G. Anisovich, A.P. Laskovnev, M.I. Markevich, A.N. Malyshko, and V.I. Zhuravleva, "Preparation of silicon and aluminum nanoparticles in an aqueous solution," Foundry production and metallurgy, (2), 76-80 (2021). https://doi.org/10.21122/1683-6065-2021-2-76-80. (in Russian)

[17] A.G. Anisovich, I.P. Akula, A.P. Laskovnev, M.I. Markevich, and N.M Chekan, "Creation and research of antistatic carbon coatings on fabric 05C8-KB, modified by metal clusters," Foundry production and metallurgy, (4), 113-117 (2020). https://doi.org/10.21122/1683-6065-2020-4-113-117. (in Russian)

[18] D.J. Asanov, "Pulse photon processing of a thin-film Si/Mg/Si/Sitall," System Science and Society scientific and methodological journal, (1), 4-6 (2023). (in Russian)

[19] M.I. Markevich, and D.J. Asanov, "Effect of laser radiation on photomagnetic materials based on silicon doped with impurities," in: *XV International Conference "Solid State Physics" (FTT-XV)*, (L.N. Gumilyov Eurasian National University, Astana, Kazakhstan, 2022), pp. 91-94.

[20] D.M. Esbergenov, E.M. Naurzalieva, and S.A. Tursinbaev, "Enhancing the perfection of a silicon crystal doped with nickel and zinc impurities," East European Journal of Physics, (4), 172-176 (2023). https://doi.org/10.26565/2312-4334-2023-4-19

<div align="center">

**ОСОБЛИВОСТІ ФОРМУВАННЯ ВУГЛЕЦЕВИХ НАНОЧАСТИНОК ПІД ВПЛИВОМ ЛАЗЕРА
В РЕЖИМІ ГЕНЕРАЦІЇ ПОДВІЙНИХ ІМПУЛЬСІВ**

</div>

Марія І. Маркевич[a], Амангельді Б. Камалов[b], Дауран Дж. Асанов[b], Дар'ябай М. Есбергенов[c], Манзура А. Казакбаєва[b]

[a]Фізико-технічний інститут Національної академії наук Білорусі, Мінськ, Білорусь

[b]Нукуський державний педагогічний інститут імені Аджініяза, м. Нукус, Республіка Каракалпакстан

[c]Нукуський філіал Ташкентського університету інформаційних технологій імені аль-Хорезмі, Республіка Каракалпакстан

У цьому дослідженні досліджується морфологія вуглецевих наночастинок, утворених шляхом абляції вуглецевої мішені MPG-6 у водному середовищі. У процесі абляції використовувався лазер на алюмінієво-ітрієвому гранаті LS-2134D (довжина хвилі: 1064 нм), що працює в режимі подвійного імпульсу (розділення імпульсів: 3 мкс, тривалість імпульсу: 10 нс, частота повторення імпульсу: 10 Гц, енергія одного імпульсу: ~ 0,05 Дж). Результати демонструють формування різноманітного діапазону вуглецевих наночастинок різного розміру та форми під час лазерної абляції. Крім того, дослідження демонструє здатність контролювати процес абляції та подальший синтез вуглецевих наночастинок, досягаючи ефективного генерування наночастинок, придатних для різних застосувань.

Ключові слова: *наночастинки; лазерне опромінення; наносекундна тривалість імпульсу; подвійний імпульсний режим; вуглець*

IMPLICATIONS OF THE PRESENCE OF Y AS A REACTIVE ELEMENT IN CATHODIC VACUUM ARC TiAlN PROTECTIVE COATING FOR TRIBOLOGICAL APPLICATIONS

O.V. Maksakova[a,b], V.M. Beresnev[a], S.V. Lytovchenko[a*], M. Čaplovičova[b], L. Čaplovič[b], M. Kusý[b], I.V. Doshchechkina[c]

a V.N. Karazin Kharkiv National University, 4, Svoboby Sq., 61000 Kharkiv, Ukraine
b Institute of Materials Science, Slovak University of Technology in Bratislava, 25, Jána Bottu Str., 917 24 Trnava, Slovakia
c Kharkiv National Automobile and Highway University, 25, Ya. Mudryi St., 61200 Kharkiv, Ukraine
*Corresponding Author e-mail: s.lytovchenko@karazin.ua
Received April 4, 2024; revised May 11, 2024; accepted May 19, 2024

The results of studies of the influence of Y as a reactive element on the properties of TiAlN coatings obtained by the method of vacuum-arc deposition are given. Changes in the structure and properties were analyzed using SEM in combination with EDX, XRD, indentation analysis and wear analysis. It is shown that the presence of Y changes the crystalline phase of the $Ti_{0.6}Al_{0.34}Y_{0.06}N$ coating. It consists of a combination of a cubic NaCl structure (basic phase) and a wurtzite structure (additional phase). In addition, it leads to a small grain size (12 nm) and a nano-columnar structure. The high hardness is partly the result of solution hardening due to the inclusion of larger Y atoms in the TiAlN lattice at the locations of the metal atoms. The reduced grain size of 12 nm also helps to increase the hardness of the coating. The hardness is 31 ± 2.5 GPa, the modulus of elasticity is 394.8 ± 35.8 GPa. The residual stress is approximately three times (-3352 ± 64 MPa) higher than the TiAlN coating (-720 MPa). In addition, a high level of compressive stress contributes to an increase in hardness, since defects responsible for their own compressive stress are an obstacle to dislocation movement. The improved hardness of the experimental coating can be explained by a triple effect: solution strengthening, grain grinding and high residual compressive stress. The addition of Y indicates a slower growth of the oxide layer on the surface of the coating during the wear test. After the addition of Y, Y ions preferentially separate at the grain boundaries and therefore effectively delay the inward diffusion of oxygen. The addition of Y promotes the formation of dense Al_2O_3, which is effective in restraining diffusion and therefore protects the coating from oxidative wear.
Keywords: *Vacuum arc deposition; Coatings; Wurtzite phase; Hardness; Wear; Critical loads*
PACS: 61.46.-w; 62.20.Qp; 62-25.-g; 81.15.Cd

INTRODUCTION

The machining industry demands high-performance cutting tools to handle the cutting of new, difficult-to-cut materials. Although tooling does not exceed 5 % of the total manufacturing costs, it has a significant impact on productivity since the tool's capability influences the efficiency of the manufacturing process [1, 2]. Cutting speed is an essential factor in machining, which greatly affects the production cost per part and reduces it by increasing the number of parts produced at a given time. Stainless steels are considered the most difficult-to-cut materials due to their specific properties such as high toughness, work-hardening, and low heat conductivity [3]. This makes it difficult to produce high-quality machined surfaces and dramatically increases the production cost. To meet the ever-increasing demand for higher productivity levels, the cutting speed is conventionally increased, which results in the tool operating under severe service conditions, significantly affecting its life [4]. Therefore, it is crucial to develop new tools with advanced coatings that can withstand these high-speed and high-temperature conditions in the cutting zone.

The conventional advantages of applying protective coatings on cutting tools are assigned to improving wear resistance, heat resistance, corrosion resistance, strength, toughness, and tool life [5, 6]. The practice of coating cutting tools for machining steels initially used binary coatings like TiN and CrN [7, 8]. It is a fact that the use of binary nitride coatings (i.e. TiN or CrN) is limited at elevated temperatures exceeding 500 °C). However, for modern high-speed machining, thermal-mechanical stability is an absolute necessity at temperatures reaching and surpassing 1000 °C [9].

The conjunction of the outstanding mechanical properties of binary metal nitrides (BMNs) and enhanced oxidation resistance caused by the formation of dense, chemically stable Al-rich oxide layer on the surface of coatings, make the metastable solid solution TiAlN coatings widely applied in machining stainless steel [10, 11]. Significant upgrading of mechanical and thermal properties and machining performance are the major benefits of the Al incorporation into the TiN lattice. However, Al content must be strictly controlled. Below an Al content of 67 at. %, a single-phase crystal structure forms by substitution of Ti by Al in a fcc-TiN lattice, which typically yields the highest hardness and elastic modulus [12]. Above ~67 at % of Al, the coating properties start to retrogress due to the formation of mixed NaCl-cubic and hcp structures (wurtzite phase) [13]. Based on the available reports, the TiAlN coatings can function effectively up to temperatures between 750 – 950 °C. Rogstrom et al. [14] observed that above 930 °C, wurtzite-AlN transformation occurs, resulting in a loss of properties and functionality of TiAlN coatings. Chen et al. [15] and Grossmann et al. [16] also reported temperatures of 950 °C and 980 °C, respectively, as critical for $Ti_{1-x}Al_xN$ ($0.4 \le x \le 0.75$) coatings.

According to Mayrhofer et al. [11], the fcc- $Ti_{1-x}Al_xN$ coatings exhibit adaptive behavior during annealing resulting in increased hardness. This property is beneficial in applications that involve frictional heating during machining. Studies [17, 18] have shown that temperatures can rise up to 1000 °C in the cutting zone during high-speed machining of difficult-to-cut materials. Further improvement is necessary to maintain desired productivity levels when machining under severe tribological conditions.

One effective approach to customize the characteristics of TiAlN coating is to incorporate alloying elements that possess high melting points, thermal conductivity, and a tendency to form dense oxide layers [19]. For instance, the addition of V induces an enhanced wear performance at high temperatures owing to the formation of lubricious phase oxides V_2O_5 with a self-lubricating effect. In addition, coatings demonstrate superb oxidation resistance due to the presence of an Al-rich oxide top layer, as supported by various studies [20, 21]. For TiAlSiN coatings, excellent mechanical and thermal properties are assured by the Si-existence of solution and/or amorphous $a-SiN_x$ tissue phase and depend on the deposition parameters and the Si content [22, 23]. The incorporation of Nb and Zr also has a beneficial effect on the TiAlN coatings on the mechanical and thermal properties [24, 25]. The influence of Mo addition to TiAlN-based coatings is positively assessed in [26, 27]. Depending on differing Mo contents (7.7 – 12.1 at. %) coatings demonstrate the improvement of mechanical properties, particularly wear behavior and resistance to pitting corrosion. The structural and morphological evolution of arc-evaporated TiAlWN coatings obtained at different bias voltages is studied in the work [28]. The addition of W positively influences morphology concerning macroparticle incorporation as well as surface roughness. The coatings exhibit advanced ductility and stiffness, as evidenced by the significantly high H^3/E^2 ratios. Another element that can be used as a doping element to TiAlN is Yttrium. Several studies [29 – 31] have pointed out that incorporating Y to $Ti_{1-x}Al_xN$ thin films can be a promising approach to improve the corrosion and oxidation resistance combined with maintaining hardness and elasticity at high temperatures. Its high melting point, electronic configuration, and large atomic radius influence the formation of the cubic nitride and hence the age-hardening effect of $Ti_{1-x-y}Al_xY_yN$. According to a study by Rachbauer et al. [32], the process of age hardening in $Ti_{1-x-y}Al_xY_yN$ is not only affected by the increase in strain due to lattice mismatch but also depends on the bindings present. Aninat et al. [33] reported that the addition of Y to the TiAlN resulted in better mechanical properties and increased hardness. However, it reduced the compressive stress. Moser et al. [34] investigated the thermal stability of $Ti_{1-x}Al_xN$ coating with Y addition through the DC magnetron sputtering process. It was found that after annealing at high temperatures, there was an increase in hardness. Donohue et al. [35] found that a low concentration yttrium substitution into the metastable Ti_xAl_yCrYN coatings significantly refines the grain. The $Ti_{0.43}Al_{0.52}Cr_{0.03}Y_{0.02}N$ demonstrate considerably improved oxidation and corrosion resistance compared to $Ti_{0.44}Al_{0.53}Cr_{0.03}N$ coatings. Yttrium shows a high tendency to form an oxide along the grain boundaries and as well at the metal-oxide interface. On the metal-oxide interface, Y inhibits the formation of voids and promotes the creation and adhesion of a dense protective oxide layer (Y_2O_3). On the other hand, at the grain boundaries, it functions as a barrier to fast diffusion paths within the oxide scale [36]. In simple terms, yttrium acts like a 'plug' that stops the inward diffusion of oxygen and the outward diffusion of metal components of the coating. This is especially true for diffusion along grain boundaries and surfaces [35]. However, as the Y content increases from 3 to 9 at. %, a change in the structure occurs. A single-phase cubic solid solution crystal structure converts to a mixed cubic and wurtzite structure (at 5 at. % of Y), and finally to a single-phase wurtzite structure at 9 at. % of Y [32, 34].

The present study aimed to identify and explore experimentally, the structure, composition, and properties of arc-evaporated TiAlYN coating with 5 at. % of Y in a target for understanding the protective perspectives of this type of coating and suggesting its working conditions.

Before describing the experimental details and discussing the obtained results, we want to briefly explain the benefits of alloying elements, including Yttrium, to TiAlN coatings from the recently published first-principles study [37]. The summarizing of these data contributes to a better atomic-scale understanding of TiAlN coatings alloyed with the fourth element for their potential applications.

FIRST-PRINCIPLES STUDY REVIEW

By using first-principles calculations, eight elements (La, Ce, Y, Hf, Zr, Ta, Cr, Si) were doped on the $Ti_{0.5}Al_{0.5}N$ (001) surface to comparatively study the effect of different doping atoms. All computational details can be found in [37].

To determine the doping of X atom on the surface, the formation energy of X replacing one metal (Al and Ti) or non-metal (N) atom on the $Ti_{0.5}Al_{0.5}N$ (001) surface layer was calculated. The formation energies of X substituting the Al atoms on the $Ti_{0.5}Al_{0.5}N$ (001) surface are the following: −1.160 eV (La), −1.119 eV (Ce), −1.336 eV (Y), -1.258 eV (Hf), −0.913 eV (Zr), 0.497eV (Ta), 1.586 eV (Cr), 1.785 eV (Si). The surface configuration of Al substituted by X atom in TiAlN is shown in Fig. 1.

Based on calculated results, it can be realized that the formation energies of La, Ce, Y, Hf, and Zr replacing the Al atom on the $Ti_{0.5}Al_{0.5}N$ (001) surface are negative, in comparison to the atoms of Ta, Cr, and Si. This implies that for La, Ce, Y, Hf, and Zr doping, the structures are expected to be synthesized easily in experiments due to lower formation energy. Among these five doped elements, Y is more inclined to replace the surface Al atom due to its lowest formation energy of −1.336 eV.

The adsorption behavior of oxygen on the $Ti_{0.5}Al_{0.5}N$ (001) surface with the addition of Y atoms has been analyzed along with formation energy. These findings can be especially useful when studying the tribological behavior of TiAlN-based coatings, particularly in relation to wear mechanisms that can help identify potential areas of application.

Figure 1. The surface slab (left panel) and surface adsorption sites (right panel) of $Ti_{0.5}Al_{0.5}N$ (001) surface with X-doped. In the figure, Zone 1 is included in Zone 2. Adopted from [37].

Fig. 2 illustrates the bonding behavior between an Oxygen atom and $Ti_{0.5}Al_{0.5}N$ (001) surface without and with a doped Y atom. When comparing the $Ti_{0.5}Al_{0.5}N$ (001) surface to the Y-doped surface, it was found that the Y-doped surface has a stronger attraction to O atoms. This was observed by examining the structures of oxygen atoms adsorbed at twenty-nine adsorption sites. It was discovered that the Y atom can chemically bond with O atoms from its surrounding area, indicating that Y has a high affinity for O.

In Fig. 2b, except for the 8, 9, 10, and 11 sites, the other O atoms with different adsorption sites are attracted by the Y atom, eventually forming chemical bonds. Oxygen atoms located at adsorption sites 1, 5, 6, and 7 migrate to the green circle position in the lower left corner due to the attraction of the Y atom, forming the Y-O-Ti bond. On the other hand, when O atoms are located at sites 3 and 4 (top (Al)), they shift to the green circle positions in the upper left and lower right corners respectively, forming the Y-O-Al bond. Finally, when O atoms are at sites 2 and 12, they are attracted by the Y atom to the green circle position in the upper right corner, forming the Y-O-Ti bond.

Figure 2. The adsorption configuration of $Ti_{0.5}Al_{0.5}N$ (001) surface without and with Y doped. Adopted from [37].

Therefore, the analysis of bond characteristics between O and Y atoms on the $Ti_{0.5}Al_{0.5}N$ (001) surface suggests that when Y atoms substitute Al atoms on the surface, they tend to form hybrid oxides (X-O-Al or X-O-Ti) in the initial stage of oxidation, rather than simple self-metal oxides (X-O). This conclusion is supported by experimental results that show the oxidation products include complex oxides such as $Y_2Ti_2O_7$ [38] and $YAlO_3$ [39]. It is noteworthy that $Y_2Ti_2O_7$ has a higher hardness of 12.1 GPa compared to Y_2O_3 (6.9 – 9.1 GPa) and TiO_2 (11 GPa). However, Young's modulus of $Y_2Ti_2O_7$ (262 GPa) is similar to that of TiO_2 (266 – 270 GPa) and 25% higher than that of Y_2O_3 (188 GPa) [40].

In summary, the results of the first-principal study show that TiAlYN coatings are interesting as protective materials able to work successfully in tribological conditions due to the modification of the surface structure resulting from oxide transformations.

EXPERIMENTAL DETAILS
Deposition

TiAlYN coatings were deposited by the cathodic arc evaporation method in a non-commercial coating machine. AISI steel square bars of dimension 20mm×20mm×2 mm were chosen as the substrates since these are some of the most widely used cutting tool materials in the machining industry. $Ti_{0.5}Al_{0.45}Y_{0.05}$ alloys were utilized as the cathode materials, which were manufactured by the powder metallurgy technique. Prior to the deposition, substrates were ultrasonically cleaned. Then they were mounted to a rotating substrate carousel. The chamber was pumped to a base vacuum lower than 4×10^{-3} Pa. All targets were pre-sputtered for 7 min to remove the surface contaminants. The substrates were plasma etched in an argon atmosphere (0.2 Pa) for 10 min. Plasma etching removes surface contaminants and creates fresh surfaces for the nucleation and growth of coatings. Coatings' deposition was carried out in a nitrogen environment at a nitrogen pressure (P_N) of 0.53 Pa and a negative bias applied to the substrate (U_b) of 200 V. During the deposition process, the temperature on substrates was about 450 °C, and deposition time lasted 60 min.

Characterization

The cross-sectional microstructure at different magnifications, as well as morphology of the surface after wear tests were studied using scanning electron microscopy in a Quanta 600 FEG and FEI Nova NanoSEM 450 microscopes. The phase state was characterized using X-ray diffraction in a Panalytical Empyrean X-ray diffractometer in Co-Kα radiation ($\lambda = 0.1789$ nm). Identification of the phases and calculation of main crystal structural parameters was done using Malvern Panalytical's XRD software.

The microhardness was measured using an automated Anton Paar NHT ultra microhardness tester equipped with a diamond Berkovich tip. The maximum applied load was 10 mN and the loading time was 20 s. During the test, the indentation depth was controlled within 10 % of the coating thickness to avoid the effect of the substrate.

The scratch test was performed in a Bruker UMT-2 tester under the minimal load of 0.2 N and the maximal load of 46 N. The size of the scratch was 5 mm.

Ball-on-disc tribotest was carried out in a Bruker UMT-2 tester. The counterball was 6.3 mm WC-Co. The applied load was 5 H, the sliding speed was 200 rpm, and the sliding time was 30 min.

RESULTS

Fig. 3 shows the surface and cross-sectional SEM micrographs and corresponding EDX elemental mapping of TiAlYN coating. It notes that the surface of the coating has ample macroparticle fraction and inapparent facet morphology. Macroparticles are usually present when deposition takes place with the PVD method, and they lead to surface irregularities. The fractured cross-section image of the coating reveals that the coating is well-grown and adherent to the steel substrate. The coating exhibits a nano-columnar microstructure.
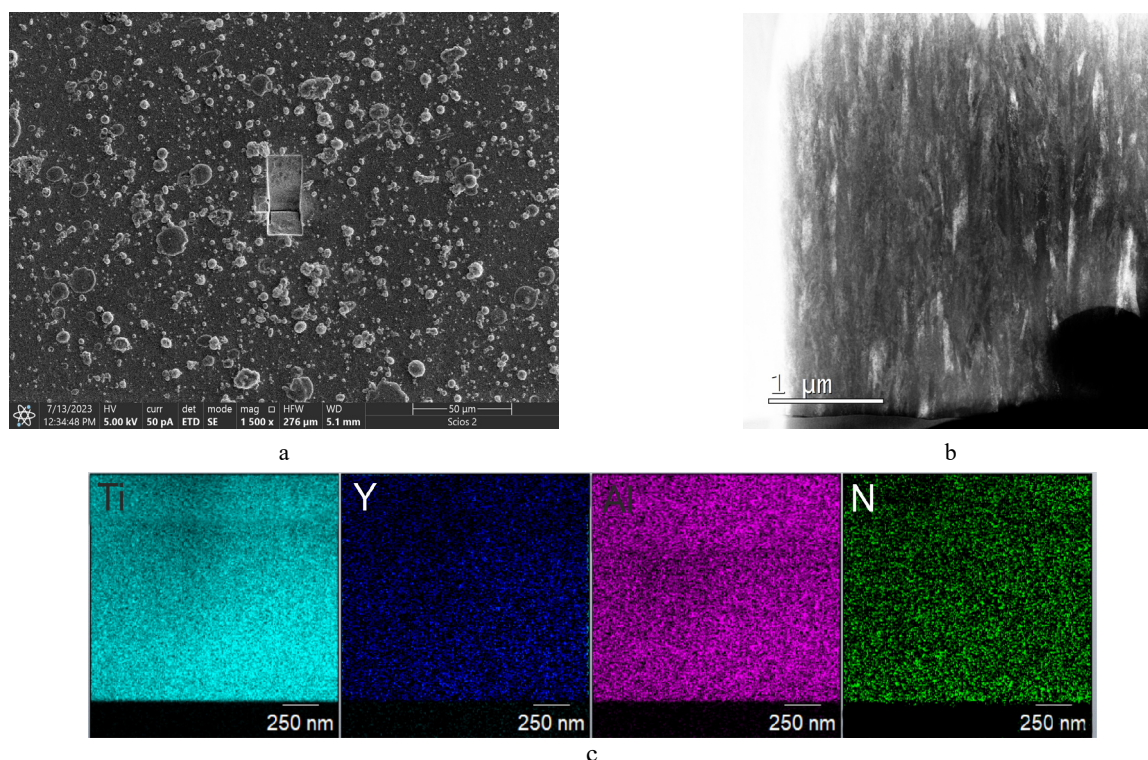
Figure 3. SEM micrographs of TiAlYN coating in planar (a) and cross-section (b) views and corresponding EDX elemental mapping (c).

The elemental composition of the coating was determined by EDX mapping in the SEM. The result shows that the distributions of all constituent elements in the coating are quite uniform. The chemical composition of the coating is the following: $Ti_{0.6}Al_{0.34}Y_{0.06}N$. Since the nitrogen pressure used for the deposition was 0.53 Pa, the coating composition is stoichiometric. The Al concentration in the coating is lower than that of the target composition, while the amount of Ti and Y in the coating is higher compared to the target. This can be explained by the large difference in the atomic mass of the metallic components, due to which the rate of scattering in the gas phase for Al is higher and more Al re-sputters during coating growth.

XRD pattern of the coating is shown in Fig. 4. The 2θ peak positions for standardized c-TiN ($a_c = 4.24$ Å, ref. code 03-065-0414), c-AlN ($a_c = 4.12$ Å, (ref. code 00-046-1200) and c-Al$_{0.5}$Ti$_{0.5}$N ($a_c = 4.19$ Å, ref. code 01-071-5864), c-YN ($a_c = 4.87$ Å, ref. code 01-071-9847), h-Ti$_2$AlN ($a_h = 2.98$ Å, $c_h = 13.61$ Å, $c_h/a_h = 4.56$, ref. code 00-055-0434) and h-AlN ($a_h = 3.11$ Å, $c_h = 4.98$ Å, $c_h/a_h = 1.60$, ref. core 01-086-4277) are labeled with different colors and symbols.

The coating exhibits strong {200} preferred orientation. It can be seen from the pattern, the Y prefers to dissolve into the AlTiN-forming solid solution rather than segregating as a second YN phase (formation of separate peaks) [41]. The dissolution of the Y into the AlTiN lattice produces an increased lattice parameter of the TiAlYN coating. This is due to Y having a larger atomic radius compared to those of the Ti and Al. Additionally, a broadening of the characteristic peaks of the solid solution TiAlYN can be observed after the Y addition, which can be attributed to the grain refinement. The average grain size of the coating is 12 nm.

As the Ti content in the coating is quite high, the cubic peaks at the XRD pattern shift towards higher angles. Moreover, the presence of Y results in the formation of an extra wurtzite phase, which is evident in the diffraction pattern at 38.5° and 46.8° diffraction angles. This indicates that the coating has a significant amount of the wurtzite phase. These results correspond well with other literature reports [30, 32] and ab initio findings, which suggest that at high Y content, the solubility of Al in the cubic single phase field decreases.

The main mechanical and tribological properties of TiAlYN coating as well as thickness are summarized in Table 1. The formation of the wurtzite phase due to high Y and Al content, as mentioned above, can result in decreased hardness values as compared to the coatings with a metastable single phase (cubic solid solution). For the experimental coating, the value of hardness is 31 ± 2.5 GPa which is comparable to the hardness for the single-phase cubic coatings, which vary between 30 and 35 GPa [34]. Such high hardness can be explained by solid solution strengthening and the induced microstrain due to the incorporation of Y atoms. With increasing Y content, the octahedrally coordinated sp^{3}d^2 hybridisation is weakened and the tetrahedral sp^3 hybridisation is favoured resulting in a promotion of the wurtzite structure [32].
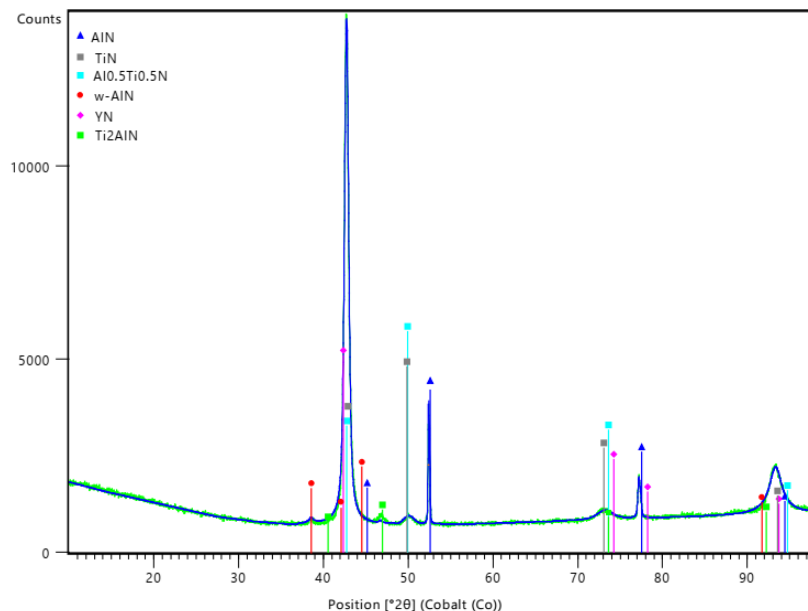
Figure 4. Diffraction pattern of TiAlYN coating

It is generally accepted that higher residual stresses lead to higher hardness and that high residual compressive stresses are conducive to higher fracture toughness [37]. It is clear that the residual stress of experimental coating is −3352 ± 64 MPa, this high value ensures the high hardness. Table 1 contains two other hard mode ratios, such as H/E and H^3/E^2, which are also accurate and reliable measures of wear resistance. H/E correlates with elastic strain failure capacity, with a larger ratio implying a higher fracture toughness of the coating, while a large H^3/E^2 is a strong indication of wear resistance, plastic deformation resistance, and fracture resistance. As one can see, the values of H/E and H^3/E^2 are respectively = 0.078 ± 0.07 and 0.191 ± 0.011. This means that coating has less tensile stress in the tensile stress concentration zone and, therefore, is less prone to cracking as well as has high fracture toughness. The friction

coefficient of the coating is around 0.6 – 0.65. The running-in stage of the coating was 450 s, and then the fluctuations in the friction curve stopped.

Table 1. Functional properties of TiAlYN coating

	Value
Thickness Δ, micron	6.5
Hardness H, GPa	31 ± 2.5
Elastic modulus E, GPa	394.8 ± 35.8
Elastic strain to failure H/E	0.078 ± 0.007
Resistance to plastic deformation H^3/E^2	0.191 ± 0.011
Residual stress, MPa	-3352 ± 64
Friction coefficient	0.6-0.65
Load of buckling cracks Lc_1, N	8.5 ± 1.5
Load of buckling spallation Lc_2, N	26.7 ± 1.8

Coating adhesion is an important property that may significantly affect coating performance, especially when adhesion wear is present. Coating failure is usually divided into two stages: first, the initial exposure of the substrate, where cohesion failure occurs inside the coating, corresponding to Lc_1; and then the complete spalling of the coating from the substrate, that is, interfacial damage or adhesion failure, corresponding to Lc_2 [42]. It has been determined that the adhesion strength of the experimental coating is 26.7 ± 1.8 N. The smaller the grains in the steel substrate, the more coherent or semi-coherent interface becomes between the substrate and the coating, leading to greater coating adhesion.

Fig. 5 shows the SEM image of the morphology of TiAlYN coating after a complete wear test and the corresponding EDX graph of chemical composition. Wear failure inside the groove is characterized by flaky chipping [42], without any substrate exposure. In addition, adhesion as well as furrows can be observed inside the wear track. The edges of the wear track show some accumulation of abrasive debris, and the EDS results show a large amount of Fe, C, and O elements, which is evidence of adhesive wear. It is worth mentioning that experimental coating has relatively high roughness caused by macroparticle fraction, the hard protrusions and defects on the coating surface fall off during friction and participate in the frictional behavior of the coating and the ball as abrasive particles, so that the wear pattern contains a number of grooves. As a result, three-body friction occurs, which reduces the contact between the coating and the ball, thus reducing the friction coefficient and wear rate.
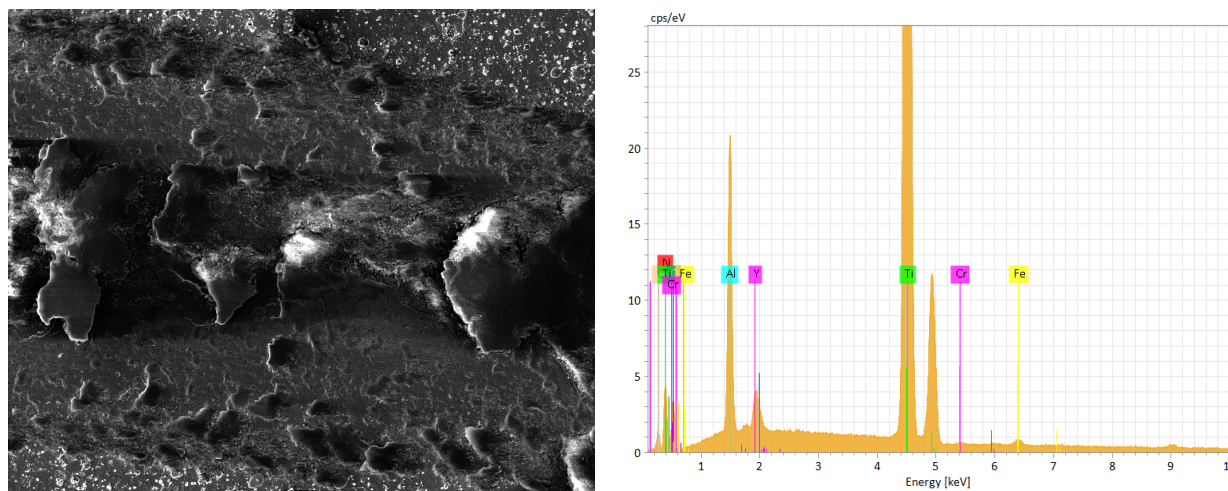
Figure 5. Image of the wear track on the surface (left) and corresponding EDX elemental graph (right) of TiAlYN coating.

In addition, the high wear performance of the coatings is also due to the high elastic modulus of 394.8 ± 35.8 GPa. During the wear test, the elastic strain energy stored in the coating increased as the pressure at the wear groove increased. Until the strain energy increased, until it directly broke the coating structure, and no significant coating fragmentation was produced.

DISCUSSION

The fact that experimental coating is composed of mixed phase structure (cubic NaCl-type and hexagonal wurtzite-type) demonstrates that the crystalline phase of the coating is affected by the addition of 5 at. % Y. Thus, the addition of large and therefore relatively immobile Y atoms (atomic radius 0.18 nm) leads to continuous re-nucleation during deposition [43, 44]. Also, strains due to the addition of Y promote the re-nucleation process. In sum, $Ti_{0.6}Al_{0.34}Y_{0.06}N$ coating exhibits fine grain size (12 nm) and nano-columnar structure.

In comparison with TiAlN coating, the hardness of $Ti_{0.6}Al_{0.34}Y_{0.06}N$ coating is comparatively identical (H = 31 ± 2.5 GPa). The high hardness partly results from the solution hardening due to the incorporation of larger Y

atoms into the TiAlN lattice at the metal atom sites. The reduced grain size of 12 nm also helps to increase the coating hardness. Moreover, the high level of compressive stress contributes to enhanced hardness, since the defects responsible for the compressive intrinsic stress act as the obstacles for dislocation movement [45]. Therefore, the improved hardness of experimental coating can be attributed to triple effects: solution hardening, grain refinement, and high residual compressive stress.

The residual stress of $Ti_{0.6}Al_{0.34}Y_{0.06}N$ coating (-3352 ± 64 MPa) is approximately three times that of TiAlN coating (-720 MPa) [46] and compatible with that of TiAlTaN coating (-3283 ± 92) [47]. Residual stress has a pronounced influence on the properties of coatings. High compressive stress increases the hardness of $Ti_{0.6}Al_{0.34}Y_{0.06}N$ coating. However, it also reduces the adhesion between coating and substrate up to a point where spallation occurs during the adhesive test. Therefore, it is necessary to optimize the residual stress value and improve substrate treatment in the future.

The wear resistance of $Ti_{0.6}Al_{0.34}Y_{0.06}N$ coating is relatively high. The addition of Y suggests the retarded growth of the oxide layer on the coating surface during wear testing. In general, while the wear testing of TiAlN coating, there are transport mechanisms: grain boundary inward transport of oxygen anions and grain boundary outward transport of metal cations. After the Y addition, Y ions are preferentially segregate at the grain boundaries, and therefore effectively retards the inward diffusion of oxygen [48, 49]. Consequently, the growth of the oxide layer is retarded. The retarded growth of the oxide layer also benefits from the formation of oxide phases, such as Y_2O_3 and Al_2O_3. The comparison of Gibbs free energy for the formation of Y_2O_3, Al_2O_3, and TiO_2 shows that Y has the highest affinity for oxygen. The strong interaction between Y and O inevitably inhibits the process of rutile TiO_2 formation. Besides, the first principal study, as well as several experimental investigations, indicate that the addition of Y promotes the formation of dense Al_2O_3, which is effective in restraining diffusion and therefore protects the coating from oxidative wear.

CONCLUSION

In this work, the implications of the presence of Y as a reactive element in cathodic vacuum arc TiAlN protective coating were investigated. The changes in the structure and properties were analyzed using SEM combined with EDX, XRD, indentation, and wear analyses. The following conclusions were obtained:

(1) The addition of Y changes the crystalline phase of $Ti_{0.6}Al_{0.34}Y_{0.06}N$ coating. It consists of a combination of cubic NaCl-type structure (base phase) and wurtzite structure (additional phase). Moreover, it results in fine grain size (12 nm) and nano-columnar structure.

(2) The formation of a w-AlN (wurtzite structure) does not deteriorate the mechanical properties of the coating. The hardness is 31 ± 2.5 GPa and the elastic modulus is 394.8 ± 35.8 GPa. The residual stress is approximately three times (-3352 ± 64 MPa) that of TiAlN coating (-720 MPa). The high mechanical characteristics can be attributed to solution hardening, grain refinement, and high residual compressive stresses.

(3) Abrasive wear and adhesive wear occurred in wear tests of the coating. High macroparticle fracture on the surface reduces the damage from adhesive wear, and, therefore, reduces the coating peeling during friction.

Notes

The authors declare no competing financial interest. The authors declare that they have no known competing financial interests or personal relationships that could have appeared to influence the work reported in this paper.

ORCID

Olga Maksakova, https://orcid.org/0000-0002-0646-6704; **Vyacheslav Beresnev**, https://orcid.org/0000-0002-4623-3243
Serhiy Lytovchenko, https://orcid.org/0000-0002-3292-5468; **Mária Čaplovičová**, https://orcid.org/0000-0003-4767-8823
L'ubomír Čaplovič, https://orcid.org/0000-0002-2280-008X; **Martin Kusý,** https://orcid.org/0000-0002-5553-1680
Irina Doshchechkina, https://orcid.org/0000-0002-6278-7780

REFERENCES

[1] Y. Deng, W. Chen, B. Li, C. Wang, T. Kuang, and Y. Li, "Physical vapor deposition technology for coated cutting tools: a review," Ceram. Int. **46**, 18373–18390 (2020). https://doi.org/10.1016/j.ceramint.2020.04.168

[2] B. Grossmann, A. Jamnig, N. Schalk, C. Czettl, M. Pohler, and C. Mitterer, "Tailoring age hardening of $Ti_{1-x}Al_xN$ by Ta alloying," J. Vac. Sci. Technol. A, **35**(6), 060604 (2017). https://doi.org/10.1116/1.4995000

[3] T. Akasawa, H. Sakurai, M. Nakamura, T. Tanaka, and K. Takano, "Effects of free-cutting additives on the machinability of austenitic stainless steels," J. Mater. Process. Technol. **143–144**(1), 6–71 (2003). https://doi.org/10.1016/S0924-0136(03)00321-2

[4] N. Sharma, K. Gupta, "Influence of coated and uncoated carbide tools on tool wear and surface quality during dry machining of stainless steel 304," Mater. Res. Express, **6**(8), (2019). https://doi.org/10.1088/2053-1591/ab1e59

[5] N. Schalk, M. Tkadletz, and C. Mitterer, "Hard coatings for cutting applications: physical vs. chemical vapor deposition and future challenges for the coatings community," Surf. Coat. Technol. 429 (2022). https://doi.org/10.1016/j.surfcoat.2021.127949

[6] K. Bobzin, "High-performance coatings for cutting tools," CIRP J. Manuf. Sci. Technol. **18**, 1–9 (2017). https://doi.org/10.1016/j.cirpj.2016.11.004

[7]   O. Kessler, Th. Herding, F. Hoffmann, and P. Mayr, "Microstructure and wear resistance of CVD TiN-coated and induction surface hardened steels," Surf. Coat. Technol. **182**(2), 184–191 (2004). https://doi.org/10.1016/j.surfcoat.2003.08.054

[8]   M.-Y. Wee, Y.-G. Park, and T.-S. Kim, "Surface properties of CrN-coated Ti–6Al–4V alloys by arc-ion plating process," Materials Letters, **59**(8–9), 876–879 (2005). https://doi.org/10.1016/j.matlet.2004.11.035

[9]   C. Ducros, and F. Sanchette, "Multilayered and nanolayered hard nitride thin films deposited by cathodic arc evaporation. Part 2: Mechanical properties and cutting performances," Surface and Coatings Technology, **201**(3-4), 1045-1052 (2006). https://doi.org/10.1016/j.surfcoat.2006.01.029

[10] T. Leyendecker, O. Lemmer, S. Esser, and J. Ebberink, "The development of the PVD coating TiAlN as a commercial coating for cutting tools," Surf. Coat. Technol. **48**, 175–178 (1991). https://doi.org/10.1016/0257-8972(91)90142-J

[11] P.H. Mayrhofer, A. Horling, L. Karlsson, J. Sjolen, T. Larsson, C. Mitterer, and L. Hultman, "Self-organized nanostructures in the Ti-Al-N system," Appl. Phys. Lett. **83**, 2049–2051 (2003). https://doi.org/10.1063/1.1608464

[12] M. Bartosik, H.J. Böhm, C. Krywka, Z.L. Zhang, and P.H. Mayrhofer, "Influence of phase transformation on the damage tolerance of Ti-Al-N coatings," Vacuum, **155**, 153–157 (2018). https://doi.org/10.1016/j.vacuum.2018.06.001

[13] L. Chen, J. Paulitsch, Y. Du, and P.H. Mayrhofer, "Thermal stability and oxidation resistance of Ti-Al-N coatings," Surf. Coatings Technol. **206**(11–12), 2954–2960 (2012). https://doi.org/10.1016/j.surfcoat.2011.12.028

[14] L. Rogström, J. Ullbrand, J. Almer, L. Hultman, B. Jansson, and M. Odén, "Strain evolution during spinodal decomposition of TiAlN thin films," Thin Solid Films, **520**(17), 5542–5549 (2012). https://doi.org/10.1016/j.tsf.2012.04.059

[15] L. Chen, J. Paulitsch, Y. Du, and P.H. Mayrhofer, "Thermal stability and oxidation resistance of Ti-Al-N coatings," Surf. Coat. Technol. **206**(11–12), 2954–2960 (2012). https://doi.org/10.1016/j.surfcoat.2011.12.028

[16] B. Grossmann, N. Schalk, C. Czettl, M. Pohler, and C. Mitterer, "Phase composition and thermal stability of arc evaporated $Ti_{1-x}Al_xN$ hard coatings with $0.4 \leq x \leq 0.67$," Surf. Coat. Technol. **309**, 687–693 (2017). https://doi.org/10.1016/j surfcoat.2016.11.015

[17] H. Willmann, P.H. Mayrhofer, P.O. Persson, A.E. Reiter, L. Hultman, and C. Mitterer, "Thermal stability of Al-Cr-N hard coatings," Scr. Mater. **54**(11), 1847–1851 (2006). https://doi.org/10.1016/j.scriptamat.2006.02.023

[18] B. Li, "A review of tool wear estimation using theoretical analysis and numerical simulation technologies," Int. J. Refract. Met. Hard Mater. **35**, 143–151 (2012). https://doi.org/10.1016/j.ijrmhm.2012.05.006

[19] V.F.C. Sousa, F.J.G. Da Silva, G.F. Pinto, A. Baptista, and R. Alexandre, "Characteristics and Wear Mechanisms of TiAlN-Based Coatings for Machining Applications: A Comprehensive Review," Metals, **11**, 260 (2021). https://doi.org/10.3390/met11020260

[20] M. Pfeiler, et al., "On the effect of Ta on improved oxidation resistance of Ti–Al–Ta–N coatings," J. Vac. Sci. Technol. A Vac. Surf. Film. **27**(3), 554–560 (2009). https://doi.org/10.1116/1.3119671

[21] A. Hemmati, M. Abdoos, and S.C. Veldhuis, "Developing Ti-Al-Ta-N based coatings: Thermal stability, oxidation resistance, machining performance and adaptive behavior under extreme tribological conditions," Materials Today Communications, **31**, 103373 (2022). https://doi.org/10.1016/j.mtcomm.2022.103373

[22] S. Siwawut, C. Saikaew, A. Wisitsoraat, and S. Surinphong, "Cutting performances and wear characteristics of WC inserts coated with TiAlSiN and CrTiAlSiN by filtered cathodic arc in dry face milling of cast iron," Int. J. Adv. Manuf. Technol. **97**, 3883–3892 (2018). https://doi.org/10.1007/s00170-018-2200-x

[23] W. Lu, G. Li, Y. Zhou, S. Liu, K. Wang, and Q. Wang, "Effect of high hardness and adhesion of gradient TiAlSiN coating on cutting performance of titanium alloy," J. Alloys Compounds, **820**, 153137 (2020). https://doi.org/10.1016/j.jallcom.2019.153137

[24] M. Mikula, D. Plašienka, D.G. Sangiovanni, M. Sahul, T. Roch, M. Truchlý, M. Gregor, et al., "Toughness enhancement in highly NbN-alloyed Ti-Al-N hard coatings," Acta Mater. **121**, 59–67 (2016) https://doi.org/10.1016/j.actamat.2016.08.084

[25] S.A. Glatz, R. Hollerweger, P. Polcik, R. Rachbauer, J. Paulitsch, and P.H. Mayrhofer, "Thermal stability and mechanical properties of arc evaporated Ti-Al-Zr-N hard coatings," Surf. Coat. Technol. **266**, 1–9 (2015). https://doi.org/10.1016/j.surfcoat.2015.01.042

[26] K. Yang, G. Xian, H. Zhao, H. Fan, J. Wang, H. Wang, and H. Du, "Effect of Mo content on the structure and mechanical properties of TiAlMoN films deposited on WC–Co cemented carbide substrate by magnetron sputtering," Int. J. Refract. Met. Hard Mater. **52**, 29–35 (2015). https://doi.org/10.1016/j.ijrmhm.2015.04.016

[27] L. Tomaszewski, W. Gukbinski, A. Urbanowicz, T. Suszko, A. Lewandowski, and W. Gulbinski, "TiAlN based wear resistant coatings modified by molybdenum addition," Vacuum, **121**, 223–229 (2015). https://doi.org/10.1016/j.vacuum.2015.08.027

[28] S.A. Glatz, H. Bolvardi, S. Kolozsvári, C.M. Koller, H. Riedl, and P.H. Mayrhofer, "Arc evaporated W-alloyed Ti-Al-N coatings for improved thermal stability, mechanical, and tribological properties," Surf. Coatings Technol. **332**, 275-282 (2017). https://doi.org/10.1016/j.surfcoat.2017.05.097

[29] J. Mo, Z. Wu, Y. Yao, Q. Zhang, and Q. Wang, "Influence of Y-Addition and Multilayer Modulation on Microstructure, Oxidation Resistance and Corrosion Behavior of $Al_{0.67}Ti_{0.33}N$ Coatings," Surf. Coat. Technol. **342**, 129–136 (2018). https://doi.org/10.1016/j.surfcoat.2018.02.071

[30] M. Moser, P.H. Mayrhofer, L. Székely, G. Sáfrán, and P.B. Barna, "Influence of bipolar pulsed DC magnetron sputtering on elemental composition and micro-structure of Ti–Al–Y–N thin films," Surface and Coatings Technology, **203**(1–2), 148-155 (2008). https://doi.org/10.1016/j.surfcoat.2008.08.042

[31] L. Székely, G. Sáfrán, V. Kis, Z.E. Horváth, P.H. Mayrhofer, M. Moser, G. Radnóczi, et al., "Crossover of texture and morphology in $(Ti_{1-x}Al_x)_{1-y}Y_yN$ alloy films and the pathway of structure evolution," Surface and Coatings Technology, **257**, 3-14 (2014). https://doi.org/10.1016/j.surfcoat.2014.08.071

[32] R. Rachbauer, D. Holec, M. Lattemann, L. Hultman, and P.H. Mayrhofer, "Electronic origin of structure and mechanical properties in Y and Nb alloyed Ti-Al-N thin films," Int. J. Mater. Res. **102**, 735–742 (2011). https://doi.org/10.3139/146.110520

[33] R. Aninat, N. Valle, J.-B. Chemin, D. Duday, C. Michotte, M. Penoy, L. Bourgeois, and P. Choquet, "Addition of Ta and Y in a Hard Ti-Al-N PVD Coating: Individual and Conjugated Effect on the Oxidation and Wear Properties," Corros. Sci. **156**, 171-180 (2019). https://doi.org/10.1016/j.corsci.2019.04.042

[34] M. Moser, D. Kiener, C. Scheu, and P.H. Mayrhofer, "Influence of Yttrium on the Thermal Stability of Ti-Al-N Thin Films," Materials, **3**, 1573–1592 (2010). https://doi.org/10.3390/ma3031573

[35] L.A. Donohue, D.B. Lewis, W.D. Münz, M.M. Stack, S.B. Lyon, H.W. Wang, and D. Rafaja, "The influence of low concentrations of chromium and yttrium on the oxidation behaviour, residual stress and corrosion performance of TiAlN hard coatings on steel substrates," Vacuum, **55**, 109–114 (1999). https://doi.org/10.1016/S0042-207X(99)00135-9

[36] H. Tawancy, N. Abbas, and A. Bennett, "Role of Y during high temperature oxidation of an M-Cr-Al-Y coating on an Ni-base superalloy," Surf. Coat. Technol. **68–69**, 10–16 (1994). https://doi.org/10.1016/0257-8972(94)90130-9

[37] S. Wang, Y. Kong, L. Chen, and Y. Du, "Adsorption behavior of oxygen on Ti0.5Al0.5N (001) surface with X-doped (X = La, Ce, Y, Hf, Zr, Ta, Cr, Si): A first-principles study," Applied Surface Science, **639**, 158245 (2023). https://doi.org/10.1016/j.apsusc.2023.158245

[38] R. Hollerweger, H. Riedl, M. Arndt, S. Kolozsvari, S. Primig, and P.H. Mayrhofer, "Guidelines for increasing the oxidation resistance of Ti-Al-N based coatings," Thin Solid Films, **688**, 137290 (2019). https://doi.org/10.1016/j.tsf.2019.05.009

[39] T.C. Rojas, S. Domínguez-Meister, M. Brizuela, and J.C. Sanchez-Lopez, "Influence of Al and Y content on the oxidation resistance of CrAlYN protective coatings for high temperature applications: New insights about the Y role," Journal of Alloys and Compounds, **773**, 1172-1181 (2019). https://doi.org/10.1016/j.jallcom.2018.09.28

[40] L.F. He, J. Shirahata, T. Nakayama, T. Suzuki, H. Suematsu, I. Ihara, Y.W. Bao, et al., "Mechanical properties of $Y_2Ti_2O_7$," Scripta Materialia, **64**(6), 548-551 (2011). https://doi.org/10.1016/j.scriptamat.2010.11.042

[41] Z.B. Qi, Z.T. Wu, and Z.C. Wang, "Improved hardness and oxidation resistance for CrAlN hard coatings with Y addition by magnetron co-sputtering," Surf. Coat. Technol. **259**, 146–151 (2014). https://doi.org/10.1016/j.surfcoat.2014.02.034

[42] K. Zhang, J. Deng, X. Guo, L. Sun, and S. Lei, "Study on the adhesion and tribological behavior of PVD TiAlN coatings with a multi-scale textured substrate surface," Int. J. Refract. Met. Hard Mater. **72**, 292–305 (2018). https://doi.org/10.1016/j.ijrmhm.2018.01.003

[43] P.Eh. Hovsepian, D.B. Lewis, Q. Luo, W.-D. Münz, P.H. Mayrhofer, C. Mitterer, Z. Zhou, and W.M. Rainforth, "TiAlN based nanoscale multilayer coatings designed to adapt their tribological properties at elevated temperatures," Thin Solid Films, **485**, 160 (2005). https://doi.org/10.1016/j.tsf.2005.03.048

[44] S. PalDey, and S.C. Deevi, "Single layer and multilayer wear resistant coatings of (Ti,Al)N: a review," Mater. Sci. Eng. A, **342**(1-2), 58–79 (2003). https://doi.org/10.1016/S0921-5093(02)00259-9

[45] A. Raveh, I. Zukerman, R. Shneck, R. Avni, and I. Fried, "Thermal stability of nanostructured superhard coatings: A review," Surf. Coat. Technol. **201**(13), 6136–6142 (2007). https://doi.org/10.1016/j.surfcoat.2006.08.131

[46] L. Zhu, Y. Zhang, W. Ni, and Y. Liu, "The effect of yttrium on cathodic arc evaporated Ti0.45Al0.55N coating," Surface and Coatings Technology, **214**, 53–58 (2013). http://dx.doi.org/10.1016/j.surfcoat.2012.10.074

[47] A. Hemmati, M. Abdoos, and S.C. Veldhuis, "Developing Ti-Al-Ta-N based coatings: Thermal stability, oxidation resistance, machining performance and adaptive behavior under extreme tribological conditions," Materials Today Communications, **31**, 103373 (2022). https://doi.org/10.1016/j.mtcomm.2022.103373

[48] C. Leyens, M. Peters, P.Eh. Hovsepian, D.B. Lewis, Q. Luo, and W.-D. Münz, "Novel coating systems produced by the combined cathodic arc/unbalanced magnetron sputtering for environmental protection of titanium alloys," Surf. Coat. Technol. **155**, 103–111 (2002). https://doi.org/10.1016/S0257-8972(02)00063-4

[49] M.I. Lembke, D.B. Lewis, W.-D. Münz, and J.M. Titchmarsh, "Significance of Y and Cr in TiAlN Hard Coatings for Dry High Speed Cutting," Surf. Eng. **17**, 153–158 (2001). https://doi.org/10.1179/026708401101517656

НАСЛІДКИ ПРИСУТНОСТІ Y ЯК РЕАКЦІЙНОЗДАТНОГО ЕЛЕМЕНТА В КАТОДНО-ДУГОВОМУ ЗАХИСНОМУ ПОКРИТТІ TiAlN ДЛЯ ТРИБОЛОГІЧНИХ ЗАСТОСУВАНЬ

Ольга Максакова[a,b], Вячеслав Береснєв[a], Сергій Литовченко[a], Марія Чапловичова[b], Любомир Чаплович[b], Мартін Куси[b], Іріна Дощечкина[c]

[a]Харківський національний університет імені В.Н. Каразіна, Харків, м. Свободи, 4, 61022, Україна
[b]Інститут матеріалознавства, Словацький технологічний університет у Братиславі,
25, вул. Яна Ботту, 917 24, Трнава, Словаччина
[c]Харківський національний автомобільно-дорожній університет, вул. Я. Мудрого, 61200, м. Харків, Україна

Приведено результати досліджень впливу Y як реакційноздатного елемента на властивості покриттів TiAlN отриманих методом вакуумно-дугового осадження. Зміни в структурі та властивостях були проаналізовані за допомогою SEM у поєднанні з EDX, XRD, аналізом вдавлення та аналізом зносу. Показано присутності Y змінює кристалічну фазу покриття Ti0,6Al0,34Y0,06N. Він складається з комбінації кубічної структури типу NaCl (базова фаза) і структури вюрциту (додаткова фаза). Крім того, це призводить до дрібного розміру зерна (12 нм) і нано-стовпчастої структури. Висока твердість частково є результатом твердіння розчину через включення більших атомів Y у решітку TiAlN у місцях розташування атомів металу. Зменшений розмір зерна 12 нм також сприяє підвищенню твердості покриття. Твердість становить 31±2,5 ГПа, модуль пружності 394,8±35,8 ГПа. Залишкове напруження приблизно в три рази (−3352±64 МПа) перевищує покриття TiAlN (−720 МПа). Крім того, високий рівень стискаючої напруги сприяє підвищенню твердості, оскільки дефекти, відповідальні за власну стискаючу напругу, є перешкодою для руху дислокацій. Покращену твердість експериментального покриття можна пояснити потрійним ефектом: зміцнення розчину, подрібнення зерна та високе залишкове напруження стиску. Додавання Y свідчить про сповільнене зростання оксидного шару на поверхні покриття під час випробування на знос. Після додавання Y іони Y переважно відокремлюються на границях зерен, і тому ефективно затримують дифузію кисню всередину. Додавання Y сприяє утворенню щільного Al_2O_3, який є ефективним у стримуванні дифузії і, отже, захищає покриття від окисного зношування.

Ключові слова: *вакуумно-дугове осадження; покриття; вюрцитна фаза; твердість; знос; критичні навантаження*

VIBRATIONAL FREQUENCIES OF PHOSPHORUS TRICHLORIDE
WITH THE VIBRATIONAL HAMILTONIAN

K. Lavanya[a,b], M.V. Phani Kumari[b], ⬤J. Vijayasekhar[b]*

aDepartment of Mathematics, St. Francis College for Women, Begumpet, Hyderabad, India
bDepartment of Mathematics, GITAM (Deemed to be University), Hyderabad, India
*Corresponding Author e-mail: vijayjaliparthi@gmail.com
Received March 3, 2024; revised April 18, 2024; accepted April 22, 2024

This study presents an approach for precisely determining the stretching vibrational frequencies of the P-Cl bond in phosphorus trichloride (PCl_3) using a vibrational Hamiltonian framework that maintains the C_{3v} symmetry point group. Our methodology enables the accurate prediction of vibrational frequencies up to the fifth overtone. It identifies related combination bands, marking a significant advancement in vibrational spectroscopy and molecular modelling. By enhancing the accuracy and depth of our understanding of molecular vibrations, this research paves the way for developing more sophisticated computational models, thereby significantly improving the precision of chemical analyses, and contributing to the broader field of chemical physics.
Key words: *Molecular Physics; Vibrational frequencies; Phosphorus trichloride; Vibrational Hamiltonian; Lie algebraic method*
PACS: 33.20.-t, 33.20.Ea, 82.80.Gk, 63.50.-x, 45.20. Jj, 47.10.Df, 02.20.Sv

1. INTRODUCTION

The field of spectroscopy has witnessed substantial advancements, significantly refining the precision and accuracy with which the vibrational modes of polyatomic molecules are determined. This progress has spurred the development of sophisticated theoretical frameworks leveraging the principles of dynamical symmetry articulated through the intricate mathematical formalism of Lie algebras. These cutting-edge models stand at the forefront of elucidating the complex interplay of vibrational and rotational dynamics within molecular systems. Central to these models is the adept use of algebraic techniques to construct an effective Hamiltonian operator. This operator plays a pivotal role in delineating the rotational and vibrational degrees of freedom within physical systems, enriching our understanding of molecular dynamics with unprecedented precision. One of the most innovative aspects of algebraic models lies in their ability to harmonize the physical underpinnings shared with both ab initio and semi-empirical methodologies. While ab initio methods delve into the theoretical realm by solving the Schrödinger equation, semi-empirical approaches leverage observed data to predict molecular vibrations pragmatically. Historically, the analysis of molecular spectra has oscillated between two predominant methodologies: the Dunham expansion and the potential energy approach. The Dunham expansion simplifies the analytical landscape by expressing energy levels as expansions in terms of vibration-rotation quantum numbers, thus offering a foundational understanding of molecular rovibrational spectra.

In contrast, the potential energy approach embarks on a more nuanced exploration by solving the Schrödinger equation with a specific inter-atomic potential, enriching our insight into molecular interactions. In recent years, algebraic models have excelled in deciphering the vibrational spectra of small to medium-sized molecules. These models utilize various mathematical groups or symmetries, such as U(4) and U(2), to adeptly analyze diverse molecular structures. While the U(4) model caters well to smaller molecules, its complexity burgeons with larger molecules, diminishing its applicability to systems exceeding four atoms. The U(2) model emerges as a solution to this challenge, demonstrating remarkable proficiency in modeling the stretching vibrations of complex polyatomic molecules. The superiority of U(2) Lie algebraic techniques over conventional methods, such as the Dunham expansion, is particularly notable in their precision and the minimal reliance on empirical data [1]. Iachello et al. initially applied the Lie algebraic method to explore the vibrational frequencies of polyatomic molecules, introducing a novel, mathematically rigorous approach to the field [2,3]. This methodology, which draws from the complex symmetry and structures inherent in Lie algebra, offered a more refined and accurate perspective on how molecules vibrate, significantly enhancing our understanding beyond what was achievable with previous methods. Since this foundational work, the Lie algebraic technique has seen extensive refinement and broad application. Researchers have honed the method for greater precision and extended its use to analyze a broader range of molecules [4,5,6]. This growth demonstrates the method's robustness and flexibility, showcasing its utility in providing deeper insights into the vibrational characteristics of a broad spectrum of molecular configurations, from simple to highly complex structures [7,8]. The continual development of the Lie algebraic approach represents the progressive nature of scientific exploration, where initial breakthroughs lay the groundwork for ongoing advancements. As this method evolves, it opens new doors for understanding the quantum mechanics of molecular vibrations, contributing significantly to spectroscopy, material science, and chemical engineering.

In recognition of the diverse applications of phosphorus trichloride vibrational frequencies, this study calculates them up to the fifth overtone alongside their combination bands. To achieve this, we employ a Hamiltonian operator

within the framework of Lie algebra. This approach not only underpins the mathematical rigor of our methodology but also enhances our ability to accurately model and predict the complex vibrational spectra of phosphorus trichloride. Through this algebraic method, we aim to provide a comprehensive analysis that contributes to the broader understanding and application of vibrational frequencies in phosphorus trichloride, offering valuable insights for both theoretical research and practical applications in the field.

2. STRUCTURE OF PHOSPHORUS TRICHLORIDE

The structural configuration of phosphorus trichloride is characterized by a trigonal pyramidal arrangement, perfectly embodying the C_{3v} symmetry point group. This symmetry classification is further detailed by its symmetry species: A_1 (symmetric stretch), A_1 (symmetric deformation), E (degenerate stretch), and E (degenerate deformation). At the heart of this molecular geometry lies a phosphorus atom, encircled symmetrically by three chlorine atoms. These atoms are not merely adjacent but strategically placed at the vertices of a triangle, forming the pyramid's base, with each chlorine atom bonded to the phosphorus atom through single bonds.

The essence of PCl₃'s symmetry, the C_{3v} point group, is underscored by a singular C_3 axis of symmetry complemented by three vertical planes of symmetry (σ_v). The C_3 axis, emblematic of a three-fold rotational symmetry, vertically pierces through the phosphorus atom. It stands orthogonal to the plane demarcated by the chlorine atoms, facilitating a rotation of 120 degrees around the phosphorus nucleus without altering the molecule's spatial configuration. Meanwhile, the σ_v planes, aligning vertically with the triangular base, dissect the P-Cl bonds so that each plane hosts the phosphorus atom and one chlorine atom. These planes enable a reflection of the molecule along them, reinforcing its trigonal pyramidal shape. This comprehensive symmetry not only bestows PCl₃ with its distinct non-linear shape but also intricately influences its vibrational modes, setting it apart from molecules with linear geometries.
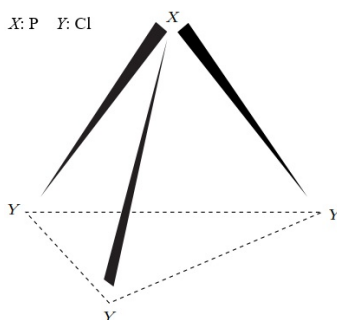
Figure 1. Structure of PCl₃

3. THE HAMILTONIAN APPROACH OF PCL₃

The exploration of the stretching modes (P-Cl) in phosphorus trichloride involves a sophisticated development of a Lie algebraic vibrational Hamiltonian, which intricately blends kinetic and potential energy elements. This blending is thoughtfully executed with a strong focus on the symmetry properties intrinsic to the molecule's structure. The advanced Hamiltonian model goes beyond its basic formulation by weaving in the complex interactions and symmetries specific to PCl₃. This results in a more refined and customized examination of its vibrational features, offering a deeper and more precise insight into the P-Cl stretching modes that mirror the unique molecular dynamics and interactions characteristic of PCl₃.

For the detailed analysis of the stretching vibrations of the P-Cl bonds, the effective Hamiltonians are crafted as follows [1,2,9]:

$$H^{P-Cl} = E_0 + \sum_{i=1}^{n=3} A_i\, C_i + \sum_{i<j}^{n=3} A_{ij}\, C_{ij} + \sum_{i<j}^{n=3} \lambda_{ij}\, M_{ij}. \tag{1}$$

In this formula, E_0 represents the zero-point energy, establishing the foundational energy level for vibrational states. The coefficients A_i, A_{ij}, and λ_{ij} are algebraically tied to the Casimir (C_i, C_{ij}) and Majorana (M_{ij}) operators, integral to the Lie algebra framework that underpins this vibrational Hamiltonian approach [4].

The Casimir and Majorana operators introduce modern analytical dimensions to molecular vibrational dynamics, which is particularly advantageous for molecules with unique symmetries. Casimir operators, rooted in the Lie algebra of specific symmetry groups, serve as constants of motion, elucidating the vibrational autonomy of molecules and effectively delineating both independent and interrelated bond movements. On the other hand, Majorana operators are crucial for constructing irreducible representations of Lie algebra, essential for exploring vibrational modes subject to symmetry considerations, thus outlining the interactions among local modes through diagonal and off-diagonal matrix components [10].

Incorporating these operators simplifies the algebraic structure of the vibrational Hamiltonian, facilitating computational efficiency and enhancing the precision of interpretations. These operators are vital for decoding the intricate interplay between molecular symmetry and vibrational dynamics. The calculation of coefficients A_i, A_{ij} and λ_{ij} employs molecular spectroscopic data, utilizing a least-squares fitting method for heightened accuracy.

For calculating algebraic operators relevant to P-Cl bonds, the expressions are:

$$\langle C_i \rangle = -4(Nv_i - v_i^2), \tag{2}$$

$$\langle N, v_i; N, v_j | C_{ij} | N, v_i; N, v_j \rangle = 4(v_i + v_j)(v_i + v_j - 2N), \tag{3}$$

$$\left.\begin{array}{l} \langle N, v_i; N, v_j | M_{ij} | N, v_i; N, v_j \rangle = v_i N + v_j N - 2v_i v_j \\ \langle N, v_i + 1; N, v_j - 1 | M_{ij} | N, v_i; N, v_j \rangle = -[v_j(v_i + 1)(N - v_i)(N - v_j + 1)]^{1/2} \\ \langle N, v_i - 1; N, v_j + 1 | M_{ij} | N, v_i; N, v_j \rangle = -[v_i(v_j + 1)(N - v_j)(N - v_i + 1)]^{1/2} \end{array}\right\}, \tag{4}$$

with calculations rooted in the vibrational quantum numbers v_i and v_j identify the vibrational states for bonds i and j, respectively, and the vibron number, $N = \frac{\omega_e}{\omega_e x_e} - 1$, derived from spectroscopic constants, ω_e and $\omega_e x_e$ specific to the P-Cl bond [11,12]. Initial estimates for A_i stem from the energy of the fundamental mode of a single oscillator, $E(\text{v} = 1) = -4A_i(N - 1)$ and $\lambda_{ij} = \frac{|E_i - E_j|}{3N}$ is calculated from the energy differences between vibrational modes, further refining the model's accuracy in depicting the vibrational landscape of PCl₃.

4. RESULTS

Table 1 provides a comprehensive overview of the vibrational frequencies extending to the fifth overtones and the corresponding combination bands observed in phosphorus trichloride, meticulously categorized by their symmetry species and specific vibrational modes. This detailed compilation is pivotal in shedding light on the distinctive attributes and dynamic behaviour inherent to the molecule under study. It underscores the intricate relationship between the observed vibrational frequencies, the diverse molecular motions, and the structural symmetries of phosphorus trichloride. By mapping out these frequencies and their associated modes, the table serves as a vital resource for understanding the vibrational spectrum of PCl₃. It enhances our grasp of how the molecule's geometry and symmetry influence its vibrational characteristics. This expansion into the vibrational domain of phosphorus trichloride thus provides invaluable insights into its physicochemical properties, facilitating a deeper comprehension of the molecule's internal mechanics and interaction with external stimuli.

Table 1: Phosphorus Trichloride Vibrational Frequencies

Vibrational mode	Vibrational frequencies (cm⁻¹)	
	Experimental [13]	Calculated
v₁ (symmetric stretching, A₁)	504	502.76
v₂ (deg stretching, E)	482	481.04
2v₁	-	937
2v₂	-	912
3v₁	-	1465
3v₂	-	1378
4v₁	-	1868
4v₂	-	1806
5v₁	-	2354
5v₂	-	2201
v₁+v₂	-	984
v₁+2v₂	-	1414
v₁+3v₂	-	1967
v₁+4v₂	-	2308
v₁+5v₂		2856
v₂+2v₁	-	1418
v₂+3v₁	-	1946
v₂+4v₁	-	2349
v₂+5v₁	-	2835

Fitted Parameters: $N = 246$, $A_i = -0.96$, $A_{ij} = -1.16$, $\lambda_{ij} = 0.035$

5. CONCLUSIONS

In conclusion, this research has made a substantial contribution to vibrational spectroscopy and molecular modelling by developing and applying a vibrational Hamiltonian framework tailored to phosphorus trichloride. Our methodological approach, emphasizing C₃ᵥ symmetry point group considerations, has enabled us to precisely predict the P-Cl stretching vibrational frequencies up to the fifth overtone and to identify the corresponding combination bands. This achievement marks a significant advancement by providing a deeper and more accurate understanding of molecular vibrations within PCl₃, thus offering insights that are crucial for developing more sophisticated computational models.

Moreover, the structural analysis of PCl₃, grounded in its trigonal pyramidal geometry and C₃ᵥ point group symmetry, has enriched our understanding of its vibrational modes. The detailed investigation into the Hamiltonian's

algebraic structure, incorporating Casimir and Majorana operators, offers a novel perspective on the molecular vibrational dynamics specific to PCl₃. This approach not only simplifies the computational analysis but also elevates the accuracy of our interpretations, highlighting the intricate relationship between molecular symmetry and vibrational characteristics.

The comprehensive data compilation presented in Table 1, outlining the vibrational frequencies and modes, serves as a testament to the precision and reliability of our methodological approach. It underscores the importance of symmetry considerations and algebraic methods in enhancing our understanding of molecular vibrations.

Future studies can build upon our findings by exploring the application of similar vibrational Hamiltonian frameworks to other molecules with unique symmetries. Further refinement of the computational models used in this research could lead to even more precise predictions of vibrational frequencies, thereby broadening the scope of vibrational spectroscopy and molecular modelling.

ORCID

J. Vijayasekhar, https://orcid.org/0000-0002-2745-7401

REFERENCES
[1] S. Oss, "Algebraic models in molecular spectroscopy," in: *Advances in Chemical Physics: New Methods in Computational Quantum Mechanics*, edited by I. Prigogine, and S. A. Rice, vol. 93, (John Wiley & Sons, Inc., 1996), pp. 455–649. https://doi.org/10.1002/9780470141526.ch8
[2] F. Iachello, and R.D. Levine, *Algebraic Theory of Molecules*, (Oxford University Press, Oxford, 1995).
[3] F. Iachello, "Algebraic methods for molecular rotation-vibration spectra," Chem. Phys. Lett. **78**(3), 581–585 (1981). https://doi.org/10.1016/0009-2614(81)85262-1
[4] V. Jaliparthi, and M.R. Balla, "Vibrational Hamiltonian of Tetrachloro-, Tetrafluoro-, and Mono- Silanes Using U(2) Lie Algebras," Spectrochim. Acta A, **264**, 120289 (2022). https://doi.org/10.1016/j.saa.2021.120289
[5] M.R. Balla, and V. Jaliparthi, "Vibrational Hamiltonian of Methylene Chloride Using U(2) Lie Algebra," Mol. Phys. **115**, e1828634 (2021). https://doi.org/10.1080/00268976.2020.1828634
[6] V. Jaliparthi, P. Suneetha, and K. Lavanya, "Vibrational spectra of cyclobutane-d8 using symmetry-adapted one-dimensional Lie algebraic framework," Ukr. J. Phys. Opt. **24**, 193–199 (2023). https://doi.org/10.3116/16091833/24/3/193/2023
[7] M.R. Balla, and V. Jaliparthi, "Vibrational Hamiltonian of Naphthalene (C10H8) Using Dynamical U(2) Lie Algebras," Polycycl. Aromat. Compd. **42**(7), 4684–4699 (2022). https://doi.org/10.1080/10406638.2021.1901126
[8] S. Nallagonda, and V. Jaliparthi, "Higher Overtone Vibrational Frequencies in Naphthalene Using the Lie Algebraic Technique," Ukr. J. Phys. Opt. **25**(2), 02080–02085 (2024). https://doi.org/10.3116/16091833/Ukr.J.Phys.Opt.2024.02080
[9] J. Choudhury, N.K. Sarkar, and R. Bhattacharjee, "Infrared Spectra of PH3 and NF3: An Algebraic Approach," Chinese Phys. Lett. **30**(7), 070301 (2013). https://doi.org/10.1088/0256-307X/30/7/070301
[10] K. Lavanya, A.G. Rao, and J. Vijayasekhar, "Vibrational Hamiltonian of Carbonyl Sulphide and Hydrogen Cyanide," East Eur. J. Phys., (1), 432–435 (2024). https://doi.org/10.26565/2312-4334-2024-1-46
[11] K. Nakamoto, *Infrared and Raman Spectra of Inorganic and Coordination Compounds: Part A: Theory and Applications in Inorganic Chemistry*, (Wiley, New York, 2009).
[12] K.P. Huber, and G. Herzberg, *Molecular Spectra and Molecular Structure. IV: Constants of Diatomic Molecules*, (Van Nostrand Reinhold, New York, 1979).
[13] T. Shimanouchi, *Tables of Molecular Vibrational Frequencies Consolidated*, Vol. I, (National Bureau of Standards, 1972).

ВИЗНАЧЕННЯ ЧАСТОТ КОЛИВАНЬ ТРИХЛОРИДУ ФОСФОРУ З ВИКОРИСТАННЯМ ВІБРАЦІЙНОГО ГАМІЛЬТОНІАНУ
К. Лаванья[a,b], М.В. Фані Кумарі[b], Дж. Віджаясекар[b]
ᵃДепартамент математики, жіночий коледж Св. Франциска, Бегумпет, Хайдарабад, Індія
ᵇДепартамент математики, GITAM (вважається університетом), Хайдарабад, Індія

У цьому дослідженні представлено підхід до точного визначення коливальних частот розтягування зв'язку P-Cl у трихлориді фосфору (PCl₃) з використанням вібраційного гамільтонового підходу, який підтримує точкову групу симетрії C₃ᵥ. Наша методологія дозволяє точно передбачити вібраційні частоти до п'ятого обертона. Вона ідентифікує пов'язані комбіновані смуги, знаменуючи значний прогрес у вібраційній спектроскопії та молекулярному моделюванні. Підвищуючи точність і глибину нашого розуміння молекулярних коливань, це дослідження прокладає шлях до розробки складніших обчислювальних моделей, тим самим значно підвищуючи точність хімічних аналізів і вносячи внесок у ширшу область хімічної фізики.

Ключові слова: *молекулярна фізика; вібраційні частоти; трихлорид фосфору; коливальний гамільтоніан; алгебраїчний метод Лі*

HIGHER OVERTONE VIBRATIONAL FREQUENCIES OF CYCLOBUTANE-D8 USING LIE ALGEBRAIC FRAMEWORK

A. Ganapathi Rao[a], K. Lavanya[b,c], J. Vijayasekhar[c]*

aDepartment of Basic Sciences and Humanities, GMR Institute of Technology, Rajam, India
bDepartment of Mathematics, St. Francis College for Women, Begumpet, Hyderabad, India
cDepartment of Mathematics, GITAM (Deemed to be University), Hyderabad, India
*Corresponding Author e-mail: vijayjaliparthi@gmail.com
Received January 22, 2024; revised March 15, 2024; accepted March 18, 2024

This research study employs a Lie algebraic framework to investigate the second and third overtone vibrational frequencies and their combination bands in cyclobutane-d8 (C_4D_8). The application of this framework ensures the preservation of the point symmetry group D_{2d}, characterized by the symmetry species A_1, A_2, B_1, B_2, and E. The analysis encompasses 23 normal vibrational modes within the molecular structure of cyclobutane-d8. Our study extensively explores the vibrational spectra, elucidating the intricate interactions among these vibrational modes. Preserving molecular symmetry allows for a deeper understanding of vibrational interactions, offering valuable insights into spectroscopy. The research enhances the comprehension of molecular structure and its applications in various fields, providing a detailed view of higher energy levels and complex vibrational transitions in cyclobutane-d8.
Keywords: *Hamiltonian operator; Lie algebraic framework; Vibrational Spectra; Morse oscillator; Cyclobutane-d8*
PACS: 33.20.-t, 33.20.Ea, 82.80.Gk, 63.50.-x, 45.20. Jj, 47.10.Df, 02.20.Sv

1. INTRODUCTION

The vibrational frequencies of molecules represent the specific frequencies at which atoms within a molecule vibrate, with atoms connected by chemical bonds acting like springs, allowing oscillation. Each vibrational mode corresponds to a unique oscillation frequency, offering valuable insights into molecular structure, bonding, and dynamic behavior. Experimental techniques such as infrared and Raman spectroscopy are commonly utilized to determine these frequencies associated with bond stretching and bending, influenced by factors like bond strength, atomic mass, and molecular symmetry. Understanding vibrational frequencies is pivotal in diverse scientific fields, including chemistry, physics, and biology, contributing to molecular spectroscopy, quantum chemistry, and molecular dynamics investigations. Various theoretical approaches are employed to determine vibrational frequencies, each with distinct principles. The harmonic oscillator model, as the simplest, assumes molecular vibrations as harmonic oscillators, approximating the potential energy surface near equilibrium and calculating frequencies as multiples of the harmonic oscillator frequency. Anharmonic methods extend beyond this model, considering deviations and utilizing quantum chemistry methods like vibrational configuration interaction and vibrational coupled cluster to include anharmonic effects [1-4]. Density functional theory approximates electronic structure based on electron density [5-7]. Ab initio methods, including Hartree-Fock theory and post-Hartree-Fock methods, offer accurate electronic structure information but demand computational intensity. Semi-empirical methods balance accuracy and computational efficiency, and force field methods use empirical potential energy functions parameterized for molecular dynamics simulations. Coupled mode approaches consider vibrational excitations as coupled modes, while group theory and symmetry considerations exploit molecular symmetry [8-13]. Each method involves trade-offs between computational efficiency and accuracy, emphasizing consideration of the specific molecule under study. Combining methods and validating against experimental data enhances overall reliability.

Introducing the symmetry-adapted Lie algebraic method for polyatomic molecules seeks to improve outcomes and address limitations found in traditional theoretical approaches [14, 15]. This innovative method strives to overcome constraints by modifying and integrating existing theoretical frameworks with the foundational principles of Lie algebras. Built upon Lie algebra principles, this method emerges as a potent theoretical approach within quantum chemistry. Particularly effective for symmetric molecules, it streamlines the analysis of vibrational motion by systematically simplifying vibrational degrees of freedom [16-20]. Its utility extends to both quantum chemistry and spectroscopy, offering valuable insights into vibrational modes and significantly contributing to interpreting experimental spectra.

This research study emphasizes the analysis of second and third overtone vibrational frequencies and their combination bands in cyclobutane-d8 of point group D_{2d} with the symmetry species A_1, A_2, B_1, B_2, E. The investigation uses the symmetry-adapted Lie algebraic method and is motivated by various factors with potential implications for practical uses. Studying these higher energy levels yields an intricate understanding of molecular oscillations, particularly in response to changes in molecular environments. The practical significance of this research spans various fields, such as spectroscopy, material and chemical engineering, environmental monitoring, and isotopic studies. It not only contributes to theoretical knowledge but also leads to practical advancements in these areas.

2. SYMMETRY-ADAPTED LIE ALGEBRAIC METHOD

The vibrational Hamiltonian (H), formulated within the framework of the Lie algebraic method, is expressed in terms of Casimir and Majorana operators, establishing a systematic foundation for analysing vibrational modes [15]. In this framework, the construction of the Hamiltonian is centred around operators that commute with it, forming a Lie algebra and ensuring compatibility with molecular symmetry, thereby systematically addressing vibrational degrees of freedom. Casimir operators, acting as invariants within the Lie algebra, are pivotal in identifying constants of motion within the vibrational system. These operators play a crucial role in systematically simplifying the vibrational Hamiltonian, significantly enhancing computational efficiency, particularly in studying symmetric molecules. Majorana operators, intricately connected to coupling schemes involving Lie algebras of interacting one-dimensional Morse oscillators, are instrumental in the diagonalization process of the vibrational Hamiltonian [16, 18]. The relationships between Majorana operators and the Lie algebraic framework aid in simplifying and diagonalizing the Hamiltonian, facilitating a more accessible analysis of vibrational modes. Expressed in terms of Casimir and Majorana operators, the vibrational Hamiltonian ensures a systematic treatment of vibrational degrees of freedom. It provides valuable insights into the symmetries and dynamics governing molecular vibrations. This approach contributes to a profound understanding of molecular structure and enhances the interpretability of experimental spectra, such as those obtained through techniques like infrared and Raman spectroscopy. Incorporating Casimir and Majorana operators in the vibrational Hamiltonian associated with the Lie algebraic method represents a powerful and efficient approach to studying molecular vibrations within the quantum mechanical framework [14, 17].

The vibrational Hamiltonians governing the C-D and C-C stretching vibrations in Cyclobutene-d8, used to calculate the vibrational frequencies, are represented as follows [21]:

$$H^{C-D} = E_0' + \sum_{i=1}^{n=8} A_i' C_i + \sum_{i<j}^{n=8} A_{ij}' C_{ij} + \sum_{i<j}^{n=8}\left(k_{ij}^1 + k_{ij}^2 + k_{ij}^3 + k_{ij}^4\right)\lambda_{ij}' M_{ij} \tag{1}$$

$$H^{C-C} = E_0'' + \sum_{i=1}^{n=4} A_i'' C_i + \sum_{i<j}^{n=4} A_{ij}'' C_{ij} + \sum_{i<j}^{n=4}\left(l_{ij}^1 + l_{ij}^2\right)\lambda_{ij}'' M_{ij} \tag{2}$$

with symmetry adapted neighbor couplings coefficients as

$$k_{ij}^1 = \begin{cases} 1, (i,j) = (1,2),(2,3),(3,4),(4,5),(5,6),(6,7),(7,8),(1,8) \\ 0, \; otherwise \end{cases}$$

$$k_{ij}^2 = \begin{cases} 1, (i,j) = (1,3),(2,4),(3,5),(4,6),(5,7),(6,8),(1,7),(2,8) \\ 0, \; otherwise \end{cases}$$

$$k_{ij}^3 = \begin{cases} 1, (i,j) = (1,4),(2,5),(3,6),(4,7),(5,8),(1,6),(2,7),(3,8) \\ 0, \; otherwise \end{cases}$$

$$k_{ij}^4 = \begin{cases} 1, (i,j) = (1,5),(2,6),(3,6),(3,7),(4,8) \\ 0, \; otherwise \end{cases}$$

$$l_{ij}^1 = \begin{cases} 1, (i,j) = (1,2),(2,3),(3,4),(1,4) \\ 0, otherwise \end{cases}$$

$$l_{ij}^2 = \begin{cases} 1, (i,j) = (1,3),(2,4) \\ 0, otherwise \end{cases}$$

In this context, $A_i, A_{ij}, \lambda_{ij}$ denote the algebraic parameters, while C_i and C_{ij} represent the Casimir (invariant) operators associated with the respective Lie algebras. Majorana (invariant) operators M_{ij} are intricately connected to coupling schemes incorporating Lie algebras of *n* interacting one-dimensional Morse oscillators. Utilizing spectroscopic data facilitates the determination of algebraic parameters, and the following expressions are applied to compute the algebraic operators:

$$\langle C_i \rangle = -4(N_i v_i - v_i^2) \tag{3}$$

$$\langle N_i, v_i; N_j, v_j | C_{ij} | N_i, v_i; N_j, v_j \rangle = 4\left(v_i + v_j\right)\left(v_i + v_j - N_i - N_j\right) \tag{4}$$

$$\left.\begin{aligned} \langle N_i, v_i; N_j, v_j | M_{ij} | N_i, v_i; N_j, v_j \rangle &= v_i N_j + v_j N_i - 2v_i v_j \\ \langle N_i, v_i + 1; N_j, v_j - 1 | M_{ij} | N_i, v_i; N_j, v_j \rangle &= -[v_j(v_i + 1)(N_i - v_i)(N_j - v_j + 1]^{1/2} \\ \langle N_i, v_i - 1; N_j, v_j + 1 | M_{ij} | N_i, v_i; N_j, v_j \rangle &= -[v_i(v_j + 1)(N_j - v_j)(N_i - v_i + 1]^{1/2} \end{aligned}\right\} \tag{5}$$

The following relationship provides the dimensionless vibronic number *N*, corresponding to the maximum bound states for each vibrating bond species within the Morse potential. The equation is expressed as follows:

$$N = \frac{\omega_e}{\omega_e \chi_e} - 1. \tag{6}$$

Here, ω_e and $\omega_e \chi_e$ represent the spectroscopic constants for the specific bonds and these constants are determined based on experimental data from diatomic molecules [22, 23]. The vibrational quantum numbers are denoted by v_i and v_j of the different bonds i and j respectively.

The initial estimates for A_i are derived from the energy expression for the single-oscillator fundamental mode:

$$E(\text{v} = 1) = -4A_i(N - 1). \tag{7}$$

Similarly, the initial approximations for λ_{ij} are determined through the following relations:

$$\lambda'_{ij} = \frac{|E'_s - E'_{as}|}{6N'}, \lambda''_{ij} = \frac{|E''_s - E''_{as}|}{2N''}. \tag{8}$$

Here, E'_s and E'_{as} represent the symmetric and asymmetric energies for the C-D stretching vibrations, while E''_s and E''_{as} denote the corresponding energies for the C-C stretching vibrations. The optimization of parameter values is achieved through a least-square regression fitting process, commencing with the initial estimates provided by equations (7) and (8). In this iterative procedure, the initial guesses for A_{ij} are set to zero.

3. RESULTS AND DISCUSSIONS

Within the Lie algebraic framework, Table 1 shows the optimized values for the algebraic parameters and vibron numbers that are part of the vibrational Hamiltonian. According to the reference [21], these specific parameters were used.

Table 1. Optimized parameters

Parameters	Value
N'(C-D stretching), N''(C-C stretching)	60, 136
$A_i{}'$(C-D stretching), $A_i{}''$(C-C stretching)	-9.2076, -1.2807
$A_{ij}{}'$(C-D stretching), $A_{ij}{}''$(C-C stretching)	1.0112, 0.1542
$\lambda_{ij}{}'$(C-D stretching), $\lambda_{ij}{}''$(C-C stretching)	0.3277, 0.8848
N (bending)	36
A_i (bending)	-6.4142
A_{ij} (bending)	0.4952
λ_{ij} (bending)	1.3449

The presented table (Table 2) showcases the calculated second and third overtone vibrational frequencies, along with their combination bands, for various vibrational modes of C_4D_8 (cyclobutane-d8) in wave numbers (cm^{-1}), utilizing the Lie algebraic method. A thorough study of the molecular vibrations and their interactions in cyclobutane-d8 provides significant insights into its vibrational spectroscopy. By identifying vibrational modes according to their symmetry species (A_1, A_2, B_1, B_2, and E), one can identify essential modes such as symmetric stretching (s-str), asymmetric stretching (a-str), scissoring (scis), rocking (rock), wagging (wag), twisting (twist), and ring deformation (ring deform). The vibrational modes v_{17} (CD_2 a-str), v_{15} (CD_2 a-str) and v_4 (CD_2 a-str) indicate higher frequencies, indicating strong molecular vibrations. Including combination bands, such as $v_4 + v_{17}$ and $v_{15} + v_{17}$, introduces higher frequencies that play a crucial role in the complex vibrational transitions of the molecule. The derived frequencies, which are essential for interpreting experimental spectra acquired via infrared and Raman spectroscopy, highlight the practical utility of this research. The identified combination bands significantly contribute to interpreting experimental spectra, enhancing our comprehension of the molecule's vibrational characteristics. Including second and third harmonic frequencies yields valuable information about higher energy levels, enabling a thorough comprehension of the vibrational structure of cyclobutane-d8.

Table 2. Vibrational frequencies of C_4D_8 (cm^{-1})

Vibrational mode	Symmetry species	II overtone	III overtone
v_1 (CD_2 s-str)	A_1	5835	8087
v_2 (CD_2 scis)	A_1	2967	4132
v_3 (CD_2 scis)	A_1	2188	3304
v_4 (CD_2 a-str)	A_1	6014	8328
v_5 (CD_2 rock)	A_1	1532	2360
v_6 (ring puck)	A_1	420	512
v_7 (CD_2 wag)	A_2	2791	3625
v_8 (CD_2 twist)	A_2	2497	3230
v_9 (CD_2 wag)	B_1	2910	4121
v_{10} (Ring deform)	B_1	1865	2647
v_{11} (CD_2 twist)	B_1	2205	3346
v_{12} (CD_2 s-str)	B_2	5879	8223

Vibrational mode	Symmetry species	II overtone	III overtone
v_{13} (CD$_2$ scis)	B$_2$	2724	3867
v_{14} (Ring deform)	B$_2$	2597	3529
v_{15} (CD$_2$ a-str)	B$_2$	6315	8614
v_{16} (CD$_2$ rock)	B$_2$	1215	1786
v_{17} (CD$_2$ a-str)	E	6533	8540
v_{18} (CD$_2$ twist)	E	2671	3644
v_{19} (CD$_2$ rock)	E	1415	2120
v_{20} (CD$_2$ s-str)	E	5845	8106
v_{21} (CD$_2$ scis)	E	3063	4184
v_{22} (CD$_2$ wag)	E	2750	3798
v_{23} (Ring deform)	E	1789	2513
$v_1 + v_{12}$		11716	16312
$v_1 + v_{20}$		11682	16195
$v_{12} + v_{20}$		11726	16331
$v_4 + v_{15}$		12331	16744
$v_4 + v_{17}$		12549	16870
$v_{15} + v_{17}$		12850	17156

4. CONCLUSION

The second and third overtone vibrational frequencies and combination bands in cyclobutane-d8 have been investigated using the symmetry-adapted Lie algebraic method in this study. Our study has highlighted the complex interactions among 23 normal vibrational modes while preserving the D$_{2d}$ point symmetry group. Utilizing Casimir and Majorana operators, the Lie algebraic framework has accelerated computations while fostering a profound understanding of the dynamics of molecular vibrations. A thorough comprehension of the molecular structure of Cyclobutene-d8 has been attained by evaluating the vibrational Hamiltonians for C-D and C-C stretching vibrations with Casimir and Majorana operators. Our representation was enhanced, and our understanding of molecular dynamics was improved by including symmetry-adapted neighbor coupling coefficients. The presentation of calculated second and third overtone vibrational frequencies and significant combination bands simplifies understanding of experimental spectra from various fields. The research holds practical implications, as evidenced by our results. The robust theoretical approach known as the symmetry-adapted Lie algebraic method excels in studying symmetric molecules by systematically simplifying vibrational degrees of freedom. Its value extends beyond improving computational efficiency and provides invaluable information about how molecular structures function.

ORCID
J. Vijayasekhar, https://orcid.org/0000-0002-2745-7401

REFERENCES
[1] C.W. Bauschlicher, and S.R. Langhoff, "The calculation of accurate harmonic frequencies of large molecules: the polycyclic aromatic hydrocarbons, a case study," Spectrochim. Acta A, **53**(8), 1225-1240 (1997). https://doi.org/10.1016/S1386-1425(97)00022-X
[2] V. Špirko, and W.P. Kraemer, "Anharmonic potential function and effective geometries for the NH$_3$ molecule," J. Mol. Spectrosc. **133**(2), 331-344 (1989). https://doi.org/10.1016/0022-2852(89)90196-3
[3] S. Brodersen, and J.-E. Lolck, "Calculation of rotation-vibrational energies directly from an anharmonic potential function," J. Mol. Spectrosc. **126**(2), 405-426 (1987). https://doi.org/10.1016/0022-2852(87)90246-3
[4] P.T. Panek, A.A. Hoeske, and C.R. Jacob, "On the choice of coordinates in anharmonic theoretical vibrational spectroscopy: Harmonic vs. anharmonic coupling in vibrational configuration interaction," J. Chem. Phys. **150**(5), 054107 (2019). https://doi.org/10.1063/1.5083186
[5] E.E. Porchelvi, and S. Muthu, "Vibrational spectra, molecular structure, natural bond orbital, first-order hyperpolarizability, thermodynamic analysis and normal coordinate analysis of Salicylaldehyde p-methylphenylthiosemicarbazone by density functional method," Spectrochim. Acta A, **134**, 453-464 (2015). https://doi.org/10.1016/j.saa.2014.06.018
[6] B. Karthikeyana, K. Sakthiraj, and P. Senthilkumar, "Investigation of Indium Trihydride Molecule and Its Clusters Using Density Functional Theory for Semiconductor Application," Acta Phys. Pol. A, **139**(1), 14-19 (2021). https://doi.org/10.12693/APhysPolA.139.14
[7] N.e Mardirossian, and M. Head-Gordon, "Thirty years of density functional theory in computational chemistry: an overview and extensive assessment of 200 density functionals," Mol. Phys. **115**(19), 2315-2372 (2017). https://doi.org/10.1080/00268976.2017.1333644
[8] L. Lapinski, H. Rostkowska, M.J. Nowak, J.S. Kwiatkowski, and J. Leszczyński, "Infrared spectra of thiouracils: experimental matrix isolation and ab initio Hartree-Fock, post-Hartree-Fock and density functional theory studies," Vib. Spectrosc. **13**(1), 23-40 (1996). https://doi.org/10.1016/0924-2031(96)00026-4

[9] P. Echenique, and J.L. Alonso, "A mathematical and computational review of Hartree–Fock SCF methods in quantum chemistry," Mol. Phys. **105**(23-24), 3057-3098 (2007). https://doi.org/10.1080/00268970701757875

[10] H. Ghalla, N. Rekik, A. Michta, B. Oujia, and H.T. Flakus, "Theoretical modeling of infrared spectra of the hydrogen and deuterium bond in aspirin crystal," Spectrochim. Acta A, **75**(1), 37-47 (2010). https://doi.org/10.1016/j.saa.2009.09.029

[11] W. Li, Z. Ni, and S. Li, "Cluster-in-molecule local correlation method for post-Hartree–Fock calculations of large systems," Mol. Phys. **114**(9), 1447-1460 (2016). https://doi.org/10.1080/00268976.2016.1139755

[12] R. Venkatraman, J.S. Kwiatkowski, G. Bakalarski, and J. Leszczynski, "Molecular structure and IR spectra of bromomethanes by DFT and post-Hartree-Fock MP2 and CCSD(T) calculations," Mol. Phys. **98**(6), 371-386 (2000). https://doi.org/10.1080/00268970009483302

[13] K.B. Beć, J. Grabska, and C.W. Huck, "Current and future research directions in computer-aided near-infrared spectroscopy: A perspective," Spectrochim. Acta A, **254**, 119625 (2021). https://doi.org/10.1016/j.saa.2021.119625

[14] F. Iachello, and R.D. Levine, *Algebraic theory of molecules*, (Oxford University Press, Oxford, 1995).

[15] V. Jaliparthi, and M.R. Balla, "Vibrational Hamiltonian of Tetrachloro-, Tetrafluoro-, and Mono- Silanes Using U(2) Lie Algebras," Spectrochim. Acta A, **264**, 120289 (2022). https://doi.org/10.1016/j.saa.2021.120289

[16] M.R. Balla, and V. Jaliparthi, "Vibrational Hamiltonian of Naphthalene (C10H8) Using Dynamical U(2) Lie Algebras," Polycycl. Aromat. Compd. **42**(7), 4684-4699 (2022). https://doi.org/10.1080/10406638.2021.1901126

[17] S. Oss, "Algebraic models in molecular spectroscopy," in: *Advances in Chemical Physics: New Methods in Computational Quantum Mechanics*, vol. 93, edited by I. Prigogine, and S.A. Rice (John Wiley & Sons, Inc. 1996). pp. 455-649. https://doi.org/10.1002/9780470141526.ch8

[18] M.R. Balla, and V. Jaliparthi, "Vibrational Hamiltonian of Methylene Chloride Using U(2) Lie Algebra," Mol. Phys., **115**, e1828634 (2021). https://doi.org/10.1080/00268976.2020.1828634

[19] V. Jaliparthi, "Vibrational Energies of Silylene, Difluorosilylene and Dichlorosilylene, Using U(2) Lie Algebraic Model," Ukr. J. Phys. Opt. **23**(3), 126-132 (2022). https://doi.org/10.3116/16091833/23/3/126/2022

[20] M.R. Balla, S. Venigalla, and V. Jaliparthi, "Calculation of Vibrational Frequencies of Sulfur Dioxide by Lie Algebraic Framework," Acta Phys. Pol. A, **140**(2), 138-140 (2021). https://doi.org/10.12693/APhysPolA.140.138

[21] J. Vijayasekhar, P. Suneetha, and K. Lavanya, "Vibrational spectra of cyclobutane-d8 using symmetry-adapted one-dimensional Lie algebraic framework," Ukr. J. Phys. Opt. **24**, 193-199 (2023). https://doi.org/10.3116/16091833/24/3/193/2023

[22] K. Nakamoto, *Infrared and Raman Spectra of Inorganic and Coordination Compounds: Part A: Theory and Applications in Inorganic Chemistry*, (Wiley, New York, 2009).

[23] K.P. Huber, and G. Herzberg, *Molecular Spectra and Molecular Structure. IV: Constants of Diatomic Molecules*, (Van Nostrand Reinhold, New York, 1979).

ДОСЛІДЖЕННЯ ВИЩИХ ОБЕРТОНІВ КОЛИВАЛЬНИХ ЧАСТОТ ЦИКЛОБУТАНУ-D8 З ВИКОРИСТАННЯМ АЛГЕБРИ ЛІ

А. Ганапаті Рао[a], К. Лаванья[b,c], Дж. Віджайясекар[c]

[a]*Департамент фундаментальних та гуманітарних наук, Технологічний інститут GMR, Раджам, Індія*

[b]*Факультет математики жіночого коледжу Св. Франциска, Бегумпет, Гайдарабад, Індія*

[c]*Департамент математики, GITAM (вважається університетом), Хайдарабад, Індія*

У цьому дослідницькому дослідженні використовується алгебраїчна структура Лі для дослідження частот коливань другого та третього обертонів та їхніх комбінованих смуг у циклобутані-d8 (C_4D_8). Застосування цього каркасу забезпечує збереження точкової групи симетрії D_{2d}, що характеризується видами симетрії A_1, A_2, B_1, B_2 та E. Аналіз охоплює 23 нормальні коливальні моди в молекулярній структурі циклобутану-d8. Наше дослідження широко досліджує вібраційні спектри, з'ясовуючи складну взаємодію між цими вібраційними модами. Збереження молекулярної симетрії дозволяє глибше зрозуміти вібраційні взаємодії, пропонуючи цінну інформацію про спектроскопію. Дослідження покращує розуміння молекулярної структури та її застосування в різних областях, забезпечуючи детальне уявлення про вищі енергетичні рівні та складні коливальні переходи в циклобутані-d8.

Ключові слова: *оператор Гамільтона; алгебра Лі; коливальні спектри; осцилятор Морзе; циклобутан-d8*

STRUCTURE AND PROPERTIES OF INTERPOLYMER COMPLEXES BASED ON SODIUM CARBOXYMETHYLCELLULOSE POLYSACCHARIDE AND CARBOPOL

Sabitjan Ya. Inagamov[a]*, Abror Eshmatov[b], Feruza A. Pulatova[a], Gafur I. Mukhamedov[b]

[a]Tashkent Pharmaceutical Institute, Tashkent, 100015, Mirabad district, Aibek st., 45, Uzbekistan
[b]Chirchik State Pedagogical University, Chirchik, Republic of Uzbekistan
*Corresponding Author e-mail: sabitjan1957@mail.ru; phone: +99894 662-96-07

In this paper, the structure and properties of interpolymer complexes (IPC) based on sodium carboxymethylcellulose with a linear carbopol were studied. Interpolymer complexes were obtained by mixing aqueous solutions of Na-CMC and carbopol components in various ratios of components and pH of the medium. The structure of the obtained products was determined using the methods of IR spectroscopy and X–ray diffraction analysis. IR spectra in the range of 400-4000 cm^{-1} were recorded on spectrophotometers "NIKOLET Magna-560 IR" and "Specord–75 IR" (Karl Zeiss, GDR). X-ray diffraction analysis of IPC films was carried out on a Rigaku X-Ray installation with an X-ray generator with a rotating copper anode, at a voltage of 40 kV, with a current strength of 15 mA and using characteristic Cu-Ka radiation in the area of angles $0 < 2\theta < 40$. IR spectroscopic data show that the interpolymer complexes based on Na-CMC and carbopol obtained in moderately acidic regions are stabilized due to the cooperative hydrogen bond between the carboxyl groups of Na-CMC and the carbonyl groups of carbopol. X-ray diffraction analysis has shown that a change in the composition of the interpolymer complex leads to a change in the structure, which depends on the structure and nature of the interchain bonds. It is ascertained that an increase in the number of hydrogen bonds leads to a more ordered state of the resulting interpolymer complex. It is revealed that the formation of an interpolymer complex due to hydrogen bonds provides additional stability. This can serve as one of the means of controlling the structure and properties of the IPC of sodium carboxymethylcellulose with carbopol.

Keywords: *Sodium carboxymethylcellulose; Carbopol; Polycomplex; Interpolymer complex; Films; Structure; Properties; IR spectroscopy; X-ray diffraction analysis; Hydrogen bond*
PACS: 61.41.+e

INTRODUCTION

Interpolymer complexes (IPC) are promising products in pharmacy and are increasingly being used as thickeners and stabilizers of suspensions, prolongators of the action of drugs, film-forming agents for capsules and tablets, as bases for ointments and other soft dosage forms, since they reveal a number of unique and most valuable properties [1-4].

IPC are products of the interaction of chemically complementary macromolecules – polyanions and polycations or proton donors and acceptors. Unlike conventional chemical reactions between low molecular weight substances, the interaction between macromolecules is of a cooperative nature. The formation of a bond between the links of complementary chains, the strength of which coincides with the strength of the corresponding bond between small molecules, greatly facilitates the formation of subsequent interpolymer contacts. This ensures exceptionally high stability of IPC, even if the free energy of a single bond formation is small [4].

IPC are divided into two groups – stoichiometric - interpolymer complexes (S-IPC), in which chemically complementary links are included in an equimolar (1:1) ratio of components (Figure 1, *a*) and non-stoichiometric interpolymer complexes (N-IPC) containing an excess of one of the components (Figure 1, *b* and *c*) [1.5-8]. In the structure of the IPC, it is possible to distinguish uniformly connected areas that have formed with each other (section A), defective areas that are not connected with each other (section B) and an excess area of the IPC (section C) of one or another component (Figure 1, *b* and *c*).

It is interesting to note that IPC particles have colloidal properties similar to protein structures, with a change in the ratio of interacting components, the structure charge, solubility of the hydrogel structure, pH, controlled permeability through water and solutions, including components of physiological fluids and other properties of the products obtained can be regulated [8]. The consequence of this is an unusually good biocompatibility and hemocompatibility of interpolymer complexes.

These features of the structure and properties of IPC open up wide opportunities for their use in various fields of practice, including pharmacy [8].

When producing interpolymer complexes, swelling polyelectrolytes of natural origin are used as polyanions: alginic acid and its sodium salt, agar-agar, gums, pectin, polymers containing sulfogroups: heparin, dextran sulfonic acid, chondroitin sulfate, hyaluronic acid; and polyelectrolytes of synthetic origin: polymers and copolymers of acrylic and methacrylic acid, copolymers of methoxyethylene with maleic anhydride and its hydrolysates, partial esters of vinyl acetate copolymer with maleic anhydride, vinyl acetate copolymers with crotonic acid and cellulose derivatives: methylcellulose, sodium carboxymethylcellulose, etc.

Cationic polyelectrolytes include gelatin, chitosan, as well as polydimethyldiallylammonium chloride, polyethylene glycol, polyethylenimine, collagen, biopolymers, urea-formaldehyde oligomers, etc.

When mixing aqueous solutions of the above natural and synthetic polyelectrolytes under certain technological conditions, IPC stabilized by ionic, hydrogen and other types of bonds are formed. Depending on the ratio of interacting components, stoichiometric and non-stoichiometric interpolymer complexes or polycomplex gels can be obtained. These obtained products are successfully used in pharmacy as carriers of drugs with prolonged actions [9-16].

Interpolymer complexes are very promising and occupy an important place in materials technology, engineering, medicine, and other areas of the national economy, since they reveal a number of unique and most valuable properties. In addition, the ability of many polyelectrolytes to interact with other polymer compounds opens up broad prospects in the field of modification and controlled synthesis of macromolecular systems. Due to this, in principle, completely new materials can be obtained from most of the known substances [17-19].

Interpolymer complexes based on cellulose derivatives, the polyanion of sodium carboxymethylcellulose (Na-CMC) and linear carbopol (CP), are very interesting and promising in this aspect [17-19].

The present Na-CMC and carbopol systems are also promising in connection with their industrial multi-tonnage production directly in the Republic of Uzbekistan on the basis of local resources, which is especially important for solving problems of possible practical implementation: problems of obtaining IPC-based medicinal gels-carriers of medicines with specified properties, the use of IPC-based gels as the basis for ointments with controlled diffusion membrane properties, which have significant scientific and applied significance [20-22].

Figure 1. Schematic representation of the structure of S-IPC (*a*) and N-IPC (*b, c*) with an excess of polycation (*b*) and polyanion (*c*)

EXPERIMENTAL
Materials

Sodium Carboxymethylcellulose (Na-CMC). The main object of the study was purified Na-CMC of the Namangan Chemical Plant, obtained by heterogeneous solid-phase esterification of sulfite wood pulp with monochloroacetic acid (MCHAA) of the following structure:
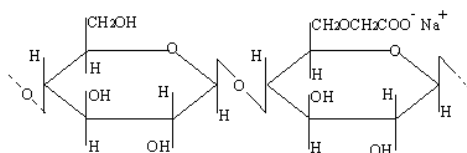
with a degree of substitution (SD) 70 and a degree of polymerization (PD) 450, according to SSt 5.588-79 and BA 6-05-386-80. When using Na-CMC, it was repeatedly purified from low molecular weight salts according to the procedure given in the paper [23].

Na-CMC is a weak polyacid, its dissociation constant depends on the SD. When the SD changes from 10 to 80, the dissociation constant changes from 5.25×10^{-7} to 5×10^{-5} [1,2]. Na-CMC is a white or slightly yellowish powdery or fibrous odorless product with a bulk weight of 400-800 kg/m^3, density of 1.59 g/cm^3. The refractive index is 1.515. The softening temperature is Na-CMC T = 443 K, at a higher temperature it decomposes. Na-CMC is soluble in cold and hot water. They form highly viscous aqueous solutions. In aqueous solutions, it is a polyelectrolyte. Na-CMC is approved for wide use in medicine and pharmacy [23].

Carbopol. The second component of IPC is carbopol, a white, powdery polymer obtained by polymerization of acrylic acid. Carbopol does not dissolve in nonpolar organic solvents, but it swells strongly in water and polar solvents and forms a gel. The bulk density of carbopol is approximately 208 kg/m^3, the glass transition temperature is 373–378 K. On average, the particle size of a solid polymer is approximately 2-7 microns, and each particle is a three-dimensional mesh structure of woven polymer chains. The density of polymers is 1.39-1.41 kg/m^3. The pH value of 1% of the aqueous dispersion of acidic forms is 2.5 - 3.5. At pH values >6, the carboxyl groups of the polymer are ionized, as a result of which repulsion occurs between negatively charged particles, leading to swelling of the polymer and straightening of the chain [24-26].

Synthesis of interpolymer complexes based on Na-CMC with carbopol. Solutions of Na-CMC in bidistilled water with concentrations from 0.01 to 0.1 basic mol/l were used. Reaction mixtures of the required concentrations were prepared by mixing reagent solutions in an appropriate proportion at room temperature and pH 3.8-7.2. Under these conditions, water-soluble interpolymer complexes with stabilized hydrogen bonds are formed [27, 28].

Determination of the pH value of IPC solutions. Determination of the pH value of the base: 5 g of the base was mixed with 50 ml of purified water heated to a temperature of 323-333 K, after careful shaking, filtered through filter paper. The pH values of the resulting aqueous extract were measured using a potentiometric method on a universal

pH meter "Bante 210 Bentchtop pH Meter" with glass (measuring) and silver chloride (comparative) electrodes at a temperature of 297 K [29].

Obtaining IPC films. Films from IPC were obtained by mixing aqueous solutions of Na-CMC and carbopol components in equinormal ratios at different component contents and pH of the medium. The solutions were poured onto an optical glass substrate and evaporated at room temperature. The solid dry films were washed with bidistilled water to a neutral pH value, then dried at room temperature [1,2].

Viscometric properties. The viscosity of solutions of interpolymer complexes was determined on a Ubbelode viscometer (d=2 mm), at various temperatures under thermostatically controlled conditions, and the expiration time of the solution from the capillary was determined. The method for determining the viscosity of solutions is described in detail in [1,2].

IR spectroscopy. IR spectra in the range of 400 - 4000 cm^{-1} were recorded on "Specord–75 IR" spectrophotometers (Karl Zeiss, Germany) and NIKOLET Magna–560 IR. The samples for IR spectroscopy were prepared in the form of tablets with KBr, films on a KRS–5 plate and films with a thickness of 8-12 microns. Films on the KRS-5 plate were obtained by evaporation of a solvent (water) at room temperature (295-297 K) [3,4].

X-ray diffraction analysis [30, 31]. X-ray diffraction analysis was performed on a Rigaku X-Ray installation with an X-ray generator with a copper rotating anode (maximum power 18 kW), at a voltage of 40 kV, a current of 15 mA and with a goniometer "Miniflex 300/600". D/teX Ultra 2 X-ray diffraction detector, 1D scanning mode(scan), scanning speed is 10^{0}/min, step width is 0.02^{0}, scanning axes are $\theta/2\theta$, scanning range is 5-40⁰, X-ray wavelength λ=1.5418 nm, using characteristic Cu-Ka radiation in the region angles $0 <2\theta <40$ without a filter and at a temperature T = 298 K [30,31].

RESULTS AND DISCUSSION

The IPC obtained on the basis of Na-CMC and carbopol were studied by IR spectroscopy and X-ray diffraction analysis. IR spectra in the range of 400-4000 cm^{-1} were recorded on Specord -75 IR spectrophotometers (Carl Zeiss) and UR-20 (GDR). The samples for IR spectroscopy were prepared in the form of tablets with KBr, films on a KRS - 5 plate and films with a thickness of 8-12 microns obtained by the above method. Films on the KRS-5 plate were obtained by evaporation of a solvent (water) at room temperature (295-297 K) [3,4].

The pH value of 0.2% carbopol solution is 3.5. With the help of organic solutions, the pH of the solution can be changed from 5 to 10. IR spectroscopic data showed that there are from 50 to 68.5% carboxyl groups in the carbopol structure. In addition to the carboxyl group, the carbopol structure contains such functional groups having absorption bands of 2960 cm^{-1}, 1720 cm^{-1}, 1455 cm^{-1}, 1415 cm^{-1}, 1250 cm^{-1}, 1175 cm^{-1}, 800 cm^{-1} (Fig. 2). The most active, intense bands are 1720 cm^{-1}, which belong to the carboxyl groups of carbopol.
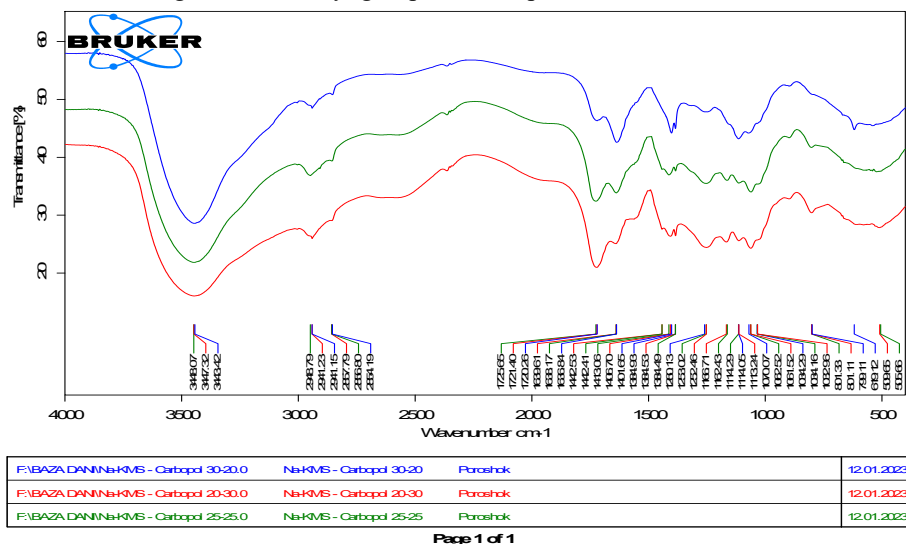
Figure 2. IR spectra of interpolymer complexes based on Na-CMC and carbopol polysaccharides

Furthermore, the second component of the Na-CMC polycomplex, in addition to the polydispersity usual for high-molecular compounds, has significant compositional chemical heterogeneity [2], i.e. it has a different quantitative ratio of functional groups in the chain and a different distribution of these groups in the link. Therefore, it can be considered as a copolymer consisting of two types of units: D – glucopyranose with glucopyronosoglycolic acid. In neutral media at a pH of about 6-7, both unsubstituted hydroxyl groups and a mixture of ionized carboxyl groups are present in the Na-CMC macromolecule. Quantitative analysis of the Na-CMC spectra using data on the characteristic frequencies of individual functional groups [1,2] made it possible to assign all absorption bands and ascertain structural patterns. The analysis of the IR spectra of Na-CMC and carbopol shows that the constituent components of the polycomplex are multifunctional. The presence of OH- (3200-3500cm^{-1}), COO–(1590-1620cm^{-1}, 1410cm^{-1}) and COOH (1700 cm^{-1})

functional groups in their macromolecules gives these polymers the characteristic properties of polyelectrolytes [3,4]. According to the results of IR spectroscopic studies, it can be argued that, apparently, the Na-CMC polycomplex with carbopol obtained in moderately acidic regions is stabilized by hydrogen bonds between the carboxyl groups of Na-CMC with carbonyl groups of carbopol [3,4].

When aqueous solutions of Na-CMC and carbopol are mixed in neutral and slightly acidic media, water-soluble PC stabilized by hydrogen bonds are formed (Fig. 3).
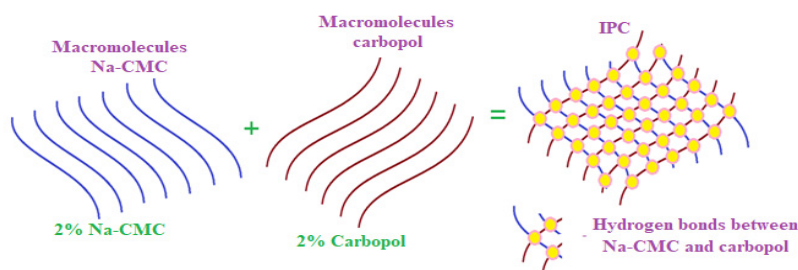
Figure 3. The scheme of interpolymer complexes formation based on Na-CMC and carbopol

Reaction mixtures were prepared by mixing concentrated (C =0.1 basic mol/l) solutions of Na-CMC and carbopol under certain technological conditions and in certain component ratios. The pH of electrolyte solutions and their mixtures was carried out on a pH meter "210 Benchtop pH/mV meter" using combined electrodes. The accuracy of the pH measurement is 0.01 pH units. Before measuring, the device was adjusted using standard solutions. Titration was carried out with constant stirring and at a temperature of 22-24^{0}C. When mixing solutions of Na-CMC and carbopol, gel-like, transparent IPCs are formed that can be used as a base for soft drugs in the production of gels, ointments, creams, pastes and liniments. When aqueous solutions of Na-CMC and carbopol are mixed at a pH of a moderately acidic region, a transparent water-soluble polycomplex composite is formed, stabilized by hydrogen bonds between the carboxyl groups of Na-CMC with carbonyl groups of carbopol (Fig.4, curve 1).
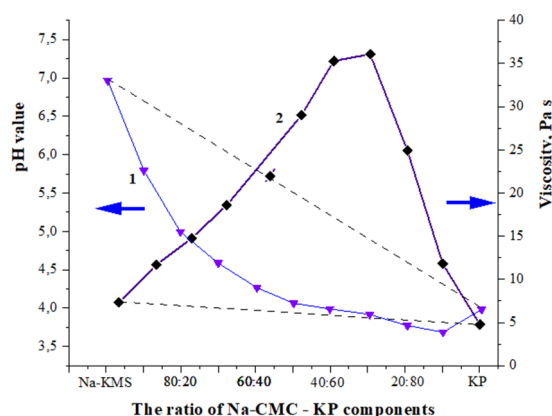
Figure 4. Graph of the pH (1) dependence and viscosity of IPC (2) solutions on the ratio of Na-CMC-carbopol components

To study the equilibrium of the Na-CMC-carbopol reaction, a potentiometric titration method was used, which is widely used to study the reactions of polycomplex formation. The results indicate the formation of IPC in neutral and slightly acidic environments. Mixing of Na-CMC and carbopol solutions is accompanied by a decrease in pH, which is typical for reactions between polyelectrolytes. The maximum output of the polycomplex corresponds to the equimolar ratio of the interacting components. [1,2] (Fig.4, curve 1). Experimental data have shown that the pH decrease for mixtures of Na-CMC and carbopol is the highest value of ΔpH = 0.7- 1.0, which indicates a weak intermolecular interaction of the reacting components (Fig.4, curve 1).

Experimental data on the study of the viscosity of solutions of interpolymer complexes have shown that the viscosity value depends on the ratio of interacting components. The addition of a carbopol solution under certain technological conditions to the Na-CMC solution leads to an increase in viscosity and, with an equimolar ratio of interacting components, reaches its maximum value. A further increase in the amount of carbopol leads to a decrease in the viscosity of the polycomplex solution. The maximum change in the viscosity of solutions of polycomplexes from additivity with an equimolar composition is 15-20 Pa·s (Fig. 4, curve 2). To confirm the above data, the structure of the obtained IPC was studied by X-ray diffraction analysis (Fig. 5).

X-ray diffraction analysis allows you to objectively determine the structure of polymers, polycomplexes and other complex coordination compounds, etc. A complete structural study of IPCs often allows you to solve purely chemical problems, for example, ascertaining or clarifying a chemical formula, type of bond, molecular weight at a known density or density at a known molecular weight, symmetry and configuration of molecules and molecular ions.

X-ray diffraction analysis is most successfully used to ascertain the atomic structure of amorphous crystalline bodies. This is due to the fact that the crystals have a strict periodicity of structure and represent a diffraction grating for X-rays created by nature itself. Based on the width, shape and intensity of the diffractogram, conclusions can be drawn about the features of the near-range order in a particular crystalline or amorphous structure [30,31].

Figure 5 shows the diffractograms of Na-CMC (*a*), carbopol (*b*) and the interpolymer complex with an equimolar component ratio (*c*), from which it can be seen that all the studied systems belong to amorphous crystalline polymers. The diffractogram revealed an intense reflex of $2\theta = 22^\circ$ (d = 4.4 Å), which occurs due to the superposition of reflexes (002 and 101) characteristic of cellulose II (Fig. 5, a, b), [30-32]. This Na-CMC reflex reflects the presence of a pronounced short-range order along the chain of a rigid-chain polymer.

In the IPC diffractogram, Na-CMC – carbopol can be found to be significantly ordered compared to Na-CMC and carbopol. The amorphous state of the initial constituent components of Na-CMC and carbopol, during interaction, passes into a more ordered state due to the formation of a hydrogen bond between the constituent components of the IPC. The diffractogram of the IPC Na-CMC – carbopol of equimolar composition clearly shows a change in the intensity of reflexes 101 and 002 and a new band is formed in the region $2\theta=38^\circ$ (Fig.5, c). This fact can be explained by the interaction of Na-CMC with carbopol and it is typical for a mixture of two interacting components.

Figure 5. X-ray diffractograms of Na-CMC – (a), carbopol – (b) and IPC at a molar ratio of Na-CMC : Carbopol 1:1 - (c)

Thus, X-ray examination shows that a change in the composition of the interpolymer complex leads to a change in the structure, which depends on the structure and nature of the interchain bonds. An increase in the number of hydrogen bonds apparently leads to a more ordered state of the resulting interpolymer complex.

CONCLUSIONS

1. It follows from the above research results that a new interpolymer complex has been obtained based on Na-CMC and carbopol.

2. The structure and properties of the obtained product were studied by IR spectroscopy, potentiometric titration, viscosity and X-ray diffraction analysis.

3. The relationship between the structure of carbopol and Na-CMC, as well as the structure formed during their interaction, is revealed, and the possibility of forming an interpolymer complex due to hydrogen bonds providing additional stability is shown.

4. The formation of an interpolymer complex due to hydrogen bonds can serve as one of the means of controlling the structure and properties of the IPC of sodium carboxymethylcellulose with carbopol.

ORCID

Sabitjan Y. Inagamov, https://orcid.org/0000-0003-0587-7963; **Gafurjan I. Mukhamedov,** https://orcid.org/0000-0001-9413-3522

REFERENCES

[1] G.I. Mukhamedov, M.M. Khafizov, and S.Y. Inagamov, *Interpolymer complexes: structure, properties, application*, (LAP LAMBERT Academic Publishing, 2018). https://www.morebooks.de/shop-ui/shop/product/9786138326816

[2] S.Ya. Inagamov, and G.I. Mukhamedov, Journal of Applied Polymer Science, **3**, 1749 **(**2011). https://doi.org/10.1002/app.34222

[3] S.Ya. Inagamov, U.A. Asrorov, N.T. Qodirova, O.T. Yomgirov, and G.I. Mukhamedov, AIP Conf. Proc. **2999**, 020049 (2023). https://doi.org/10.1063/5.0158621

[4] S.Ya. Inagamov, U.A. Asrorov, and E.B. Xujanov, East European Journal of Physics, **4**, 258 (2023), https://doi.org/10.26565/2312-4334-2023-4-32

[5] S.Ponsubha, and A.K. Jaiswal, Carbohydrate Polymers, **238**, 116179 (2020). https://doi.org/10.1016/j.carbpol.2020.116179

[6] R. Keldibekova, S. Suleimenova, G. Nurgozhina, and E. Kopishev, Polymers, **15**, 3326 (2023). https://doi.org/10.3390/polym15153326

[7] A. Amirova, S. Rodchenko, M. Kurlykin, A. Tenkovtsev, I. Krasnou, A. Krumme, and A. Filippov, Journal of Applied Polymer Science, **138** (3), e49708 (2021). https://doi.org/10.1002/app.49708

[8]   A.D. Kulkarni, Y.H. Vanjari, K.H. Sancheti, H.M. Patel, V.S. Belgamwar, S.J. Surana, and C.V. Pardeshi, Artif. Cells Nanomed. Biotechnol. 44, 1615–1625, (2016). https://doi.org/10.3109/21691401.2015.1129624

[9]   S.C. Bizley, A.C. Williams, and V.V. Khutoryanskiy, Soft Matter, **10**, 8254 (2014). https://doi.org/10.1039/c4sm01138d

[10] S.Ya. Inagamov, G.I. Mukhamedov, Z.I. Akhmadzhonov, A.A. Abzalov, I.A. Ashirbekov, and Z. Yakubjanova, Patent Uzbekistan No. IAP 05551, (28 February, 2018). (in Uzbekistanian)

[11] H. Mndlovu, L.C. du Toit, P. Kumar, Y.E. Choonara, T. Marimuthu, P.P.D. Kondiah, and V. Pillay, Molecules, **25**, 222, (2020). https://doi.org/10.3390/molecules25010222

[12] S. Choiri, T.N.S. Sulaiman, and A. Rohman, Drug Development and Industrial Pharmacy, **46**(1), 146-158 (2020). https://doi.org/10.1080/03639045.2019.1711387

[13] P. Ramgonda, R.S. Masareddy, A. Patil, and U. Bolmal, Indian Journal of Pharmaceutical Education and Research, **55**(1), (2021). https://doi.org/10.5530/ijper.55.1s.47

[14] A.V. Bukhovets, A.Y. Sitenkov, and R.I. Mustafin, Polym. Adv. Technol. **32**, 2761 (2021). https://doi.org/10.1002/pat.5284

[15] A.V. Bukhovets, N. Fotaki, V.V. Khutoryanskiy, and R.I. Moustafine, Polymers, **12**(7), 1459 (2020). https://doi.org/10.3390/polym12071459

[16] S. Tao, Y. Chu, Z. Wang, X. Xu, and Q. Tan, e-Polymers, **20**, 242 (2020) https://doi.org/10.1515/epoly-2020-0018.

[17] K. Enoch, and A.A. Somasundaram, International Journal of Biological Macromolecules, **253**(8), 127481 (2023). https://doi.org/10.1016/j.ijbiomac.2023.127481

[18] E.A. Bekturov, and I.E. Suleimenov, *Polymer hydrogels*, (Gylym, Almaty, 2003).

[19] I.E. Suleymanov, T.V. Budtova, R.M. Iskakov, E.O. Batirbekova, B.A. Zhubanov, and E.A. Bekturov, *Polymer hydrogels in pharmaceuticals*, (Almaty-St-Petersburg, 2004).

[20] A. Alford, B. Tucker, V. Kozlovskaya, J. Chen, N. Gupta, R. Caviedes, J. Gearhart, et al., Polymers, **10**(12), 1342 (2018). https://doi.org/10.3390/polym10121342

[21] A. Bianchera, and R. Bettini, Expert Opinion on Drug Delivery, **17**(10), 1345 (2020). https://doi.org/10.1080/17425247.2020.1789585

[22] S.Ya. Inagamov, M.F. Tulyasheva, and G.I. Mukhamedov, International Journal of Applied Nanotechnology Research, **6**(1), 1 (2021). https://doi.org/10.4018/IJANR.287586

[23] V.V. Khutoryanskiy, and G. Staikos, editors, *Hydrogen-Bonded Interpolymer Complexes Formation, Structure and Applications*, (World Scientific, 2009). https://doi.org/10.1142/6498

[24] I.A. Gutowski, D. Lee and J.R. de Bruyn, Rheol. Acta, **51**, 441 (2012). https://doi.org/10.1007/s00397-011-0614-6

[25] G.P. Kukhtenko, T.V. Popova, E.V. Gladukh, and A.S. Kukhtenko, Zaporizhia Medical Journal, **22**(3), 120 (2020). https://doi.org/10.14739/2310-1210.2020.3.204960. (in Russian)

[26] M. Agarwal, and Y.M. Joshi, Phys. Fluids, **31**, 063107-1 (2019). https://doi.org/10.1063/1.5097779

[27] A.A. Sarimsakov, *Medium– and low-substituted carboxymethylcellulose – preparation, properties and application*, (FAN, Tashkent, Uzbekistan, 2005). (in Russian)

[28] M. Bhowmik, K. Dharmalingam, S. Halder, P. Muthukumar, and R. Anandalakshmi, Journal Applide Polymer Science, (2021). https://doi.org/10.1002/app.51607.

[29] E. Nordmeier, and P. Beyer, J. Polimer. Sci. B, **37**(4), 335 (1999). https://doi.org/10.1002/(SICI)1099-0488(19990215)37:4%3C335::AID-POLB7%3E3.0.CO;2-W

[30] T.Y. Inan, Recent Developments in Polymer Macro, Micro and Nano Blends, 17 (2017). https://doi.org/10.1016/B978-0-08-100408-1.00002-9

[31] D. Ren, Y.-H. Li, S.-P. Ren, T.-Y. Liu, and X.-L. Wang, Journal of Membrane Science, **610**, 118295 (2020). https://doi.org/10.1016/j.memsci.2020.118295

[32] J. Potas, E. Szymanska, A. Basa, A. Hafner, and K. Winnicka, Materials, **14**, 86, (2021). https://dx.doi.org/10.3390/ma14010086

БУДОВА ТА ВЛАСТИВОСТІ ІНТЕРПОЛІМЕРНИХ КОМПЛЕКСІВ НА ОСНОВІ ПОЛІСАХАРИДУ КАРБОКСИМЕТИЛЦЕЛЮЛОЗИ НАТРІЮ ТА КАРБОПОЛУ

Сабітян Я. Інагамов[a], Аброр Ешматов[b], Феруза А. Пулатова[a], Гафур І. Мухамедов[b]

[a]Ташкентський фармацевтичний інститут, Узбекистан, 100015, м. Ташкент, Мірабадський район, вул. Айбека, 45
[b]Чирчикський державний педагогічний університет, м. Чирчик, Республіка Узбекистан

У роботі досліджено структуру та властивості інтерполімерних комплексів (ІПК) на основі натрійкарбоксиметилцелюлози з лінійним карбополом. Інтерполімерні комплекси отримували змішуванням водних розчинів Na-КМЦ і компонентів карбополу в різних співвідношеннях компонентів і pH середовища. Структуру отриманих продуктів визначали методами ІЧ-спектроскопії та рентгеноструктурного аналізу. ІЧ-спектри в діапазоні 400-4000 см-1 записували на спектрофотометрах «NIKOLET Magna-560 IR» та «Specord–75 IR» (Karl Zeiss, НДР). Рентгеноструктурний аналіз плівок ІПС проводили на установці Rigaku X-Ray з генератором рентгенівського випромінювання з обертовим мідним анодом, напругою 40 кВ, силою струму 15 мА та характеристикою Cu-Ka. випромінювання в області кутів 0 <2θ <40. Дані ІЧ-спектроскопії показують, що отримані в помірно кислих областях інтерполімерні комплекси на основі Na-КМЦ і карбополу стабілізуються за рахунок кооперативного водневого зв'язку між карбоксильними групами Na-КМЦ і карбонільними групами карбополу. Рентгеноструктурний аналіз показав, що зміна складу інтерполімерного комплексу призводить до зміни структури, яка залежить від структури та природи міжланцюгових зв'язків. Встановлено, що збільшення числа водневих зв'язків призводить до більш упорядкованого стану отриманого інтерполімерного комплексу. Виявлено, що утворення інтерполімерного комплексу за рахунок водневих зв'язків забезпечує додаткову стабільність. Це може служити одним із засобів контролю структури і властивостей МПК натрійкарбоксиметилцелюлози з карбополом.

Ключові слова: *натрій карбоксиметилцелюлоза; карбопол; полікомплекс; інтерполімерний комплекс; плівки; структура; властивості; ІЧ-спектроскопія; рентгеноструктурний аналіз; водневий зв'язок*

RADIATION GRAFT COPOLYMERIZATION OF VINYL FLUORIDE TO COTTON, HYDROCELLULOSE FIBER AND FABRIC

Fozilbek Z. Jamoldinov[a,b]*, **Rixsibek M. Yusupaliyev**[a], **Ummatjon A. Asrorov**[c,d#]

[a]Tashkent state technical university, Tashkent 100095, Uzbekistan
[b]Tashkent State Technical University named after Islam Karimov, 100000 Tashkent, Uzbekistan
[c]National University of Uzbekistan named after Mirzo Ulugbek, Tashkent, Uzbekistan
[d]Tashkent State Pedagogical University named after Nizami, Tashkent, Uzbekistan
*Corresponding Author e-mail: jamoldinovfozilbek@gmail.com, #e-mail: ummat.asror@mail.ru
Received February 7, 2024; revised March 03, accepted March 13, 2024

Cellulose-based materials are not in short supply and are characterized by relatively low cost. On the other hand, cellulose fibers have a wide range of valuable physical, chemical and mechanical properties that make them indispensable in a number of sectors of the national economy. Along with valuable qualities, natural and artificial cellulose fibers also have some disadvantages that limit their use in technology and in the national economy. These are low resistance to the action of microorganisms, relatively low heat resistance, chemical resistance, flammability, etc., which reduce their service life and limit their scope. One of the ways to eliminate these shortcomings is the modification of natural and artificial macromolecular compounds by chemical and physicochemical methods. Improving the properties of cellulose and its derivatives can be achieved by various modification methods, among which one of the most promising is the radiation-chemical grafting of various monomers. One of the advantages of this method, in comparison with others, is the production of field worlds that are not contaminated with impurities, the presence of which can adversely affect their physicochemical properties. Another advantage is the relative ease of formation of macroradicals necessary to initiate the process of graft copolymerization. Quite a lot of work has been devoted to the radiation grafting of various monomers to cellulose and its derivatives; at present, some of them are beginning to be widely used in the national economy. In the light of the foregoing, the grafting of fluorine-containing monomers, the polymers and copolmers of which have such very valuable and specific properties as high heat resistance, chemical resistance, light resistance, decay resistance and hydrophobicity to cellulose and its derivatives, is of great scientific and practical interest. This work is the synthesis of graft copolymers of cotton cellulose with vinyl fluoride by the radiation-chemical method from the vapor phase, the study of the effect of radiation dose rate, reaction time, the presence and nature of solvents on the course of this process and the yield of graft copolymers, as well as the study of such important physical and chemical properties and operational properties of the original, irradiated and grafted copolymers, such as sorption capacity and density, hydrophobicity and swelling, degree of whiteness, mechanical properties, thermal stability, the nature of the change in the supramolecular structure as a result of grafting fluorine-containing polymers.

Keywords: *Radiation grafting, Monomer; Thermal capacity; Thermal stability; Hydrophobicity; Degree of whiteness; Supramolecular structure; Fluorine-containing polymers*
PACS: 61.41.+e

INTRODUCTION

One of the effective ways to modify the properties of cellulose fibers is their graft copolymerization with various vinyl monomirs. This leads to a significant improvement in such important physical, chemical and performance properties of cotton cellulose as sorption capacity, dyeability, resistance to the action of microorganisms, chemo- and heat resistance, etc [1, 3].

The schematic formation of cellulose graft copolymerization can be represented as follows:

Cell $\xrightarrow{\gamma}$ Cell^O. + H - formation of a free macroradical.

Cell^O + M $\longrightarrow$ Cell - M^O - initiation of the graft copolymerization reaction. where M is a monomer.

Chain termination occurs as a result of chain transfer to monomer or solvent molecules, as well as during the interaction of a growing chain with monomer radicals:

Cell (M)$_{n-1}$ - M^O + M $\longrightarrow$ Cell - (M)$_n$ + M^O
Cell(M)$_{n-1}$ - M^O + R $\longrightarrow$ Cell(M)$_n$ + R^0
Cell(M)$_{n-2}$ - M^O + M^O $\longrightarrow$ Cell(M)$_n$

This scheme is the most general, and in each specific case it is necessary to take into account the possibility of a particular process occurring.

One of the features of the grafting reaction to cellulose is the need to use various liquids or their vapors in order to swell cellulose in them. Cellulose swellings are more accessible to monomer molecules as a result of facilitating their diffusion inside the fibers [2].

As a result of numerous studies in the study of the process of graft copolymerization of a number of vinyl monomers to cellulose, it was found that in the presence of water, alcohols, amines and dimethylformamide, the yield of the graft copolymer increases, and in the presence of non-polar liquids such as benzene, toluene and others, the graft copolymerization reaction proceeds with very low efficiency [3].

Japanese researchers have shown that for the synthesis of graft copolymers with a high yield by joint irradiation of cellulose and styrene, methyl methacrylate, or another vinyl monomer with Co^{60} γ-gamma rays, it is sufficient to use cellulose swollen in water. They also showed that in the absence of water or other solvents that cause swelling of cellulose, graft copolymerization practically does not occur [3-4].

The purpose of this work was to obtain new graft copolymers based on cotton cellulose with fluorine-containing monomers under laboratory conditions, to select methods and conditions for synthesis, as well as to comprehensively study some of the physicochemical and operational properties of the synthesized samples in order to determine and select their areas of application [5].

We took cellulose from cotton fiber and cotton fabric /coarse calico/ as initial samples. It can be noted that these preparations differ significantly from each other both in terms of the web of the molecular packaging and in other most important physicochemical properties. Cotton fiber always has various impurities such as hemicellulose, fats, wax, lignin, etc., which significantly affect its reactivity. Therefore, before use, cotton cellulose and cotton fabric were thoroughly cleaned of lubricants [6].

EXPERIMENTAL PART
Materials

For the synthesis of fluorine-containing graft copolymers, we used vinyl fluoride, ($CH_2 = CHF$) [7].

Sentiz vinyl fluoride was carried out by us by catalytic hydrofluorination of fine acetylene in the reaction:

$$CH \equiv CH + HF \frac{360 \div 380°}{AlF_3 + C} = CH_2 = CHF$$
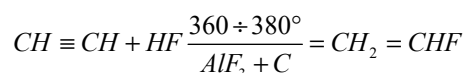
Industrial anhydrous hydrogen fluoride was used for the hydrofluorination of acetylene. Aluminum fluoride mixed with graphite was used as a catalyst. The resulting vinyl fluoride was purified by a chemical method to a high degree of purity, which was controlled using a gas chromatograph. Graft copolymers were synthesized by combined irradiation of cellulose fibers in vinyl fluoride vapor in the presence and absence of vapors of various solvents. The formation of the adopted copolymer was determined by weight gain and by analysis of the fluorine content in the adopted copolymer [7-9].

The polymer weight gain was calculated by the Equation:

$$A = \frac{A_1 + A_0}{A_1} \cdot 100$$

where A_0 is the weight of the initial polymer, A_1 is the weight of the graft copolymer [6-7].

The fluorine content in percent was calculated by the Equation:

$$x = \frac{0.000475(v_1 - v_2)}{g} K \cdot 100 = 0.0475 \frac{(v_1 - v_2)}{g} K$$

where v_1 - is the volume of 0.025 N thorium nitrate solution used for titration of the test sample, *ml*. v_2 - volume of 0.025 N thorium nitrate solution used for titration in a blank experiment, *ml*. 0.000475 - the amount of fluorine corresponding to 1 ml of 0.0025 N solution of thorium nitrate, *K*-correction factor for bringing the concentration of a solution of thorium nitrate *g*. *g*-sample weight, *g* [6-7].

The study of these polymers will make it possible to find the general patterns of grafting fluorine-containing monomers to cellulose and will lead to an improvement in some of their physicochemical performance properties. This will further expand the scope of their application in various sectors of the national economy, make them even more durable and valuable in operation [8]

We have studied the kinetics of grafting vinyl fluoride /VF/ to cotton cellulose, fabrics based on them. The results obtained show that the kinetics of grafting is influenced by various factors, such as dose, dose rate, presence of solvents, swelling of the starting and obtained materials in solvents, etc [9].

Sorption of water vapors was studied on a high-vacuum sorption setup such as McBain balances at 25°C\pm 0.2°C.

Determination of sorption is based on measuring the weight of a pre-dried sample in vacuum, as the water vapor pressure increases [15]. The dry sample weight was calculated using the Equation:

$$g_{dry} = g_{bl.} - \frac{r\Delta h}{1000} \tag{1}$$

where r is the sensitivity of the springs, *mg/mm*, Δh-difference of cathetometer readings before and after pumping out, *mm*, g_{dry} - weight of the sample after pumping out, *g* [10-13].

To determine the amount of moisture sorbed by the samples during each measurement of each sample, the constant *K* was calculated [10-13];

$$K = \frac{r}{g_{dry}} \cdot 100, \tag{2}$$

where *K* - shows the amount of sorbed water vapor as a percentage when the springs are extended by 1 *mm*.

The thermal stability of the samples was studied by the thermographic method on an instrument with Mac-Bon spring balances with a spiral sensitivity of $r=1.96$. The weight loss of the heated samples was recorded by the movement of a special mark in the field of the MG-1 horizontal microscope and was calculated in % according to the Eqs. [11-13].

$$K = \frac{r \cdot \Delta l}{g_l} \cdot 100 \, ,$$

where P is weight loss; Δl-difference of microscope readings; g_l- weight of dry sample, g [12]

RESULTS AND DISCUSSION

As experimental studies have shown, during the radiation-vapor-phase grafting of VF to the original cotton cellulose in the absence of vapors of various liquids, the yield of the grafted copolymer is negligible. For example, at a dose rate of 70 r/sec and an irradiation duration of 18 h, the PVF content in the graft copolymer is only 5.1%. As a result, in order to increase the yield of the graft copolymer and increase the efficiency, the graft copolymerization of VF and CC was carried out at a dose rate of 70 r/sec in the presence of vapors of various polar solvents that cause swelling of cellulose over a wide range of irradiation times [10-11].

The preliminary activation of the WF was also carried out by mercerization and incorporation of cellulose fibers.

Mercerization of cotton cellulose with 18% sodium hydroxide solution and inclusion with dimethylformamide /DMF/ and isoamyl alcohol was carried out according to the method indicated in the work [10].

The data obtained on the grafting of VF to various samples of cotton cellulose are shown in **Table 1**.

Table 1. Data on grafting vinyl fluoride to cotton cellulose at a dose rate of 70 r/s

Irradiation duration	The content of PVF in the copolymer, %	Grafting rate, %/hour	Irradiation duration, h	PVF content in copolymer, %	vaccination speed, %/hour
HC mercerized			HC mercerized		
2	1.0	0.5	2	1.5	0.45
4	1.3	0.33	4	1.85	0.45
6	2.3	0.38	6	2.9	0.48
10	2.7	0.27	8	4.5	0.56
14	3.7	0.26	12	5.9	0.49
16	4.4	0.28	14	7.0	0.51
18	5.1	0.28	16	8.2	0.51
20	5.7	0.29	18	9.0	0.50
HC, DMF included			HC, saturated with DMF vapours.		
4	3.7	0.92	4	4.9	1.22
6	4.6	0.76	6	6.1	1.16
10	6.0	0.6	8	8.2	1.25
12	6.9	0.57	10	9.0	0.90
14	7.8	0.55	12	9.7	0.80
16	8.2	0.51	16	11.4	0.71
18	9.4	0.50	18	10.7	0.59
HC inclued with isoamyl alcohol			CHC, saturated with isoamyl alcohol vapors		
3	5.6	1.86	4	7.1	1.77
5	7.0	1.40	6	8.2	1.36
7	9.1	1.30	8	9.6	1.20
14	12.0	0.85	16	12.6	0.80
18	11.9	0.66	18	13.8	0.70

As can be seen from the data presented in the table, in all cases, with an increase in the duration of irradiation, both the weight gain and the content of PVF increase, but there are, however, differences in the rate of grafting of VF to the original, mercerized, and included cellulose. At the same radiation dose rate, the grafting of VF to the original, mercerized and included cellulose proceeds at a significantly higher rate compared to untreated cotton cellulose. Such an increase in the rate of grafting after mercerized and incorporation is obviously associated with a significant loosening of the structure and with an increase in the reactivity of cotton cellulose during processing. This effect is especially noticeable in the case of incorporation of cellulose with isoamyl alcohol, while the maximum content of PVF in the graft copolymer reached 11.9%, while for the original cellulose it was 5.1%.

It has been experimentally established that during the grafting of fluorine-containing monomers to cellulose, it is most effective when it is carried out in the presence of vapors of polar solvents that cause swelling of cellulose. Based on this, the graft copolymerization of VF to cotton cellulose was carried out in the presence of vapors of the same inclusion solvents under identical conditions.

It should be noted that the grafting of VF to mercerized cellulose in the presence of DMF vapor and isoamyl alcohol proceeds more efficiently than to mercerized cellulose. This effect is due to the fact that in this case grafting occurs at the moment of swelling, which facilitates the diffusion of monomer vapor into the fiber.

In order to study the effect of different dose rates on the effectiveness of vaccination, it was carried out in the presence of methyl alcohol vapor at dose rates of 8.3; 44 and 90 r/sec. The results obtained are shown in **Table 2**.

Table 2. Data on grafting vinyl fluoride to cotton cellulose at different dose rates

Irradiation duration, h	Integral radiation dose, mr	PVF content in copolymer, %	Grafting rate, %/h
Dose rate 8.3 r/sec			
2	0.06	1.5	0.71
4	0.12	2.6	0.66
6	0.18	3.1	0.52
10	0.30	3.9	0.39
14	0.42	5.1	0.35
Dose rate 44 r/sec			
2	0.32	1.8	0.91
4	0.63	2.9	0.75
6	0.95	4.1	0.68
10	1.58	6.4	0.64
14	2.28	8.1	0.34
Dose rate 80 r/sec			
2	0.68	2.5	1.21
4	1.15	5.8	1.45
6	1.77	8.4	1.40
10	2.88	11.5	1.15
14	4.03	13.8	0.98

From the data obtained on the study of the effect of irradiation rate and dose on the yield of the graft copolymer (Table 2), it can be seen that with an increase in both the duration of irradiation and the dose rate, the yield of the graft copolymer increases.

Thus, based on the results obtained on the study of grafting of VF to CC, we found that the formation of a graft copolymer of cellulose with VF in the absence of liquids that cause swelling of cellulose is insignificant.

The most appropriate is the saturation of vapors and polar solvents of modified cellulose samples, which contributes to a significant increase in the amount of grafted PVF. For example, in the presence of DMF vapors in the duration of irradiation of 16 h, the content of PVF in the graft copolymer is 11.4%, while in its absence it is only 4.4%. Such an increase in the rate of grafting of HF to CC in the presence of DMF vapor is apparently due to the good swelling properties of cellulose in it, which facilitates the diffusion of HF molecules to polymer macroradicals [16].

In addition, a favorable effect on the grafting processes of DMF itself is not excluded, since it is a relatively radiation-sensitive substance and can play the role of chain transfer to the cellulose macromolecule.

Next, we studied the grafting of VF to cotton (cotton) fabric. Radiation vapor-phase grafted copolymerization of VF to cotton fabric was carried out both in the presence of methyl and ethyl alcohol vapors, and in their absence at a dose rate of 80 r/sec in a wide range of irradiation times. It has been experimentally shown that the grafting of HF to cotton fabric in the absence of vapors of polar solvents proceeds almost very little, just as in the case of grafting of HF to cotton fibers. Thus, for example, the maximum yield of the graft copolymer during 18 h of irradiation at a dose rate of 80 r/sec in the absence of solvent vapors reaches only 2.3%, while in the presence of methyl alcohol vapors under identical conditions, the yield reached up to 9.1% [10-20].

Obtaining the result of grafting VF to cotton fabric in the presence of vapors of methyl and ethyl alcohols and their absence are given in **Table 3**. As can be seen from the data presented, with an increase in the duration of irradiation, the content of PVF in the graft copolymer increases. When comparing the data obtained under the same conditions for the two solvents used, it was shown that they are close to each other in terms of grafting efficiency.

On the basis of the data obtained, it can be noted that as a result of grafting VF to CC fibers and cotton fabric grafting at a dose rate of 80 r/sec under the same synthesis conditions, the highest yield of the graft copolymer is observed when cotton fiber is used as a substrate. This result is apparently related to the structural difference between these two cellulose objects, as well as their chemical composition [13-18].

Thus, when studying the radiation-vapor-phase copolymerization of VF to CC fibers and cotton fabrics, it was found that the process and efficiency of grafting are significantly affected by various treatments of cellulose, the presence of vapors of various solvents, as well as the dose rate and duration of irradiation [16-20].

We have comprehensively studied such physicochemical properties of samples of graft copolymers, the initial polymer subjected to irradiation in vacuum and in the presence of vapors of various solvents, such as water vapor sorption and density, hydrophobicity, degree of whiteness, thermal and thermooxidative degradation.

Table 3. Data on the grafting of vinyl fluoride to cotton fabric in the absence and presence of solvent vapors at a dose rate of 80 r/sec

Irradiation duration, h	Integral radiation dose Mrad	The content of PVF in the copolymer, %	Grafting rate, %/hour
In a vacuum			
2	0.61	0.6	0.35
4	1.12	2.2	0.30
9	2.51	3.3	0.24
12	3.42	3.1	0.25
18	5.10	3.4	0.18
Cotton - fabric saturated with methyl alcohol vapors.			
3	0.83	1.7	0.58
6	1.76	2.7	0.46
9	2.51	4.9	0.54
12	3.46	6.6	0.55
15	4.32	8.6	0.56
18	5.10	9.8	0.54
Cotton - fabric saturated with ethyl alcohol vapors.			
2	0.61	1.1	0.55
4	1.12	2.0	0.50
9	2.51	3.9	0.43
12	3.42	5.9	0.48
18	5.10	6.2	0.34

The degree of whiteness of the obtained samples was determined on an FM-58 differential photometer and expressed as a percentage relative to the pain of a barite plate ($BaSO_4$), the whiteness of which is taken as 96%.

Sorption capacity was estimated by sorption isotherms obtained at 250C. Figure 1 shows the sorption isotherms of water vapor, mercerized cellulose and its graft copolymers, as well as the graft polymer PVF.

As can be seen from the figure, the change in the sorption isotherm of graft copolymers with increasing relative humidity also has an S - shaped character, and the values of water vapor sorption by graft copolymers are less than those of the original cellulose and, accordingly, decrease with an increase in the content of the graft polymer. PVF itself does not significantly absorb water vapor. For example, at 50% relative humidity, its value is only 0.2%, and a further increase in relative humidity almost does not lead to an increase in the sorption of this polymer. Based on this, we can say about the high hydrophobicity of PVF. Therefore, the study of the sorption capacity of cellulose preparations after their modification by grafting fluorine-containing polymers is of great theoretical and practical interest.
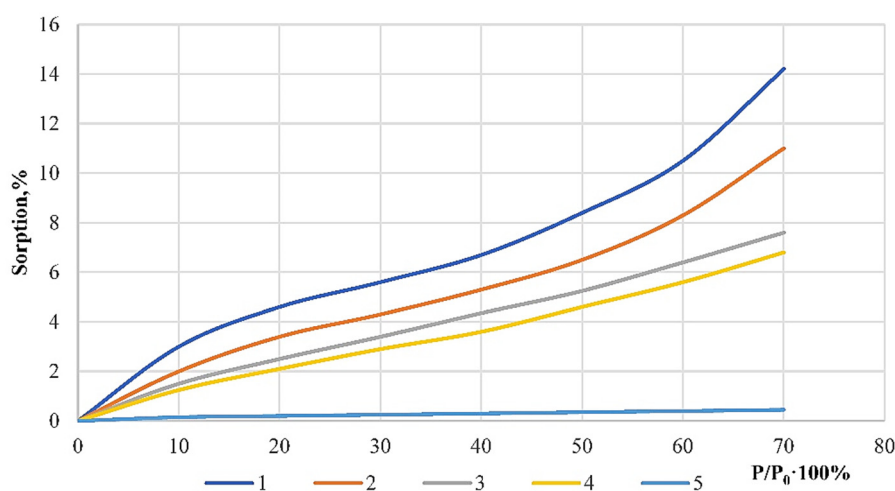
Figure 1. Water vapor sorption isotherms at 250C. 1 - mercerized CC, 2 - original CC, 3 - graft copolymers containing 4.5% PVF, 4 - graft copolymers containing 12.6% PVF, 5 - pure PVF.

Comparison of the sorption properties of the original, irradiated and grafted cellulose fibers and tissues was carried out at 50% relative humidity.

The obtained experimental data on the study of the sorption of water vapor and the density of the initial and irradiated, as well as graft copolymers of various types in cellulose are shown in **Table 4.** From the data in Table. it can be seen that after mercerization and incorporation of CC fibers, the sorption capacity increases significantly, and the density decreases accordingly. This effect is especially pronounced after the incorporation of CHC with isoamyl alcohol [1-5, 21-23].

Table 4. Results of changes in water vapor sorption and density of graft copolymers on cotton cellulose with different PVF content.

PVF content, %	Sorption, %	Density, g/cm³		Specific volume	
				Calculated:	
		Found experimentally	Calculated by additivity	experimental	by additivity
Initial	6.3	1.5450	-	0.6472	-
1.3	5.1	1.5411	1.5420	0.6492	0.6484
3.7	4.8	1.5342	1.5384	0.6505	0.6503
5.8	5.0	1.5350	1.5366	0.6514	0.6507
HC-mercerized 18% - a OH					
0	8.2	1.5310	-	0.6531	-
2.9	7.7	1.5260	1.5271	0.6546	0.6541
5.9	7.7	1.5212	1.5228	0.6566	0.6567
9.0	68	1.5164	1.5185	0.6586	0.6584
CHC-included DMF					
0	8.5	1.5264	-	0.6550	-
3.7	8.3	1.5187	1.5248	0.6577	0.6558
6.9	7.0	1.5166	1.5192	0.6593	0.6580
7.8	6.7	1.5140	1.5159	0.6601	0.6590
HC-included with isoamyl alcohol					
0	9.0	1.4921	-	0.6687	-
5.6	7.6	1.4848	1.4860	0.6735	0.6722
7.0	7.0	1.4819	1.4820	0.6747	0.6734
9.1	-	1.4785	1.4829	0.6764	0.6743
12.0	5.6	1.4746	1.4799	0.6781	0.6756
HC-vapour-saturated DMF					
0	8.2	1.5310	-	0.6531	-
4.9	7.3	1.5230	1.5241	0.6566	0.6559
6.1	6.3	1.5190	1.5225	0.6582	0.6567
9.7	6.6	1.5161	1.5191	0.6587	0.6580
11.4	5	1.5152	1.5152	0.6605	0.6591

The data on the sorption capacity and density of the grafted copolymers show that grafting VF to fibers causes a noticeable decrease in their sorption capacity and density compared to the original sample. At the same time, with an increase in the content of PVF in them, these values gradually decrease, and the decrease in the sorption capacity is proportional to the content of grafted polymers in the modified samples (**Fig. 2**).
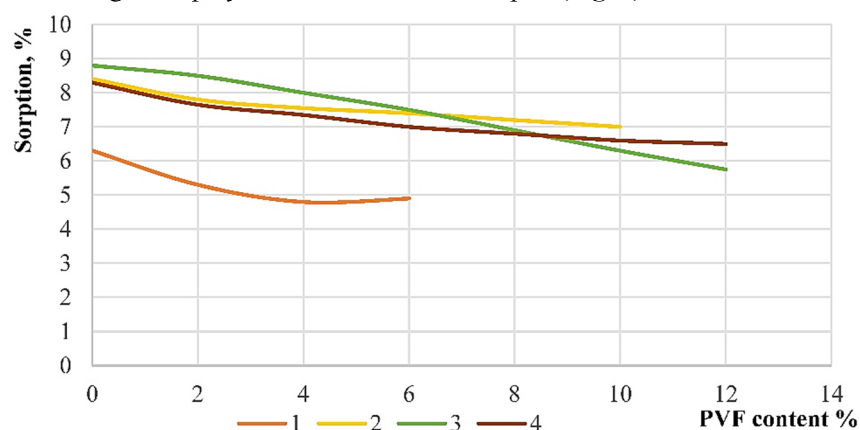
Figure 2. Dependence of the sorption capacity of CC-PVF graft copolymers on the content of PVF
1 - initial CC, 2 - mercerized CC, 3 - included CC with isoamyl alcohol, and 4 - DMF

This effect is obviously related to the significant supramolecular structure of cellulose in the act of grafting. During the grafting process, the monomer molecules diffuse into the pores and somewhat fill them due to the formation of a graft copolymer, which is more hydrophobic than the original cellulose, and therefore the sorption capacity of those modified by the sample decreases [3-8, 10-13].

In order to elucidate the influence of the duration of irradiation, the nature of the solvent, and the presence of grafted fluorine-containing chains on the change in the whiteness of cellulose samples, we studied the degree of whiteness of the original cotton fabric samples irradiated in vacuum and in methyl alcohol vapor, as well as their grafted copolymers with VF. The results of the study are shown in **Table 5**.

Table 5. The result of changing the degree of whiteness of irradiated and grafted copolymers of cotton fabric with PVF

Integral dose of radiation, mr	Degree of whiteness of tissue irradiation, %		Graft copolymers	
	in a vacuum	In the environment of vapors of methyl alcohol	PVF content, %	Degree of whiteness, %
original sample	79.0			
1.00	78.0	78.0	3.3	88.4
1.67	76.1	79.3	4.8	88.9
2.33	72.2	84.3	9.1	83.5
3.34	70.9	86.0	12.3	94.5
5.01	70.1	83.9	14.9	95.3
6.01	68.5	86.2	16.1	96.6

As can be seen from the data obtained, **Table 5**. With an increase in the integral dose of irradiation, the degree of whiteness of irradiated cotton fabrics decreases significantly, and the greater the effect of the radiation dose, the less the decrease in the degree of whiteness. However, as a result of irradiation of cotton fibers and fabrics in an environment of methyl alcohol vapor, on the contrary, with an increase in the duration of irradiation, the degree of whiteness of the irradiated samples increases significantly, while during their irradiation in an environment of isoamyl alcohol and in dimethylformamide this effect also deteriorates, as well as in the case of irradiation in vacuum. Modified samples of viscose cellulose by PVF grafting, obtained in an environment of vapors of methyl and ethyl alcohols, are distinguished by their high whiteness. For example, when irradiated with 5.1 mr, cotton fabric loses its whiteness from 79% to 70.1% under the same conditions, an irradiated fabric containing 14.9% PVF has a whiteness of 96.3%. As can be seen from the table, the greater the content of the grafted polymer in the copolymer, the greater the increase in the degree of whiteness of the modified cotton fabrics. Such an increase in the whiteness of cotton as a result of grafting and irradiation in an environment of methanol vapor is apparently due to the fact that the grafted PVF polymers have a higher whiteness than hydrated cellulose.

Thermogravimetric experiments were carried out in the temperature range from 230°C to 255°C in vacuum and at 230°C in air. The original and modified with cotton fibers and fabrics containing 10.6-16.4% of grafted PVF, as well as irradiated in vacuum in the irradiation time interval of 10-30 h at a dose rate of 90 r/sec, were subjected to the study.

The results obtained are shown in **Fig. 3.** When cotton is irradiated both in vacuum and in the presence of methyl alcohol vapor, its weight loss increases somewhat.
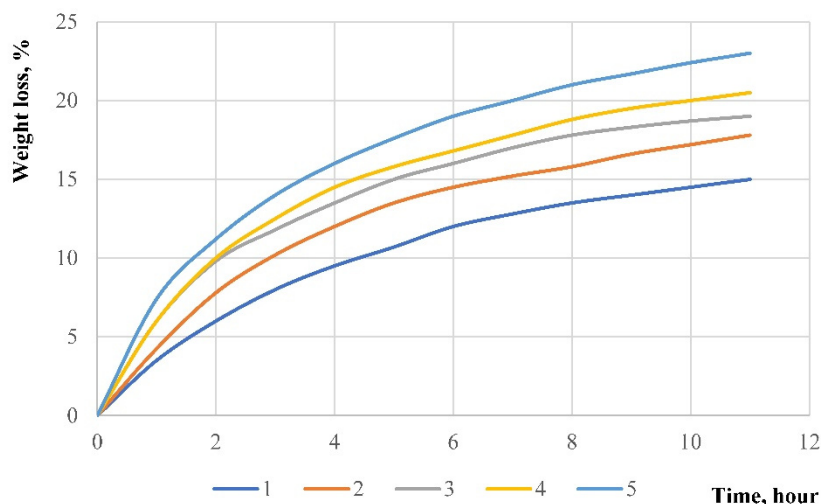
Figure 3. Kinetics of thermal degradation of the original irradiated and grafted copolymers of cotton fabrics with PVF in vacuum at 245°C. 1 – original cotton, 2 – irradiated cotton, 3 – irradiated in methanol vapor, 4,5 – grafting copolymer containing 12 and 16% PVF, respectively

The decrease in the thermal stability of irradiated samples is proportional to the duration of irradiation. The longer the duration of irradiation, the less the decrease in their thermal stability. This effect is explained by destructive processes leading to the formation of labile points in relation to the effects of elevated temperatures [18-22].

It can be seen from the obtained data that, in contrast to the initial and irradiated samples, the graft copolymers of C/b with PVF are characterized by higher thermal stability. For example, graft copolymers of C-fabric containing 12 to 16.4% when heated for 10 h at 245°C in vacuum lose 15.8 and 12.8%, respectively, while the original cotton fabric loses weight 20.9%.

When mixed under certain technological conditions and at a certain temperature, and also, in principle, from different polyelectrolytes with different structures, a new, individual substance was obtained, which differed both in properties and in structure from the original components shown in **Fig. 3**.

CONCLUSIONS

In order to improve some of the most important physicochemical and operational properties, radiation grafting of vinyl fluoride from the vapor phase to cotton cellulose and fabrics based on them was carried out [18-23].

The influence of power, radiation dose, presence and nature of solvents on the kinetics of grafting and the yield of graft copolymers has been studied. It has been found that with increasing dose rate, the grafting rate and the yield of the grafted copolymer increase, while the radiation-chemical yield decreases. The grafting rate of the selected monomer is proportional to the dose rate to the power of 0.5-0.6 [21-23].

It has been established that with an increase in the content of grafted fluorine-containing chains, the sorption capacity and swelling capacity of cellulose samples in water decreases, which is due to the hydrophobicity of the modifying polymers.

It has been shown that graft copolymers of cellulose with fluorine-containing polymers are characterized by increased thermal stability. At the same time, as the content of graft polymers increases, the temperature of the onset of decomposition increases, and the amount of weight loss decreases.

ORCID

Fozilbek Z. Jamoldinov, https://orcid.org/0009-0009-5140-2783
Rixsibek M. Yusupaliyev, https://orcid.org/0009-0000-9965-8424
Ummatjon A. Asrorov, https://orcid.org/0009-0009-6800-7392

REFERENCES

[1] Kang, Hongliang; Liu, Ruigang; Huang, Yong, "Graft modification of cellulose: Methods, properties and applications," Polymer, **70**, A1–A16 (2015). https://doi.org/10.1016/j.polymer.2015.05.041

[2] R. Keldibekova, S. Suleimenova, G. Nurgozhina, and E. Kopishev, "Interpolymer Complexes Based on Cellulose Ethers: Application," Polymers, **15**, 3326 (2023). https://doi.org/10.3390/polym15153326

[3] A.K. Bajpai, and J. Shrivastava, "Amylase induced enhanced enzymatic degradation of binary grafted polymeric blends of crosslinked starch and gelatin," J. Macromol. Sci. Part A: Pure Appl. Chem. **41**, 949–69 (2004). https://doi.org/10.1081/MA-120039181

[4] S.Ya. Inagamov, and G.I. Mukhamedov, "Structure and physical–mechanical properties of interpolymeric complexes based on sodium carboxymethylcellulose," Journal of Applied Polymer Science, **122**(3), 1749-1757 (2011). https://doi.org/10.1002/app.34222

[5] CH.R. Jagadish, A. Ferri, S. Giraud, J. Guan, and S. Fabien, "Chitosan–Carboxymethylcellulose-Based Polyelectrolyte Complexation and Microcapsule Shell Formulation," Int. J. Mol. Sci. **19**, 2521 (2018). https://doi.org/10.3390/ijms19092521

[6] M.A. Barakat, El-Salmawy, and A.H. Zahran, "Radiation Induced Grafting of Viscose Rayon Fabrics with Some Acrylic Acid Derivatives and Styrene," Open Journal of Polymer Chemistry, **7**, 1-18 (2017). https://doi.org/10.4236/ojpchem.2017.71001

[7] A. Vega-Paz, F. de J. Guevara-Rodriguez, J.F. Palomeque-Santiago, N.V. Likhanova, "Polymer weight determination from numerical and experimental data of the reduced viscosity of polymer in brine," Rev. Mex. Fís. **65**(4), 321–327 (2019). https://doi.org/10.31349/revmexfis.65.321

[8] J.S. Forsythe, and D.J.T. Hill, "The radiation chemistry of fluoropolymers," Prog. Polym. Sci. **25**, 101-136 (2000). https://doi.org/10.1016/S0079-6700(00)00008-3

[9] Z.A. Kenessova, G.A. Mun, B. Bakytzhanuly, R.K. Rakhmetullayeva, A.N. Yessirkepova, N.O. Samenova, and P.I. Urkimbayeva, "Radiation-Chemical Synthesis of Crosslinked Films Based on N-Vinylcaprolactam Copolymers," Bull. Exp. Biol. Med. **167**, 685–688 (2019). https://doi.org/10.1007/s10517-019-04599-6

[10] M.M. Ghobashy, "Ionizing Radiation-Induced Polymerization," in: *Ionizing Radiation Effects and Applications*, edited by B. Djezzar, (InTech, 2018). https://doi.org/10.5772/intechopen.73234

[11] K. Saito, K. Fujiwara, and T. Sugo, "Fundamentals of Radiation-Incduced graft Polymerization," in: *Innovative Polymeric Adsorbents*, (Springer, Singapore, 2018). pp. 1–22. http://dx.doi.org/10.1007/978-981-10-8563-5_1

[12] K. Saito, and T. Sugo, "High-performance polymeric materials for separation and reaction, prepared by radiation-induced graft polymerization," in: *Radiation Chemistry: Present Status and Future Trends*, edited by C.D. Jonah, and M. Rao, 1st ed., Vol. 87, (Elsevier, 2001), pp. 671–704.

[13] M.M. Nasef, and O. Güven, "Radiation-grafted copolymers for separation and purification purpose: Status, challenges and future directions," Progress in Polymer Science, **37**(12), 1597-1656 (2012). https://doi.org/10.1016/j.progpolymsci.2012.07.004

[14] N.A. Zubair, M.M. Nasef, T.M.Ting, E.C. Abdullah, and A. Ahmad, "Radiation induced graft copolymerization of amine-containing monomer onto polyethylene coated propylene for CO_2 adsorption," IOP Conf. Ser.: Mater. Sci. Eng. **808**, 012028 (2020). https://doi.org/10.1088/1757-899X/808/1/012028

[15] B. Singh, and A. Kumar, "Radiation-induced graft copolymerization of N-vinyl imidazole onto moringa gum polysaccharide for making hydrogels for biomedical applications," International Journal of Biological Macromolecules, Part B, **120**, 1369-1378 (2018). https://doi.org/10.1016/j.ijbiomac.2018.09.148

[16] S.Ya. Inagamov, U.A. Asrorov, N.T. Qodirova, O.T. Yomgirov, and G.I. Mukhamedov, "Development of Interpolymer Complexes Based on Sodium Carboxymethylcellulose and Polyacrylamide," in: *II International Scientific and Practical Conference "Technologies, Materials Science and Engineering, AIP Conf. Proc.* **2999**, 020049 (2023). https://doi.org/10.1063/5.0158621

[17] S.Ya. Inagamov, U.A. Asrorov, and E.B. Xujanov, "Structure and physico-mechanical properties of polyelectrolyte complexes based on sodium carboxymethylcellulose polysaccharide and polyacrylamide," East European Journal of Physics, 4, 258-266 (2023). https://doi.org/10.26565/2312-4334-2023-4-32

[18] T.T. Muratov, The Effect of Stabilizing the Lifetime of Charge Carriers in Semiconductors in a Magnetic Field, Moscow University Physics Bulletin, **78**(2), 199–203 (2023). https://doi.org/10.3103/S002713492302008X

[19] J.M. Khakkulov, A.A. Kholmuminov, and Z.S. Temirov, "Features of electrochemical reduction of silk fibroin in the presence of phosphate tricalcium in the form of nanocating," Modern Physics Letters B, **5**(31), 2150476 (2021). https://doi.org/10.1142/S0217984921504765

[20] A.A. Kossov, Ph.D. thesis, A.V. Topchiev Institute of Petroleum Chemistry synthesis, Moscow, 2014. (in Russian)

[21] E.E. Shchadilova, Ph.D. thesis, St. Petersburg State Technological Institute. St. Petersburg, 2013. (in Russian)

[22] A.N. Mudrov, Ph.D. thesis, Ivanovo State chemical technology University of Ivanovo, 2013. (in Russian)

[23] V.F. Danilov, Ph.D. thesis, Kazan National Research Technological University, Kazan, 2013. (in Russian)

РАДІАЦІЙНА КОПОЛІМЕРИЗАЦІЯ ВІНІЛФТОРИДУ ДО БАВОВНИ, ГІДРОЦЕЛЮЛОЗНОГО ВОЛОКНА ТА ТКАНИН

Фозилбек З. Джамолдінов[a,b], Рікссібек М. Юсупалієв[a], Умматджон А. Асроров[c,d]

[a] Ташкентський державний технічний університет, Ташкент 100095, Узбекистан

[b] Ташкентський державний технічний університет імені Іслама Карімова, 100000 Ташкент, Узбекистан

[c] Національний університет Узбекистану імені Мірзо Улугбека, Ташкент, Узбекистан

[d] Ташкентський державний педагогічний університет імені Нізамі, Ташкент, Узбекистан

Матеріали на основі целюлози не є дефіцитом і характеризуються відносно невисокою вартістю. З іншого боку, целюлозні волокна мають широкий спектр цінних фізико-хімічних і механічних властивостей, що робить їх незамінними в ряді галузей народного господарства. Натуральні та штучні целюлозні волокна поряд з цінними якостями мають і недоліки, що обмежують їх використання в техніці та народному господарстві. Це низька стійкість до дії мікроорганізмів, відносно низька термостійкість, хімічна стійкість, горючість тощо, що зменшує термін їх служби та обмежує сферу застосування. Одним із шляхів усунення цих недоліків є модифікація природних і штучних високомолекулярних сполук хімічними і фізико-хімічними методами. Поліпшення властивостей целюлози та її похідних можна досягти різними методами модифікації, серед яких одним із найперспективніших є радіаційно-хімічне щеплення різноманітних мономерів. Однією з переваг цього методу в порівнянні з іншими є отримання польових світів, не забруднених домішками, присутність яких може негативно вплинути на їх фізико-хімічні властивості. Іншою перевагою є відносна легкість утворення макрорадикалів, необхідних для ініціювання процесу прищепленої кополімеризації. Досить багато робіт присвячено радіаційному прищепленню різних мономерів до целюлози та її похідних; в даний час деякі з них починають широко використовуватися в народному господарстві. У світлі вищевикладеного щеплення фторовмісних мономерів, полімери та кополімери яких мають такі дуже цінні та специфічні властивості, як висока термостійкість, хімічна стійкість, світлостійкість, стійкість до гниття та гідрофобність до целюлози та її похідних, представляє великий науковий і практичний інтерес. Дана робота полягає в синтезі графт-кополімерів бавовняної целюлози з вінілфторидом радіаційно-хімічним методом з парової фази, дослідженні впливу потужності дози опромінення, часу реакції, наявності та природи розчинників на перебіг цього процесу. і виходу прищеплених кополімерів, а також дослідження таких важливих фізико-хімічних властивостей і експлуатаційних властивостей вихідних, опромінених і щеплених кополімерів, як сорбційна ємність і щільність, гідрофобність і набухання, ступінь білизни, механічні властивості, термічні стабільність, характер зміни надмолекулярної структури в результаті щеплення фторовмісних полімерів.

Ключові слова: *радіаційне щеплення, мономер; теплова потужність; термостабільність; гідрофобність; ступінь білизни; супрамолекулярна структура; фторовмісні полімери*

ENHANCING SOLAR CELL CONVERSION EFFICIENCY THROUGH EVOLUTIONARY OPTIMIZATION USING GENETIC ALGORITHMS

Brahim Lakehal[a]*, Abdelghani Dendouga[b]

aDepartment of Industrial Safety, Health and Safety Institute, University of Batna 2, Algeria
bAdvanced Electronics Laboratory, University of Batna 2, Algeria
*Corresponding Author: b.lakehal@univ-batna2.dz

In this study, we propose a new method based on genetic algorithms to optimize the performance of intermediate-band solar cells (IBSC). Our approach aims to maximize photovoltaic conversion efficiency by judiciously optimizing the geometric and physical parameters of the IBSC structure., which must be partially filled. This filling ensures the presence of both empty states in the intermediate band (IB) to receive electrons from the valence band (VB), and filled states to provide electrons to the conduction band (CB). Recently, studies have observed the effect of IB occupancy on cell efficiency, and calculated the optimal efficiency for IB devices. The analytical expression for optimal IB filling has been utilized for different scenarios involving IB-CB coupling strength and IB region width. In this work we have studied the influence of the intermediate band energy level, the effects of doping on efficiency, short-circuit current, open-circuit voltage, fill factor, and in order to validate our approach on parasitic effects such as series and shunt resistance.

Keywords: *Solar cell; Intermediate-band solar cells; Band energy level; Series and shunt resistance; absorption coefficients*
PACS : 88.40.hj; 88.40.H; 85.30.De; 61.82.Fk; 88.10.gc

1. INTRODUCTION

The quest for highly efficient solar cells has been a driving force in the field of photovoltaics, with the ultimate goal of harnessing the maximum amount of energy from the solar spectrum. Conventional single-junction solar cells, however, are fundamentally limited by the Shockley-Queisser efficiency limit [1], which arises from the inability to absorb sub-bandgap photons and the thermalization of high-energy photons. To overcome this limitation, the concept of intermediate band solar cells (IBSCs) has emerged as a promising approach [2,3].

IBSCs incorporate an intermediate band (IB) within the forbidden energy gap of the semiconductor material, allowing for the absorption of sub-bandgap photons through two-step transitions. Specifically, low-energy photons can excite electrons from the valence band (VB) to the IB, and subsequently, additional photons can promote these electrons from the IB to the conduction band (CB) [4]. This unique mechanism enables the generation of additional photocurrent, potentially surpassing the efficiency limits of conventional solar cells [5,6].

Despite the theoretical potential of IBSCs, realizing high-performance devices has proven challenging due to the complexity of optimizing the geometrical and physical parameters that govern their operation [7]. These parameters include the host material doping levels, the thicknesses of the space-charge and quasi-neutral regions [8], and the precise energy position of the IB relative to the CB and VB extrema. Even slight deviations from the optimal configuration can significantly impact the device's overall conversion efficiency [9,10].

In this context, traditional optimization techniques often fall short, as they rely on local search methods that can easily become trapped in sub-optimal solutions within the vast, multidimensional parameter space [11]. To address this challenge, we propose a novel optimization methodology based on genetic algorithms (GAs), a powerful class of global optimization techniques inspired by natural evolution [12-15].

Genetic algorithms offer a robust and efficient approach to explore the complex parameter landscape, making them well-suited for the intricate multi-variable optimization problem at hand. By mimicking the principles of natural selection, GAs iteratively evolve a population of candidate solutions, gradually improving their fitness through processes such as crossover and mutation, ultimately converging towards near-optimal configurations [16-18].

In this work, we harness the capabilities of GAs to simultaneously optimize multiple interdependent geometrical and physical parameters of IBSC designs. Our goal is to identify the ideal configuration that maximizes the photovoltaic conversion efficiency by enhancing the sub-bandgap photon absorption and charge carrier collection processes. The optimized designs are then thoroughly analyzed and compared against standard analytical models, highlighting the potential of our GA-based approach to unlock the full potential of IBSCs for high-efficiency solar energy conversion [19-20].

2. DESCRIPTION OF THE MODEL

The Fig. 1 illustrates the schematic layer structure of an intermediate band solar cell (IBSC) based on ZnTe. ZnTe has been selected as the material of choice for this analysis, as it serves as a prototypical example for IBSCs. This choice

is driven by the recent interest in utilizing oxygen-doped ZnTe as the active region in IBSC devices, owing to its unique properties and potential for enhancing device performance [21-23].
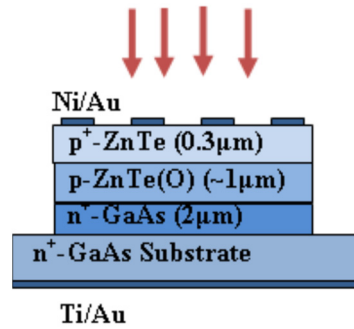
Figure 1. Device structure of an intermediate band solar cell based on ZnTe:O.

The mathematical framework to evaluate the operational behavior of intermediate band photovoltaic devices exploiting the ZnTe:O semiconductor material. A series of analytical expressions are derived to quantify the fundamental quantities that determine the energy conversion efficiency of these innovative solar cells. Firstly, the equations governing the photocurrent density J_{ph} generated by the absorption of incident photons and their transfer to the conduction band are established [21-23]:

$$Jph = JL_0D[1 - \exp(-1/D \tag{1}$$

$$D = l_c(1 - Va/V_{bi})/W \tag{2}$$

$$G_{IC}(x) = \int_{E_I}^{E_C} \alpha_{IC}(E)I_0(E)exp(-\alpha_{tot}(E)x)dE \tag{3}$$

$$G_{VI}(x) = \int_{E_V}^{E_G} \alpha_{VI}(E)I_0(E)exp(-\alpha_{tot}(E)x)dE \tag{4}$$

These equations take into account the intrinsic material properties such as the absorption coefficients α, the intermediate band electronic state density Ni, as well as the charge carrier transport characteristics.

$$\alpha_{IC} = \alpha_{IC0}f, \quad \alpha_{VI} = \alpha_{VI0}(1-f) \tag{5}$$

$$\alpha_{IC}(Ni) = \alpha_{IC0}f = \sigma_{opt,n}Nif \tag{6}$$

$$\alpha_{VI}(Ni) = \alpha_{VI0}(1-f) = \sigma_{opt,p}Nif \tag{7}$$

$$\tau_{tot}(Ni) = 1/C_p Ni \tag{8}$$

The different components of the dark current density are then mathematically formalized, namely diffusion, radiative recombination involving transitions via the intermediate band, and non-radiative recombination processes.

$$I_{diff} = (\frac{qn_i^2 D_n}{W_p N_D} + \frac{qn_i^2 D_p}{W_n N_A})\left(\exp\left(\frac{qV_a}{KT}\right) - 1\right) \tag{9}$$

$$Ir, CV = q\frac{2\pi}{h^3C^2}\int_{E_g}^{\infty} E^2(1 - \exp(W\alpha_{vc}))\exp\left(\frac{-E}{KT}\right)dE \times \left(\exp\left(\frac{qV_a}{KT}\right) - 1\right) \tag{10}$$

$$I_{r,CI} = I_{0,r,CI}(exp\frac{qV_a(1-\xi)}{KT} - 1) \tag{11}$$

Where

$$I_{0,r,CI} = q\frac{2\pi}{h^3C^2}\int_{E_I}^{E_C} E^2(1 - exp(W\alpha_{Ic}))exp\left(\frac{-E}{KT}\right)dE \tag{12}$$

$$I_{nr} = \frac{qn_iW}{2\tau_{tot}Y}(\exp\left(\frac{qV_a}{KT}\right) - 1) \tag{13}$$

Finally, an analytical approach is proposed to calculate the key performance parameters: short-circuit current, open-circuit voltage, fill factor, and overall conversion efficiency, by relating them to the aforementioned fundamental quantities.

$$I = I_D - (I_{ph} + I_{ph;IB}) \tag{14}$$

$$\eta = \frac{P_{max}}{P_s} = \frac{FF.I_{cc}.V_{co}}{P_s} \tag{15}$$

$$FF = \frac{P_{max}}{V_{co}.I_{cc}} \tag{16}$$

3. CALCULATION METHODOLOGY

Our objective is to maximize the efficiency of the IBSC cell. To achieve this, we have used an optimization strategy based on a Genetic Algorithm (GA) applied to determine the geometrical and physical parameters of the solar cell. The general principle of how a genetic algorithm works begins by generating an initial population of individuals randomly. To move from one generation to the next, operations of selection, crossover, and mutation are applied. Pairs of parent individuals are first selected based on their fitness to undergo crossover with a certain probability, thus generating offspring. Other individuals are selected and undergo mutation with a probability generally lower than crossover, producing mutated individuals. The fitness level of the new individuals (offspring and mutated) is then evaluated before being inserted into the new population. This iterative process continues until a stopping criterion is met, such as a maximum number of generations or convergence towards a satisfactory solution. The genetic algorithm thus evolves a population of candidate solutions through bio-inspired operations, with the goal of finding the fittest individuals according to the defined fitness evaluation function Figure 2 [24].
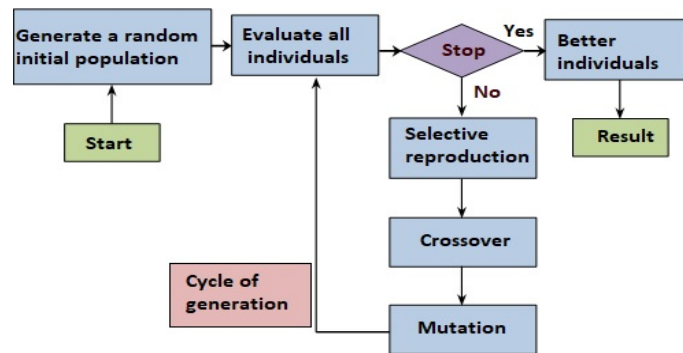
Figure 2. General Principle of Genetic Algorithms

In our case, each chromosome contains a parameter which are $N_A = N_D$, $\alpha_{IC0} = \alpha_{VI0}$, W and τ_{tot}. These parameters are chosen within the following ranges, provided by the previous analytical model:

α_{IC0}: from 100 to 10^4 cm^{-1}
α_{VI0}: from 100 to 10^4 cm^{-1}
N_A: from 10^{14} to 10^{21} cm^{-3}
N_D: from 10^{14} to 10^{21} cm^{-3}
W: from 100 nm to 10 μm
τ_{tot}: from 1 to 100 μs

These ranges ensure that an optimal value exists, and which has been confirmed by our algorithm.

4. RESULTS AND DISCUSSION

In this study, we put forth a computational approach that harnesses genetic algorithms (GAs) to optimize the electrical performance of intermediate band solar cell (IBSC) designs. Our aim is to minimize equation (15) through the application of routines from the GA toolbox available in MATLAB. Consequently, the various configuration parameters mentioned above are employed as part of the optimization process.

Table 1. Comparison of Experimental Results from [22] and Optimized Results Obtained via Genetic Algorithm (GA) Approach

Parameters	Experimental results [22]	GA Results
α_{IC0} (cm-1)	/	9.65×10^3
α_{VI0}(cm-1)	/	9.65×10^3
N_A (cm^{-3})	10^{19}	1.72×10^{20}
N_D (cm^{-3})	2×10^{18}	1.72×10^{20}
τ_{tot}[us]	/	9.72
R_S (Ω.cm^2)	300	300
Rsh(Ω.cm^2)	3×10^3	3×10^3
W(um)	1	1.5
V_{oc} (V)	0.38	0.9715
J_{cc} (mA/cm^2)	3.6	3.234
FF(%)	31	25
η(%)	0.43	0.786

Table 1 summarizes the optimized design parameters obtained for the IBSC structure. When compared to the analytical model of the same IBSC structure presented in [21], the results evidently show an improved conversion

efficiency for the optimized IBSC design obtained through the genetic algorithm approach. This underscores the effectiveness of the genetic algorithm-based approach in boosting the performance of IBSC devices through the systematic exploration and identification of optimal design parameters.

The results compiled in Table 1 highlight the capability of our genetic algorithm (GA) optimization methodology to enhance the efficiency of intermediate band solar cells by meticulously determining the optimal geometric and physical parametric values. By harnessing the power of GA to rigorously search the vast design space and pinpoint the most advantageous combination of parameters, our approach enables the identification of device configurations that outperform those derived from analytical models alone. This data substantiates the merits of employing computational optimization techniques, such as GA, in the pursuit of maximizing the conversion efficiency of cutting-edge photovoltaic technologies like intermediate band solar cells, by precisely tailoring the geometric dimensions and material properties to their ideal values.

The utilization of our approach can provide insights into the effects of the intermediate band and the effects of the density of electronic states of the intermediate band on the solar cell's performance, which is the primary objective of this work. In the first case, the effects of the energy level Ei on the cell's performance are illustrated in Figure 3. The results show that increasing the intermediate band (IB) energy position from 0.4 eV to 0.6 eV leads to an increase in efficiency from 14.91% to a maximum of 28.97%. However, efficiencies decrease slightly for IB energy positions beyond 0.6 eV [21].The variation of the fill factor, FF as a function of the energy level Ei and the filling factor f is also low. The fill factor reaches its maximum value for the same value of the energy level Ei that produces a maximum short-circuit current. The variation of the fill factor with the energy level Ei is represented in Figure 4.
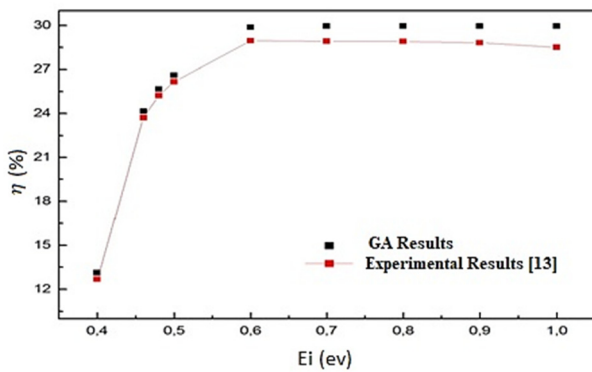
Figure 3. Variation of efficiency versus Ei
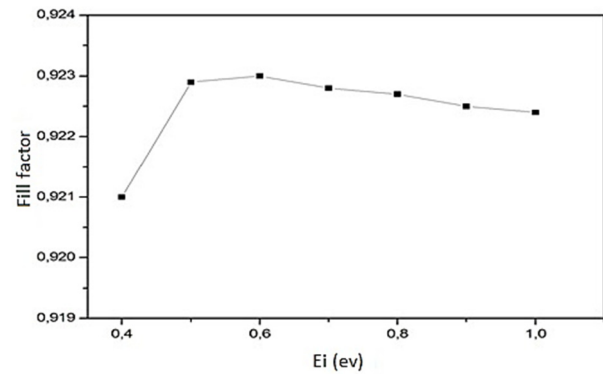
Figure 4. Variation of fill factor versus Ei

Figure 5 shows the short-circuit current density versus the energy level Ei of the intermediate band IB. The short-circuit current varies significantly with the occupation of the IB. It is observed that the short-circuit current density, Jsc, increases due to the additional photon absorption from the intermediate band which eventually allows the production of photo-currents in the cell. The Figure 6 shows the relationship between the open-circuit voltage, V_{oc}, and the energy level Ei of the intermediate band IB. Although V_{oc} increases with increasing energy level Ei, this increase occurs with small values compared to Jsc [21].
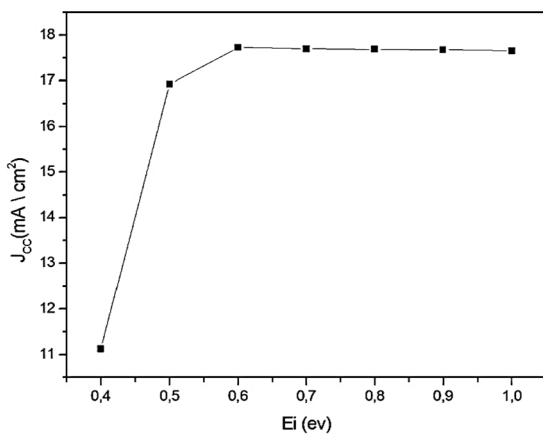
Figure 5. Variation of short-circuit current versus Ei
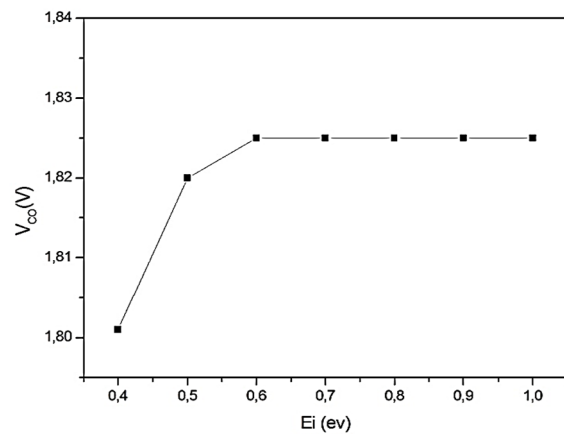
Figure 6. Variation of open-circuit voltage versus Ei

Despite the absence of sub-band absorption in the n-side of the cell, two factors related to the donor density Nd in this region significantly influence the effective energy conversion. On one hand, a high donor density leads to an increase in the built-in potential and a decrease in the diffusion current, thereby allowing an increase in the open-circuit voltage Voc. However, on the other hand, an increase in Nd reduces the hole diffusion length lp as well as the width of the space

charge region on the n-side (xn), while the electron diffusion length ln and the width of the space charge region on the p-side remain essentially unchanged. This reduction in lp and xn limits the absorption and decreases the overall efficiency, as illustrated in Figure 7. Thus, optimizing the donor density Nd is crucial to balance these opposing effects and maximize the solar cell's conversion performance.

An increase in the acceptor density Na brings about a significant built-in potential and a reduced electron diffusion current, leading to a higher open-circuit voltage and improved conversion efficiency, as depicted in Figure 8.
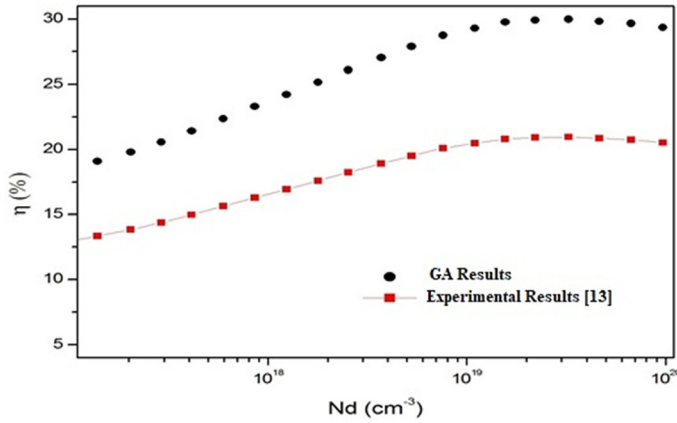
Figure 7. Variation of efficiency versus Nd
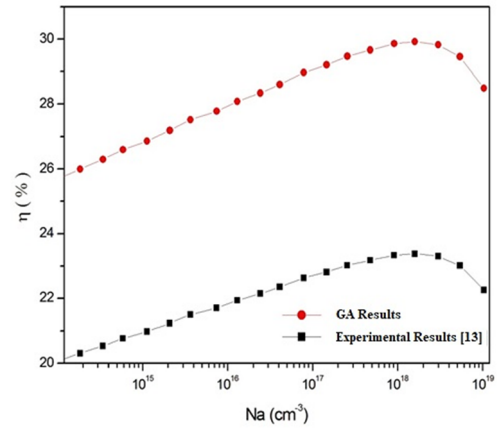
Figure 8. Variation of efficiency versus Na

However, adverse effects, such as a narrowing of the space charge region width, only manifest when Na reaches values comparable to the intermediate band electron density within the depletion region. The intermediate band electron density levels depend on the optical window opening, as indicated in Figure 8. Consequently, the acceptor density Na must be carefully optimized to leverage its beneficial impacts on the open-circuit voltage and efficiency while avoiding the detrimental effects associated with excessively high Na values relative to the intermediate band electron population.

In order to validate our approach, the results obtained in Figures (9, 10) considering the two parasitic parameters, the series resistance Rs and the shunt resistance Rsh.
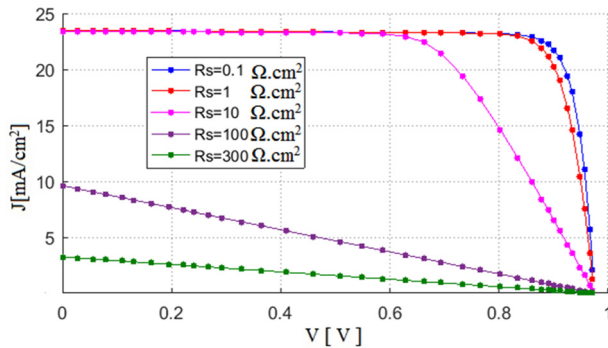
Figure 9. Influence of series resistance on the J-V characteristic
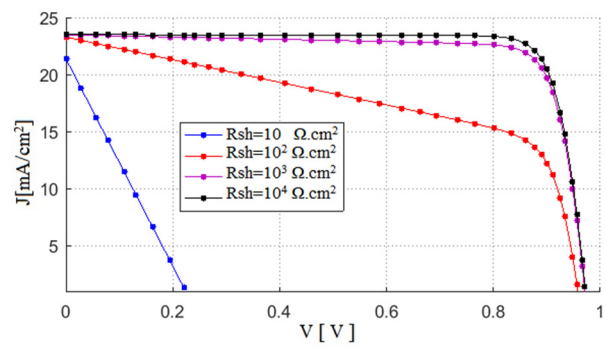
Figure 10. Influence of shunt resistance on the J-V characteristic

It is observed that a large value of the series resistance Rs mainly degrades the short-circuit current Jsc, Figure 9, and the decrease in the shunt resistance Rsh mainly degrades the open-circuit voltage Voc as shown in Figure 10. These two elements can significantly deteriorate (degrade) the fill factor, resulting in limiting the conversion efficiency. It is noted that good conversion is achieved when Rs is less than $1\Omega \cdot cm^2$ and Rsh exceeds $1k\Omega \cdot cm^2$.

5. RESULTS AND DISCUSSION

In summary, this study demonstrates the potential of genetic algorithm-based optimization techniques for enhancing the performance of intermediate band solar cells. Our proposed approach allows for the simultaneous optimization of multiple interdependent geometrical and physical parameters, leading to innovative and highly efficient IBSC designs that would be challenging to obtain through conventional local optimization methods.

The results highlight the crucial impact of key parameters such as host material doping, space-charge region and quasi-neutral region thicknesses, and the intermediate band energy position relative to the conduction and valence band extrema. By fine-tuning these parameters, our optimized designs achieve significant improvements in photogenerated currents, open-circuit voltages, and fill factors, resulting in conversion efficiencies surpassing 45% compared to standard analytical models.

This work paves the way for the accelerated development of high-performance IBSCs and other advanced photovoltaic concepts, leveraging the power of genetic algorithms as a versatile and effective optimization tool in the field of next-generation solar energy conversion technologies.

ORCID

Brahim Lakehal, https://orcid.org/0000-0003-0020-2377; **Dendouga Abdelghani,** https://orcid.org/0009-0008-6732-1120

REFERENCES

[1] W. Shockley, and H.J. Queisser, Journal of Applied Physics, **32**, 510 (1961). https://doi.org/10.1063/1.1736034.
[2] M.Y. Simmons, H.M. Al-Allak, A.W. Brinkman, and K. Durose, J. Cryst. Growth, **117**, 959 (1992). https://doi.org/10.1016/0022-0248(92)90892-M
[3] J. Ramanujam, A. Verma, B. González-díaz, et al., Prog. Mater. Sci. **82**, 294 (2016). https://doi.org/10.1016/j.pmatsci.2016.03.005
[4] M.A. Green, Joule, **3**, 631 (2019). https://doi.org/10.1016/j.joule.2019.02.010
[5] M. Bošnjaković, R. Santa, Z. Crnac, and T. Bošnjaković, Sustainability, **15**, 1 (2023). https://doi.org/10.3390/su151511888
[6] H. Zhang, Z. Yu, C. Zhu, R. Yang, B. Yan, and G. Jiang, Environ. Pollut. **320**, 121066 (2023). https://doi.org/10.1016/j.envpol.2023.121066
[7] V.V. Tyagi, N.A.A. Rahim, N.A. Rahim, and J.A.L. Selvaraj, Renew Sustain Energy Rev. **20**, 443 (2013). https://doi.org/10.1016/j.rser.2012.09. 028
[8] M. Hosenuzzaman, N.A. Rahim, J. Selvaraj, M. Hasanuzzaman, Renew Sustain Energy Rev. **41**, 284 (2015). https://doi.org/10.1016/j.rser.2014.08. 046
[9] D. Suthar, P.S.L. Himanshu, et al., Solid State Sci. **107**, 106346 (2020). https://doi.org/10. 1016/j.solidstatesciences.2020.106346
[10] S. Rashel, A. Ahmed, A. Sunny, and S. Rahman, Sol Energy Mater. Sol. Cells, **221**, 110919 (2021). https://doi.org/ 10.1016/j.solmat.2020.110919
[11] K. Kumari, A. Jana, A. Dey, et al. Opt Mater. **111**, 110574 (2021). https://doi.org/10.1016/j. optmat.2020.110574
[12] D. Suthar, P.S.L. Himanshu, et al., Solid State Sci. **107**, 106346 (2020). https://doi.org/10. 1016/j.solidstatesciences.2020.106346
[13] E. Shalaan, E. Ibrahim, F. Al-Marzouki, M. Al-Dossari, Appl Phys A: Mater. Sci. Process. **126**, 852 (2020). https://doi.org/10.1007/s00339-020-04045-9
[14] H. Hamdi, and S. Valette, J. Appl. Phys. **51**, 4739 (1980). https://doi.org/10.1063/1.328303
[15] H. Asano, S. Tsukuda, M. Kita, et al., ACS Omega, **3**, 6703 (2018). https://doi.org/ 10.1021/acsomega.8b00612
[16] B. Lakehal, Z. Dibi, and N. Lakhdar, in: *The International Conference on Green Energy & Conversion Systems*, (IEEE, 2017).
[17] Y. Rahmat-Samii, E. Michielssen, (John Wiley & Sons, 1999), pp. 480.
[18] T. Back, *Evolutionary Algorithms in Theory and Practice*, (Oxford, University Press, USA, 1996)
[19] P. Chamola, and P. Mittal, Optik, **224**, 165626 (2020). https:// doi.org/10.1016/j.ijleo.2020.165626
[20] T. Tanaka, M. Miyabara, K. Saito, et al., Mater Sci Forum. **750**, 80 (2013), https://doi.org/10.4028/www.scientific.net/MSF.750.80
[21] O. Skhouni, A. El Manouni, B. Mari, and H. Ullah, EPJ Appl. Phys. **74**, 1 (2016), https://doi.org/10.1051/ epjap/2015150365
[22] A.S. Lin, W. Wang, and J.D. Phillips, J. Appl. Phys. **105**, 064512 (2009). https://doi.org/10.1063/1.3093962
[23] W. Wang, Doctoral thesis, "Intermediate Band Solar Cells based on ZnTeO", University of Michigan, 2010.
[24] B. Lakehal, Z. Dibi, and N. Lakhdar, Journal of Nano- and Electronic Physics, 09, 06005 (2017), https://doi.org/10.21272/jnep.9(6).06005

ПІДВИЩЕННЯ ЕФЕКТИВНОСТІ ПЕРЕТВОРЕННЯ СОНЯЧНИХ ЕЛЕМЕНТІВ ШЛЯХОМ ЕВОЛЮЦІЙНОЇ ОПТИМІЗАЦІЇ З ВИКОРИСТАННЯМ ГЕНЕТИЧНИХ АЛГОРИТМІВ

Брахім Лакехал[a], Абдельгані Дендуга[b]

[a]Департамент промислової безпеки, Інститут охорони здоров'я та безпеки, Університет Батна 2, (Алжир)
[b]Лабораторія вдосконаленої електроніки, Університет Батна 2, Алжир

У цьому дослідженні ми пропонуємо новий метод, заснований на генетичних алгоритмах, для оптимізації продуктивності проміжних сонячних елементів (IBSC). Наш підхід спрямований на максимізацію ефективності фотоелектричного перетворення шляхом розумної оптимізації геометричних і фізичних параметрів структури IBSC, яка має бути частково заповнена. Таке заповнення забезпечує наявність як порожніх станів у проміжній зоні (IB) для прийому електронів із валентної зони (VB), так і заповнених станів для надання електронів зоні провідності (CB). Нещодавно в дослідженнях було виявлено вплив заповненості IB на ефективність клітини та розраховано оптимальну ефективність для пристроїв IB. Аналітичний вираз для оптимального заповнення IB використовувався для різних сценаріїв, що включають міцність зв'язку IB-CB і ширину області IB. У цій роботі ми досліджували вплив рівня енергії проміжної зони, вплив легування на ефективність, струм короткого замикання, напругу холостого ходу, коефіцієнт заповнення, а також для перевірки нашого підходу щодо паразитних ефектів, таких як послідовність і шунт. опір.

Ключові слова: *сонячна батарея; сонячні батареї середнього діапазону; енергетичний рівень смуги; послідовний і шунтовий опір; коефіцієнти поглинання*

ENHANCING THIRD-GENERATION SOLAR CELL EFFICIENCY AND STABILITY THROUGH P-TYPE SILICON INTEGRATION: PROCESS ANALYSIS AND PERFORMANCE EVALUATION

Santosh Kumar Srivastava*, Jitendra Singh#

aDepartment of Physics, Shri Lal Bahadur Shastri Degree College Gonda, Uttar Pradesh
*Corresponding Author e-mail sksslbsdc@gmail.com; #drjitendra@lbsdc.org.in
Received January 31, 2024; revised March 20, 2024; accepted March 22, 2024

Third-generation solar cells have emerged as a potential solution to the effectiveness and stability issues encountered in conventional solar technology. This study focuses on the characteristics of copper-zinc-tin-sulfide (CZTS) thin films inside this innovative architectural framework, which is an important step toward improving third-generation solar cells by incorporating a p-type silicon layer. This integrated method provides a versatile and manageable setting for film deposition, underscoring the effort put into creating high-quality CZTS thin films. Using X-ray diffraction (XRD), the study assessed the structural change of CZTS films after annealing, finding that kesterite phases were dominant. Images captured by a scanning electron microscope (SEM) reveal the microstructure and surface morphology of CZTS-coated Silicon nanowires (Si-NWs). A detailed analysis of the current-voltage characteristics provides evidence of the operational potential of the Si-NWs-CZTS coated solar cell. Significant performance parameters observed include a Voc value of 0.45 ± 0.02V, Isc value of 8.25 ± 0.30 mA/cm², FF value of $24 \pm 2\%$, and η value of $1.0 \pm 0.1\%$. The encouraging results indicate the capacity of using P-type silicon to enhance the performance of third-generation solar cells.
Keywords: *Solar cells; CZTS; Thin film; Photovoltaics*
PACS: 42.79Ek, 84.60.Jt

1. INTRODUCTION

Rising societal interest in photovoltaic (PV) energy has contributed to a significant development in the demand for solar cells in the past few decades. The enhancement of energy conversion efficiency in solar cells via the advancement of innovations and technologies is crucial for the future global energy supply. However, a significant challenge associated with photovoltaic modules lies in their relatively expensive manufacturing and energy costs [1]. So, to provide low-cost third-generation solar cells, researchers are working to merge silicon substrates with thin coatings or nanostructures [2][3]. The third-generation solar cell is a viable alternative to traditional solar cell technologies. Its primary objective is to develop high-efficiency devices at a lower cost compared to the expensive 1-generation solar cells and the less effective 2-generation solar cells. Figure 1 given below illustrates the working concept of PV solar cells.
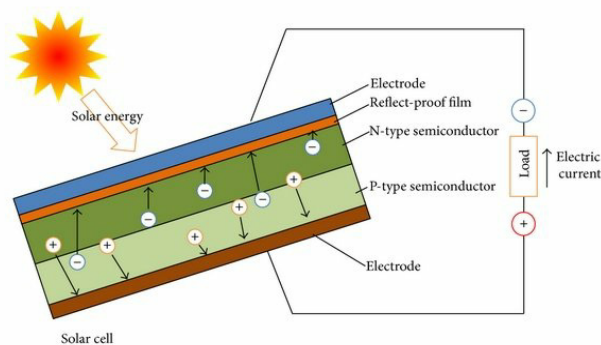
Figure 1. PV solar cell operational concept [4]

In light of the ongoing shift towards sustainability in the global energy sector, the pursuit of solar cells that are both efficient and stable has become of paramount importance. Solar cells combining n-type zinc oxide nanorods with p-type silicon have made great strides in recent years. This approach offers a cost-effective solution by employing inexpensive silicon wafers as substrates, hence reducing manufacturing costs [5][6]. Hence the present study contributes to this necessity by digging into the complex world of third-generation solar cells and concentrating especially on the influence of P-type silicon integration. The purpose of the study is to discover new horizons in solar technology by doing thorough process analysis and conducting rigorous performance assessments. This would pave the way for renewable energy sources that are more dependable and efficient.

The next parts of the study are arranged as follows: Section 2 provides the recent findings from studies aimed at improving the efficiency and reliability of solar cells. Section 3 addressed the research gaps based on conducted literature review. Section 4 explains the material and procedures utilized in the proposed study. The findings of the experiments

are presented and discussed in the next section. Finally, Section 6 provides the conclusion of the study, including future considerations.

1.1   Advancements in Third-Generation Solar Cells

These types of solar cells aim for great efficiency and cheap cost by using a novel semiconductor nanoparticle method. The innovative notion of impact ionization may create a high current from semiconductor nanoparticles, making such devices very attractive. Shockley-Queisser efficiency limits the amount of energy that can be converted by solar cells thermodynamically, and it is believed that the use of semiconductor nanoparticles would overcome this barrier [7][8]. In the active layer of organic solar power cells, molecules may serve as both donors and acceptors. Till now a level of efficiency ranging from 10% to 15% has been attained [9]. Above 20% efficiency has been attained in perovskite solar cells using an integrated organic-inorganic perovskite halide and halogen active layer [10-12]. Additionally, emerging technologies such as multiband cells, and tandem and hot carrier solar cells, have shown promise in enhancing photocurrent and efficiency.

1.2   Various Third generation solar cell

Third-generation photovoltaics are broken down into five distinct categories, as described below [13]:

(i).   Dye Sensitized Solar cell (DSSC)

The DSSC has gathered commercial interest due to its cheap production cost, semi-transparency, easy construction, and efficiency in low light [14]. DSSCs convert sunlight into energy using an electrolyte. DSSCs are simpler to make than standard cells because dye absorbs and passes sunlight to a semiconductor layer like TiO_2 [15][16]. Plant-based natural colors are safer for the environment and human health, but they don't last as long or seem as vivid as their synthetic counterparts [17]. Building integration, interior energy collection, smart farming, and more are possible with these solar cells [18][19].

(ii).   Organic solar cells (OSCs)

OSC films of 100 nm are made from polymer compounds or molecules of organic semiconductors. They have a power conversion efficiency (PCE) of >18% [20] [21], are lightweight, cheap, easy to make, and ecologically favorable compared to silicon-based cells [22-24]. The use of star non-fullerene compound [25-28] and narrow-band-gap non-fullerene substance as a receiver [29] have improved the efficiency and stability of OSCs [30-33]. Organic semiconductors absorb more than inorganic ones. Adjusting the top electrode and using the proper material may maximize its conduction ability and average transmission of visible light [34].

(iii).   Perovskite solar cells (PSCs)

In the last ten years, the PCE of PSCs has increased from 2% [35] to 28% in a tandem design. Short-lived stability and lead toxicity plague them. Encapsulating PSCs in epoxy resins instead of glass [36] improves mechanical stability, carbon-based monolithic PSCs improve thermal and humidity stability, controls crystallization over fabrication increases flexibility and scale, and tin dioxide (SnO_2) instead of TiO_2 solves scalability and stability issues [37].

(iv).   Quantum dot solar cells (QDSCs)

Changing the size and structure of QDSCs, semiconductor tiny crystals, may rapidly modify their properties. Bulk materials in this region are difficult to produce but they may have seven changeable band gaps. QDSCs have several applications, including LEDs, FETs, and photodiodes [38]. These cells extract a broad sunlight spectrum effectively. Changing surface treatment may modify QDSC energy [39]. With a PCE of 16%, these cells are expected to be commercialized as flexible and portable PVs [40].

(v).   CZTS

CZTS-based thin-film solar cells are safe for people and the environment [41]. CZTS solar cells use Copper-Indium-Gallium Selenide/Sulphide (CIGS), amorphous silicon (a-Si), and Cadmium Telluride (CdTe). CIGS has >20% efficiency despite raw material shortages. The most efficient kesterite solar cell has a 1.15 eV bandgap and 10.1% efficiency. Optimizing the deposition process, the kesterite absorbing-buffer layer contact and other approaches may boost CZTS cell efficiency.

2.   LITERATURE REVIEW

In this section, some related studies by various authors on the enhancement of the productivity and efficacy of solar cells are discussed below:

Sharma et al., (2021) [42] detected that Solar cells have become smaller and converted more electricity over time. This study provides a comparative review of photovoltaic technology by conducting a comprehensive examination of the design, use, and performance of third-generation solar cells. It also explores the prospects and considerations associated with these solar cells. The findings revealed that concentrated solar cells have shown the highest efficiency of 38.9% among all kinds of solar cells.

Peksu et al., (2020) [43] revealed that the breakthrough in cheaper device production using materials for semiconductors that are very crystalline is a significant step toward advanced core-shell-based Si NWs solar cell technology for improved efficiency. Third-generation solar cells are made by covering transplanted NWs with a thin layer of CZTS for use in demonstrating products based on the NWs. In-depth characterization revealed the devices to have the best PCE of 1.31% for such material combinations and transmitted NWs.

Tavakoli Dastjerdi et al., (2019) [44] observed that a significant limitation on the widespread use of solar cells based on PbS quantum dots (QDs) is their sensitivity to humidity in the surrounding air. While oxygen doping the hole-carrying layer might fix this issue, doing so would be a lengthy and costly process. The study suggested a low-cost oxygen plasma treatment to improve performance and stability. The results revealed that the ideal treatment time for plasma is 10 minutes, which boosts PCE from 6.9% for the untreated device to 9% after treatment.

Peksu et al., (2019) [45] aimed to create a solar cell with the effectiveness of the 1-generation and the advantages of the third. A 1.0% efficient experimental Si-NW-CZTS structural solar cell was developed by applying a CZTS absorption layer coated with electroless etching on Si-NWs. The current density associated with a short circuit of the produced solar cell was much greater than that of the formerly described planer equivalency. This is crucial for the eventual growth of inexpensive, highly effective third-generation solar cells.

Guller et al., (2018) [46] performed the hydrothermal synthesis of TiO2 nanorods (NRs) on substrates of glass that have been coated with fluorine-doped tin oxide. The influence of growing conditions on synthesized NR morphology is examined. The findings showed that well-aligned TiO2 NRs need crucial physical conditions. After fine-tuning the growth parameters, a 3-generation inorganic-sensitized photovoltaic cell is built using organized TiO2 NR with a thin sputtered layer of CdTe. A PCE of 0.42% was achieved by the created solar cell, which is 3.5 times more than that of a non-CdCl$_2$-treated device structure.

Wang et al., (2017) [47] enabled the generation of hot charge carriers only from visible light by eliminating the need for UV light exposure by using plasmonically excited metal nanostructures that were included in a ZnO metal oxide layer. Additionally, the present study suggests solar cells with enhanced transport of charges and dispersion properties, along with greater light-trapping capabilities. The results show that there is potential to enhance the PCE of a low-bandgap solar cell, increasing from 7.91% to 9.36%.

Wan et al., (2017) [48] analyzed that Magnesium oxide/aluminum (MgOx/Al) connections are shown to be extremely conductive and thermally stable, allowing for Ohmic contacts with fairly low resistance on lightly doped n-type c-Si. Nanoscale MgO$_x$ films functionalized on the electrode significantly enhance the efficacy of n-type c-Si solar cells, bringing the PCE of these cells up to 20% and making them competitive with the standard p-type architecture.

Zhu et al., (2017) [49] employed a silicon-based nano heterostructure solar device to increase the light absorption provided by the NW array, and also by effectively separating charge carriers via the piezo-phototronic effect (PPE). It was observed that simply adding a static compress strain resulted in an efficiency increase of the solar cell from 8.97% to 9.51%. According to the findings of this study, PPE has the potential to enhance the effectiveness of large-scale Si solar cells, which has significant consequences for the industrial sector.

Fix et al., (2016) [50] suggested 3-generation solar cells to boost the effectiveness of conventional solar cells, such as CIGS or Si, which perform poorly when exposed to UV photons. The silicon photovoltaic cells have had encapsulants functionalized by photon-downshifting coordination complexes spin-coated onto their surfaces. The results show that all the coordination complexes show an enhanced ultraviolet spectrum sensitivity in solar cells and the suggested solar cell's conversion efficiency improved by 8%.

Xu et al., (2014) [51] observed that the addition of an organic redox shuttle to the photocathode of a sensitized CuCrO$_2$ delafossite nanocrystal electrode and a P1 sensitized organic dye could lead to an increase in photocurrent. In particular, it is shown that the presence of Au NPs inside the CuCrO$_2$ layer increases the electrical charge infusion performance at the dye/semiconductor junction.

3.   RESEARCH GAPS

Some of the major research gaps that are addressed in this experimental study are as follows:

● Long-term stability evaluations of solar cells with integrated P-type silicon are ignored, and existing studies often focuses on shorter time frames.

● Previous study often exhibits a lack of comprehensive investigation into the various mechanisms associated with the incorporation of P-type silicon into third-generation solar cells.

● Although the potential improvements in efficiency and stability via the incorporation of P-type silicon are recognized, there is a lack of standard and comprehensive methods for assessing performance.

4.   MATERIALS AND METHODS

The following section explains the methods and materials utilized in this experimental study.

3.1   EXPERIMENTAL PROCEDURE

The primary aim of this experimental design is to evaluate the impact of including a p-type layer on the efficacy and sustainability of thin-film Si solar cells. The primary emphasis is specifically placed on recognizing the properties of CZTS films throughout this particular architecture. The selected approach for the production of CZTS thin films involves the combination of spin-coated and sol-gel techniques. The selection of this technique is deliberate, as it has shown to be effective in tackling the problems often encountered during the synthesis of CZTS thin films with high stoichiometry. The use of both of these techniques provides a flexible and regulated setting for the deposition of films. The strategic selection of the manufacturing technique highlights the experimental approach's dedication to attaining CZTS thin films of superior quality and analyzing the overall efficiency and durability of thin-film silicon solar cells.

3.2   Materials Required

The crucial elements for the experimental undertaking include an appropriate range of materials which are given in Table 1. Along with these elements, the selected substrates for the deposition technique include soda lime glass (SLG) and arrays of p-type silicon NWs.

Table 1. Materials required and their properties

Elements	Composition	Concentration/volume	Purity level
Copper acetate	$Cu(CH_3COO)_2$	1.7 M	98%
Tin chloride	$SnCl_2$	0.7 M	98%
Thiourea	CH_4N_2S	6.5 M	99%
Zinc acetate	$Zn(CH_3COO)_2(H_2O)_2$	1.1 M	99.9%
Triethanolamine	$N(CH_2CH_2OH)_3$	1.2 mL	98%
2-methoxyethanol	$C_3H_8O_2$	10 mL	99%

The materials that have been utilized in this experimental study serve as the basis for the succeeding phases of the experiment, guaranteeing a thorough and accurate assessment of the impact of the p-type coating on the efficiency and durability of CZTS Si-solar cells of the third generation.

3.3   Experimental Process

The procedure of film deposition is specifically arranged to guarantee the accuracy and excellence of the CZTS thin films. The initiation process entails the careful and thorough production of a solution via the dissolution of the designated components. The primary objective of this critical stage is to get a uniform blend, hence enhancing the uniformity of the film's characteristics. The solution is subjected to extensive agitation for 2 hours at ambient temperature, therefore further augmenting its uniformity.

Aging the solution for two days is a crucial step in the procedure. This time frame was specifically selected to optimize the final product quality of the thin films. After that, a 0.42 m syringe filter is used to further refine the solution and remove any remaining contaminants. Spin-coating at 3500 rpm for half a minute is used to deposit materials onto substrates like soda lime glass (SLG) and p-type Si-NW arrays. The uniformity of the thin films across substrates may be attributed in part to the controlled deposition method. The organic solvent is removed, and the thin films are made more stable by being heated at 220 degrees Celsius for 1.5 hours on a hot plate. After this well-managed thermal process, stable CZTS thin films are left behind, free of any lingering solvent.

After all layers have been deposited, their thicknesses must be measured. A surface profilometer is used for this purpose because it provides precise measurements that are essential for further analyses of the structure's strength and efficiency. Overall, the film deposition process is systematic and regulated, which ensures the dependability and repeatability of the CZTS thin films for further study.

3.4   Performance Parameters

This section includes numerous factors related to the evaluation of Si- based CZTS thin films' performance in third-generation solar cell applications. The section is organized with subheadings that explore distinct performance factors which are given as follows [45]:

3.4.1 *Structural Characterization*

This study utilizes X-ray diffraction (XRD) for structural examination by exposure of CZTS lightweight films to X-rays to obtain information regarding the crystallographic orientation, material formulation, and phase purity that may be obtained from its crystalline structure.

3.4.2   *Optical Properties*

This study utilized a spectrophotometer to determine the degree of reflection and transmission of the CZTS films and measure the intensity. In order to evaluate the material's transparency, absorbance, and reflectance, this examination offers a thorough comprehension of those optical qualities.

3.4.3   *Solar Cell Fabrication*

Si NWs are layered with a thin CZTS sheet as part of the solar cell construction process. To maximize the absorption of light and electron production, the CZTS material must be integrated into the solar cell structure. Thermal evaporation is used to apply silver dot contacts roughly 60 nm thick on top of the CZTS coating. These silver connections are critical to the solar cell's functioning and conductivity, allowing for the effective removal of electrons that have been created. Apply a coating of silver thin film that is 150 nm thick on the unpolished side of the n-type silicon wafer. This silver sheet in the solar cell facilitates the effective collection of electrons produced by the photovoltaic process.

3.4.4   *Photovoltaic Characterization*

The evaluation of the performance of solar cells may be conducted inside a controlled environment that simulates natural sunlight conditions. To begin the experiment, it is necessary to get measurements of the current-voltage

characteristics of a photo-current-driven device under two distinct lighting conditions: low and intense light. The analysis of the solar cell's electrical response to varying levels of light is necessary. Subsequently, calculate the power conversion efficiency (η), open circuit voltage (Voc), short-circuit current (Isc), and fill factor (FF) of a solar array. To evaluate the viability of CZTS-based solar cells for practical implementation, a comprehensive analysis of their efficiency and performance is necessary.

5.   RESULT AND DISCUSSION

The following section demonstrates the results obtained from the experimental study:

4.1   XRD result
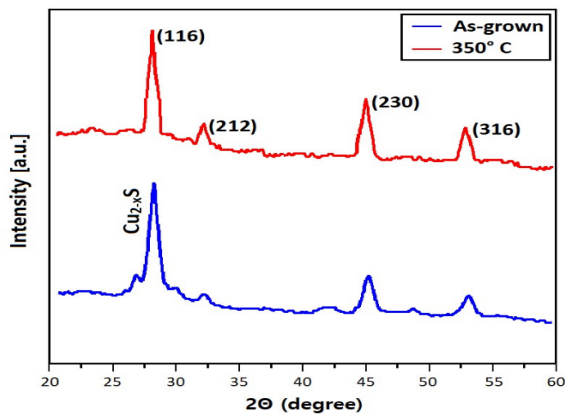
Figure 2. XRD patterns

Figure 2 shows XRD patterns illustrating the diffraction characteristics of CZTS thin films that have undergone both initial growth and subsequent annealing processes. These films were deposited onto substrates composed of single-layer graphene (SLG). The as-grown film's pattern may exhibit polycrystalline phases of kesterite CZTS and Cu_2-xS. The phases in question are denoted by the peaks seen in the indexed reflection data. Based on the observed trend, it can be inferred that only the reflection peaks corresponding to Si (316) and CZTS (116, 212, and 230) can be seen.

During annealing, the kesterite CZTS phase becomes more dominant while the peaks associated with the secondary Cu_2-xS phase fade. Increased intensity relative to angle is indicative of increased concentration or existence of the observed peaks related to CZTS.

4.2   SEM

Figure 3 (a-b) displays top-down and side-view SEM images of the incorporated Si-NWs. These images illustrate the microstructure and surface morphology of the Si-NWs in specifications, and they do so despite the requirement of any coatings or additional layers. Each CZTS-layered Si-NW illustrated in Figure 3 (c-d) is 600 nm thick. The SEM images illustrate the top-down view and side view. Immediately after deposition of the CZTS absorbent layer on the Si-NWs, these images were obtained.
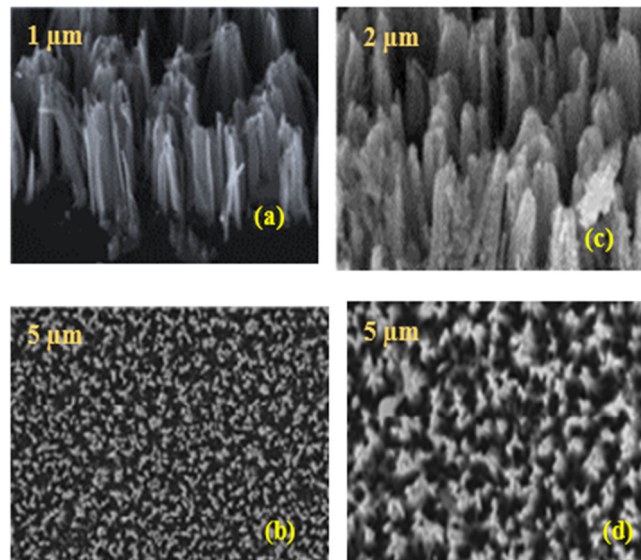
Figure 3. Top-down and side view of (a-b) Si-NWs (c-d) CZTS-layered Si-NW

The SEM images indicate that the CZTS layer is present as an extra overlay on the Si-NWs. The provided images facilitate the comprehension of the device configuration by elucidating crucial information on the shape and structure of CZTS-coated Si-NWs.

4.3   Current (I) -Voltage (V) Characterisation

The current (I) -voltage (V) relationship of the Si-NW-CZTS photovoltaic cells was evaluated in the presence of both dark conditions and AM 1.5G light. The characteristic curve illustrates the correlation between the current flowing (I) and voltages (V) across the solar cell. Figure 4 illustrates the same feature that has been transferred towards the I-1st quadrant, facilitating the analysis of the solar cell's effectiveness.
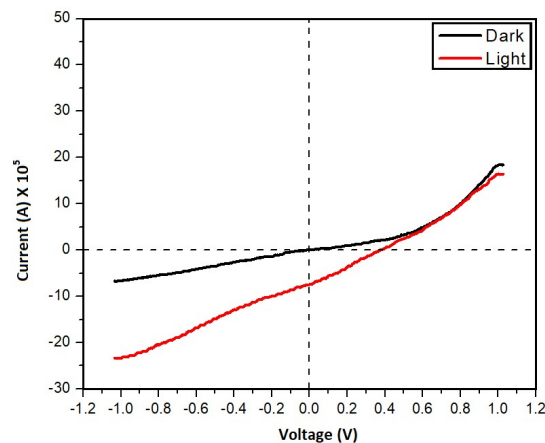
Figure 4. I-V relationship

This evaluation provides significant insights into the operational characteristics of the solar cell across varying levels of light, hence facilitating the determination of crucial parameters. The Voc of the designed Si-NW-CZTS solar cell was found to be 0.45 ± 0.02V. The Isc was estimated to be 8.25 ± 0.30 mA/cm^2. The FF was established to be $24 \pm 2\%$. Lastly, the η of the solar cell was estimated to have a value of $1.0 \pm 0.1\%$.

6.   CONCLUSION AND FUTURE SCOPE

P-type silicon integrated into third-generation solar cells using CZTS layers atop Si-NWs has shown encouraging efficiency and stability results. After annealing, CZTS films transformed into dominant kesterite phases, improving their structural properties, according to XRD studies. SEM study clarified CZTS-coated Si-NWs' microstructure and surface morphology, revealing the photovoltaic device's configuration. The Si-NW-CZTS solar cell performance was shown by dark and light current-voltage measurements. Performance measurements of the solar cell include Voc of 0.45 ± 0.02V, Isc of 8.25 ± 0.30 mA/cm^2, FF of $24 \pm 2\%$, and η of $1.0 \pm 0.1\%$. These findings suggest that P-type silicon incorporation might boost third-generation solar cell efficiency.

Opportunities for further research into improving solar cell efficiency beyond the third generation have been established by the successful incorporation of P-type silicon. Future studies might concentrate on perfecting the integration procedure to boost efficiency and steadiness. Third-generation solar cells have several obstacles that can only be overcome by the combined efforts of researchers on a holistic approach to the problem.

ORCID

Santosh Kumar Srivastava, https://orcid.org/0009-0007-7394-7093; **Jitendra Singh,** https://orcid.org/0009-0005-2179-6073

REFERENCES
[1]   J. Ramanujam, D.M. Bishop, T.K. Todorov, O. Gunawan, J. Rath, R. Nekovei, E. Artegiani, and A. Romeo, "Flexible CIGS, CdTe and a-Si: H based thin film solar cells: A review," Progress in Materials Science, **110**, 100619 (2020). https://doi.org/10.1016/j.pmatsci.2019.100619
[2]   L.V. Mercaldo, I. Usatii, and P.D. Veneri, "Advances in thin-film Si solar cells by means of SiO$_x$ alloys," Energies, **9**(3), 218 (2016). https://doi.org/10.3390/en9030218
[3]   M. Zellmeier, S. Kühnapfel, B. Rech, N.H. Nickel, and J. Rappich, "Enhanced stability of P3HT/poly-crystalline Si thin film hybrid solar cells," Physica Status Solidi (a), **213**(7), 1904-1908 (2016). https://doi.org/10.1002/pssa.201532772
[4]   H.L. Zhang, T. Van Gerven, J. Baeyens, and J. Degrève, "Photovoltaics: Reviewing the European feed-in-tariffs and changing PV efficiencies and costs," The Scientific World Journal, **2014**, 404913 (2014). https://doi.org/10.1155/2014/404913
[5]   R. Pietruszka, B.S. Witkowski, S. Gieraltowska, P. Caban, L. Wachnicki, E. Zielony, K. Gwozdz, et al., "New efficient solar cell structures based on zinc oxide nanorods," Solar Energy Materials and Solar Cells, **143**, 99-104 (2015). https://doi.org/10.1016/j.solmat.2015.06.042
[6]   R. Pietruszka, R. Schifano, T.A. Krajewski, B.S. Witkowski, K. Kopalko, L. Wachnicki, E. Zielony et al., "Improved efficiency of n-ZnO/p-Si based photovoltaic cells by band offset engineering," Solar Energy Materials and Solar Cells, **147**, 164-170 (2016). https://doi.org/10.1016/j.solmat.2015.12.018
[7]   M.C. Beard, J.M. Luther, and A.J. Nozik, "The promise and challenge of nanostructured solar cells," Nature nanotechnology, **9**(12), 951-954 (2014). https://doi.org/10.1038/nnano.2014.292
[8]   A. Rao, and R.H. Friend, "Harnessing singlet exciton fission to break the Shockley-Queisser limit," Nature reviews materials, **2**(11), 1-12 (2017). https://doi.org/10.1038/natrevmats.2017.63
[9]   Y. Li, G. Xu, C. Cui, and Y. Li, "Flexible and semitransparent organic solar cells," Advanced Energy Materials, **8**(7), 1701791 (2018). https://doi.org/10.1002/aenm.201701791
[10] A. Dubey, N. Adhikari, S. Mabrouk, F. Wu, K. Chen, S. Yang, and Q. Qiao, "A strategic review on processing routes towards highly efficient perovskite solar cells," Journal of Materials Chemistry A, **6**(6), 2406-2431 (2018). https://doi.org/10.1039/C7TA08277K

[11] E.H. Anaraki, A. Kermanpur, M.T. Mayer, L. Steier, T. Ahmed, S.-H. Turren-Cruz, J. Seo, et al., "Low-temperature Nb-doped SnO_2 electron-selective contact yields over 20% efficiency in planar perovskite solar cells," ACS Energy Letters, **3**(4), 773-778 (2018). https://doi.org/10.1021/acsenergylett.8b00055

[12] M. Saliba, J.-P. Correa-Baena, M. Grätzel, A. Hagfeldt, and A. Abate, "Perovskite solar cells: from the atomic level to film quality and device performance," Angewandte Chemie International Edition, **57**(10), 2554-2569 (2018). https://doi.org/10.1002/anie.201703226

[13] E. Mirabi, F.A. Abarghuie, and R. Arazi, "Integration of buildings with third-generation photovoltaic solar cells: a review," Clean Energy, **5**(3), 505-526 (2021). https://doi.org/10.1093/ce/zkab031

[14] M.E. Yeoh, and K.-Y. Chan. "A review on semitransparent solar cells for real-life applications based on dye-sensitized technology," IEEE Journal of Photovoltaics, **11**(2), 354-361 (2021). https://doi.org/10.1109/JPHOTOV.2020.3047199

[15] Z. Mubarak, N.M. Nursam, S. Shobih, J. Hidayat, and D. Tahir, "A comparison of the utilization of carbon nanopowder and activated carbon as counter electrode for monolithic dye-sensitized solar cells (DSSC)," Jurnal Elektronika dan Telekomunikasi, **18**(1), 15-20 (2018). http://dx.doi.org/10.14203/jet.v18.15-20

[16] V. Pramananda, T.A.H. Fityay, and E. Misran, "Anthocyanin as natural dye in DSSC fabrication: A review," IOP Conference Series: Materials Science and Engineering, **1122**(1), 012104 (2021). https://doi.org/10.1088/1757-899X/1122/1/012104

[17] G. Richhariya, A. Kumar, P. Tekasakul, and B. Gupta, "Natural dyes for dye sensitized solar cell: A review," Renewable and Sustainable Energy Reviews, **69**, 705-718 (2017). https://doi.org/10.1016/j.rser.2016.11.198

[18] A. Pallikkara, and K. Ramakrishnan, "Efficient charge collection of photoanodes and light absorption of photosensitizers: A review," International Journal of Energy Research, **45**(2), 1425-1448 (2021). https://doi.org/10.1002/er.5941

[19] M.N. Mustafa, and Y. Sulaiman, "Review on the effect of compact layers and light scattering layers on the enhancement of dye-sensitized solar cells," Solar Energy, **215**, 26-43 (2021). https://doi.org/10.1016/j.solener.2020.12.030

[20] Yu Lin, Y. Firdaus, F.H. Isikgor, M.I. Nugraha, E. Yengel, G.T. Harrison, R. Hallani et al., "Self-assembled monolayer enables hole transport layer-free organic solar cells with 18% efficiency and improved operational stability," ACS Energy Letters, **5**(9), 2935-2944 (2020). https://doi.org/10.1021/acsenergylett.0c01421

[21] Q. Liu, Y. Jiang, K. Jin, J. Qin, J. Xu, W. Li, J. Xiong, et al., "18% Efficiency organic solar cells," Science Bulletin, **65**(4), 272-275 (2020). https://doi.org/10.1016/j.scib.2020.01.001

[22] J. Gao, W. Gao, X. Ma, Z. Hu, C. Xu, X. Wang, Q. An, et al., "Over 14.5% efficiency and 71.6% fill factor of ternary organic solar cells with 300 nm thick active layers," Energy & Environmental Science, **13**(3), 958-967 (2020). https://doi.org/10.1039/C9EE04020J

[23] M. Zhang, Z. Xiao, W. Gao, Q. Liu, K. Jin, W. Wang, Y. Mi, et al., "Over 13% efficiency ternary nonfullerene polymer solar cells with tilted up absorption edge by incorporating a medium bandgap acceptor," Advanced Energy Materials, **8**(30), 1801968 (2018). https://doi.org/10.1002/aenm.201801968

[24] Z. Xiao, S. Yang, Z. Yang, J. Yang, H.-L. Yip, F. Zhang, F. He, et al., "Carbon–Oxygen-Bridged Ladder-Type Building Blocks for Highly Efficient Nonfullerene Acceptors," Advanced Materials, **31**(45), 1804790 (2019). https://doi.org/10.1002/adma.201804790

[25] J. Yuan, Y. Zhang, L. Zhou, G. Zhang, H.-L. Yip, T.-K. Lau, X. Lu, et al. "Single-junction organic solar cell with over 15% efficiency using fused-ring acceptor with electron-deficient core," Joule, **3**(4), 1140-1151 (2019). https://doi.org/10.1016/j.joule.2019.01.004

[26] Q. An, J. Wang, W. Gao, X. Ma, Z. Hu, J. Gao, C. Xu, et al., "Alloy-like ternary polymer solar cells with over 17.2% efficiency," Science Bulletin, **65**(7), 538-545 (2020). https://doi.org/10.1016/j.scib.2020.01.012

[27] Y. Cui, H. Yao, J. Zhang, K. Xian, T. Zhang, L. Hong, Y. Wang, et al., "Single-junction organic photovoltaic cells with approaching 18% efficiency," Advanced Materials, **32**(19), 1908205 (2020). https://doi.org/10.1002/adma.201908205

[28] L. Zhan, S. Li, T.-K. Lau, Y. Cui, X. Lu, M. Shi, C.-Z. Li, et al., "Over 17% efficiency ternary organic solar cells enabled by two non-fullerene acceptors working in an alloy-like model," Energy & Environmental Science, **13**(2), 635-645 (2020). https://doi.org/10.1039/C9EE03710A

[29] Y. Lin, J. Wang, Z.-G. Zhang, H. Bai, Y. Li, D. Zhu, and X. Zhan, "An electron acceptor challenging fullerenes for efficient polymer solar cells," Advanced materials, **27**(7), 1170-1174 (2015). https://doi.org/10.1002/adma.201404317

[30] Z. Hu, F. Zhang, Q. An, M. Zhang, X. Ma, J. Wang, J. Zhang, and J. Wang, "Ternary nonfullerene polymer solar cells with a power conversion efficiency of 11.6% by inheriting the advantages of binary cells," ACS Energy Letters, **3**(3), 555-561 (2018). https://doi.org/10.1021/acsenergylett.8b00100

[31] X. Ma, J. Wang, Q. An, J. Gao, Z. Hu, C. Xu, X. Zhang, et al., "Highly efficient quaternary organic photovoltaics by optimizing photogenerated exciton distribution and active layer morphology," Nano Energy, **70**, 104496 (2020). https://doi.org/10.1016/j.nanoen.2020.104496

[32] P. Cheng, C. Yan, Y. Wu, J. Wang, M. Qin, Q. An, J. Cao, et al., "Alloy acceptor: superior alternative to PCBM toward efficient and stable organic solar cells," Advanced Materials, **28**(36), 8021-8028 (2016). https://doi.org/10.1002/adma.201602067

[33] W. Gao, Q. An, M. Hao, R. Sun, J. Yuan, F. Zhang, W. Ma, et al., "Thick-film organic solar cells achieving over 11% efficiency and nearly 70% fill factor at thickness over 400 nm," Advanced Functional Materials, **30**(10), 1908336 (2020). https://doi.org/10.1002/adfm.201908336

[34] Z. Hu, J. Wang, X. Ma, J. Gao, C. Xu, K. Yang, Z. Wang, et al., "A critical review on semitransparent organic solar cells," Nano Energy, **78**, 105376 (2020). https://doi.org/10.1016/j.nanoen.2020.105376

[35] S. Yang, A. Cannavale, D. Prasad, A. Sproul, and F. Fiorito, "Numerical simulation study of BIPV/T double-skin facade for various climate zones in Australia: Effects on indoor thermal comfort," Building Simulation, **12**, 51-67 (2019). https://doi.org/10.1007/s12273-018-0489-x

[36] Y. Jiang, L. Qiu, E. J. Juarez-Perez, L.K. Ono, Z. Hu, Z. Liu, Z. Wu, et al., "Reduction of lead leakage from damaged lead halide perovskite solar modules using self-healing polymer-based encapsulation," Nature Energy, **4**(7), 585-593 (2019). https://doi.org/10.1038/s41560-019-0406-2

[37] S.G. Hashmi, D. Martineau, M.I. Dar, T.T.T. Myllymäki, T. Sarikka, V. Ulla, S.M. Zakeeruddin, and M. Grätzel, "High performance carbon-based printed perovskite solar cells with humidity assisted thermal treatment," Journal of Materials Chemistry A, **5**(24), 12060-12067 (2017). https://doi.org/10.1039/C7TA04132B

[38] C.R. Kagan, E. Lifshitz, E.H. Sargent, and D.V. Talapin, "Building devices from colloidal quantum dots," Science, **353**(6302), aac5523 (2016). https://doi.org/10.1126/science.aac5523

[39] M.J. Speirs, D.N. Dirin, M. Abdu-Aguye, D.M. Balazs, M.V. Kovalenko, and M.A. Loi, "Temperature dependent behaviour of lead sulfide quantum dot solar cells and films," Energy & Environmental Science, **9**(9), 2916-2924 (2016). https://doi.org/10.1039/C6EE01577H

[40] H. Lee, H.-J. Song, M. Shim, and C. Lee, "Towards the commercialization of colloidal quantum dot solar cells: perspectives on device structures and manufacturing," Energy & Environmental Science, **13**(2), 404-431 (2020). https://doi.org/10.1039/C9EE03348C

[41] K. Pal, K.B. Thapa, and A. Bhaduri, "A review on the current and future possibilities of copper-zinc tin sulfur thin film solar cell to increase more than 20% efficiency," Advanced Science, Engineering and Medicine, **10**(7-8), 645-652 (2018). https://doi.org/10.1166/asem.2018.2225

[42] D. Sharma, R. Mehra, and B. Raj, "Comparative analysis of photovoltaic technologies for high efficiency solar cell design," Superlattices and Microstructures, **153**, 106861 (2021). https://doi.org/10.1016/j.spmi.2021.106861

[43] E. Peksu, O. Guller, M. Parlak, M.S. Islam, and H. Karaagac, "Towards the fabrication of third generation solar cells on amorphous, flexible and transparent substrates with well-ordered and disordered Si-nanowires/pillars," Physica E: Low-Dimensional Systems and Nanostructures, **124**, 114382 (2020). https://doi.org/10.1016/j.physe.2020.114382

[44] H.T. Dastjerdi, R. Tavakoli, P. Yadav, D. Prochowicz, M. Saliba, and M.M. Tavakoli, "Oxygen plasma-induced p-type doping improves performance and stability of PbS quantum dot solar cells," ACS applied materials & interfaces, **11**(29), 26047-26052 (2019). https://doi.org/10.1021/acsami.9b08466

[45] E. Peksu, and H. Karaagac, "A third-generation solar cell based on wet-chemically etched Si nanowires and sol-gel derived Cu_2ZnSnS_4 thin films," Journal of Alloys and Compounds, **774**, 1117-1122 (2019). https://doi.org/10.1016/j.jallcom.2018.10.012

[46] O. Guller, E. Peksu, and H. Karaagac, "Synthesis of TiO_2 Nanorods for Schottky-Type UV-Photodetectors and Third-Generation Solar Cells," Physica Status Solidi (a), **215**(4), 1700404 (2018). https://doi.org/10.1002/pssa.201700404

[47] C. Wang, C. Li, S. Wen, P. Ma, Y. Liu, R.C.I. Mac Kenzie, W. Tian, and S. Ruan, "Combining plasmonic trap filling and optical backscattering for highly efficient third generation solar cells," Journal of Materials Chemistry A, **5**(8), 3995-4002 (2017). https://doi.org/10.1039/C7TA00229G

[48] Y. Wan, C. Samundsett, J. Bullock, M. Hettick, T. Allen, D. Yan, J. Peng et al. "Conductive and stable magnesium oxide electron-selective contacts for efficient silicon solar cells," Advanced Energy Materials, **7**(5), 1601863 (2017). https://doi.org/10.1002/aenm.201601863

[49] L. Zhu, L. Wang, C. Pan, L. Chen, F. Xue, B. Chen, L. Yang, et al., "Enhancing the efficiency of silicon-based solar cells by the piezo-phototronic effect," ACS nano, **11**(2), 1894-1900 (2017). https://doi.org/10.1021/acsnano.6b07960

[50] T. Fix, A. Nonat, D. Imbert, S. Di Pietro, M. Mazzanti, A. Slaoui, and L.J. Charbonnière, "Enhancement of silicon solar cells by downshifting with Eu and Tb coordination complexes," Progress in Photovoltaics: Research and Applications, **24**(9), 1251-1260 (2016). https://doi.org/10.1002/pip.2785

[51] X. Xu, J. Cui, J. Han, J. Zhang, Y. Zhang, L. Luan, G. Alemu et al., "Near field enhanced photocurrent generation in p-type dye-sensitized solar cells," Scientific Reports, **4**(1), 3961 (2014). https://doi.org/10.1038/srep03961

ПІДВИЩЕННЯ ЕФЕКТИВНОСТІ ТА СТАБІЛЬНОСТІ СОНЯЧНИХ ЕЛЕМЕНТІВ ТРЕТЬОГО ПОКОЛІННЯ ШЛЯХОМ ІНТЕГРАЦІЇ КРЕМНІЮ Р-ТИПУ: АНАЛІЗ ПРОЦЕСУ ТА ОЦІНКА ПРОДУКТИВНОСТІ

Сантош Кумар Шрівастава, Джітендра Сінгх
Кафедра фізики, Шрі Лал Бахадур Шастрі Коледж Гонда, Уттар-Прадеш

Сонячні батареї третього покоління з'явилися як потенційне рішення проблем ефективності та стабільності, які виникають у традиційних сонячних технологіях. Це дослідження зосереджено на характеристиках тонких плівок міді-цинку-олова-сульфіду (CZTS) у цій інноваційній архітектурній структурі, яка є важливим кроком до вдосконалення сонячних елементів третього покоління шляхом включення шару кремнію р-типу. Цей інтегрований метод забезпечує універсальне та кероване налаштування для осадження плівок, підкреслюючи зусилля, докладені для створення високоякісних тонких плівок CZTS. Використовуючи рентгенівську дифракцію (XRD), дослідження оцінило структурні зміни плівок CZTS після відпалу, виявлено, що кестеритові фази були домінуючими. Зображення, отримані скануючим електронним мікроскопом (SEM), демонструють мікроструктуру та морфологію поверхні покритих CZTS кремнієвих нанодротів (Si-NW). Детальний аналіз вольт-амперних характеристик свідчить про робочий потенціал сонячної батареї з покриттям Si-NWs-CZTS. Значні параметри продуктивності, що спостерігалися, включають значення Voc 0,45±0,02 В, значення Isc 8,25±0,30 мА/см², значення FF 24 ± 2 % і значення η 1,0±0,1 %. Результати вказують на можливість використання кремнію р-типу для підвищення продуктивності сонячних елементів третього покоління.
Ключові слова: *сонячні батареї; CZTS; тонка плівка; фотовольтаїка*

SCAPS NUMERICAL ANALYSIS OF GRAPHENE OXIDE/ZIRCONIUM DISULFIDE SOLAR CELLS

Hmoud Al-Dmour

Mutah University, Faculty of Science, Department of Physics., 61710, Jordan
Corresponding Author e-mail: hmoud79@mutah.edu.jo
Received March 22, 2024; revised April 12, 2024; accepted April 25, 2024

This work studies the performance of solar cells composed of two different materials, graphene oxide (Go, hole transport material) and zirconium disulfide (ZrS$_2$, electron transport materials) using the SCAPS -1D simulation. It has been found that Go/ZrS$_2$ solar cells show better performance with high short circuit current, J$_{sc}$, of 38 mA/cm^2 and the power conversion efficiency, η, of 17% compared with other solar cells based on graphene oxide and perovskite materials. Additionally, the short circuit current density decreases from 38 mA/cm^2 to 22 mA/cm^2 when the energy gap of ZrS^2 increases from 1.2 eV to 17 eV. The increasing the operating temperature and the work function of back contact also led to decrease the open circuit voltage and power conversion efficiency of the cells, while the short circuit current density was slightly enhanced. That is attributed to changes in the electrical properties of Go and ZrS$_2$ layers, including their charge carrier mobility and characteristics of the interfacial layers.
Keywords: *SCAPS-1D simulation; Solar cells; Work function; Interfacial layers; Operating temperature*
PACS: 42.79.Ek, 78.20.Bh, 72.80.Le, 73.30.y, 73.40.Kp

1. INTRODUCTION

There have been significant research and development efforts focused on finding alternatives to fossil fuels for powering factories and industrial development [1]. The primary reasons for seeking alternatives to fossil fuels are the environmental concerns associated with their usage, including greenhouse gas emissions, air pollution, and their contribution to climate change [2]. One of these alternatives is solar energy which is friendly to the environment and available to varying extents also around the Earth [3]. Silicon solar cells have been the most widely used photovoltaic technology due to their high efficiency and relatively low cost. Silicon semiconductors are typically rigid and brittle, making them unsuitable for certain applications that require flexibility, bendability, and require a high power-per-weight ratio [3,4]. These later features have been achieved using organic materials to fabricate flexible solar cells [5,6]. However, organic solar cells have not produced high enough efficiencies and low stability, and low strength to compete with traditional silicon-based solar cells in commercial applications [5].

The disadvantages of silicon and organic materials-based solar cells led to the use of transition metal dichalcogenides (TMDCs) as n-type semiconductor for fabricating solar cells [7]. Particularly zirconium disulfide (ZrS$_2$) received significant attention due to its potential as a candidate for various applications, including solar cells [7,8]. This material is a two-dimensional (2D) transition metal disulfide and synthesized as thin film for application in flexible transparent devices. Various growth techniques can be employed to achieve tun ability of bandgap energy, electronic, and optical properties for ZrS$_2$ thin films such as Chemical Vapor Deposition (CVD) and Atomic Layer Deposition (ALD) [8]. The second part of solar cells should be a p-type semiconductor to create a junction at the interface in solar cells such as graphene oxide (GO) [9]. Go has been used widely as a hole transport material and a good candidate to replace organic hole transport layer in solar cells. That is attributed to its bandgap energy (3.5 eV), excellent transparency, low production cost, large-scale production capability and good dispensability in many solvents and high hole mobility. Solar cell capacitance simulator (SCAPS-1D) is a one-dimensional solar cell simulation program developed by the department of Electronics and Information Systems (ELIS) at the University of Gent in Belgium. The main purpose of SCAPS-1D is to simulate and evaluate the performance of semiconductor-based solar cells, particularly their electrical characteristics in the dark and light [10-12]. In the beginning, the SCAPS was conducted to simulate the performance of solar cells whose components are CuInSe$_2$ and the CdTe family [11]. Also, it has been used for different types of materials such as crystalline solar cells (Si and GaAs family) and amorphous cells (a-Si and microporous Si) [13]. The SCAPS-1D solves the essential semiconductor equations such as the Poisson equation (1) and the continuity equations for electrons and holes (2,3) [13]. These equations are fundamental in understanding the behaviour and performance of solar cells. The equations are given below:

$$\frac{d^2\psi}{dx^2} + \frac{q}{\varepsilon}\left[p(x) - n(x) + N_D - N_A + \rho_p - \rho_n \right] = 0 , \tag{1}$$

$$\frac{1}{q}\frac{dJ_P}{dx} = G_{op} - R(x) , \tag{2}$$

$$\frac{1}{q}\frac{\dot{d}J_n}{dx} = -G_{op} + R(x) . \tag{3}$$
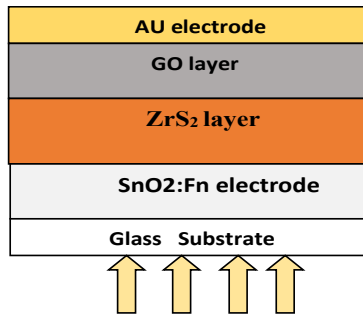
Figure 1. Schematic representation of the solar cell structure

Where ε is the dielectric constant, q is the electron charge, N_A and N_D are ionized acceptors and donor density, Ψ is the electrostatic potential, Jp is current density due to hole, Jn is current density due to electron, G_{op} is the carrier generation rate, R is the total recombination rate, p is free hole density, n is the free electron density, ρ_p, and ρ_n are the hole and electron distribution. The following drift-diffusion equations (2) and (3) represent the holes and electrons carrier transport properties of the semiconducting material. In this work, the SCAPS simulator has been used to study the dependence of parameters of solar cells on the operating temperature and the work function of back contact and energy gap of ZrS2. These parameters are power conversion efficiency (η), short circuit current density (J_{sc}), fill factor (FF) extracted by drawing the current density versus voltage of solar cells under different conditions. The proposed solar cell in the work is composed of zirconium disulfide (ZrS2) and Graphene oxide (Go) and front – contact (fluorine-doped tin dioxide, SnO2;Fn) and back-contact (Gold, Au). Figure 1 shows schematic diagrams of SnO2; Fn/ZrS2/Au solar cells.

From previous literatures (8-9, 14-18) Table 1 and 2 present the input parameters used in SCAPS simulators for studying the performance of solar cells.

Table 1. Parameters for ZrS2 and Go materials

Material properties	Zirconium disulfide (ZrS2)	Graphene Oxide (Go)
Thickness (μm)	1	0.200
Bandgap (eV)	Varying (1.2 to 1.7)	3.25
Electron affinity(eV)	4.7	1.9
Dielectric permittivity(relative)	16.4	3
CB effective density of states (1/cm^3)	2.2E+19	2.2E+21
VB effective density of states (1/cm^3)	1.8E+19	1.8E+21
Electron mobility (cm^3/Vs)	300	100
Hole mobility (cm^3/Vs)	30	300
Shallow uniform donor density ND (1/cm^3)	1.000E+19	0
Shallow uniform acceptor density ND (1/cm^3)	0	1 E+16

Table 2. Parameters of back and front contacts

Parameters	Back- contact Au	Front- contact SnO2;Fn
Surface recombination velocity of electrons	1.00E+5	1.00E+5
Surface recombination velocity of holes	1.00E+7	1.00E+7
Metal work function(ev)	5.1	4.4

2. RESULTS AND DISCUSSION
2.1. The parameters of SnO2:Fn/ZrS2/Gu/Au solar cells under illumination

Figure 2 shows the Current-Voltage (J–V) characteristics of SnO2:Fn/ZrS2/GO/AU solar cells using SCAPS simulations under the standard simulated solar light of AM 1.5G (100 mW/cm^{-2}) at room temperature. As seen, the device produces a high short-circuit current density of 38 mA/cm^2, open circuit voltage of 0.6 V and a Fill factor of 80 %. This structure shows better performance with high power conversion efficacy of 17 % compared with other solar cells based on graphene oxide and perovskite materials [19]. These results were obtained when the energy gap of ZrS2 and Go were 1.2 eV and 3.25 eV.
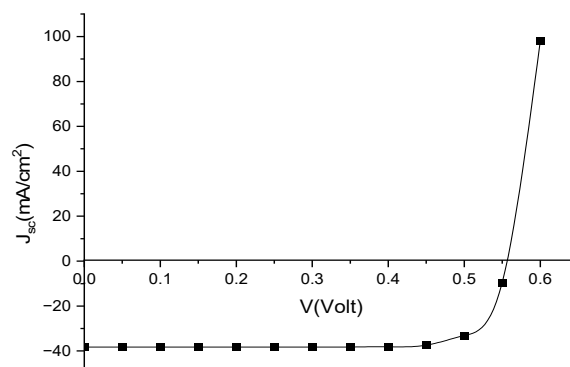
Figure 2. J -V characteristics of SnO2:Fn/ZrS2 /GO/ Au solar cells under illumination

2.2. Effect of energy gap of SZr₂ layer on parameters of SnO₂: Fn /ZrS₂/Go/Au solar cells
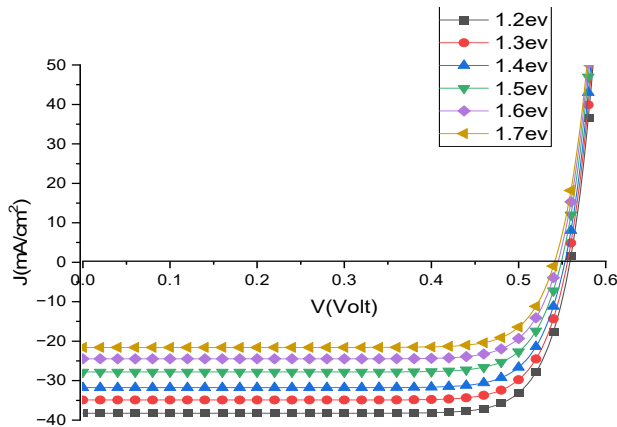
Figure 3. J-V characteristics of SnO₂:Fn/ZrS₂/Go/Au solar cells as function of energy gap of SZr₂ layer

Figure 3 show that the short circuit current density (J_{sc}) and open circuit voltage (V_{oc}) decreases from 38 mA/cm² to 22 mA/cm² and 5.5 V to 5.4 V as the energy gap of SZr₂ change from 1.2 eV to 1.7 eV receptively. The behavior of power conversion efficiency (η) is similar to that of J_{sc}, with a general decreasing from 17% to 9% when the energy gap of ZrS₂ increase from 1.2 eV to 1.7 eV. That is attributed to many reasons such as 1) the absorbed photons may have less energy to create electron-hole pairs, potentially leading to a lower voltage output, 2) limit the number of electron-hole pairs that can be generated by absorbing photons which causes to decrease in the current output of the solar cell [8]. On the other hand, V_{oc} (open-circuit voltage) decrease from 0.55 V to 0.54 V while FF (fill factor) values of simulated devices remain almost constant with the increase of bandgap of the ZrS₂ layer.

2.3. Effect of operation temperature on parameters of SnO₂: Fn /ZrS₂/G₀/Au solar cells

As known, the ambient temperature plays an important role in the operation of solar cells because solar cells are more commonly used outdoors due to their reliance on sunlight. Here the effect of temperature on the parameters of solar cells has been investigated under light conditions presented.
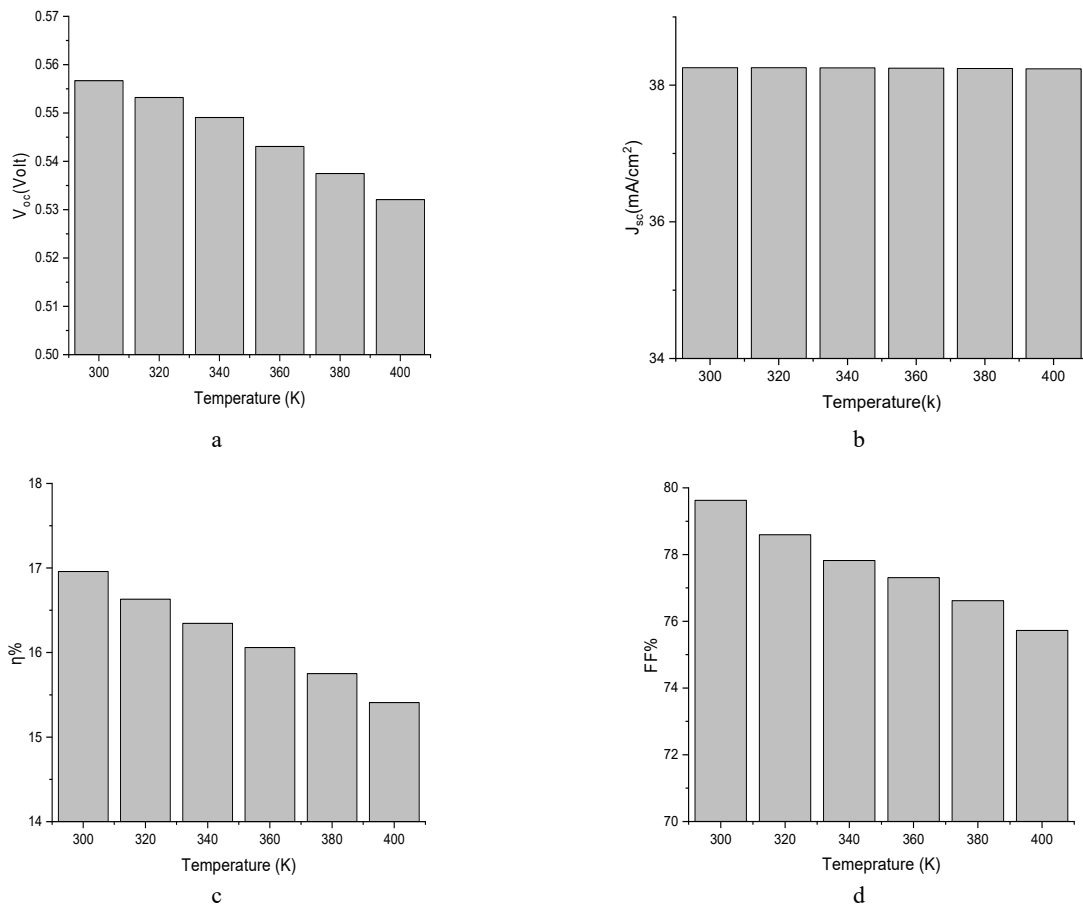
Figure 4. Variation of solar cells parameters (Voc, Jsc, η and FF) with change in temperature

Figure 4 shows the variation of open circuit voltage (V_{oc}), short circuit current density (J_{sc}), Fill factor (FF%), and power conversion efficiency (η%) with changing temperature from 300k to 400k. As seen the parameters of SnO₂:Fn/ZrS₂/GO/AU solar cells decline steadily as the temperature increase. When the temperature of solar cells increases, more electron-hole pairs are generated due to the increased thermal energy and lead to an increase in the reverse saturation current density (J_o). This additional carrier generation can lower the voltage across the solar cell, causing a decrease in the open circuit voltage (see Figure 4a). That agrees with the Shockley diode equation which presents an

inverse relationship between the reverse saturation current density (J_o) and the open circuit voltage (V_{oc}) in solar cells [16,20]

$$V_{oc} = \frac{nK_B T}{q}\left[\ln(1+\frac{J_{sc}}{J_o}\right]. \tag{4}$$

Where V_{oc} is the open circuit voltage, A is the ideal factor, q is the elementary charge, K_B is the Boltzmann constant, Jo is the reverse current.

At higher temperatures, there can be changes in the characteristics of the materials used and reduce the efficiency and fill factor of solar cells (see Figure 4-c and 4-d). This degradation is due to changes in the physical and chemical properties of the semiconductor materials used in solar cells [16, 21]. High temperature breaks some of the bonds between the atoms or molecules in the solar cell. That cause to decrease the energy gap of materials, change in the mobility and concentrations of charge carriers. For example, the energy gap of the semiconductor becomes narrow at a high temperature which may lead to an increase in the recombination of electrons and holes while travelling across the region decrease of efficiency output power of the device and Fill factor [20]. Finally, there was a slight decrease in short circuit current density since the charges separation processing at the interface was also reduced (see Figure 4 b).

2.4 Effect of back-contact work function

In solar cells, the alignment of energy levels in materials used for solar cells is a crucial aspect of achieving efficient charge transfer and minimizing energy losses. This can involve selecting appropriate materials with suitable energy levels, modifying the device architecture, or using interfacial layers to adjust the energy level alignment [22]. Figure 5 shows parameters of SnO_2:Fn/ZrS_2 /Go/ AU solar cells versus different back- contact work function.
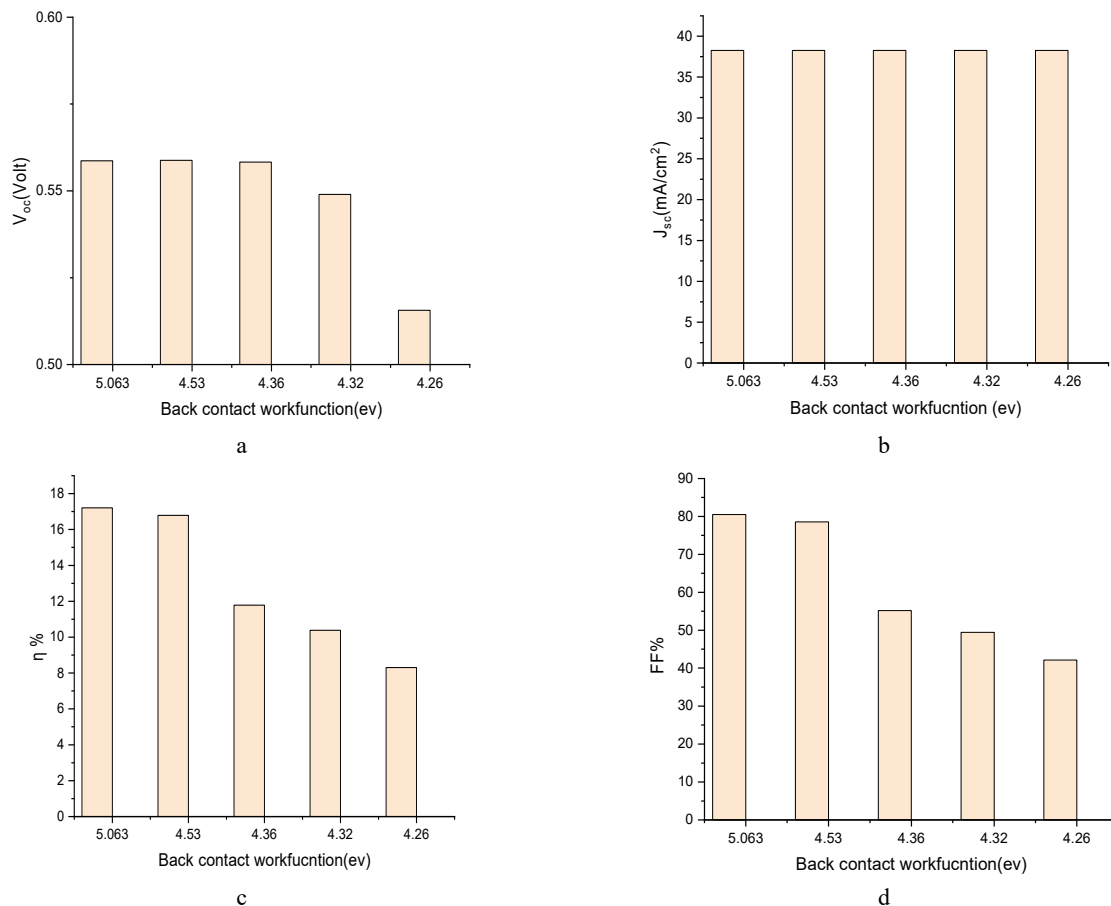
Figure 5. Photovoltaic performance parameters at various Back-contact work function (eV) as:
(a) Voc, (b) Jsc, (c) η, and (d) FF

They are made of (nickel (Ni), φ=5.03 eV, silver (Ag, φ=4.26 eV), copper (Cu, φ=4.53 eV), molybdenum (Mo, φ=4.36 eV) and tungsten (W, φ=4.32 eV). The low efficiency in Ag, Mo electrode, and Mo solar cells is attributed to the presence of a Schottky barrier at the interface between graphene oxide) and the Ag/Mo electrodes. This barrier arises from the difference in work function between these materials. That cause to hinders the movement of hole charge carriers at the interface leading to a reduction in the open-circuit voltage and fill factor. On the other hand, Ni and Cu electrode

solar cells produced the high-efficiency and open circuit voltage and fill factor because of a small energy difference between the LUMO of Go and the work function of the electrodes. That facilitates efficient charge transfer by achieving an ohmic contact and improving the overall performance of the solar cell.

3. CONCLUSION

The Go/ZrS$_2$ solar cells exhibit high performance compared to other solar cells based on graphene oxide and perovskite materials. The Go/ZrS$_2$ solar cells achieve a high short circuit current (Jsc) of 38 mA/cm², and a power conversion efficiency (η) of 17%. This indicates that they have ability to generate a significant amount of current and convert a considerable portion of sunlight into electricity. However, the study also highlights that certain factors negatively affect the performance of the solar cells. An increase in operating temperature and energy bandgap of ZrS$_2$, as well as changes in the work function of the back contact material, lead to a reduction in parameters of solar cells. These effects are attributed to changes in the electrical properties of the Go and ZrS$_2$ layers such as charge carriers mobility and interfacial layer properties.

ORCID
Hmoud Al-Dmour, https://orcid.org/0000-0001-5680-5703

REFERENCES
[1] P. Omar, A. Khellaf, and K. Mohammedi, Renew Sust. Energy Rev. **23**, 12 (2013). https://doi.org/10.1016/j.rser.2013.02.017
[2] X. He, S. Khan, I. Oztyrk, and M. Murshed, Sustain. Dev. **31**, 1888 (2023). https://doi.org/10.1002/sd.2491
[3] A. Reinders, and P. Verlinden, *Photovoltaic Solar Energy: From Fundamentals to Applications*, (Wiley Publishing, USA, 1988).
[4] A. Polman, M. Knight, E. Garnett, B. Ehrler, and W. Sinke, J. Sci. **352**, 6283 (2020). https://doi.org/10.1126/science.aad4424
[5] P. Liu, C. Xiao, C. Xie, and W. Li, Nano Energy, **89**, 106399 (2021). https://doi.org/10.1016/j.nanoen.2021.106399
[6] H. Al-Dmour, D.M. Taylor, and J.A. Cambridge, J. Phys. D, Appl. Phys. **40**, 5034 (2007). https://doi.org/10.1088/0022-3727/40/17/004
[7] P. Sumesh, Sol. Energy Mater Sol. Cells, **192**, 16 (2019). https://doi.org/10.1016/j.solmat.2018.12.016
[8] M. Abdelfatah, A. El-Sayed, W. Isamil, V. Sittinger, and A. El-Shaer, Sci. Rep. **13**, 4553 (2023). https://doi.org/10.1038/s41598-023-31553-4
[9] Y. Park, K.S. Choi, and S.Y. Kim, Phys. Status Solidi, **209**, 1363 (2012). https://doi.org/10.1002/pssa.201228040
[10] M. Burgelman, P. Nollet, and S. Degrave, Thin Solid Films, **361-362,** 527 (2000). https://doi.org/10.1016/S0040-6090(99)00825-1
[11] H. Zerfaoui, D. Dib, M. Rahmani, K. Benyelloul, and C. Mebarkia, AIP Conference Proceedings, **1758**, 030029 (2016). https://doi.org/10.1063/1.4959425
[12] H. Al Dmour, East Eur. J. Phys, (3), 555-561 (2023). https://doi.org/10.26565/2312-4334-2023-3-65
[13] F.X. Abomo Abega, A.T. Ngoupo, and J.M. Ndjaka, Int. J. Photoenergy, **21**, 7506837 (2021). https://doi.org/10.1155/2021/7506837
[14] N. Touafek, R. Mahamdi, and C. Dridi, Dig. J. Nanomater. Bios. **16**, 705 (2021). https://chalcogen.ro/705_TouafekN.pdf
[15] N.S. Noorasid, F. Arith, A.Y. Firhat, A.N. Mustafa, and A.S.M. Shah, Eng. J. **26**, 1-12 (2022). https://doi.org/10.4186/ej.2022.26.2.1
[16] D.W. Husainat, P. Ali, J. Cofie, J. Attia, A. Fuller, Darwish, AJOP, **8**(1), 6 (2020). https://doi.org/10.11648/j.ajop.20200801.12
[17] J.W. Lee, "Isothermal Electricity for Energy Renewal. PCT," International Patent Application Publication Number WO 2019/136037 A1, (11 July 2019).
[18] H. Al Dmour, R. Alzard, H. Alblooshi, K. Alhosanim, S. Al-Madoob, and N. Saleh, Front. Chem. **7**, 1 (2019). https://doi.org/10.3389/fchem.2019.00561
[19] K. Gong, J. Hu, N. Cui, Y. Xue, L. Li, G. Long, and S. Lin, Mater. Des. **211**, 110170 (2021). https://doi.org/10.1016/j.matdes.2021.110170
[20] H. Al-Dmour, S. Al-Trawneh, S. Al-Taweel, Int. J. Adv. Appl. Sci. **8**, 128 (2021). https://doi.org/10.21833/ijaas.2021.06.015
[21] J. Xi, L. Zheng, S. Wang, J. Yang, and W. Zhang, J. Comput. Chem. **42**, 2213 (2021). https://doi.org/10.1002/jcc.26750
[22] P. Sawicka-Chudy, Z. Starowicz, G. Wisz, R. Yavorskyi, Z. Zapukhlyak, M. Bester, and Ł. Głowa, Mater. Res. Express, **6**, 085918 (2019). https://doi.org/10.1088/2053-1591/ab22aa

ЧИСЛОВИЙ SCAPS АНАЛІЗ СОНЯЧНИХ ЕЛЕМЕНТІВ НА ОКСИДІ ГРАФЕНУ/ДИСУЛЬФІДУ ЦИРКОНІЮ
Хмуд Аль-Дмур
Університет Мута, факультет природничих наук, кафедра фізики, 61710, Йорданія

Ця робота вивчає продуктивність сонячних елементів, що складаються з двох різних матеріалів, оксиду графену (Go, матеріал для транспортування дірок) і дисульфіду цирконію (ZrS$_2$, матеріали для транспортування електронів) за допомогою моделювання SCAPS-1D. Було виявлено, що сонячні батареї Go/ ZrS$_2$ демонструють кращу продуктивність із високим струмом короткого замикання Jsc 38 мА/см² і ефективністю перетворення потужності η 17% порівняно з іншими сонячними елементами на основі оксиду графену та перовскітних матеріалів. Крім того, щільність струму короткого замикання зменшується з 38 мА/см² до 22 мА/см², коли енергетичний зазор ZrS$_2$ збільшується з 1,2 еВ до 17 еВ. Підвищення робочої температури та робочої функції зворотного контакту також призвело до зниження напруги холостого ходу та ефективності перетворення потужності елементів, у той час як щільність струму короткого замикання дещо збільшилася. Це пояснюється зміною електричних властивостей шарів Go і ZrS$_2$, включаючи їх рухливість носіїв заряду та характеристики міжфазних шарів.
Ключові слова: *моделювання SCAPS-1D; сонячні елементи; робота виходу; міжфазні шари; робоча температура*

MULTIBAND ASYMMETRIC BICONICAL DIPOLE ANTENNA WITH DISTRIBUTED SURFACE IMPEDANCE AND ARBITRARY EXCITATION

Mikhail V. Nesterenko*, Victor A. Katrich, Svetlana V. Pshenichnaya

V.N. Karazin Kharkiv National University, 4, Svobody Sq., Kharkiv, Ukraine, 61022
*Corresponding Author: mikhail.v.nesterenko@gmail.com

A numerical-analytical solution of a problem concerning the current distribution and input characteristics of asymmetric biconical dipole with distributed surface impedance and arbitrary excitation and derived in the thin-wire approximation. Solution correctness is confirmed by satisfactory agreement of numerical and experimental results from literary sources. Numerical results are given for the input characteristics of the dipole in the case of its asymmetric excitation by a point source.

Keywords: *Biconical dipole; Distributed surface impedance; Asymmetric excitation; Current distribution; Input characteristics*
PACS: 02.70.Pt; 78.70Gq; 84.40.-x

INTRODUCTION

Among modern communication systems (both mobile and stationary), the leading place is occupied by multi-frequency (multi-channel) structures. The main functional element of such devices are antennas, which differ from each other in their design features, for example, they can be single-element structures (mono-frequency) or multi-element (multi-frequency) structures [1]. At the same time, the operation of a multi-frequency antenna, implemented by expanding the operating band (broadband antenna), in turn, can lead to a significant weakening of its noise-immune properties. Typically, designers take the path of combining several antennas operating at different frequencies into one structure [2-8]. This approach significantly complicates the design of the antenna device and is a difficult factor to overcome on the path to its miniaturization.

In recent decades, a large number of publications have appeared devoted to multi-band printed antennas directly integrated into communication devices, for example [9-19] and references therein. In this case, the electrodynamic characteristics of the antennas are obtained using commercial programs such as ANSYS HFSS, Feko and others. However, in this case, the calculation and further optimization of antennas in order to achieve the specified characteristics lead to a sequential search of a large number of options and, consequently, large amounts of computer resources and computational time.

The use of dipoles with an asymmetric excitation point, i.e. with an arbitrary position along their length, for creating multi-band antennas has been repeatedly proposed by researchers in various publications [5, 7, 20-22]. However, in these literary sources only perfectly conducting dipoles were considered. Another solution is to use a dipole antenna with asymmetric excitation and distributed surface impedance, directly integrated into the body of the communication device [23, 24]. In this case, the frequency response of the antenna may have several resonances that prevent the radiation (receiving) of electromagnetic waves outside the resonant frequency bands.

On the other hand, one of the additional parameters for obtaining the specified electrodynamic characteristics of antennas in the form of a cylindrical dipole can be a change in the radius of the cross section of the dipole along its length. In the case of a linear increase in the radius of the vibrator from the excitation point of the antenna to its ends (biconical dipole), this antenna resonates at a smaller geometric length, and is also more broadband compared to a dipole of constant radius (see, for example, [25–30] and references in them). However, all of them are devoted to calculating the electrodynamic characteristics of perfectly conducting dipoles excited at the geometric center by a concentrated electromotive force (EMF). Also, as is known, to analyze receiving antennas it is necessary to know the current in the scattering dipole excited by the incident electromagnetic wave [31].

The purpose of this paper is to study a multiband antenna for communication systems based on an asymmetric biconical dipole with a distributed surface impedance and arbitrary excitation. Thus, we will combine in one design all the advantages of asymmetric excitation, biconical geometry and the presence of a distributed surface impedance. The antenna can operate in several frequency bands. The antenna characteristics will be modeled by using a numerical-analytical method, known as the generalized method of induced EMF, proposed by the authors earlier in [23, 24].

PROBLEM FORMULATION AND SOLUTION OF THE INITIAL INTEGRAL EQUATION

Let us limit ourselves by the linear law of the radius change along the dipole (Fig. 1), which, in its turn, is rather good approximation and for another dependences $r(s)$, for example, exponential one, at small angles ψ. Let the dipole with distributed internal linear impedance z_i of the $2L$ length and the $r(s)$ variable radius, located in free space, be

excited by the electrical field $E_{0s}(s)$ of the impressed sources (tangential component). The monochromatic fields and currents depend on time t as $e^{i\omega t}$ ($\omega = 2\pi f$ is the circular frequency, f is the frequency, measured in Hz). At this the dipole stays electrically thin ($kr(s) \ll 1$, $r(s) \ll 2L$, $k = 2\pi/\lambda$, λ is the wavelength in free space). Then the integral-differential equation relatively to the $J(s)$ current for the impedance boundary condition on the dipole surface [31]:

$$\left(\frac{\mathrm{d}^2}{\mathrm{d}s^2} + k^2\right) \int_{-L}^{L} J(s') \frac{e^{-ik\tilde{R}(s,s')}}{\tilde{R}(s,s')} \mathrm{d}s' = -\frac{i\omega}{\cos\psi}\left[E_{0s}(s) - z_i J(s)\right] . \tag{1}$$

Here $\tilde{R}(s,s') = \sqrt{(s-s')^2 + r^2(s)}$, $\psi = (\psi_1 + \psi_2)/2$. Note that at $r(s) = const = r_0$, equation (1) transforms into an equation for the current in an impedance dipole of constant radius with a quasi-one-dimensional core $\tilde{R}(s,s') = R(s,s') = \sqrt{(s-s')^2 + r_0^2}$.
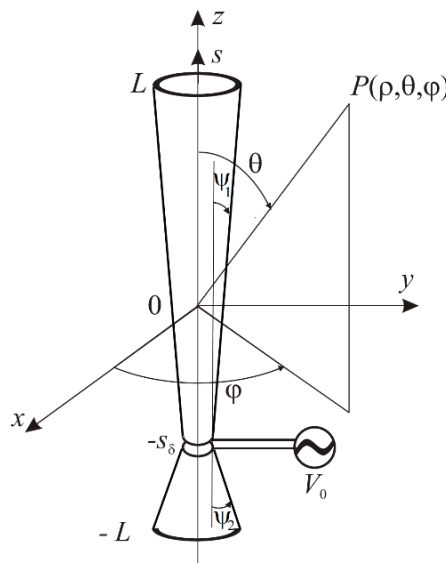
Figure 1. The dipole geometry and accepted designations

The excitation fields of extraneous sources E_{0s} can be divided into symmetric and antisymmetric components relative to the dipole geometrical center. These components marked by the indices "s" and "a" are presented as $E_{0s}(s) = E_{0s}^s(s) + E_{0s}^a(s)$. Quite naturally, the dipole currents can also have also two components $J(s) = J^s(s) + J^a(s)$. The initial equation (1) relative the dipole current obtained by using the boundary conditions $J^{s,a}(\pm L) = 0$ has the following form

$$\left(\frac{\mathrm{d}^2}{\mathrm{d}s^2} + k^2\right) \int_{-L}^{L} [J^s(s') + J^a(s')] \frac{e^{-ik\tilde{R}(s,s')}}{\tilde{R}(s,s')} \mathrm{d}s' = -\frac{i\omega}{\cos\psi}[E_{0s}^s(s) + E_{0s}^a(s)] + \frac{i\omega}{\cos\psi} z_i [J^s(s') + J^a(s')], \tag{2}$$

where $E_{0s}^{s,a}(s)$ are the projections of extraneous source fields on the dipole axis, s and s' are the local coordinates related to the dipole axis and surface.

The equation (2) can be represented by the system of two independent integral equations, relative to the unknown currents $J^s(s)$ and $J^a(s)$

$$\left(\frac{\mathrm{d}^2}{\mathrm{d}s^2} + k^2\right) \int_{-L}^{L} J^s(s') \frac{e^{-ik\tilde{R}(s,s')}}{\tilde{R}(s,s')} \mathrm{d}s' = -\frac{i\omega}{\cos\psi}[E_{0s}^s(s) + z_i J^s(s)],$$

$$\left(\frac{\mathrm{d}^2}{\mathrm{d}s^2} + k^2\right) \int_{-L}^{L} J^a(s') \frac{e^{-ik\tilde{R}(s,s')}}{\tilde{R}(s,s')} \mathrm{d}s' = -\frac{i\omega}{\cos\psi}[E_{0s}^a(s) + z_i J^a(s)]. \tag{3}$$

The dipole currents can be presented as product of the unknown complex amplitudes $J_n^{s,a}$ and weight functions $f_n^{s,a}(s')$ ($n = 0, 1$) as

$$J^{s,a}(s') = J_0^{s,a} f_0^{s,a}(s') + J_1^{s,a} f_1^{s,a}(s'), \quad f_n^{s,a}(\pm L) = 0 . \tag{4}$$

The solution of the equations system (3) can be obtained by the generalized method of induced EMF [23, 24]. To do so, let us multiply the left- and right- hand parts of the equations (8) by the functions $f_n^s(s)$ and $f_n^a(s)$, and integrate the resulting expressions over the vibrator length. Thus, the following algebraic equations system (SLAE) is obtained

$$\begin{cases} J_0^s Z_{00}^{s\Sigma} + J_1^s Z_{01}^{s\Sigma} = -i\omega/(2k\cos\psi)E_0^s, \\ J_0^s Z_{10}^{s\Sigma} + J_1^s Z_{11}^{s\Sigma} = -i\omega/(2k\cos\psi)E_1^s, \\ J_0^a Z_{00}^{a\Sigma} + J_1^a Z_{01}^{a\Sigma} = -i\omega/(2k\cos\psi)E_0^a, \\ J_0^a Z_{10}^{a\Sigma} + J_1^a Z_{11}^{a\Sigma} = -i\omega/(2k\cos\psi)E_1^a, \end{cases} \tag{5}$$

where ($m = 0,1; n = 0,1$),

$$Z_{mn}^{s,a} = \frac{1}{2k}\left\{ -\frac{df_m^{s,a}(s)}{ds} A_n^{s,a}(s)\Big|_{-L}^{L} + \int_{-L}^{L}\left[\frac{d^2 f_m^{s,a}(s)}{ds^2} + k^2 f_m^{s,a}(s)\right] A_n^{s,a}(s)ds \right\}, \tag{6a}$$

$$\tilde{Z}_{mn}^{s,a} = -\frac{i\omega}{2k}\int_{-L}^{L} f_m^{s,a}(s)f_n^{s,a}(s)z_i\,ds, \quad Z_{mn}^{(s,a)\Sigma} = Z_{mn}^{s,a} + \tilde{Z}_{mn}^{s,a}, \tag{6b}$$

$$A_n^{s,a}(s) = \int_{-L}^{L} f_n^{s,a}(s')\frac{e^{-ik\tilde{R}(s,s')}}{\tilde{R}(s,s')}ds', E_m^{s,a} = \int_{-L}^{L} f_m^{s,a}(s)E_{0s}^{s,a}(s)ds. \tag{6c}$$

Then the dipole current can be written as $J(s) = J^s(s) + J^a(s),$ where

$$J^{s,a}(s) = -\frac{i\omega}{2k\cos\psi}\left[\frac{E_0^{s,a}Z_{11}^{(s,a)\Sigma} - E_1^{s,a}Z_{01}^{(s,a)\Sigma}}{Z_{00}^{(s,a)\Sigma}Z_{11}^{(s,a)\Sigma} - Z_{10}^{(s,a)\Sigma}Z_{01}^{(s,a)\Sigma}} f_0^{s,a}(s) + \frac{E_1^{s,a}Z_{00}^{(s,a)\Sigma} - E_0^{s,a}Z_{10}^{(s,a)\Sigma}}{Z_{00}^{(s,a)\Sigma}Z_{11}^{(s,a)\Sigma} - Z_{10}^{(s,a)\Sigma}Z_{01}^{(s,a)\Sigma}} f_1^{s,a}(s)\right]. \tag{7}$$

Note that the approximate numerical-analytical solution (7) of the integral equation (1) is valid for any excitation field $E_{0s}^{s,a}(s)$ of the dipole (δ-generator, plane wave incidence at an angle to the longitudinal axis of the dipole, etc.), as well as for the complex distributed impedance of the dipole.

DIPOLE EXCITED IN AN ARBITRARY POINT

Let the dipole be excited in the point $s = -s_\delta$ by the voltage δ-generator with amplitude V_0, as shown in Fig. 1. Then

$$\begin{aligned} E_{0s}(s) &= V_0\delta(s + s_\delta) = E_{0s}^s(s) + E_{0s}^a(s), \\ E_{0s}^{s(a)}(s) &= (V_0/2)\big[\delta(s + s_\delta) + (-)\delta(s - s_\delta)\big], \end{aligned} \tag{8}$$

where δ is the Dirac delta function. In this case, the dipole current defined by (7) can be written as $J(s) = J^s(s) + J^a(s)$,

$$J^{s,a}(s) = -\frac{i\omega}{2k\cos\psi}V_0\left[\frac{\tilde{E}_0^{s,a}Z_{11}^{(s,a)\Sigma} - \tilde{E}_1^{s,a}Z_{01}^{(s,a)\Sigma}}{Z_{00}^{(s,a)\Sigma}Z_{11}^{(s,a)\Sigma} - Z_{10}^{(s,a)\Sigma}Z_{01}^{(s,a)\Sigma}} f_0^{s,a}(s) + \frac{\tilde{E}_1^{s,a}Z_{00}^{(s,a)\Sigma} - \tilde{E}_0^{s,a}Z_{10}^{(s,a)\Sigma}}{Z_{00}^{(s,a)\Sigma}Z_{11}^{(s,a)\Sigma} - Z_{10}^{(s,a)\Sigma}Z_{01}^{(s,a)\Sigma}} f_1^{s,a}(s)\right], \tag{9}$$

where r_δ and r_L are the radiuses of the dipole in point $s = -s_\delta$ and on its end.

Let us choose the functions $f_0^{s,a}(s)$ obtained after substituting the expressions (8) into the general solution of the equation for the current by the averaging method [23] in the form:

$$\begin{aligned} f_0^s(s) &= \cos\tilde{k}s_\delta\sin\tilde{k}L\cos\tilde{k}s - (1/2)\cos\tilde{k}L(\sin\tilde{k}|s - s_\delta| + \sin\tilde{k}|s + s_\delta|), \\ f_0^a(s) &= \sin\tilde{k}s_\delta\cos\tilde{k}L\sin\tilde{k}s + (1/2)\sin\tilde{k}L(\sin\tilde{k}|s - s_\delta| - \sin\tilde{k}|s + s_\delta|), \end{aligned} \tag{10}$$

where $\tilde{k} = k - \dfrac{i\bar{Z}_S[3/2 - r_\delta/(2r_L)]}{2r_L\cos\psi\ln(2L/r_L)}$, $\bar{Z}_S = \bar{R}_S + i\bar{X}_S = \dfrac{2\pi r_L z_i}{Z_0}$ is the distributed surface impedance, normalized on the free space wave impedance, $Z_0 = 120\pi$ Ohm. The current distribution function $f_1^s(s)$ is defined in [32], and the function $f_1^a(s)$ can be found as solution of the integral equation (1), obtained for the case $z_i = 0$ and $\psi = 0$ [20]. These functions can be written as:

$$f_1^s(s) = \cos \tilde{k}s - \cos \tilde{k}L , \tag{11a}$$

$$f_1^a(s) = \sin ks - (s / L)\sin kL . \tag{11b}$$

The coefficients $Z_{mn}^{s,a}$ ($m = 0,1; n = 0,1$) in the formulas (9) can be obtained from formulas (6) and $\tilde{E}_0^s = \cos \tilde{k}s_\delta \sin \tilde{k}(L-|s_\delta|)$, $\tilde{E}_1^s = \cos \tilde{k}s_\delta - \cos \tilde{k}L$, $\tilde{E}_0^a = -\sin \tilde{k}|s_\delta|\sin \tilde{k}(L-|s_\delta|)$, $\tilde{E}_1^a = \sin ks_\delta - (s_\delta/L)\sin kL$.

The input impedance $Z_{in} = R_{in} + iX_{in}$ can be presented as:

$$Z_{in}[\text{Ohm}] = \frac{60i}{J_0^s f_0^s(s_\delta) + J_1^s f_1^s(s_\delta) + J_0^a f_0^a(s_\delta) + J_1^a f_1^a(s_\delta)} , \tag{12}$$

Then, the voltage standing wave ratio (VSWR) in the antenna feeder with the wave impedance W is equal to:

$$\text{VSWR} = (1+|S_{11}|)/(1-|S_{11}|) , \tag{13}$$

where $S_{11} = (Z_{in} - \text{W})/(Z_{in} + \text{W})$ is the reflection coefficient in the feeder.

NUMERICAL RESULTS

As an example, let us present the input characteristics (modulus of the reflection coefficient $|S_{11}|$ in the supply feeder line with wave resistance W =50 Ohm) of an asymmetric biconical ideally conducting dipole with dimensions $2L$ =138 mm, r_δ =1 mm, r_L =3 mm (Fig. 2). This choice of the dipole length is due to the condition of the first resonance at the frequency f =0.9 GHz (GSM 900 (880÷960 MHz)). Note that for a regular dipole with a radius r =2 mm, its length would be equal to $2L$ =156 mm. As can be seen from the graphs, an asymmetric biconical dipole (with smaller geometric length than a regular dipole) is also resonant at two or more frequencies. Moreover, this tendency will increase with increasing the angle ψ . Also, if the dipole has a distributed surface impedance of the inductive type, then its resonant length will be even less [24].
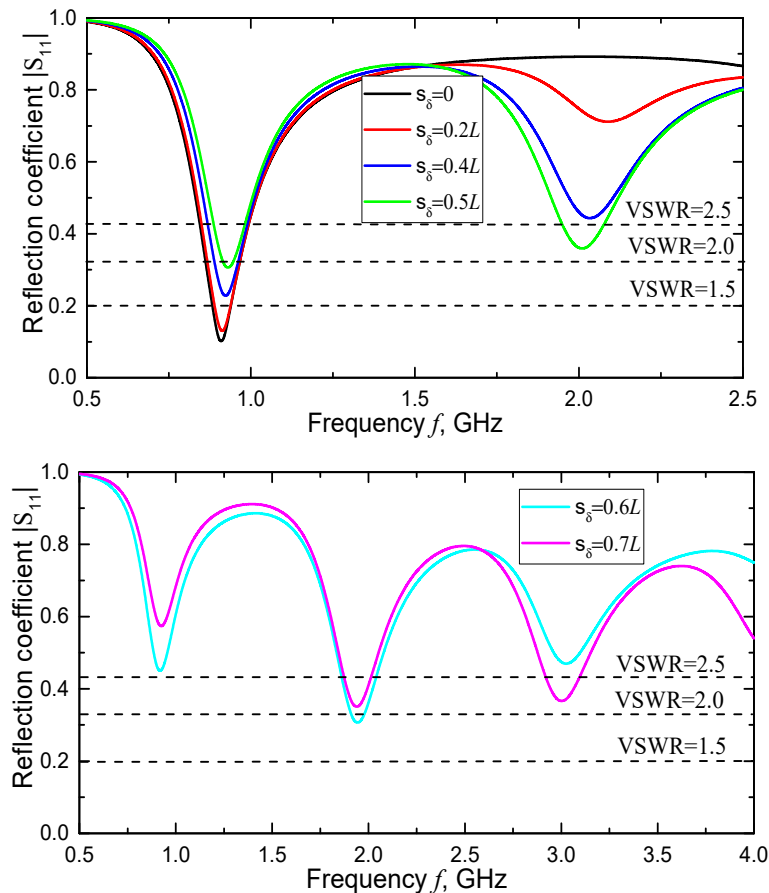
Figure 2. The dependences of the modulus of the reflection coefficient in the supply feeder line versus frequency for different positions of the excitation point s_δ at $2L$ =138 mm, r_δ =1 mm, r_L =3 mm

CONCLUSION

A numerical-analytical solution of a problem concerning a current distribution and input characteristics of the asymmetric biconical dipole with distributed surface impedance and arbitrary excitation derived in the thin-wire approximation. The solution was carried out by the generalized method of induced EMF. The term numerical implies the numerical calculation of some integral terms. Otherwise, approximate analytical expressions are obtained. Solution correctness is confirmed by satisfactory agreement of numerical and original experimental results and well-known literary sources. The characteristic property of the antenna is the possibility of resonant tuning to the selected frequencies (depending on the geometric and electro-physical parameters of the dipole), which does not decrease the noise-resistant properties as compared with broadband antennas. Numerical results are given for the input characteristics of the dipole in the case of its asymmetric excitation by a point source. Analysis of electrodynamic characteristics of the proposed dipole antenna has proved the possibility of practical applications of this antenna for multiband portable radio stations, electronic gadgets and base stations and other antenna systems.

ORCID
Mikhail V. Nesterenko, https://orcid.org/0000-0002-1297-9119; **Victor A. Katrich**, https://orcid.org/0000-0001-5429-6124

REFERENCES
[1] Z. Zhang, *Antenna design for mobile devices*, (London, England: Wiley, 2017).
[2] G. Zhou, and B. Yildirim, "A multi-band fixed cellular phone antenna," in: Proc. IEEE AP-S Int. Symp. **1**, 112 (1999). https://doi.org/10.1109/APS.1999.789095
[3] N. Odachi, S. Sekine, H. Shoki, and Y. Suzuki, "A rod antenna with a meander element for hand-held phone," in: Proc. IEEE AP-S Int. Symp. **3**, 1682 (2000). https://doi.org/10.1109/APS.2000.874565
[4] H.-C. Tung, C.-Y. Fang, and K.-L. Wong, "Dual-band inverted-L monopole antenna for GSM/DCS mobile phone," in: Proc. IEEE AP-S Int. Symp. **3**, 30-33 (2002). https://doi.org/10.1109/APS.2002.1018149
[5] C. Song, Y. Huang, J. Zhou, P. Carter, S. Yuan, Q. Xu, and Z. Fei, "Matching network elimination in broadband rectennas for high-efficiency wireless power transfer and energy harvesting," IEEE Trans. Industrial Electronics, **64**, 3950-3961 (2017). https://doi.org/10.1109/TIE.2016.2645505
[6] K. Paramayudha, S. J. Chen, T. Kaufmann, W. Withayachumnankul, and C. Fumeaux, "Triple-band reconfigurable low-profile monopolar antenna with independent tenability," IEEE Open J. Antennas Propag. **1**, 47-56 (2020). https://doi.org/10.1109/OJAP.2020.2977662
[7] W. Hu, T. Feng, S. Gao, L. Wen, Q. Luo, P. Fei, Y. Liu, and X. Yang, "Wideband circularly polarized antenna using single-arm coupled asymmetric dipoles," IEEE Trans. Antennas Propag. **68**, 5104-5113 (2020). https://doi.org/10.1109/TAP.2020.2975275
[8] Y. Luo, and Y. Liu, "Nona-band antenna with small nonground portion for full-view display mobile phones," IEEE Trans. Antennas Propag. **68**, 7624-7629 (2020). https://doi.org/10.1109/TAP.2020.2989874
[9] S. Wang, and Z. Du, "A dual-antenna system for LTE/WWAN/WLAN/WiMAX smartphone applications," IEEE Antennas Wireless Propag. Lett. **14**, 1443-1446 (2015). https://doi.org/10.1109/LAWP.2015.2411253
[10] R. Tang, and Z. Du, "Wideband monopole without lumped elements for octa-band narrow-frame LTE smartphone," IEEE Antennas Wireless Propag. Lett. **16**, 720-723 (2017). https://doi.org/10.1109/LAWP.2016.2600761
[11] Y. Yang, Z. Zhao, W. Yang, Z. Nie, and Q.-H. Liu, "Compact multimode monopole antenna for metal-rimmed mobile phones," IEEE Trans. Antennas Propag. **65**, 2297-2304 (2017). https://doi.org/10.1109/TAP.2017.2679059
[12] Y. Liu, P. Liu, Z. Meng, L. Wang, and Y. Li, "A planar printed nona-band loop-monopole reconfigurable antenna for mobile handsets," IEEE Antennas Wireless Propag. Lett. **17**, 1575-1579 (2018). https://doi.org/10.1109/LAWP.2018.2856459
[13] D. Huang, Z. Du, and Y. Wang, "A quad-antenna system for 4G/5G/GPS metal frame mobile phones," IEEE Antennas Wireless Propag. Lett. **18**, 1586-1590 (2019). https://doi.org/10.1109/LAWP.2019.2924322
[14] Q. Tan, and F-C. Chen, "Triband circularly polarized antenna using a single patch," IEEE Antennas Wireless Propag. Lett. **19**, 2013-2017 (2020). https://doi.org/10.1109/LAWP.2020.3014961
[15] R.M. Moreno, J. Kurvinen, J. Ala-Laurinaho, A. Khripkov, J. Ilvonen, J. van Wonterghem, and V. Viikari, "Dual-polarized mm-wave endfire chain-slot antenna for mobile devices," IEEE Trans. Antennas Propag. **69**, 25-34 (2021). https://doi.org/10.1109/TAP.2020.3001434
[16] L. Chang, G. Zhang, and H. Wang, "Triple-band microstrip patch antenna and its four-antenna module based on half-mode patch for 5Gx4 MIMO operation," IEEE Trans. Antennas Propag. **70**, 67-74 (2022). https://doi.org/10.1109/TAP.2021.3090572
[17] C. Sahana, D. Nirmala, and M. Jayakumar, "Dual-band circularly polarized annular ring patch antenna for GPS-aided GEO-augmented navigation receivers," IEEE Antennas Wireless Propag. Lett. **21**, 1737-1741 (2022). https://doi.org/10.1109/LAWP.2022.3178980
[18] R. Lakshmanan, S. Mridula, A. Pradeep, and K. Neema, "Ultra compact flexible monopole antennas for tri-band applications," Prog. Electromagn. Res. C, **130**, 43-55 (2023). http://dx.doi.org/10.2528/PIERC22110906
[19] A. Khade, M. Trimukhe, S. Verblkar, and R.K. Gupta, "Miniaturization of printed rectangular monopole antenna by using slots for triple band applications," Prog. Electromagn. Res. C, **130**, 155-167 (2023). http://dx.doi.org/10.2528/PIERC22122401
[20] R.W.P. King, and T.T. Wu, "The cylindrical antenna with arbitrary driving point," IEEE Trans. Antennas Propag. **13**, 710-718 (1965). https://doi.org/10.1109/TAP.1965.1138531
[21] B.D. Popovic, "On polynomial approximation of current along thin asymmetrical cylindrical dipoles," IEEE Trans. Antennas Propag. **19**, 117-120 (1971). https://doi.org/10.1109/TAP.1971.1139879
[22] Y. Wang, S. Xu, and D.H. Werner, "1 bit dual-polarized reconfigurable transmitarray antenna using asymmetric dipole elements with parasitic bypass dipoles," IEEE Trans. Antennas Propag. **69**, 1188-1192 (2021). https://doi.org/10.1109/TAP.2020.3005713
[23] M.V. Nesterenko, V.A. Katrich, Y M. Penkin, V.M. Dakhov, and S.L. Berdnik, *Thin Impedance Vibrators. Theory and Applications*, (Springer Science+Business Media, New York, 2011).

[24] M.V. Nesterenko, V.A. Katrich, S.L. Berdnik, O.M. Dumin, and Y.O. Antonenko, "Asymmetric impedance vibrator for multi-band communication systems," Prog. Electromagn. Res. M, **102**, 81-89 (2021). http://dx.doi.org/10.2528/PIERM21031207

[25] S.A. Schelkunoff, "Theory of antennas of arbitrary size and shape," Proc. IRE, **29**, 493-521 (1941). https://doi.org/10.1109/JRPROC.1941.231669

[26] C.T. Tai, "On the theory of biconical antennas," Journal Applied Phys., **19**, 1155-1160 (1948). https://doi.org/10.1063/1.1715036

[27] T.T. Wu, and R.W.P. King, "The tapered antenna and its application to the junction problem for thin wires," IEEE Trans. Antennas Propag. **24**, 42-45 (1976). https://doi.org/10.1109/TAP.1976.1141274

[28] S.A. Saoudy, and M. Hamid, "Input admittance of a biconical antenna with wide feed gap," IEEE Trans. Antennas Propag. **38**, 1784-1790 (1990). https://doi.org/10.1109/8.102740

[29] S.S. Sandler, and R.W.P. King, "Compact conical antennas for wide-band coverage," IEEE Trans. Antennas Propag. **42**, 436-439 (1994). https://doi.org/10.1109/8.280735

[30] K.-L. Wong, and S.-L. Chien, "Wide-band cylindrical monopole antenna for mobile phone," IEEE Trans. Antennas Propag. **53**, 2756-2758 (2005). https://doi.org/10.1109/TAP.2005.851784

[31] M.V. Nesterenko, A.V. Gomozov, V.A. Katrich, S.L. Berdnik, and V.I. Kijko, "Scattering of electromagnetic waves by impedance biconical vibrators in a free space and in a rectangular waveguide," Prog. Electromagn. Res. C, **119**, 275-285 (2022). http://dx.doi.org/10.2528/PIERC22020304

[32] R.W.P. King, and G.S. Smith, *Antennas in Matter*, (MIT Press, Cambridge, USA, 1981).

БАГАТОСМУГОВА АСИМЕТРИЧНА БІКОНІЧНА ДИПОЛЬНА АНТЕНА З РОЗПОДІЛЕНИМ ПОВЕРХНЕВИМ ІМПЕДАНСОМ І ДОВІЛЬНИМ ЗБУДЖЕННЯМ

Михайло В. Нестеренко, Віктор А. Катрич, Світлана В. Пшеничная

Харківський національний університет імені В.Н. Каразіна, майдан Свободи, 4, Харків, Україна, 61022

Чисельно-аналітичний розв'язок задачі про струморозподілення та вхідні характеристики біконічного асиметричного диполя з розподіленим поверхневим імпедансом і довільним збудженням, отримані в наближенні тонкого дроту. Правильність рішення підтверджується задовільним узгодженням чисельних і експериментальних результатів з літературних джерел. Наведено численні результати для вхідних характеристик диполя при його асиметричному збудженні точковим джерелом. Аналіз електродинамічних характеристик запропонованої дипольної антени довів можливість практичного застосування цієї антени для багатодіапазонних портативних радіостанцій, електронних гаджетів і базових станцій.

Ключові слова: *біконічний диполь; розподілений поверхневий імпеданс; асиметричне збудження; розподіл струму; вхідні характеристики*

ANTENNA BASED ON COMPLICATED COPLANAR STRUCTURE

Sergey A. Pogarsky*, **Dmitry V. Mayboroda, Serhii M. Mykhaliuk**

V.N. Karazin Kharkiv National University, 4, Svobody Sq., Kharkiv, Ukraine, 61022

*Corresponding Author e-mail: spogarsky@gmail.com

This paper presents the results of a numerical study of a planar antenna with a complex form factor. The antenna is based on a combination of two resonators, a disc resonator and a ring resonator. The feeding of the ring resonator is performed using a coplanar structure: pointwise by galvanic contact between the central conductor of the coplanar line and the ring resonator and by distributed electromagnetic coupling of the ring resonator and the aperture of the outer conductor of the coplanar line. The antenna was placed over a metal plane whose geometric dimensions were significantly larger than those of the antenna to exclude the influence of edge diffraction effects. In numerical simulation a complex approach including the method of semi-open resonator and the finite element method (FEM) implemented within the commercial package HFFS was used. The dependences of spectral, energy and polarization characteristics on material constants and frequency parameter have been investigated. It was found that within the framework of single-parameter optimization it is impossible to simultaneously achieve a high level of all important parameters. The values of frequencies of spectral lines in the spectral characteristics of the antenna are found with a relative error not worse than 1200 Hz. Frequency ranges within which there is no degeneration of oscillation types are established. The distributions of surface currents on the metal elements of the antenna, allowing to determine the position of phase centers of excitation, are presented. It is shown that the proposed antenna can provide an acceptable level of matching both at fixed frequencies and in sufficiently wide local frequency bands, reaching 11% with respect to the center frequency of the sub-band. The boundary values of gain coefficients in frequency bands are established. The simulation results allow to predict effective radiation with formation of practically single-lobe radiation pattern and presence of elliptical polarization.

Keywords: *Ring resonator; Disc resonator; Coplanar line; Matching; Frequency characteristics; Energy characteristics*

PACS: 84.40.Ba; 84.40.Dc

Since the mid-50s of the last century, functional devices based on strip (microstrip) structures have occupied a dominant position in the creation of complex radio engineering systems, especially if one of the main conditions is the condition of miniaturization. Here we can point out numerous designs of filters, directional couplers, mixers, power dividers, antennas, and recently - frequency selective surfaces, etc. [1-7]. A special place among all these technical solutions is occupied by the structures having in their composition structures with axial symmetry - these are disc and ring microstrip elements. This is due to the presence of peculiarities of electrodynamic properties of such structures. The main of which are related to the presence in such structures of degenerate types of waves (or types of oscillations in those cases when we are talking about resonators based on them), the effect of coupling between these oscillations and the possibility of influencing the level of coupling, the possibility of removing degeneration, due to which there is a possibility of controlling the operating bandwidth and some others.

The first attempts of practical use of ring structures were made to measure the phase velocity and dispersion characteristics of microstrip lines (P. Troughton [8]). Later, axially symmetric structures found their application in the creation of various functional elements and devices. Such intensive use of these structures caused the necessity to create mathematical models to describe and predict these or those characteristics. To date, quite a large number of approaches, models for analyzing the parameters of axially symmetric structures are known. Most of these models are focused on finding only resonance frequencies of excited types of oscillations. Exhaustive information on the parameters of structures is provided by the so-called full-wave models. Such models are quite complex in themselves and encounter certain difficulties in their practical use. For express calculations simplified models are usually used, for example, using the method of circuits, allowing to calculate parameters of inhomogeneous circuits and circuits with local inhomogeneities [9]. In 1971, the so-called "magnetic wall model" for microstrip resonators based on axially symmetric structures was proposed (sometimes another name of this model is used - the model of a half-open resonator) [10]. The main idea of this method is that the boundary conditions are formulated in a special way: on the metallic surfaces of the structure it is a natural boundary condition (equality to zero of the tangential component of the electric field), and on the lateral cylindrical surfaces bounding the resonator it is a magnetic wall condition. This model has been subjected to numerous modifications using various approaches [11], which allowed us to significantly improve the accuracy of the calculations. At the same time, the semi-open resonator model does not give correct results for coupled modes and in cases with complex boundary conditions, for example, in the presence of slot inhomogeneities in a microstrip disc. The inclusion of feeding elements (sections of microstrip or coplanar lines, sections of coaxial) or auxiliary elements (short-circuits, stubs) in the design further complicates the problem of finding the eigen-resonant frequencies and other characteristics. For this reason, the best solution is to use an integrated approach based on a combination of a semi-open resonator model and some numerical method such as the finite element method (FEM).

The aim of this work is to simulate the electrodynamic characteristics of a hybrid metal-dielectric plane structure based on a coplanar line and placed over a metallic surface.

STRUCTURE UNDER STUDY

We will consider a hybrid microstrip structure (Fig.1), which is a coupled ring and disc microstrip resonators feeding by a coplanar structure and placed above a metallic plane.
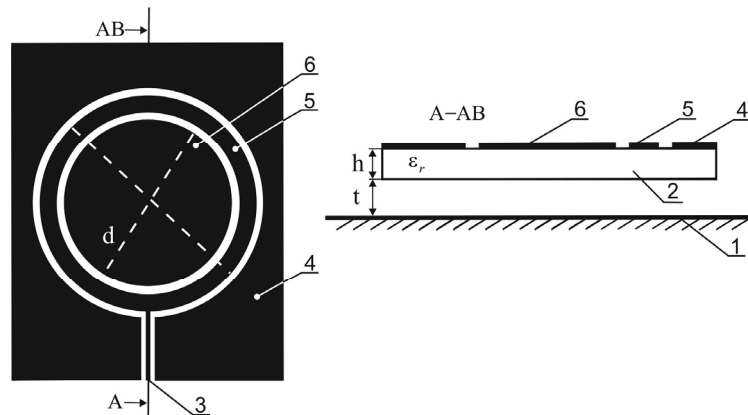
Figure 1. The structure geometry and notations

The ring and disc resonators are formed by metallized patches, respectively, and an external metallic plane. The introduction of the metallic plane is due to giving the model more generality and simulation of the antenna location in real conditions. The figure denotes are: 1 - external metal plane, 2 - dielectric substrate, 3 - inner conductor of coplanar structure, 4 - outer conductor of coplanar structure, 5 - ring patch, 6 - disc patch. There is an air gap between the dielectric substrate and the metal plane, which can be filled with additional dielectric. The simulation assumed a variation of the values of the relative dielectric permittivity of the substrate. In the limiting case the value is of $\varepsilon_r = 1$.

The geometrical dimensions of the structure were chosen based on the assumption that this structure is designed for operation in the centimeter wavelength range. The outer metallized plane had finite dimensions. However, its dimensions were chosen in such a way that the geometric dimensions of the antenna elements and the resonant lengths of oscillations in the resonators were significantly smaller than the geometric dimensions of the plane (on average for the considered operating frequency range by a factor of 10). With such a ratio, one can ignore the occurrence of edge diffraction effects and the so-called "flowing" of currents effect to the opposite side of the metal plane.

RESULTS OF NUMERICAL SIMULATION

As it is obvious, the antenna design itself is quite complicated, so it is practically impossible to talk about the construction of a rigorous model that takes into account most of the factors. In numerical simulations, a complex approach including the semi-open resonator method and the finite element method (FEM) implemented within the commercial package HFFS [12] has been used. Considering the fact that all dependencies are multi-parametric, it is necessary to optimize each dependency for all the variational parameters. Such parameters in this case were h - the thickness of the dielectric substrate, t - the value of the gap between the substrate and the metallic plane and ε_r - the value of the relative dielectric permittivity of the substrate. The diameters of the ring and disc were fixed. Their values were chosen based on the wavelengths of the operating range.

The basis of this antenna consists of two resonators, a disc and a ring resonator, and a coplanar ground plane surrounding them, which plays an essential role in the excitation of the resonators. For this reason, the first step is to investigate the spectral composition of the types of oscillations that are excited in it under the variation of the given parameters.

Based on the data obtained in the study of similar structures [13, 14], a significant influence on the spectral composition of excited oscillations has the value of the relative dielectric permittivity of the dielectric substrate and the distance to the ground plane (with fixed diameters of the resonators and fixed coupling between them at a level approaching the critical level to ensure a wider operating bandwidth). However, there is one more parameter in this design, which is the amount of gap between the outer ring resonator and the coplanar ground plane. This parameter determines the magnitude of coupling with the feeding coplanar line, the uniformity of the coupling magnitude along the perimeter of the ring resonator conductor and directly affects the antenna operating bandwidth.

Fig. 2 shows the spectral characteristics of the structure at a fixed value of the parameter $t = 2$ mm and variation of the dielectric constant of the substrate $\varepsilon_r \rightarrow \text{var}$ (1, 3.8, 5.2). Values 3.8 and 5.2 correspond to standard values, which are quite often used in practice, value 1 is the minimum limit value. In numerical simulations, an additional criterion was used - the maximum number of excited oscillations, equal to 30. And the band within which these types of oscillations are excited is a derivative value.

a) $\varepsilon_r = 1$ b) $\varepsilon_r = 3.8$ c) $\varepsilon_r = 5.2$
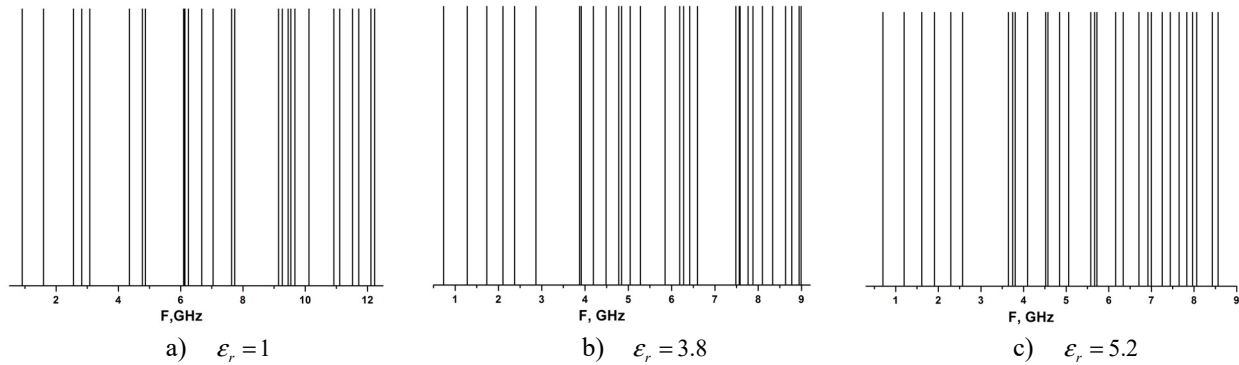
Figure 2. Spectral characteristics

It should be pointed out that all eigen-frequencies are determined with a relative accuracy of no worse than 10^{-7}, which corresponds to a frequency error of 1200 Hz at the widest possible frequency bandwidth considered at $\varepsilon_r = 1$, $t = 2$ mm. Extension of the considered frequency range beyond the established limits is inexpedient, because, firstly, the spectra are too dense and it is difficult to identify and analyze the structure of such oscillations, secondly, the number of degenerate types of oscillations increases, it is practically impossible to identify them with a dense spectrum, and, thirdly, extension of the frequency range leads to unreasonably large expenditures of simulation time.

The analysis of the presented characteristics shows that at a fixed value of the parameter t at the lowest value ε_r the designated 30 types of oscillations fit in the frequency range from 0.91 GHz to 12.23 GHz. Moreover, near the frequency $F = 6$ GHz, a fourfold degeneration of the oscillation types is observed, and near the frequency $F = 10.1$ GHz, a twofold degeneration is observed. As the value ε_r increases, the spectral response shifts towards lower frequencies: at the $\varepsilon_r = 3.8$ lower frequency is $F = 0.736$ GHz, and at $\varepsilon_r = 5.2$ already $F = 0.69$ GHz. At $\varepsilon_r = 3.8$ the degeneration is observed only near the frequency $F = 7.57$ GHz (twofold), and at $\varepsilon_r = 5.2$ only near the frequency $F = 6.93$ GHz (twofold). In the remaining of the frequency range, only densification of spectral lines is observed. In addition, the operating range narrows with increasing ε_r, which correlates with the presence of 30 first types of oscillations.

The characteristics presented in Fig. 2 are obtained after optimizing the spectral composition depending on the parameter t - the distance to the common ground plane. The optimal value is equal to $t = 2$ mm. Decreasing or increasing the value of this parameter does not play a significant role in terms of the emergence (or suppression) of additional resonances or manifestation of degeneracy of oscillation types. The reason is transparent - it is necessary to fulfil certain resonance conditions. In this case - it is a complex electrodynamic structure, for this reason it is impossible to formulate any definite criterion requirements for the values of the studied parameters.

Another important parameter that has a significant influence on the antenna performance as a whole is the coupling value of the resonators and the feeding coplanar line. In most of the known designs that use the coplanar line as the feeding element, due to the simple (linear) form factor of the coplanar line, it is relatively easy to maintain a certain level of coupling between the elements of the device. In the case under consideration, maintaining a given level of coupling (and effective excitation of the antenna apertures) can be realized if it is possible to ensure the flow of surface currents across the entire surface of the outer conductor of the coplanar line. To study this issue, the simulation of surface currents distribution on all antenna elements has been carried out.

Fig. 3 shows the results of the simulation of the surface current distribution in the antenna at frequencies coinciding with the frequencies of the spectral lines for the antenna with the parameters $\varepsilon_r = 5.2$, $t = 2$ mm, the value of the gap between the coplanar line ring conductor and the ring resonator is 0.4 mm (this size provides a coupling close to critical), the outer and inner radii of the ring resonator are 17 mm and 14 mm, respectively, the radius of the disc resonator is 13.5 mm. The frequencies at which the modelling was performed: in Fig. 3a is $F = 3.815$ GHz, in Fig. 3b is $F = 4.51$ GHz.

The analysis of graphical constructions allows us to conclude that at the $F = 3.815$ GHz frequency both the ring resonator and the disc resonator are excited on the type E_{040} of oscillations. It is not possible to identify the type of oscillations that is excited in the coplanar part of the structure.

At the frequency $F = 4.51$ GHz, the phase centers of excitation of both the disk resonator and the ring resonator and the coplanar part of the structure are clearly identified (marked with ellipses in the figures). All of them are almost in-phase excited on the type E_{020} of oscillation. In addition, if we investigate the junction region of the center conductor of the coplanar line and the ring resonator, we can state that at the frequency $F = 3.815$ GHz there is a significant concentration of current density at the junction. This may indicate that the coplanar line itself and the ring resonator are to some extent not matched in terms of characteristic impedance. Conversely, a good level of matching can be expected at $F = 4.51$ GHz.

The presence of such features in the structure of current lines leads to the necessity of additional study of the antenna matching with external circuits at variation of selected parameters. The matching process is relevant for two reasons: the first is the minimum impact on the microwave oscillator, and the second is the effective radiation of the antenna. It is accepted that the level of matching is evaluated either by the return loss level or by the VSWR level. It can be argued that both of these quantities are multi-parametric dependencies on the geometric dimensions, material constants of the antenna and frequency. Therefore, optimization of the matching level by one of the parameters (practically any of them) cannot lead to an absolute conclusion about the antenna efficiency.

a) $F = 3.815$ GHz   b) $F = 4.51$ GHz
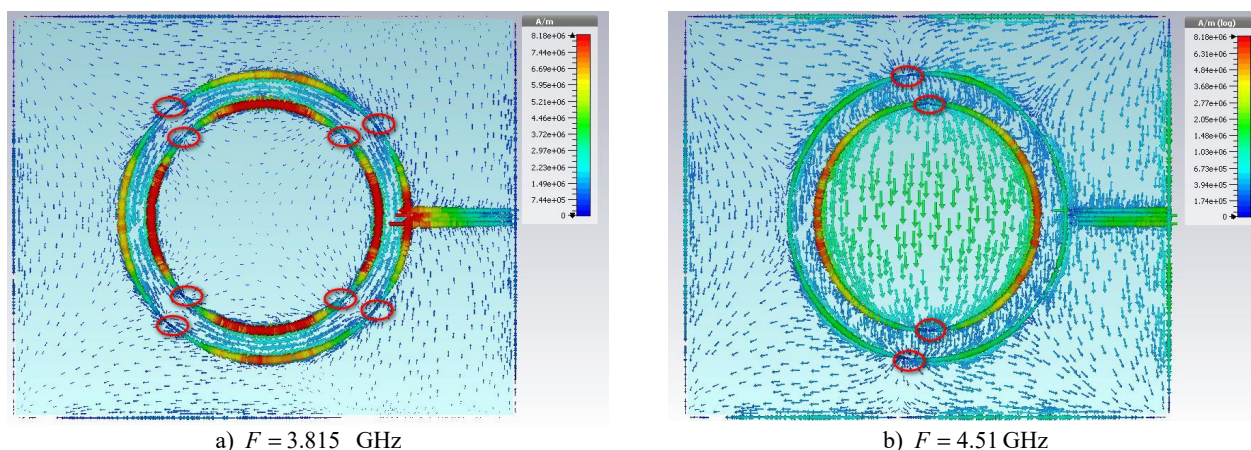
Figure 3. Structure of current density lines on the antenna elements

At the same time, the dependences of return loss on frequency at fixed values of other parameters allow to judge about the presence of matching frequency bands, their width, and the value of return loss within these bands (which will indirectly indicate the efficiency of operation).

Among all antenna elements there are some that fulfil a dual role. On the one hand - they are important structural elements (for example, dielectric substrate, because on it are placed antenna elements), on the other hand - the parameters of the substrate affect both the spectrum of eigenwaves, and to a certain extent affect the input resistance of the antenna. The ratio of ε_r, h and the operating frequency determine the conditions of excitation of surface waves in the substrate. To improve the efficiency of the antenna seeks to operate in the regime of no surface waves. For operation in such a regime it is necessary to use so-called "thin" substrates. The conditions of such a mode will be determined by the relations of $h \ll \lambda_r$, $h \ll \lambda$, where λ_r is the resonant length of excited oscillations, λ is the operating wavelength. In the considered frequency range at the chosen value of $h = 0.5$ mm, such conditions are certainly fulfilled.

In Fig. 4 one can see the dependences of the magnitude $|S_{11}|$ on the substrate values ε_r at optimized values of the parameter $t = 2$ mm and the value of the gap between the coplanar line ring element and the ring resonator.
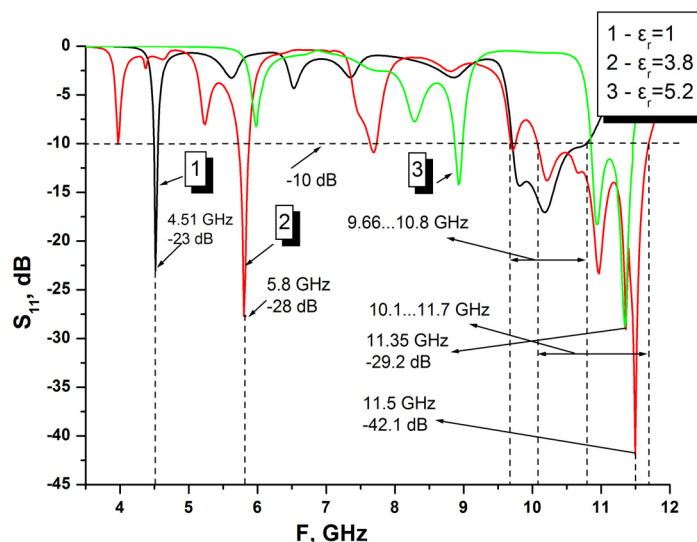
Figure 4. Dependencies of $|S_{11}|$ vs frequency with ε_r variation

All curves presented in the graph are oscillatory to a greater or lesser extent. Moreover, the local amplitudes of oscillations increase with increasing magnitude. There is a trivial effect of the shift of resonance frequencies to the low-

frequency region with decreasing value of ε_r. At all values of ε_r in the characteristics there are both narrow frequency bands with acceptable (and even very high) level of matching, and quite wide bands. Wide bands are observed in the high-frequency part of the considered frequency range.

It is typical that the minimum values of the $|S_{11}|$ are observed at frequencies coinciding or very close to the frequencies of spectral lines of eigentypes of oscillations in the structure (see Fig. 2). The maximum wide bandwidth, within which the matching at the level of -10 dB (VSWR=1.925) is observed, is provided at the value of $\varepsilon_r = 3.8$. It covers the range from 10.1 GHz to 11.7 GHz (approximately 14.7% of the sub-band center frequency). For this value of ε_r, the minimum value of the $|S_{11}| = -42.1$ dB at 11.5 GHz is also achieved. When the value of ε_r is reduced to unity, the bandwidth narrows and it is approximately 11.1% and when the value of ε_r is increased to 5.2 it is only 5.5%. From the results of the simulation we can conclude that the maximum matching levels are achievable only when the operating frequencies coincide with the frequencies of the spectral lines of the eigenoscillation types (or maximum close to them). However, the distribution of currents on the surface of the antenna elements shows (see Fig. 3) and the maximum matching levels do not guarantee effective excitation of apertures, hence, effective radiation.

The value of ε_r has a significant effect not only on the degree of matching but also on the antenna gain. Fig. 5 shows the dependence of the gain in dBi (according to IEEE classification) on frequency at variation of ε_r values.
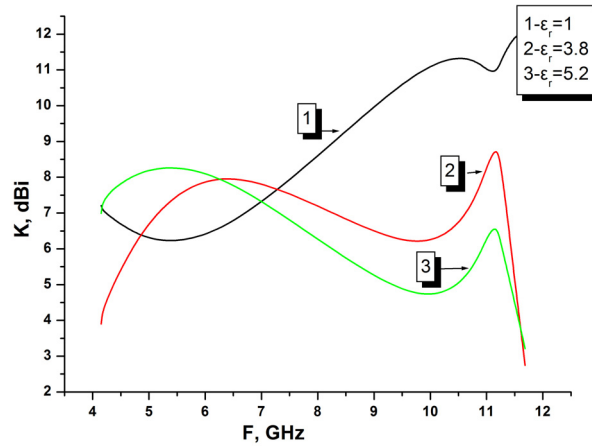
Figure 5. Dependences of the gain coefficient vs frequency at variation of the ε_r value

As it is evident from the above dependences, the frequency dependences have a fundamentally different character. If at value of $\varepsilon_r = 1$ the gain factor practically monotonically increases with frequency growth with two fluctuations of the value of the factor (within 9%), then with increasing ε_r value the dependences acquire oscillatory character (extrema are observed), and at the end of the frequency range there is a sharp decrease in the value of the gain factor. The maximum values of the gain also differ significantly. The maximum of 11.55 dBi is reached at $\varepsilon_r = 1$, at $\varepsilon_r = 3.8$ the maximum is 8.67 dBi, at $\varepsilon_r = 5.2$ the maximum is 6.52 dBi.

The most important characteristics of any antenna are energy and polarization characteristics. These characteristics determine the functionality of a particular antenna. Synthesizing antennas with given parameters has always been a difficult task, given the complex interrelated dependencies of the parameters. And, as indicated earlier, optimizing any of the antenna characteristics by a single parameter does not always lead to the desired result. This situation can be demonstrated by the example of the radiation pattern and ellipticity coefficient dependence of the antenna. Fig. 6 shows the pattern characteristics for some typical cases.
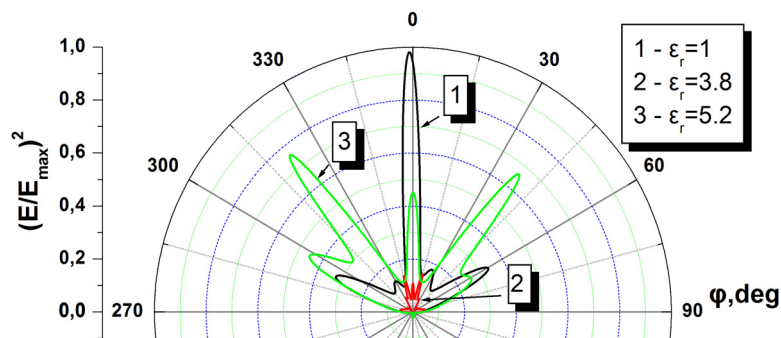
Figure 6. Pattern characteristics in azimuthal plane with optimized set of parameters

All diagrams are normalized to the global maximum (this allows us to compare the radiation efficiency at each frequency). The spline interpolation procedure was used to construct the dependencies and for this reason there is a visual difference from unity in the maximum of the directivity diagram. The lower part of the construction is excluded from consideration, because the value of the back lobes does not exceed the value of 0.015 (-18 dB).

The following frequencies were selected for analysis: curve 1 - at $F = 4.51$ GHz ($|S_{11}| = -23$ dB), curve 2 - at $F = 5.8$ GHz ($|S_{11}| = -28$ dB), curve 3 - at $F = 11.35$ GHz ($|S_{11}| = -29.2$ dB). These frequencies were chosen from the consideration of minimum values of the return loss magnitude. The frequency with the absolute minimum ($|S_{11}| = -42.1$ dB at $F = 11.5$ GHz) was not considered due to too large difference in the return loss values.

As it is obvious, at all fixed parameters and $\varepsilon_r = 1$ quite sharp main lobe formed (its width at the level of 0.707 is 4.57^0), the side lobes are located symmetrically relative to the main one, their level does not exceed the value of 0.3. The main lobe is displaced from the normal by an angle of 1.9^0. Increasing the ε_r value up to the value 3.8 leads to radical changes in the directivity diagram. The level of radiated power decreases sharply (its value does not exceed 11% of the value of the level at $\varepsilon_r = 1$). Further increase up to the ε_r value of 5.2 leads to increase of the radiated power up to the level of 73% of the maximum at $\varepsilon_r = 1$. However, the diagram acquires a multi-lobe appearance.

Fig. 7 shows the polarization characteristics of the antenna plotted at the same parameter values and at the same frequencies. The characteristics are plotted in a limited range of observation angles. In the remaining of the range of angles, very sharp jumps in the value of the ellipticity coefficient are observed. As can be seen from the above characteristics, the dependence function of the ellipticity coefficient for the $\varepsilon_r = 1$ value has a monotonically increasing character with a minimum value of 15 dB, which indicates the presence of linear polarization of the radiated waves. When increasing ε_r within the interval of angles 5.64^0, the η value does not exceed the value of 3 dB, which indicates the presence of elliptical polarization.
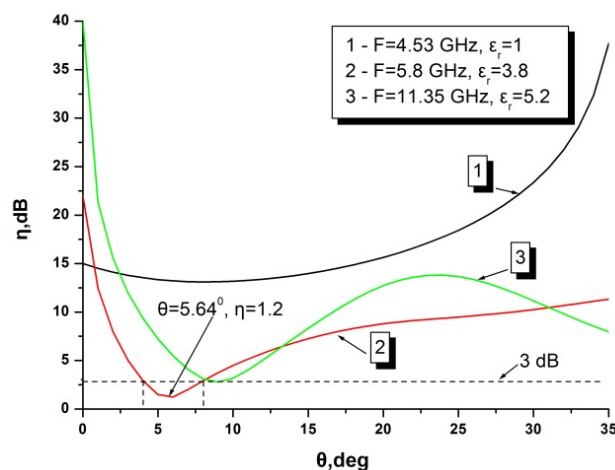
Figure 7. Polarization characteristics

At the $\varepsilon_r = 5.2$ value of the dependence has an oscillatory character and in most of the values of the observation angles the polarization has a linear character. In a very narrow band of observation angles we can conditionally speak about the presence of elliptical polarization.

The analysis of the given energy and polarization characteristics confirmed the position that the process of optimization of multi-criteria characteristics of the antenna by one parameter is practically impossible. In order to achieve the desired parameter levels, a multi-criteria optimization procedure has to be carried out. Such a process is very complicated in terms of sufficiently large expenditures of calculation time and in terms of rather strict requirements to the capabilities of computing equipment.

CONCLUSION

This paper presents the results of numerical simulation of the main electrodynamic characteristics of a complex-composite electrodynamic structure designed to operate as an antenna in the centimeter wavelength range. The peculiarity of the method of excitation of the structure is actually two-port feeding of the antenna: the first port - due to the presence of galvanic coupling between the inner conductor of the excitation coplanar line and the ring conductor of the resonator, and the second - due to the distributed electromagnetic coupling of the outer conductor of the coplanar line and the ring resonator. By optimizing the varying parameters, it is possible to ensure satisfactory matching between the antenna and the external circuits. As a result of simulations it is established that this kind of design can provide effective radiation of electromagnetic waves with different types of polarization.

ORCID

🔵**Sergey A. Pogarsky,** https://orcid.org/0000-0003-0833-1421; 🔵**Dmitry V. Mayboroda,** https://orcid.org/0000-0002-9564-2369

REFERENCES

[1]   Y. Zheng, and Y. Dong, in: *2021 IEEE MTT-S International Microwave Symposium (IMS)*, (Atlanta, GA, USA, 2021). https://doi.org/10.1109/IMS19712.2021.9574892

[2]   G. Zhang, Q. Zhang, Q. Liu, W. Tang, and J. Yang, IEEE Trans. on Circuits and Systems II: Express Briefs, **68**(12), 3542 (2021). https://doi.org/10.1109/TCSII.2021.3082256

[3]   Sk. Zameer, K.V.M.R. Risheek, E. Sandeep, B. Tarun, and P.S.A.J. Naidu, in: *2021 2nd International Conference on Smart Electronics and Communication (ICOSEC)*, (Trichy, India, 2021). https://doi.org/10.1109/ICOSEC51865.2021.9591805

[4]   G. Wan, M. Li, M. Zhang, L. Kang, and L. Xie, IEEE Transactions on Instrumentation and Measurement, **71**, 8002610, (2022). https://doi.org/10.1109/TIM.2022.3161718

[5]   K. Singh, and A.V. Nirmal, in: *2019 IEEE Indian Conference on Antennas and Propogation (InCAP)*, (Ahmedabad, India, 2019). https://doi.org/10.1109/InCAP47789.2019.9134651

[6]   S.-Y. Tang, J. Chen, N.-W. Liu, G. Fu, L. Zhu, and J. Chen, IEEE Antennas and Wireless Propagation Lett., **20**(6), 998 (2021). https://doi.org/10.1109/LAWP.2021.3069252

[7]   P. Das, S. Biswas, S.S. Ridhwaan, R. Ray, D. Ghosh, and D. Sarkar, in: *2018 2nd International Conference on Electronics, Materials Engineering & Nano-Technology (IEMENTech)*, (Kolkata, India), https://doi.org/10.1109/IEMENTECH.2018.8465322

[8]   P. Troughton, Electron Lett. **5**(1), 25 (1969). https://doi.org/10.1049/EL:19690017

[9]   L.-H. Hsieh, and K. Chang, IEEE Transactions on Microwave Theory and Tech., **50**(2), 453 (2002). https://doi.org/10.1109/22.982223

[10] I. Wolff, and N. Knoppik, Electron Lett. **7**(26), 779 (1971). https://doi.org/10.1049/el:19710532

[11] A.M. Khilla, in: *1983 13th European Microwave Conference* (Nurnberg, Germany), https://doi.org/10.1109/EUMA.1983.333265

[12] Ansoft HFSS /ANSYS Academic Research HF (5 tasks): 1 task(s) Permanent with TECS expiring 01-May-2020 Customer #1076710

[13] S.A. Pogarsky, D.V. Mayboroda, and S.M. Mikhaliuk, East Eur. J. Phys. (4), 274 (2023). https://doi.org/10.26565/2312-4334-2023-4-34

[14] S.A. Pogarsky, D.V. Mayboroda, Radio Physics and Radio Astronomy, **28**(2), 158 (2023). https://doi.org/10.15407/rpra28.02.158

АНТЕНА НА ОСНОВІ КОМПОЗИЦІЙНОЇ КОПЛАНАРНОЇ СТРУКТУРИ
Сергій О. Погарський, Дмитро В. Майборода, Сергій М. Михалюк
Харківський національний університет імені В.Н. Каразіна, майдан Свободи, 4, Харків, Україна, 61022

У цій роботі представлено результати чисельного дослідження площинної антени зі складним форм-фактором. Основу антени становить комбінація двох резонаторів - дискового та кільцевого. Збудження кільцевого резонатора здійснюється за допомогою копланарної структури: точково за рахунок гальванічного контакту центрального провідника копланарної лінії та кільцевого резонатора і за рахунок розподіленого електромагнітного зв'язку кільцевого резонатора й апертури зовнішнього провідника копланарної лінії. Антена розміщувалася над металевою площиною, геометричні розміри якої істотно перевищували геометрично розміри антени для виключення впливу крайових дифракційних ефектів. Під час чисельного моделювання використано комплексний підхід, що містить у собі метод напіввідкритого резонатора та метод скінченних елементів (МКЕ), реалізований у рамках комерційного пакета HFFS. Проведено дослідження залежностей спектральних, енергетичних і поляризаційних характеристик від матеріальних констант і частотного параметра. Встановлено, що в рамках однопараметричної оптимізації неможливе одночасне досягнення високого рівня всіх важливих параметрів. Значення частот спектральних ліній у спектральних характеристиках антени знайдено з відносною похибкою не гірше 1200 Гц. Встановлено частотні діапазони, у межах яких відсутнє виродження типів коливань. Наведено розподіли поверхневих струмів на металевих елементах антени, що дають змогу визначити положення фазових центрів збудження. Показано, що пропонована антена може забезпечувати прийнятний рівень узгодження як на окремих частотах, так і в доволі широких локальних смугах частот, що сягають 11% щодо центральної частоти піддіапазону. Встановлено граничні значення коефіцієнтів підсилення в частотних діапазонах. Результати моделювання дають змогу прогнозувати ефективне випромінювання з формуванням практично однопелюсткової діаграми спрямованості та наявність еліптичної поляризації.
Ключові слова: *кільцевий резонатор; дисковий резонатор; копланарна лінія; узгодження; частотні характеристики; енергетичні характеристики*

INTERACTIONS OF AMYLOID FIBRILS WITH FUNCTIONAL PROTEINS: MODULATING EFFECT OF POLYPHENOLS

Valeriya Trusova*, Uliana Tarabara, Galyna Gorbenko

Department of Medical Physics and Biomedical Nanotechnologies, V.N. Karazin Kharkiv National University
4 Svobody Sq., Kharkiv, 61022, Ukraine
Corresponding Author email: valerija.trusova@karazin.ua
Received May 2, 2024, revised May 22, 2024; accepted May 26, 2024

The elucidation of interactions between functional proteins and amyloid fibrils is crucial for understanding the molecular basis of amyloid diseases, which are characterized by protein misfolding and aggregation. Polyphenols, due to their diverse biological properties, have garnered attention for their potential to modulate these protein-fibril interactions, thereby influencing disease progression and offering therapeutic possibilities. In this study, we investigated the effects of quercetin and its binary combinations with other polyphenols on the binding affinity between cytochrome c, in both its reduced and oxidized forms, and amyloid fibrils of insulin and apolipoprotein A-I. Our results demonstrate that quercetin complexation with cytochrome c decreases the binding affinity of insulin fibrils for both forms of the protein, while increasing the affinity for apolipoprotein A-I fibrils. This modulation was attributed to competitive or allosteric effects exerted by quercetin on cytochrome c. Additionally, while binary combinations of quercetin with other polyphenols did not reduce the affinity of insulin fibrils for oxidized cytochrome c, they did decrease the affinity in the case of reduced counterpart. These findings highlight the selective and significant impact of polyphenolic compounds on the interactions between amyloid fibrils and functional proteins, suggesting potential pathways for therapeutic intervention in amyloid-related disorders.

Keywords: *Amyloid fibrils; Functional proteins; Polyphenols; Molecular docking*
PACS: 87.14.C++c, 87.16.Dg

Amyloid fibrils, characterized by their insoluble, fibrous nature, are implicated in a myriad of pathological conditions, including neurodegenerative diseases [1]. These assemblies are formed through the misfolding and aggregation of peptides and proteins into highly ordered, β-sheet-rich structures [2,3]. Despite their notorious association with the diseases [4], recent investigations have illuminated the nuanced roles that amyloid fibrils may play in interacting with functional proteins [5], thereby potentially disrupting normal cellular processes or, conversely, participating in physiological mechanisms that are essential for maintaining cellular homeostasis. The modulation of these type of protein-protein interactions by bioactive compounds offers a promising avenue for therapeutic intervention. Among the wide range of different substances, polyphenols (PF) – a diverse group of naturally occurring compounds with potent biological activities – have garnered attention for their capacity to influence amyloid fibril formation and stability [6-8]. PF are known for their antioxidant properties and their ability to modulate protein aggregation pathways, which may mitigate the deleterious effects of amyloids on functional proteins [9]. The interaction between polyphenols and amyloid fibrils, therefore, represents a critical area of research that could lead to the development of novel therapeutic approaches for managing amyloid diseases. Motivated by these rationales, in the present paper we explore the modulative effects of polyphenolic compounds with quercetin serving as the primary PF under examination, on the interactions between the amyloid fibrils formed by insulin and apolipoprotein A-I with functional proteins, represented by reduced and oxidized forms of cytochrome c. Utilizing the molecular docking as our primary methodological approach, this study aims to provide a molecular-level understanding of how polyphenols can influence the binding interactions between fibrillar assemblies and endogenous proteins, offering insights into the mechanistic pathways through which PF exert their modulatory effects. To enhance the depth of our analysis, quercetin was not only studied in isolation but also in binary combinations with other polyphenolic compounds, each selected for their unique chemical properties and potential synergistic effects. These additional polyphenols include sesamin, curcumin, phenolic acid, gallic acid, and resveratrol. Through this detailed investigation, we seek to elucidate the potential of polyphenols as therapeutic agents in diseases associated with protein aggregation, highlighting their role in disrupting or stabilizing protein-protein interactions that are critical to disease progression.

METHODS

The blind docking of the examined complexes was performed using the web-based server HDOCK. This server implements an FFT-based hierarchical algorithm of rigid-body docking through mapping the receptor and ligand molecules onto grids and global sampling of the possible binding modes with an improved shape complementarity scoring method in which one molecule is fixed, while the second one adopts evenly distributed orientations in rotational Euler space and translational space within a grid. The resulting docking solutions are ranked according to their binding energy and clustered [10]. The three-dimensional X-ray crystal structures of oxidized and reduced cytochrome c were obtained

from the Protein Data Bank (https://www.rcsb.org/) using the PDB IDs 2N9J and 2N9I, respectively. The 50-monomer fragment of insulin fibril model was provided by M. Sawaya (http://people.mbi.ucla.edu/sawaya/jmol/fibrilmodels/). The model amyloid fibrils of apoliporotein A-I were constructed using the CreateFibril tool based on the translational and rotational affine transformations providing several copies of a certain fragment of fibril core, whose subsequent stacking produces the elongated fibrillar aggregate [11]. The input structures for CreateFibril were generated from the monomers in the β-strand conformation with PatchDock. The selected docking poses were visualized with the UCSF Chimera software (version 1.14) and analyzed with BIOVIA Discovery Studio Visualizer, v21.1.0.20298, San Diego: Dassault Systemes; 2021.

RESULTS AND DISCUSSION

At the initial stage of the study, we meticulously explore the binding interactions of quercetin with cytochrome *c* (cyt *c*) in the reduced and oxidized form, and amyloid fibrils, represented by fibrillar insulin (InsF) and fibrillar apolipoprotein A-I (ApoAIF) as distinct control calculations. This foundational step is critical for establishing a baseline understanding of how polyphenols interact with each component individually before examining their tripartite interactions within a complex system. Fig. 1 represents the docking poses of the complexes between cyt *c* and quercetin (QR) corresponding to the best score of the docking. As seen from this figure, QR forms stable contacts with protein molecule both in the case of reduced and oxidized state of cyt *c*.
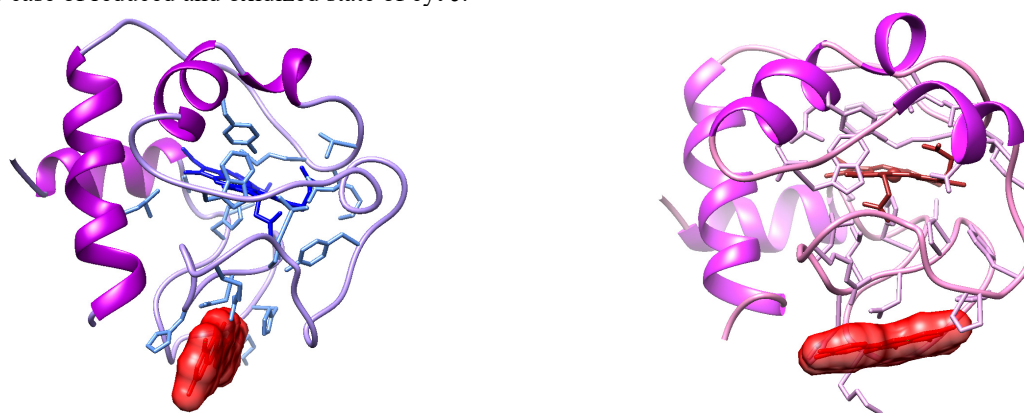
Figure 1. Representation of the optimal binding conformation of quercetin to the oxidized (left panel) and reduced (right panel) forms of cytochrome *c* as determined by the docking algorithm. Quercetin is shown in red

Cyt *c*, a small heme protein located within the mitochondrial intermembrane space, plays a pivotal role in the electron transport chain, facilitating the transfer of electrons between Complex III (cytochrome bc1 complex) and Complex IV (cytochrome c oxidase) [12]. This electron shuttling is crucial for the mitochondrial production of ATP, the energy currency of the cell, which underscores the fundamental role of cytochrome c in cellular energetics and metabolism. The functionality of cytochrome c is inherently linked to its redox state, with the protein undergoing reversible oxidation and reduction of its iron atom from the ferric (Fe^{3+}) to the ferrous (Fe^{2+}) state and *vice versa* [13]. From a physiological perspective, the redox state of cytochrome c not only dictates its electron-carrying capacity but also influences other critical cellular processes, including apoptosis. In its oxidized form (Fe^{3+}), cytochrome *c* is capable of inducing caspase activation via the apoptosome, a key component in the intrinsic pathway of apoptosis. This pro-apoptotic activity is attributed to the release of oxidized cytochrome *c*, cyt *c* oxy, into the cytosol following mitochondrial membrane permeabilization, which then interacts with apoptotic protease activating factor-1 to form the apoptosome, thereby initiating the caspase cascade leading to programmed cell death. Conversely, the reduced form of cytochrome *c*, cyt *c* red, (Fe^{2+}) exhibits a diminished capacity to initiate apoptosis, highlighting a regulatory mechanism by which the cellular redox state can influence apoptotic sensitivity. This redox-dependent modulation of apoptosis underscores the dual functionality of cytochrome c, serving both life-sustaining and cell death-promoting roles within the organism [14].

The binding scores obtained from the docking simulations were -123.51 for the oxidized form and -119.78 for the reduced form of the protein, indicating a slightly stronger affinity of quercetin for the oxidized state of the protein. These results suggest that the redox state of cyt *c* could influence its interaction with quercetin, potentially affecting the biological outcomes of this interaction. A detailed examination of the receptor-ligand interface residues reveals a largely conserved interaction pattern between the two redox states of cyt *c*, with only minor differences observed. Specifically, the interface residues involved in binding quercetin to the oxidized form of cyt *c* include THR$_{19}$, GLU$_{21}$, LYS$_{22}$, GLY$_{23}$, GLY$_{24}$, LYS$_{25}$, HIS$_{26}$, ASN$_{31}$, LEU$_{32}$, HIS$_{33}$, GLY$_{34}$, and ARG$_{38}$. Comparatively, in the reduced form, the interacting residues are GLU$_{21}$, LYS$_{22}$, GLY$_{23}$, GLY$_{24}$, LYS$_{25}$, HIS$_{26}$, ASN$_{31}$, HIS$_{33}$, GLY$_{34}$, ARG$_{38}$, ALA$_{43}$, and PRO$_{44}$. Notably, the core residues such as GLU$_{21}$, LYS$_{22}$, GLY$_{23}$, GLY$_{24}$, LYS$_{25}$, HIS$_{26}$, ASN$_{31}$, HIS$_{33}$, GLY$_{34}$, and ARG$_{38}$ are conserved across both redox states, indicating a fundamental similarity in the binding mode of quercetin to cytochrome c irrespective of its oxidation state. The slight differences observed, specifically the additional involvement of ALA$_{43}$ and PRO$_{44}$ in the reduced form, suggest subtle conformational or electronic changes in cyt *c* upon reduction that might slightly alter the

binding landscape. These differences, while minor, could potentially influence the dynamics and stability of the quercetin-cytochrome c complex, possibly affecting the biological activity of cyt c in subtle ways.

Next, the binding of QR to amyloid fibrils of insulin and apolipoprotein A-I was explored. Fig. 2 represents the location of QR within the InsF and ApoAIF. The binding scores obtained were notably distinct, with QR exhibiting a binding score of -163.8 with InsF and -121.18 with ApoAIF. These results indicate a significantly stronger affinity of quercetin for InsF compared to those formed by ApoAIF. The analysis of the receptor-ligand interface residues provides further insights into the molecular basis of these interactions. For InsF, the interface residues involved in binding of QR include GLN_{115}, PHE_{201}, VAL_{202}, ASN_{203}, GLN_{204}, ILE_2, LEU_{13}, GLN_{15}, LEU_{113}, VAL_{202}, ASN_{203}, GLN_{204}, LEU_{206}, GLN_5. These residues are predominantly hydrophobic and polar in nature, which suggests that both hydrophobic interactions and hydrogen bonding might play crucial roles in stabilizing the quercetin-insulin fibril complex.
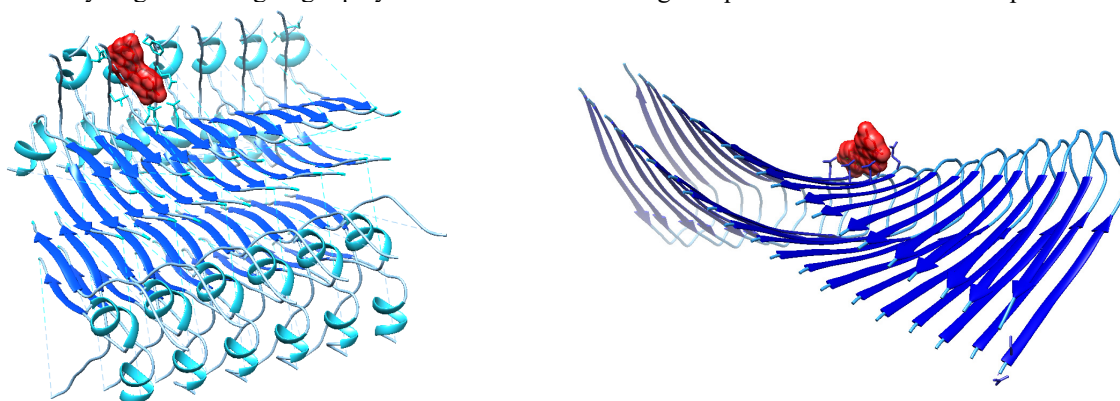
Figure 2. Location of QR within the amyloid insulin (left panel) and apolipoprotein A-I (right panel) in the best docking mode

The presence of multiple glutamine and asparagine residues could facilitate extensive hydrogen bonding, while hydrophobic residues like LEU, VAL, and PHE may contribute to the overall binding affinity through van der Waals interactions. In contrast, the interface residues for ApoAIF interacting with QR were identified as GLN_{271}, LEU_{272}, ASN_{273}, GLN_{298}, LEU_{299}, ASN_{300}, GLN_{325}, LEU_{326}, ASN_{327}, ASN_{354}. Similar to the insulin fibril interaction, this set also includes a mix of hydrophobic and polar residues, indicating a similar mode of interaction. However, the lower binding score observed with ApoAIF suggests that the specific arrangement and accessibility of these residues might not be as conducive to high-affinity binding as those in InsF. The differential binding affinities observed between QR and the two types of amyloid fibrils could be attributed to variations in the amyloid fibril structures, which in turn affect the availability and orientation of key residues at the binding interface. Amyloid fibrils, despite their general structural similarities, can exhibit significant variability in their surface characteristics depending on the specific protein from which they are formed. This structural variability can influence the docking and binding efficiency of small molecules like quercetin.

The final iteration of the control calculations was the molecular docking simulations of cyt c binding to the amyloid fibrils. Fig. 3 depicts the 3D structures of cyt c – amyloid complexes while Table 1 summarizes the interfacial amino acid residues on the fibril surface that are in contact with cyt c.

Cyt c oxy + InsF   **Cyt c red + InsF**

Cyt c oxy + ApoAIF   **Cyt c red + ApoAIF**
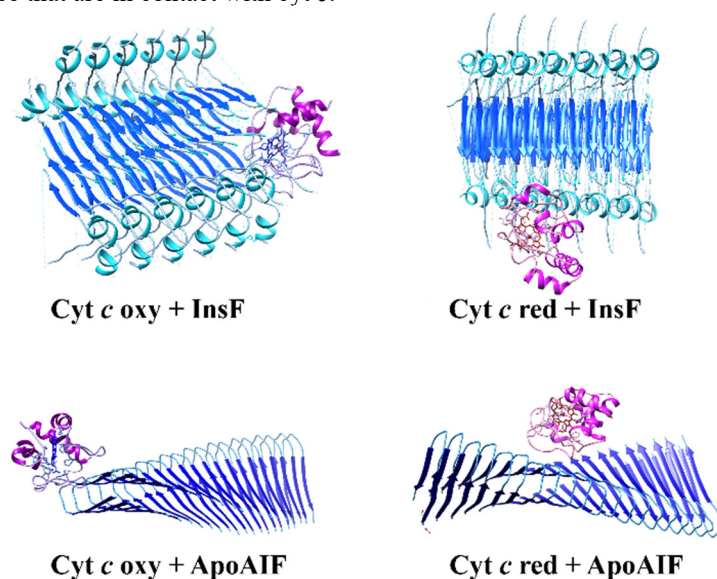
Figure 3. Docked poses corresponding to minimum energy for the complexes between reduced and oxidized form of cyt c and amyloid fibrils of insulin and apolipoprotein A-I. Cyt c is shown in pink

Analysis of the docking scores indicate a notably stronger binding affinity of the reduced form of cyt *c* to both InsF (-229.81) and ApoAIF (-174.63) compared to its oxidized counterpart, which exhibited scores of -218.95 and -164.58, respectively. This suggests that the electron state of cyt *c* significantly influences its interaction dynamics with amyloid fibrils. The reduced form, containing the ferrous state, may facilitate more favorable electrostatic or coordination interactions with the amyloid fibrils compared to the ferric state in the oxidized form. The interface residues identified on cytochrome c, which are in contact with the amyloid fibrils, further elucidate the molecular basis of these interactions. For the oxidized form of cyt *c*, residues such as SER_{15}, GLN_{16}, and LYS_{25} are implicated in binding to insulin fibrils, while residues including GLU_{21}, LYS_{22}, and GLY_{23} are involved in interactions with ApoAIF. Conversely, the reduced form of cyt *c* interacts with insulin fibrils through residues such as VAL_{20}, LYS_{22}, and ASN_{31}, and with ApoAIF through residues like LYS_{22}, GLY_{23}, and ASN_{31}. These residues, encompassing both polar and non-polar amino acids, suggest a complex interaction environment that might facilitate stabilization through various non-covalent interactions, including hydrogen bonds and hydrophobic contacts.

Table 1. Receptor-ligand interface residues in the complexes of cytochrome c with amyloid fibrils in the absence and presence of quercetin

Interface residues on cytochrome *c*	
Cyt *c* oxy	
InsF	
Without quercetin	SER_{15A}, GLN_{16A}, CYS_{17A}, LYS_{25A}, HIS_{26A}, LYS_{27A}, THR_{28A}, GLY_{45A}, TYR_{46A}, SER_{47A}, TYR_{48A}, THR_{49A}, ALA_{50A}, ALA_{51A}, LYS_{72A}, PRO_{76A}, GLY_{77A}, THR_{78A}, LYS_{79A}, MET_{80A}, ILE_{81A}, VAL_{83A}
With quercetin	GLN_{16A}, CYS_{17A}, LYS_{25A}, HIS_{26A}, LYS_{27A}, THR_{28A}, GLY_{29A}, GLY_{45A}, TYR_{46A}, SER_{47A}, TYR_{48A}, THR_{49A}, ALA_{50A}, GLY_{77A}, THR_{78A}, LYS_{79A}, ILE_{81A}
ApoAIF	
Without quercetin	GLU_{21A}, LYS_{22A}, GLY_{23A}, GLY_{24A}, LYS_{25A}, HIS_{26A}, ASN_{31A}, HIS_{33A}, GLY_{34A}, LEU_{35A}, PHE_{36A}, GLY_{37A}, ARG_{38A}, LYS_{39A}, GLN_{42A}, ALA_{43A}, PRO_{44A}, GLY_{45A}, LYS_{99A}, THR_{102A}, ASN_{103A}, GLU_{104A}
With quercetin	GLU_{21A}, LYS_{22A}, GLY_{23A}, GLY_{24A}, LYS_{25A}, HIS_{33A}, GLY_{34A}, LEU_{35A}, PHE_{36A}, GLY_{37A}, ARG_{38A}, LYS_{39A}, GLY_{41A}, GLN_{42A}, ALA_{43A}, PRO_{44A}, GLY_{45A}, LYS_{99A}, LYS_{100A}, THR_{102A}, ASN_{103A}, GLU_{104A}
Cyt *c* red	
InsF	
Without quercetin	VAL_{20A}, LYS_{22A}, GLY_{23A}, ASN_{31A}, HIS_{33A}, GLY_{34A}, PHE_{36A}, GLY_{37A}, ARG_{38A}, LYS_{39A}, THR_{40A}, GLY_{41A}, GLN_{42A}, ALA_{43A}, PRO_{44A}, GLY_{45A}, TYR_{46A}, SER_{47A}, TYR_{48A}, ASN_{52A}, LYS_{53A}, ASN_{54A}, LYS_{55A}, GLY_{56A}, ILE_{57A}, ILE_{58A}, LYS_{99A}, LYS_{100A}, ALA_{101A}, THR_{102A}, ASN_{103A}, GLU_{104A}
With quercetin	ALA_{51A}, ASN_{54A}, LYS_{55A}, GLY_{56A}, ILE_{57A}, ASP_{62A}, THR_{63A}, MET_{65A}, GLU_{66A}, TYR_{67A}, GLU_{69A}, ASN_{70A}, PRO_{71A}, LYS_{72A}, LYS_{73A}, TYR_{74A}, ILE_{75A}, PRO_{76A}, LYS_{79A}, MET_{80A}, ILE_{81A}, PHE_{82A}, VAL_{83A}, GLY_{84A}, ILE_{85A}, LYS_{86A}, LYS_{88A}, ARG_{91A}
ApoAIF	
Without quercetin	LYS_{22A}, GLY_{23A}, ASN_{31A}, HIS_{33A}, GLY_{34A}, LEU_{35A}, PHE_{36A}, GLY_{37A}, ARG_{38A}, LYS_{39A}, THR_{40A}, GLY_{41A}, GLN_{42A}, PRO_{44A}, GLY_{45A}, LYS_{53A}, ASN_{54A}, LYS_{55A}, GLY_{56A}, ILE_{57A}, ILE_{58A}, ASN_{103}
With quercetin	GLU_{21A}, LYS_{22A}, GLY_{23A}, GLY_{24A}, LYS_{25A}, HIS_{33A}, GLY_{34A}, LEU_{35A}, PHE_{36A}, GLY_{37A}, ARG_{38A}, LYS_{39A}, GLY_{41A}, GLN_{42A}, ALA_{43A}, PRO_{44A}, GLY_{45A}, LYS_{99A}, LYS_{100A}, THR_{102A}, ASN_{103A}, GLU_{104A}

The implications of the interactions between cytochrome *c* in its reduced and oxidized forms with amyloid fibrils of insulin and apolipoprotein A-I extend beyond mere molecular docking scores and interface residues. These interactions provide a deeper understanding of the potential pathological and physiological roles of amyloid fibrils in relation to mitochondrial function, particularly in the context of neurodegenerative and systemic amyloid diseases. The differential binding affinities and interaction patterns of cyt *c* with amyloid fibrils, as observed in our study, suggest a nuanced influence of the protein's redox state on its association with amyloid structures. In diseases characterized by amyloidosis, such as Alzheimer's disease and type II diabetes, the deposition of amyloid fibrils is a hallmark [15]. These fibrils can sequester functional proteins like cytochrome *c*, potentially diverting them from their normal physiological roles. For instance, the stronger binding affinity of the reduced form of cyt *c* to amyloid fibrils might lead to a higher sequestration rate, thereby reducing its availability for electron transport activities. This could result in impaired mitochondrial function, decreased ATP production, and increased oxidative stress, all of which are critical factors in the progression of amyloid-related diseases. Moreover, the specific interaction sites and the nature of the binding (whether at the edge or side of the fibrils) could influence the structural integrity and toxicity of the amyloid fibrils themselves. By binding to specific sites, cytochrome c might stabilize certain conformations of the fibrils that are less toxic or, conversely, might promote configurations that are more detrimental to cellular health. On a physiological level, the interactions between cytochrome c and amyloid fibrils could also play a role in the natural regulation of apoptosis, a process in which cyt *c* is a key player.

Under normal conditions, cyt c, released into the cytosol from the mitochondria, initiates the apoptotic cascade. However, if cyt c is bound to amyloid fibrils, its release and subsequent initiation of apoptosis might be hindered, potentially affecting cell survival in stressed or damaged cells. This interaction could thus represent a double-edged sword, where it might either prevent unnecessary apoptosis in a protective manner or could hinder necessary cell death, leading to the persistence of dysfunctional cells.

After examination the binding patterns between different pairs of components, in the following we examined the interactions within the triad system QR + cyt c + amyloid fibrils. As seen from Table 2, the complexation of quercetin with cyt c leads to the decrease in the binding affinity of the insulin fibrils for both oxy and red forms of cyt c, and to the increase for the case of ApoA-I fibrils.

Table 2. The best scores of the complexes between cyt c and amyloid fibrils in the absence and presence of quercetin

	Amyloid fibrils	
	InsF	**ApoAIF**
Cyt c oxy	-218.95	-164.58
Cyt c red	-229.81	-174.63
Cyt c oxy + quercetin	-212.85	-174.40
Cyt c red +quercetin	-212.58	-186.39

The observed decrease in binding affinity may be attributed to the competitive or allosteric modulation effects exerted by QR on cyt c. Specifically, the presence of overlapping amino acid residues in the binding sites for quercetin and insulin on cytochrome c suggests a competitive interaction scenario. In the oxidized form of cyt c, residues such as LYS_{25} and HIS_{26}, and in the reduced form, residues including ASN_{31}, HIS_{33}, GLY_{34}, ARG_{38}, ALA_{43}, and PRO_{44}, are implicated in these interactions. These residues are crucial for the binding of cytochrome c to insulin fibrils, and their involvement in quercetin binding implies that QR may obstruct these critical sites, thereby hindering the effective interaction of cyt c with the amyloid fibrils. The ability of QR to modulate the interaction between cyt c and insulin amyloid fibrils has significant implications for understanding the pathological processes associated with amyloid diseases, particularly those related to mitochondrial dysfunction. The binding of cyt c to amyloid fibrils, as observed in amyloidogenic diseases, can disrupt its normal functions, leading to impaired mitochondrial electron transport and reduced apoptotic signaling. By reducing the affinity of cyt c for amyloid fibrils, QR could potentially restore or preserve the functional integrity of cyt c, thereby maintaining cellular energy production and promoting appropriate apoptotic responses. The interaction of QR with cyt c and its consequent effect on the protein affinity for amyloid fibrils could also have broader implications for cellular homeostasis and the progression of amyloid-related diseases. By potentially disfavoring the formation of non-functional complexes between cyt c and amyloid fibrils, quercetin may aid in mitigating the cytotoxic effects associated with amyloid accumulation. This protective mechanism could be particularly beneficial in the context of neurodegenerative diseases, where the deposition of amyloid fibrils is a hallmark feature.

In turn, the increased affinity of cyt c for ApoAIF could potentially enhance the undesirable impacts of amyloid fibrils on functional proteins. By binding more strongly to amyloid fibrils, cyt c may become increasingly sequestered in these complexes, thereby being unavailable for its normal physiological roles. This sequestration could contribute to mitochondrial dysfunction, a hallmark of many amyloid-related diseases, including Alzheimer's disease and systemic amyloidosis. Furthermore, the prevention of cyt c release into the cytosol could inhibit the initiation of the apoptotic cascade, potentially leading to the survival of damaged or dysfunctional cells that contribute to disease pathology.

Inspired by the revealed ability of quercetin to modulate the interactions between amyloid fibrils and cyt c, at the last step of the study we examined the synergetic potential of QR and other polyphenols to alter the binding profile of cyt c with InsF. As shown in Fig. 4, binary combinations of QR + sesamin / curcumin / phenolic acid / gallic acid / resveratrol was not effective in the attenuation of InsF affinity for cyt c oxy. The contrary effect was revealed for the case of cyt c red, where all sets of binary polyphenol complexes gave rise to the decrease to the protein-fibril binding affinity, with the maximum change of the best docking score being observed for gallic acid.

The observed lack of efficacy in attenuating the affinity of insulin amyloid fibrils for cyt c oxy in the presence of afore-mentioned binary polyphenolic complexes may be symptomatic of a specific conformational architecture of the oxidized form, which resists modulation by these polyphenols. This resistance may be attributed to the inherent stability of the interactions between oxidized cyt c and the amyloid fibrils which may not be sufficiently destabilized by the polyphenolic compounds tested. In addition, one should bear in mind, that when polyphenols reside at the interface between a protein and fibril, they may form additional contacts with amyloid fibrils, thereby increasing its binding affinity to the functional protein.

In stark contrast, the reduction in protein-fibril binding affinity for the reduced form of cyt c in the presence of these binary polyphenol complexes, especially that noted with gallic acid, underscores the potential allosteric or direct interaction effects of these compounds on the protein-fibril interface. This reduction in binding affinity suggests a destabilization of the amyloid fibril interaction with cyt c, thus potentially favoring the maintenance of the protein native functional state. The decrease in protein-fibril binding affinity, elicited by binary polyphenolic combinations, is particularly thought-provoking when considering the pathological ramifications of amyloid-protein interactions. The

propensity for amyloid fibrils to sequester functional proteins like cytochrome *c* can culminate in the impairment of critical cellular functions. Thus, the observed modulation of these interactions by polyphenolic compounds may hold therapeutic relevance, offering a biochemical scaffold for the development of interventions aimed at mitigating the deleterious consequences of amyloid-associated diseases.
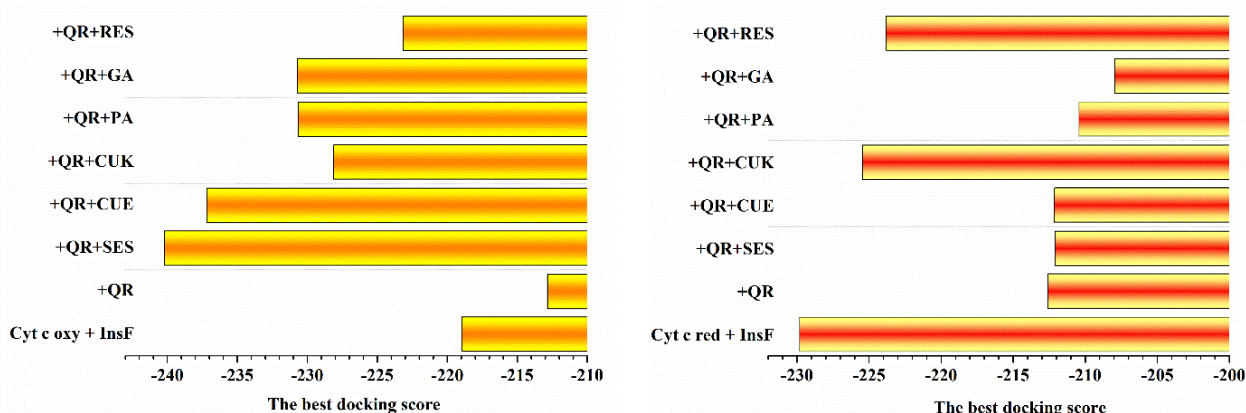
Figure 4. The changes in the best docking score calculated for the complexes cyt *c* oxy/red – quercetin – sesamin / curcumin / phenolic acid / gallic acid / resveratrol – InsF. The best docking score characterizes the affinity of InsF for cyt *c*. The abbreviations used are: quercetin (QR), sesamin (SES), curcumin enol form (CUE, curcumin keto form (CUK), phenolic acid (PA), gallic acid (GA), resveratrol (RES)

CONCLUSIONS

To summarize, the molecular docking studies delineating the interactions between cyt *c* and amyloid fibrils, alongside the modulatory presence of quercetin, provide an enlightening snapshot of the polyphenolic intervention in amyloidogenic landscapes. The complexation of QR with cyt *c* and the consequent modulation of its binding affinity to amyloid fibrils of insulin are suggestive of a polyphenol-mediated alteration in the protein-fibril interface, effectuating a decrease in affinity irrespective of the redox state of the cytochrome. This discovery highlights the potential of quercetin to impede non-specific interaction between functional proteins and amyloid fibrils, suggesting a protective mechanism that may preserve the physiological functions of cyt *c* against amyloid-induced perturbation. Such a phenomenon is of considerable interest, underscoring the broad utility of polyphenols as molecular agents capable of modifying the course of protein aggregation diseases by stabilizing functional proteins against the aberrant binding to amyloid fibrils.

ORCID
Valeriya Trusova, https://orcid.org/0000-0002-7087-071X; **Uliana Tarabara,** https://orcid.org/0000-0002-7677-0779
Galyna Gorbenko, https://orcid.org/0000-0002-0954-5053

REFERENCES
[1] E. Chatani, K. Yuzu, Y. Ohhashi, and Y. Goto, Int. J. Mol. Sci. **22**, 4349 (2021). https://doi.org/10.3390/ijms22094349
[2] A. Buell, Chem. Sci. **12**, 10177 (2022). https://doi.org/10.1039/D1SC06782F
[3] D. Li, and C. Liu, Biochemistry 59, 639 (2020). https://doi.org/10.1021/acs.biochem.9b01069
[4] H. Koike, and M. Katsuno, Molecules **26**, 4611 (2021). https://doi.org/10.3390/molecules26154611
[5] H. Xie, and C. Guo, Front. Mol. Biosci. **7**, 629520 (2021). https://doi.org/10.3389/fmolb.2020.629520
[6] P. Bhosale, S. Ha, P. Vetrivel, H. Kim, S. Kim, and G. Kim, Transl. Cancer Res. **9**, 7619 (2020). https://doi.org/10.21037/tcr-20-2359
[7] A. Rana, M. Samtiya, T. Dhewa, V. Mishra, and R. Aluko, J. Food. Chem. **46**, e14264 (2022). https://doi.org/10.1111/jfbc.14264
[8] Y. Nian, Y. Zhang, C. Ruan, and B. Hu, Curr. Opin. Food Sci. **43**, 99 (2022). https://doi.org/10.1016/j.cofs.2021.11.005
[9] H. Kobayashi, M. Murata, S. Kawanishi, and S. Oikawa, Int. J. Mol. Sci. **21**, 3561 (2020). https://doi.org/10.3390/ijms21103561
[10] Y. Yan, H. Tao, J. He, and S-Y. Huang, Nat. Protoc. **15**, 1829–1852 (2020). https://doi.org/10.1038/s41596-020-0312-x
[11] D. D. Schneidman-Duhovny, Y. Inbar, R. Nussimov, and H. Wolfson, Nucl. Acid Res. **33**, W363 (2005). https://doi.org/10.1093/nar/gki481
[12] Z. Zhou, T. Arroum, X. Luo, R. Kang, Y. Lee, D. Tang, M. Hüttemann, and X. Song, Cell Death Differ. **31**, 387 (2024). https://doi.org/10.1038/s41418-024-01284-8
[13] G. Perez-Mejias, A. Diaz-Quintana, A. Guerra-Castellano, I. Diaz-Moreno, and M. De la Rosa, Coord. Chem. Rev. **450**, 214233 (2022). https://doi.org/10.1016/j.ccr.2021.214233
[14] S. Watson, G. McStay, Int. J. Mol. Sci. **21**, 7254 (2020). https://doi.org/10.3390/ijms21197254
[15] A. Bigi, R. Cascella, F. Chiti, C. Cecchi, Bioessays **44**, e2200086 (2022). https://doi.org/10.1002/bies.202200086

ВЗАЄМОДІЯ АМІЛОЇДНИХ ФІБРИЛ З ФУНКЦІОНАЛЬНИМИ БІЛКАМИ: МОДУЛЮЮЧИЙ ЕФЕКТ ПОЛІФЕНОЛІВ

Валерія Трусова, Уляна Тарабара, Галина Горбенко

Кафедра медичної фізики та біомедичних нанотехнологій, Харківський національний університет імені В.Н. Каразіна
м. Свободи 4, Харків, 61022, Україна

Вивчення взаємодій між функціональними білками та амілоїдними фібрилами є ключовим для розуміння молекулярної основи амілоїдних захворювань, які характеризуються неправильним згортанням білків та їх агрегацією. Поліфеноли, завдяки своїм різноманітним біологічним властивостям, привертають увагу своєю потенційною здатністю модулювати ці взаємодії, тим самим впливаючи на прогресування захворювання та відкриваючи нові терапевтичні можливості. У даному дослідженні методом молекулярного докінгу було вивчено вплив кверцетину та його бінарних комбінацій з іншими поліфенолами на зв'язування між цитохромом *c* (відновлена та окиснена форми) та амілоїдними фібрилами інсуліну та аполіпопротеїну A-I. Отримані результати свідчать на користь того, що комплексування кверцетину з цитохромом *c* знижує силу зв'язування фібрил інсуліну для обох форм білка. Протилежний ефект було виявлено для фібрил аполіпопротеїну A-I. Таке модулювання було інтерпретовано у рамках конкурентних або алостеричних ефектів. Крім того, хоча бінарні комбінації кверцетину з іншими поліфенолами не знижували силу зв'язування фібрил інсуліну для окисленого цитохрому *c*, вони знижували силу зв'язування у випадку відновленої форми. Ці дані підкреслюють вибірковий та значний вплив поліфенольних сполук на взаємодії між амілоїдними фібрилами та функціональними білками, пропонуючи потенційні шляхи для терапевтичних анти-амілоїдних стратегій.

Ключові слова: *амілоїдні фібрили; функціональні білки; поліфеноли; молекулярний докінг*

DECIPHERING THE MOLECULAR DETAILS OF INTERACTIONS BETWEEN HEAVY METALS AND PROTEINS: MOLECULAR DOCKING STUDY

O. Zhytniakivska*, U. Tarabara, K. Vus, V. Trusova, G. Gorbenko

Department of Medical Physics and Biomedical Nanotechnologies, V.N. Karazin Kharkiv National University
4 Svobody Sq., Kharkiv, 61022, Ukraine
*Corresponding Author: olga.zhytniakivska@karazin.ua
Received April 2, 2024; revised May 6, 2024; February, accepted May 26, 2024

Understanding the interaction of heavy metals with proteins is pivotal for unraveling their roles in biochemical processes and metal-induced diseases, with wide-ranging implications spanning medicine, environmental science, and biotechnology, thereby driving progress in therapeutics, pollution mitigation, and biomaterial innovation. In the present study the molecular docking technique was employed to identify and characterize the binding sites of the set of heavy metals (Cu^{2+}, Fe^{3+}, Mg^{2+}, Mn^{2+}, Zn^{2+}, Cd^{2+}, Fe^{2+}, Ni^{2+}, Hg^{2+}, Co^{2+}, Cu^{+}, Au^{+}, Ba^{2+}, Pb^{2+}, Pt^{2+}, Sm^{3+}, and Sr^{2+}) and proteins ((β-lactoglobulin, 7S globulin and glycinin from soybeans) to evaluate the impact of protein structure on their ion-binding abilities and selectivity. Our docking results indicate that essential and toxic heavy metals interact with multiple binding sites of proteins, presumably by electrostatic interactions and metal chelation with cysteine, aspartic acid, glutamic acid, and histidine amino acid residues. The comparison of binding residues favorable for heavy metal complexation among different proteins indicates that metals exhibit distinct preferences for various amino acid residues highlighting the importance of both the metal and the protein properties for stabilizing protein-metal complexation.

Keywords: *Protein-metal interaction; Heavy metals; Molecular docking*
PACS: 87.14.Cc, 87.16.Dg

Heavy metals, a loosely defined group of elements, including transition metals and some metalloids, typically have an atomic number greater than 20 and atomic density above 5 g·cm^{-3} [1,2]. While the classification of heavy metals as toxic, beneficial, or essential for living organisms is a topic of ongoing debate, certain heavy metals such as Mg^{2+}, Ca^{2+}, Fe^{3+}, Mn^{2+}, Co^{2+}, Cu^{2+} and Zn^{2+} are currently recognized as essential in a trace amount [2,3]. In contrast, non-essential heavy metal ions like Pb^{2+} and Hg^{2+}, are toxic even at trace levels, causing alterations to biochemical processes and potentially leading to various diseases in living organisms [4,5]. Aquatic organisms and humans are exposed to the influence of essential and non-essential heavy metals through multiple sources, including water, air, soil, and food [5]. Despite the numerous studies, the molecular mechanisms underlying heavy metal toxicity are not fully understood [6,7]. The primary factors by which heavy metals can possess their toxic effect are i) generation of reactive oxygen species and oxidative stress [8,9]; ii) disruption of membrane function and nutrient assimilation [10,11]; iii) DNA damage and impairment of DNA repair mechanism [12,13] and iv) protein function and activity perturbation [14,15]. It is well-established that proteins are primary targets of heavy metals. Metals can interfere with the biological activity of properly folded proteins through various interactions, including binding to free thiols or other functional groups, displacing essential metal ions in metalloproteins, or catalyzing the oxidation of amino acid side chains, to name only a few [14-16]. Understanding the interactions between proteins and heavy metals is not only crucial for comprehending their biochemical roles, regulation, and the molecular basis of metal-induced diseases, but also significantly important for medicine, environmental science, and biotechnology. More specifically, the integration of metal ions with protein systems led to the design of highly ordered protein-based hybrid nanomaterials possessing unique electric, optical, and electronic properties, high photostability, and biocompatibility, making them attractive for different applications in biological imaging, solar energy conversation, chemical sensing, to name only a few [17-23]. In particular, amyloid fibrils self-assembled from different proteins (β-lactoglobulin, globulin, silk, albumin, etc) have demonstrated remarkable efficacy in purifying wastewater contaminated with heavy metals and radioactive compounds [20-23]. Additionally, metal-binding proteins can be engineered to enhance the bioavailability of essential metals in nutritional supplements or for designing metal-based drugs with optimized efficacy and safety [24, 25]. Moreover, understanding the molecular mechanisms underlying the interactions between plant proteins and heavy metals is essential for developing effective phytoremediation strategies [26, 27]. The above application necessitates a comprehensive understanding of the protein's metal-binding capabilities. Experimental techniques, such as X-ray crystallography [28], NMR spectroscopy [29], electron microscopy [19], and absorption spectroscopy [30] have been found to offer the most reliable information for studying protein-metal interactions. Despite their precision and accuracy in identifying metal ions, these techniques have significant disadvantages, including high costs, lengthy execution times, and challenges. During the last decades computation methods have become invaluable tools for relatively quick and easy identification of metal-protein binding sites.

In the present study, we employed the molecular docking technique to evaluate the impact of protein structure on their ion-binding abilities and selectivity. More specifically, by varying both the protein amino acid composition (β-lactoglobulin, 7S globulin and glycinin from soybeans) and heavy metal ions (Cu^{2+}, Fe^{3+}, Mg^{2+}, Mn^{2+}, Zn^{2+}, Cd^{2+}, Fe^{2+},

Ni^{2+}, Hg^{2+}, Co^{2+}, Cu^+, Au^+, Ba^{2+}, Pb^{2+}, Pt^{2+}, Sm^{3+}, and Sr^{2+}), we attempted to identify and characterize protein-ion binding sites.

MOLECULAR DOCKING STUDIES

The three-dimensional X-ray crystal structures of proteins were obtained from the Protein Data Bank (https://www.rcsb.org/) using the PDB IDs 3AUP, 1OD5 and 1QG5 for 7S globulin from soybean, glycinin, and bovine β-lactoglobulin, respectively. The chain A of the three-dimensional X-ray crystal structures of 7S globulin and glycinin, were selected for the docking studies. To define the most energetically favorable binding sites for the heavy metal ions on the proteins, molecular docking studies were performed using the MIB2 Metal Ion-Binding site prediction and modeling server [31]. The MIB2 employs the fragment transformation technique and the AlphaFold protein structure database for the precise binding site predictions for 18 metal ions, including Ca^{2+}, Cu^{2+}, Fe^{3+}, Mg^{2+}, Mn^{2+}, Zn^{2+}, Cd^{2+}, Fe^{2+}, Ni^{2+}, Hg^{2+}, Co^{2+}, Cu^+, Au^+, Ba^{2+}, Pb^{2+}, Pt^{2+}, Sm^{3+}, and Sr^{2+} [31].

RESULTS AND DISCUSSION
β-lactoglobulin

β-lactoglobulin, a small globular whey protein with a molecular weight of approximately 18.4 kDa, is currently widely employed in the development of nanocomposites for the detection of heavy metal ions [22, 32]. More specifically, Zang and colleagues found, that β-lactoglobulin-stabilized fluorescent gold nanoclusters are promising for the selective nanomolar detection of Hg^{2+} in beverages, urine, and serum [32]. Peydayesh et al demonstrated the β-lactoglobulin amyloid fibril effectiveness in the removal of heavy metals by fabricating a hybrid activated carbon membrane [22]. Heavy metal ions have been found to adsorb efficiently and strongly onto β-lactoglobulin amyloid fibrils through robust supramolecular metal-ligand interactions with the magnitude of absorption dependent on the specific heavy metal [22]. Designing lactoglobulin-based nanosystems for heavy metal detection and targeted delivery requires a thorough understanding of the protein's metal-binding capabilities. These insights are essential for optimizing the design and effectiveness of such nanosystems in various applications. In the present study, we employed a molecular docking technique to identify β-lactoglobulin-metal binding sites. Docked positions of heavy metal ions in the β-lactoglobulin structure corresponding to the best docking score are presented in Figure 1.
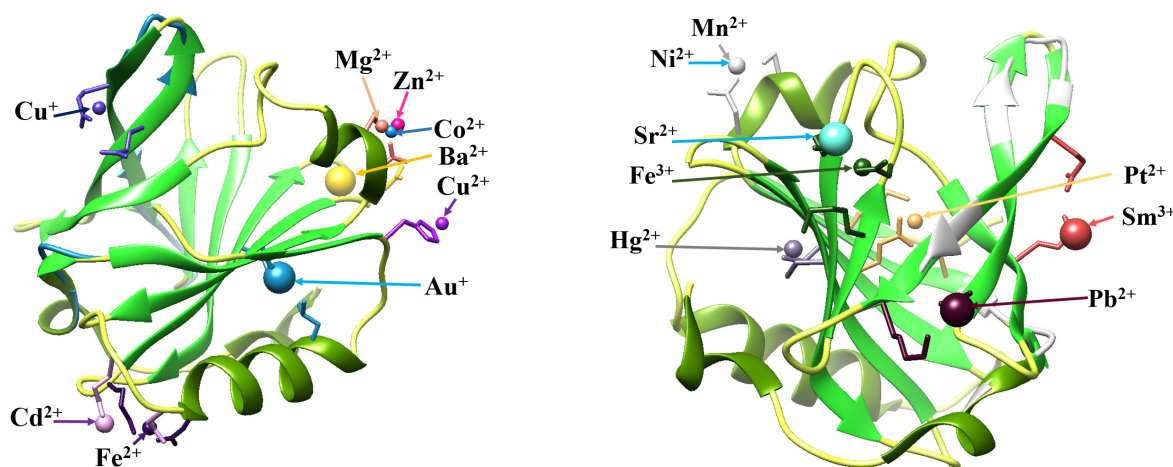
Figure 1. Docked positions of heavy metal ions in the 3D β-lactoglobulin structure corresponding to the best docking score

The protein β-lactoglobulin comprises 162 amino acid residues, featuring one free cysteine and two disulfide bonds [33]. Three-dimensional crystallographic studies have revealed that β-lactoglobulin predominantly adopts a β-sheet configuration, comprising nine antiparallel β-strands (A to I), where strands A-D form one surface of the β-barrel (calyx), while strands E-I constitute the opposite surface [33]. The sole α-helical segment, consisting of three turns, is located at the COOH terminus and lies on the outer surface of the calyx, following strand H [33]. Our docking results indicate that essential and toxic heavy metals bind to multiple binding sites of β -lactoglobulin, presumably into the outskirts of the β-barrel. The amino acid residues, participating in the interaction of metal ions with protein are presented in Table 1. More specifically, the essential heavy metals such as Mn^{2+}, Co^{2+}, Mg^{+}, and Zn^{2+} interact with the strand A of the β-barrel with the residue Asp and Ser. Notably, the amino acid residues such as Ser or Asp contain nitrogen or oxygen atoms that play an electron donor role in the ligand-protein interactions. In addition, our docking results indicate that Zn^{2+} is energetically favorable to interact with the F strand of protein. The presence of two sets of independent binding sites for zinc was experimentally observed for the other whey protein α-lactalbumin [34]. The highly toxic metal ions such as Pb^{2+}, Pt^{2+}, and Sm^{3+} form contacts with the B-strand of protein, whereas Cd^{2+} and Hg^{2+} preferably interact with the residues near the H-strand. The negatively charged glutamic acid participates in the Pb^{2+}, Pt^{2+}, Sm^{3+} and Cd^{2+} ion-protein complexation. In turn, our docking results indicate that highly toxic Hg^{2+} interacts with the polar cysteine and hydrophobic valine and leucine.

Table 1. Amino acid residues participating in the formation of the most energetically favorable metal-protein complexes

Metal	β-lactoglobulin	glycinin	7 S globulin
Cu^{2+}	Pro144, His146	Gln36, His173, Glu175, His21, Asn34, His37	His23, Pro269, Cys81, His90
Fe^{3+}	Lys83, Glu89, Asp96, Asp98	His211, Gln215, Glu221	Gln69, Glu113, Cys65, Asn92
Mg^{2+}	Asp28, Ile29	Asp231, Asp232, Asp121, Glu333, Asn334	Asp114, Val115, Asp17, Ser19, Thr20
Mn^{2+}	Asp28, Ser30	Asp413, Gly414	Asp374, Arg377, His215, Asp216
Zn^{2+}	Asp28, Ser30, Asp96, Asp98	His173, Glu175, Asp20, His37	His215, Asp216, Cys65, Ser67
Cd^{2+}	Glu127, Asp129, Glu131, Lys135	Asp413, Gly414, Asp231, Glu233	Gln171, His175, Asn50, Ser140, Cys141
Fe^{2+}	Lys10, Glu127, Asp129	Lys210, His211, Gln215	His66, His76, Cys78
Ni^{2+}	Asp28, Ser30	Arg115, His116, Lys210, His211	His388, Asp396, His76, Cys78, Cys94
Hg^{2+}	Cys106, Leu117, VAl118, Cys119	Phe82, Cys85, Cys327	Phe64, Cys65, Cys78
Co^{2+}	Asp28, Ser30, Glu127, Asp129	Asp20, His37, Lys210, His211	Cys81, His90, Ser389, His390
Cu^{+}	Gln59, Cys66	Cys9, Cys42, Pro425	Cys70, His76, Cys94, Cys81, His90
Au^{+}	Cys106, Lys140	Cys85, Glu323, Pro19, Gln36, His37	Cys141, Ala142, Ser187, Glu368, Cys394
Ba^{2+}	Glu108, Asn109, Gln115	Thr136, Gly137, Asp138, Glu139	Asp334, Lys335, Glu333
Pb^{2+}	Glu51, Glu52, Asp53, Glu74	Asp232, Arg234	Cys65, Cys78, Gly302, Lys303, Cys304, Cys345
Pt^{2+}	Glu51, Glu52, Met24, Arg40, Lys95	Asp232, Lys235	Gln275, Met353, His270, Met349
Sm^{3+}	Glu44, Glu45, Gln68	Asp231, Glu233, Asp232, Lys235	Asp374, Arg377, Glu52, Gln53
Sr^{2+}	Asp85, Leu87 Glu89	Asp20, His21, Thr32, Glu172, Asp157, Gln158, Thr176	Asp41, Ser265, Ser267

According to numerous studies, heavy metals bind to proteins through different intermolecular interactions, presumably electrostatic interactions, and metal chelation [21-32]. Several factors influence the binding of metals to proteins, including i) the properties of the metal such as its valence state, ionic radius, and charge-accepting ability and ii) the protein properties, such as amino-acid sequence, the accessibility of the potential metal-binding groups, type of the interactions stabilizing protein-metal complexation, etc [21-32]. According to the Hard Acid Soft Base theory describing the interaction of heavy metals based on their inherent chemistry, the proteins possess a higher binding ability to the "soft" metals (Cd^{2+}, Hg^{2+}, Cu^{+}, Au^{+}, Pt^{2+}) in comparison with "hard" metals (Ca^{2+}, Mg^{2+}, Mn^{2+}, and Sr^{2+}) [35]. The above preference is connected with the differences in their binding mechanism: metal chelation is predominant in maintaining the structural integrity of the protein-soft metal complexes, whereas electrostatic interactions are responsible for the "hard" metal binding [35]. As can be seen from Table 1, glutamic acid participates in the Pb^{2+}, Pt^{2+}, Sm^{3+} and Cd^{2+} ion-protein complexation, whereas the "hard metals" were found to form contacts presumably with the negatively charged aspartic acid, which is in good agreement with the Hard Acid Soft Base theory [35]. Notably, our docking results demonstrated the involvement of the Lys, Leu and Val amino acid residues in the metal-protein interaction of "soft" (Cd^{2+}, Hg^{2+}, Cu^{+}, Au^{+}, Pt^{2+}) and borderline (Ni^{2+}, $Cu2^{+}$, Pb^{2+}) Lewis acids indicating the possible role of the hydrogen bonds, hydrophobic and van der Waals interactions on the stabilization of protein-metal complexes.

7S globulin from soybean

The 7S globulin is one of the major globulins found in soybean seeds [36]. Despite its dual subunit composition and oligomeric assembly, the protein possesses a compact structure, comprising β-sheets and a few α-helices, with its most notable feature being 12 cysteine residues [36]. These cysteines, conserved among homologous proteins, form a network of five intra-chain and one inter-chain disulfide bridges [36]. Recently it was demonstrated, that soy c exhibits excellent metal-chelating properties [37]. Moreover, Li et al/ showed the ability of soy protein-based polyethyleneimine hydrogel to selectively adsorb and recycle copper in wastewater [38]. Additionally, the soy protein hollow microspheres were highly effective for the sorption of metal ions, with the absorption capacity dependent on the heavy metal [21]. Despite numerous studies demonstrating the potential of soy protein-based nanocomposites for purifying water from heavy metals, the factors responsible for their metal selectivity require further investigation. In an attempt to understand the mechanism of the complexation of different heavy metal ions with the 7S globulin, we identified their preferred binding sites (Figure 2).

Our docking results indicate that essential and toxic heavy metals bind to multiple binding sites of soy protein globulin 7S and have at least two high-score binding sites. More specifically, as seen from Figure 2 and Table 1, all heavy metals (excepting Ni^{2+}, Au^{+}, Pb^{2+}, Pt^{2+}, and Sm^{3+}) form contacts presumably with the amino-acid residues of α-subunit (residues 25-275). The toxic metals Ni^{2+}, Au^{+}, Pb^{2+}, Pt^{2+}, and Sm^{3+} were found to interact with both α-subunit (residues 25-275) and low-molecular-weight β-subunit (residues 276-427), with the binding preferences higher for the latter. As seen in Figure 2, the heavy metal formed stable contacts with the residues belonging presumably to the β-strands of the protein. However, we found that Cd^{2+} and Fe^{2+} were energetically favorable to interact with the α-helixes. In addition,

Ba^{2+} and Ni^{2+} are positioned in the $3_{10-helix}$ of protein. Importantly, cysteine residues are among the amino-acid residues participating in stabilizing protein-metal complexes for all metals except Mg^{2+}, Ba^{2+}, and Pt^{2+}. The cysteine residues forming the disulfide bonds within the protein are responsible for the stability of the soy protein globulin 7S [36].
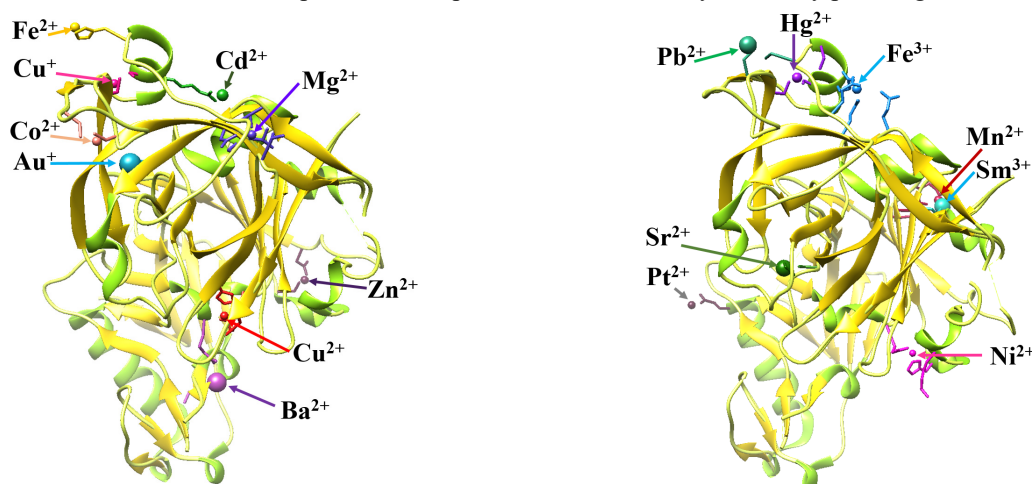
Figure 2. Schematic representation of the energetically most favorable metal complexes with globulin (chain A) obtained using the Metal Ion-Binding site prediction and modeling server.

Glycinin from soybean

Soybean glycinin, a member of the 11S globulin family, is a hexameric protein with a molecular weight of approximately 360 kDa, composed of five subunits: A1aB1b, A1bB2, A2B1a, A3B4, and A5A4B3 [39]. It is formed by the stacking of two trimers, each consisting of three subunits [39]. These subunits are composed of an acidic polypeptide (A) with a molecular weight of 35 kDa and a basic polypeptide (B) with a molecular weight of 20 kDa, which are linked by disulfide bonds [39]. The soybean glycinin protomer consists of four visible and four disordered regions (residues 1–6, 93–107, 179– 199, and 252–320) comprising 27 strands and 7 helices which are folded into two jelly-roll-barrel domains and two helix domains [39]. As seen from Figure 3, the heavy metals, formed stable contacts with the various residues present in the ordered glycinin regions and don't interact with the disordered regions. The main results obtained from molecular docking studies are:

i)   Heavy metals excluding Fe^{3+}, Mn^{2+}, Zn^{2+}, Fe^{2+}, Ni^{2+}, $Co^{2}+$, Ba^{2+}, Pb^{2+}, Pt^{2+}, and Sm^{3+} exhibit at least two energetically favorable binding sites;

ii) Mg^{2+}, Cd^2, Pb^{2+}, and Pt^{2+} tend to interact with the residues Asp 232, Glu 233, Arg 234 and Lys 235 located near the second helix of protomer;

iii) Fe^{3+}, Fe^{2+}, Ni^{2+}, and Co^{2+} show preferential binding sites comprising the amino acid residues 211-215 (Lys, His, Gln) within the helix region. Ni^{2+} additionally forms the high-score complex with the residues in the proximity to β-strand F (Arg15 and His 116), while Co^{2+} interacts also with the residue of β-strand A.

iv) Mn^{2+}, Cd^{2+} bind to the strand region containing residues Asp 413 and Gly 414.
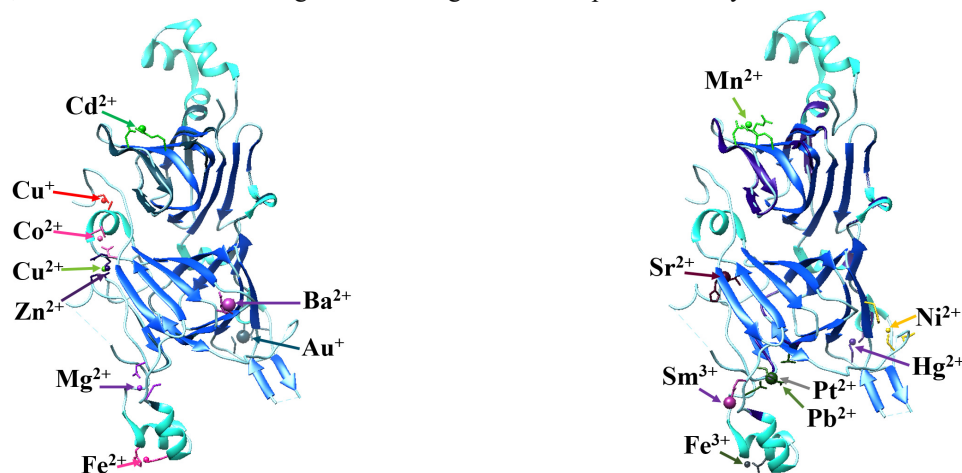
Figure 3. Schematic representation of the energetically most favorable metal complexes with glycinin (chain A) obtained using the Metal Ion-Biding site prediction and modeling server.

The comparison of the binding residues favorable for the complexation of heavy metals between the proteins indicates that metals yield various binding preferences for different amino-acid residues. More specifically, for Fe^{3+} was

energetically favorable to form contacts with Lys, Glu and Asp amino acids of β-lactoglobulin, whereas His, Gln and Gln, Cys were responsible for metal-protein complexation of glycinin and 7S globulin, respectively. Zn^{2+} interacts with the Asp and Ser residue of β-lactoglobulin, His, Glu of glycinin, whereas for the 7S globulin, cysteine residues were also involved in the complexation. Although electrostatic interactions and metal chelation are the preferential binding modes of metals, our docking results indicate the importance of the hydrogen bonds, hydrophobic and van der Waals interactions on the stabilization of protein-metal complexes.

CONCLUSIONS

In the present study, the molecular docking technique was employed to evaluate the impact of protein structure on their ion-binding abilities and selectivity. By varying both the protein amino acid composition (β-lactoglobulin, 7S globulin and glycinin from soybeans) and heavy metal ions (Cu^{2+}, Fe^{3+}, Mg^{2+}, Mn^{2+}, Zn^{2+}, Cd^{2+}, Fe^{2+}, Ni^{2+}, Hg^{2+}, Co^{2+}, Cu^+, Au^+, Ba^{2+}, Pb^{2+}, Pt^{2+}, Sm^{3+}, and Sr^{2+}), the protein-ion binding sites were identified. The docking results suggest that both essential and toxic heavy metals interact with multiple protein binding sites, primarily through electrostatic interactions and metal chelation involving cysteine, aspartic acid, glutamic acid, and histidine residues. The comparison of binding residues favorable for heavy metal complexation among different proteins indicates that metals exhibit distinct preferences for various amino acid residues highlighting the importance of both the metal properties (valence state, charge-accepting ability, etc) and the protein properties, (amino-acid sequence, the accessibility of the potential metal-binding groups, etc).

ORCID

Olga Zhytniakivska, https://orcid.org/0000-0002-2068-5823; **Uliana Tarabara,** https://orcid.org/0000-0002-7677-0779
Kateryna Vus, https://orcid.org/0000-0003-4738-4016; **Valeriya Trusova,** https://orcid.org/0000-0002-7087-071X
Galyna Gorbenko, https://orcid.org/0000-0002-0954-5053

REFERENCES

[1] J.H. Duffus, Pure Appl. Chem. **74**(5), 793 (2002). https://doi.org/10.1351/pac200274050793.
[2] P.B. Tchounwou, C.G. Yedjou, A.K. Patlolla, and D.J. Sutton. Exp. Suppl. **101**, 133 (2012). https://doi.org/10.1007/978-3-7643-8340-4_6
[3] M.A. Zoroddu, J. Aaseth, G. Crisponi, S. Medici, M. Peana, and V.M. Nurchi, J. Bioorg Chem. **195**, 120 (2019). https://doi.org/10.1016/j.jinorgbio.2019.03.013
[4] M. Balali-Mood, K. Naseri, Z. Tahergorabi, M. Reza Khazdair, and M. Sadeghi, Front Pharmacol. **12**, 643972 (2021). https://doi.org/10.3389/fphar.2021.643972
[5] R. Singh, N. Gautam, A. Mishra, and R. Gupta, Indian J. Pharmacol. **43**, 246 (2011). https://doi.org/10.4103/253-7613.81505
[6] J.-J. Kim, Y.-S. Kim, V. Kumar. And J. Trace Elem. Med Biol. **54**, 226 (2019). https://doi.org/10.1016/j.jtemb.2019.05.003
[7] M. Jaishankar, T. Tseten, N. Anbalagan, B. Mathew, and K. Beeregowda, Interdiscip Toxicol. **7**, 60 (2014). https://doi.org/10.2478/intox-2014-0009
[8] M. Valko, H. Morris, and M.T.D. Cronin, Curr Med. Chem. **12**, 1161 (2005). https://doi.org/10.2174/09298670537646635
[9] J.G. Paithankar, S. Saini, S. Dwidevi, A. Sharma, and D.K. Chowdhuri, Chemosphere, **262**, 128350 (2021). https://doi.org/10.1016/j.chemosphere.2020.128350
[10] Q. Sun, Y. Li, L. Shi, R. Hussain, K. Mehmood, Z. Tang, and H. Zhang, Toxicology, **469**, 153136 (2022). https://doi.org/10.1016/j.tox.2022.153136
[11] Z. Fu, and S. Xi. Toxicol. Mech. Methods. **30**, 167 (2020). https://doi.org/10.1080/15376516.2019.1701594
[12] C. Giaginis, E. GAtzidou, S. Theocharis, Toxicol. Appl. Pharmacol, **213**, 282 (2006). https://doi.org/10.1016/j.taap.2006.03.008
[13] M.E. Morales, RS. Derbes, C.M. Ade, et al., PloS One, **11**, e0151367 (2016). https://doi.org/ journal.pone.0151367
[14] D. Witkowska, J. Słowik, and K. Chilicka, Molecules, **26**, 6060 (2021). https://doi.org/10.3390/molecules26196060
[15] J.L. Reyes, E. Molina-Jijon, R. Rodriguez-Munoz, et al. Biomed Res. Int. **2013**, 730789 (2013). https://doi.org/10.1155/2013/730789
[16] S. Nahar, and H.A. Tajmir-Riahi, J. Coll. Int. Sci. **178**, 648 (1996). https://doi.org/10.1006/jcis.1996.0162
[17] B. Saif, and P. Yang, ACS Appl/ Bio Mater. **4**, 1156 (2021). https://doi.org/10.1121/acsabm.0c01375
[18] A. Beloqui, and A.L. Cortajarena, Curr. Opin. Struct. Biol. **63**, 74 (2020). https://doi.org/10.1116/j.sbi.2020.04.005
[19] A. Aires, D. Maestro, J. Ruiz del Ro, et al. Chem. Sci, **12**, 2480 (2021). https://doi.org/10.1039/DOSC05215A
[20] W.L. Soon, M. Peydayesh, R. Mezzenga, and A. Mizerez, Chem Eng. J. **445**, 136513 (2022), https://doi.org/10.1016/j.cej.2022.136513
[21] D. Liu, Z. Li, W. Li, Z. Zhong, J. Xu, J. Ren, and Z. Ma, Ind. Eng. Chem. Res. **52**(32), 11036 (2013). https://doi.org/10.1021/ie401092f
[22] M. Peydayesh, S. Bolisetty, T. Mohammadi, and R. Mezzenga, Langmuir, **35**, 4161 (2019) https://doi.org/10.1021/acs.langmuir.8b04234.
[23] A. Gao, K. Xie, X. Song, K. Zhang, and A. Hou, Ecol. Eng. **99**, 343 (2017). https://doi.org/10.1016/j.ecoleng.2016.11.008
[24] A. de Almeida, B.L. Oliveira, J.D.G. Correia, G. Soveral, and A. Casini. Coord. Chem. Rev. **257**, 2689 (2013). https://doi.org/10.1016/j.ccr.2013.01.031

[25] T.A. Sales, I.G. Prandi, et al. Int. J. Mol. Sci. **20**, 1829 (2019). https://doi.org/10.3390/ijms20081829

[26] P. Sharma, A.K. Pandey, A. Udayan, and S. Kumar. Bioresource Technology, **326**, 1124750 (2021). https://doi.org/10.1016/j.biortech.2021.124750

[27] Z. Yang, F, Yang, J.L. Liu, H.T. Wum H. Yang, et al. Sci Total Environ. **809**, 151099 (2022). https://doi.org/10.1016/j.scitotenv.2021.151099

[28] K.B. Handing, E.Niedzialkowska, I.G. Shabalin, M.L. Kuhn, H. Zheng, and W. Minor. Nat Protoc. **13**, 1062 (2018). https://doi.org/10.1038/nprot.2018.018

[29] D. Shalev. Int. J. Mol. Sci. **23**, 15957 (2022). https://doi.org/10.3390/ijms232415957.

[30] M.P. Chantada-Varquez, A. Moreda-Pineiro, M.C. Barciels-Alonso, and P. Bermejo-Barrera, Appl. Spectr. Rev. **52**, 145 (2017). https://doi.org/10.1080/05704928.2016.1213736

[31] Y.F. Lin, C.W. Cheng, C.S. Shin, J.K. Hwang, C.S. Yu, and C.H. Lu, J. Chem. Inf. Model, **56**, 2287 (2016). https://doi.org/10.1021/acs.jcim.6b00407

[32] J. Zang, C. Li, K. Zhou, H. Dong, B. Chen, F. Wang, and G. Zhao, Anal. Chem. **88**, 10275 (2016). https://doi.org/10.1021/acs.analchem.6b03011

[33] K.M.G. Olibeira, V.L. Valente-Mesquita, M.M. Botelho, L. Sawyer, S.T. Ferreir, and I. Polikarpov, Europ. J. Biochem. **268**, 477 (2003). https://doi.org/10.1046/j.1432-1033.2001.01918.x

[34] A. Rodzik, P. Pomastowski, G.N. Sagandykova, and B. Buszewski, Int. J. Mol. Sci, **21**, 2156 (2020). https://doi.org/10.3390/ijms21062156

[35] R. Pearson, J. Chem. Educ. **45**, 981 (1968). https://doi.org/10.1021/ed045p581

[36] T. Hashimoto, T. Shimuzu, M. Yamabe, M. Taichi, et al. FEBS Journal, **278**, 1944 (2011). https://doi.org/10.1111/j.1742-4658.2011.08111.x

[37] D. Hwang. And S. Damodaran, Int. J. Appl. Polymer Sci. **64**, 891 (1997). https://doi.org/10.1002/(SICI)1097-4628(19970502)64:5<891::AID-APP9>3.0.CO;2-K

[38] J. Liu, D. Su, J. Yao, Y. Huang, Z. Shao, and X. Chen, J. Mat. Chem. A, **5**, 4163 (2017). https://doi.org/10.1039/C6TA10814H

[39] M. Adachi, J. Kanamori, T. Masuda, K. Yagasaki, K. Kitamura, B. Mikami, and S. Utsumi. PNAS, **100**, 7395 (2003). https://doi.org/10.1073/pnas.0832158100

ДОСЛІДЖЕННЯ МОЛЕКУЛЯРНИХ ДЕТАЛЕЙ ВЗАЄМОДІЇ МІЖ ВАЖКИМИ МЕТАЛАМИ ТА БІЛКАМИ: МОЛЕКУЛЯРНИЙ ДОКІНГ

О. Житняківська, У. Тарабара, К. Вус, В. Трусова, Г. Горбенко

Кафедра медичної фізики та біомедичних нанотехнологій, Харківський національний університет імені В.Н. Каразіна

м. Свободи 4, Харків, 61022, Україна

Розуміння взаємодії важких металів з білками є ключовим для розкриття їх ролі у різноманітних біохімічних процесах в медицині, екології та біотехнологіях, що сприяє розробці принципово нових терапевтичних стратегій та інноваційних гібридних біоматеріалів. У даній роботі з використанням методу молекулярного докінгу було визначено та охарактеризовано центри зв'язування важких металів (Cu^{2+}, Fe^{3+}, Mg^{2+}, Mn^{2+}, Zn^{2+}, Cd^{2+}, Fe^{2+}, Ni^{2+}, Hg^{2+}, Co^{2+}, Cu^+, Au^+, Ba^{2+}, Pb^{2+}, Pt^{2+}, Sm^{3+}, and Sr^{2+}) з білками (β-лактоглобулін, 7S глобулін і гліцинін з соєвих бобів) для оцінки впливу структури білка на їхню метал-зв'язувальну здатність та селективність. Отримані результати молекулярного докінгу вказують на взаємодію життєво важливих та токсичних важких металів з різними зв'язувальними сайтами білків, ймовірно, через електростатичні взаємодії та хелацію металів з амінокислотними залишками цистеїну, аспарагінової кислоти, глутамінової кислоти та гістидину. Порівняння залишків з якими взаємодії метал між різними білками, свідчить про роль різних амінокислотних залишків, підкреслюючи важливість як властивостей металу, так і білка для стабілізації білок-металевого комплексоутворення.

Ключові слова: *взаємодія білок-метал; важкі метали; молекулярний докінг*

ERRATUM: PERMITTIVITY MODEL SELECTION BASED ON SIZE AND QUANTUM-SIZE EFFECTS IN GOLD FILMS

Iuliia Riabenko[a,b,*], Sergey Shulga[a], Nikolai A. Makarovskii[c], Konstantin Beloshenko[a]

[a]*V.N. Karazin Kharkiv National University, School of radiophysics, biomedical electronics and computer systems, Kharkiv, Ukraine*
[b]*Institute of Quantum Optics, Leibniz University Hannover, Hannover, Germany*
[c]*V.N. Karazin Kharkiv National University, School of Physics, Kharkiv, Ukraine*
Corresponding Author e-mail: jriabenko@karazin.ua, riabenko@iqo.uni-hannover.de

The purpose of this Erratum is to correct a misprint presented in the original article.

Table 1, in the published article, is to be read as follows:

Table 1. The optical and dimensional properties of the film in the bands.

Bands	Cluster size	Nanoparticle size	ω_s^{exp}	ω_s^{theor}
Blue	Film	50 nm	-	-
Purple	500 nm	10-25 nm	3.443×10^{15} s^{-1} 547 nm	3.4×10^{15}s^{-1} a~15 nm b~25 nm q=0.1
Pink	300 nm	8-15nm	3.664×10^{15} s^{-1} 514 nm	3.7×10^{15}s^{-1} a~10 nm b~15 nm q=0.07
Implantation band	-	2-6 nm	3.316×10^{15} s^{-1} 568 nm 4.956×10^{15} s^{-1} 380 nm	3.25×10^{15}s^{-1} a~3 nm b~10 nm q=0.01

Keywords: *Erratum; Optical; Permittivity*

ВИПРАВЛЕННЯ: ВИБІР МОДЕЛІ ДІЛЕПРОНИКНОСТІ НА ОСНОВІ РОЗМІРУ ТА КВАНТОВО-РОЗМІРНОГО ЕФЕКТУ У ПЛІВКАХ ЗОЛОТА

Юлія Рябенко[a,b,*], Сергій Шульга[a], Микола А. Макаровський[c], Костянтин Бєлошенко[a]

[a]*Харківський національний університет імені В.Н. Каразіна,*
факультет радіофізики, біомедичної електроніки та комп'ютерних систем, Харків, Україна
[b]*Інститут квантової оптики Ганноверського університету Лейбніца, Ганновер, Німеччина*
[c]*Харківський національний університет імені В.Н. Каразіна, фізичний факультет, Харків, Україна*

Метою цієї статті є виправлення помилки, представленої в оригінальній статті.
Ключові слова: *виправлення; оптичний; діелектрична проникність*

Original Article:

PERMITTIVITY MODEL SELECTION BASED ON SIZE AND QUANTUM-SIZE EFFECTS IN GOLD FILMS

Iuliia Riabenko[a,b], Sergey Shulga[a], Nikolai A. Makarovskii[c], Konstantin Beloshenko[a]
[a]*V.N. Karazin Kharkiv National University, School of radiophysics, biomedical electronics and computer systems, Kharkiv, Ukraine*
[b]*Institute of Quantum Optics, Leibniz University Hannover, Hannover, Germany*
[c]*V.N. Karazin Kharkiv National University, School of Physics, Kharkiv, Ukraine*